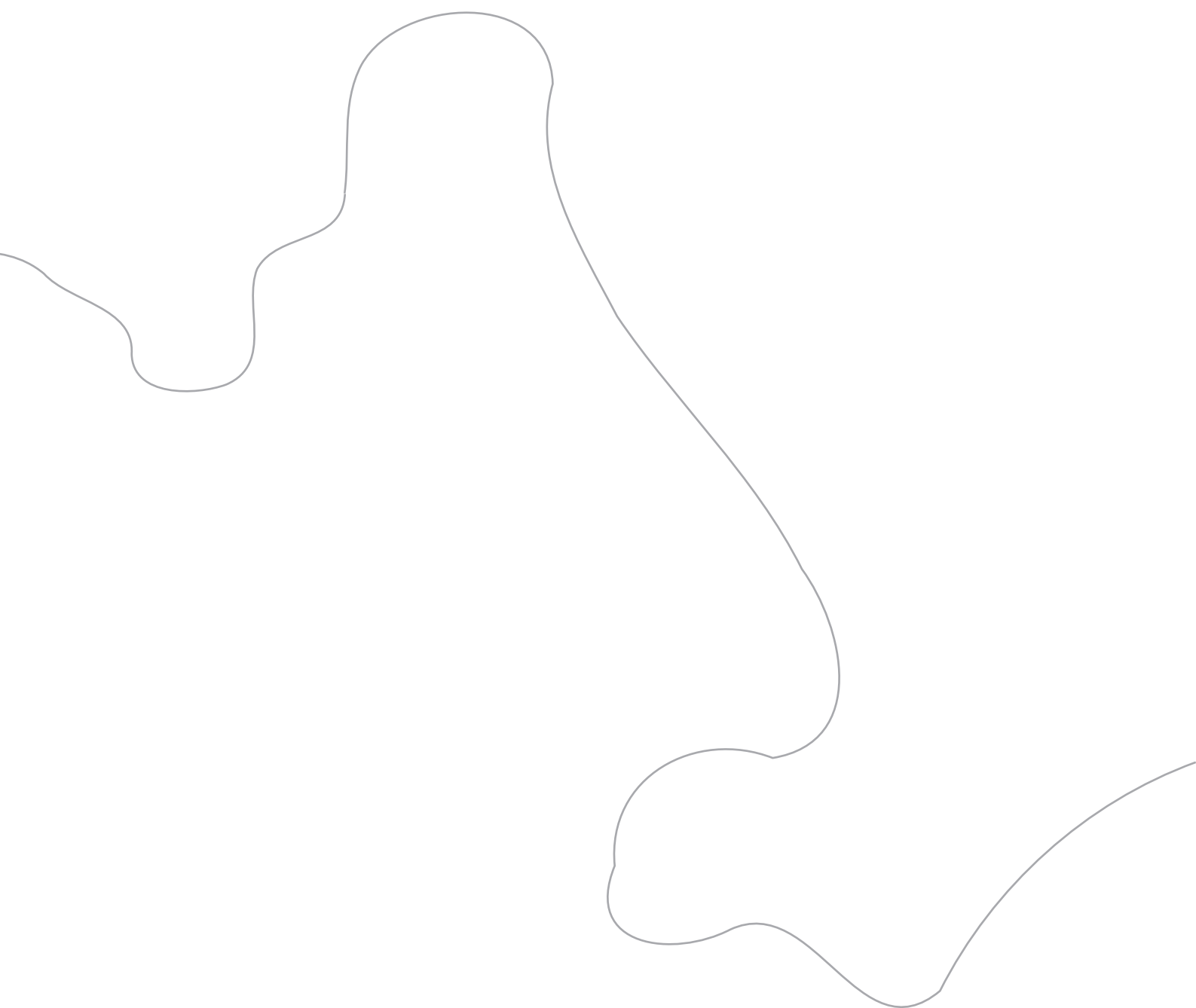# DISCHARGE REGIMES, TIDES AND MORPHOMETRY IN THE MAHAKAM DELTA CHANNEL NETWORK

M.G. Sassi

Discharge regimes, tides and morphometry in the Mahakam delta channel network

M. G. Sassi

Thesis committee

Promotor
Prof. dr. ir. R. Uijlenhoet
Professor of Hydrology and Quantitative Water Management
Wageningen University

Co-promotor
Dr. ir. A.J.F. Hoitink
Associate professor, Hydrology and Quantitative Water Management Group
Wageningen University

Other members
Prof. dr. J. Best, University of Illinois, USA
Prof. dr. S. Lane, Université de Lausanne, Switzerland
Prof. dr. H.H.G. Savenije, TU Delft
Prof. dr. J. Molenaar, Wageningen University

Discharge regimes, tides and morphometry in the Mahakam delta channel network

M.G. Sassi

Abstract

The Mahakam delta in Indonesia constitutes a text book example of a mixed tide and fluvial dominated delta. Understanding the factors that control the division of water and sediment discharge over channels in the delta is relevant in the contexts of geology, ecology and river engineering. In the Mahakam river and its delta, the tide interacts with the river outflow. River-tide interaction exerts an influence on the discharge regimes and on the division of water and sediment at the bifurcations in the delta. Bifurcations control the dispersal of sediments that eventually govern the shape and evolution of the delta. In this thesis, spatial and temporal aspects of delta evolution are shown to be reflected in scaling relations between the geometric properties of delta channels and the discharge conveyed by the channels, which is known as downstream hydraulic geometry (HG). Downstream HG relations as established in this research, feature a transition from the landward part to the seaward part of the delta characterized by a clear break in scaling behavior. The variation of river discharge throughout the network is largely impacted by river-tide interaction, which is captured by downstream HG relations.

Acknowledgments

Contents

Chapter 1

Introduction

1.1 Context

River deltas are fundamental landforms where the sediment transported by the river is being deposited. Deltas around the world provide mankind with opportunities for agriculture, aquaculture and fisheries, and a direct connectivity between the hinterland and the open waters. A number of factors such as sediment input, sea-level and tectonics, control the long-term (millennial) evolution of modern river deltas. At shorter time scales, however, it has been recognized recently that the sustainability of deltas around the world is more threatened by human intervention than by climate change (*Syvitski*, 2008). River discharge and sediment delivery to the world's oceans is known to have changed in relatively short time-spans by both climatic and anthropogenic factors (*Milliman et al.*, 1999; *Syvitski et al.*, 2005a; *Milliman et al.*, 2008), readily affecting the discharge input to river deltas (*Meade*, 1996). Studies on sea-level rise have shown that anthropogenic influence is typically more dominant than climate-change (*Ericson et al.*, 2006). Human intervention acting on such short time-scales has resulted in completely new redefinitions (*Syvitski and Saito*, 2007) of existing architectural river delta classification schemes (see Fig. 1.1, *Galloway*, 1975). The future evolution of river deltas resulting from a complex combination of natural and human activity, however, can only be challenged if the present state can be understood (c.f. *Geleynse et al.*, 2011). Thus, the scaling, stability and transformation of delta distributary networks constitute subjects of great importance in studies of river deltas.

Distributary channels control the dispersal of sediment, nutrients and contaminants to the coastal zone, exerting a large impact on the morphology and the ecology of river deltas (*Syvitski et al.*, 2005b). Unlike drainage networks in rivers upland, that follow almost a universal scaling behavior (*Jerolmack*, 2009), the scaling behavior of delta channel networks is highly dependent on the competing processes acting in the delta (*Geleynse et al.*, 2011). Competing processes,
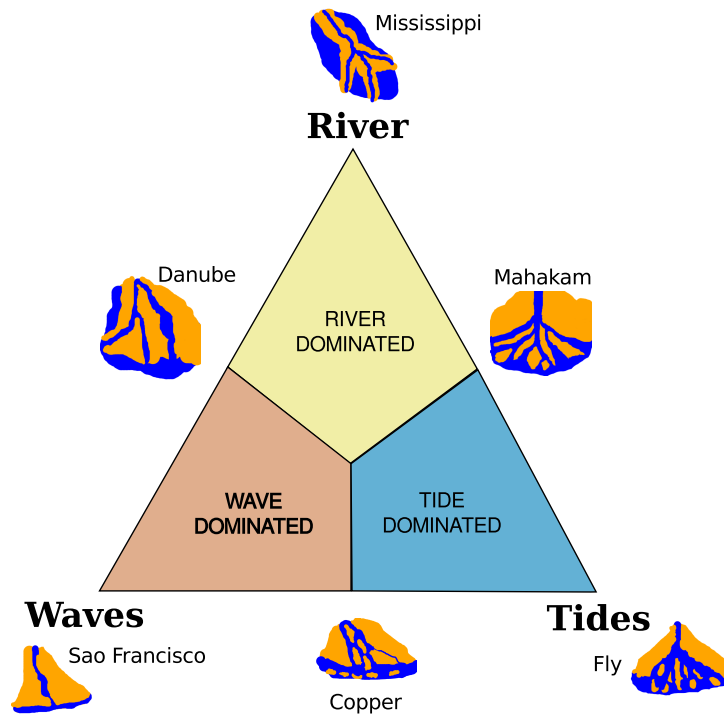
Figure 1.1: Triangular classification of deltaic depositional systems (modified after *Galloway* (1975)).

driven by fluvial input, tides and the action of waves on the coast (*Galloway*, 1975), have been placed in a wider context to include also the sediment caliber (*Orton and Reading*, 1993), different degrees of human intervention (*Syvitski and Saito*, 2007) and the role of cohesion and vegetation (*Edmonds and Slingerland*, 2010). Deltas are known to evolve through time driven by these competing processes, separately or in combination (*Tanabe et al.*, 2003, 2006). Despite these processes acting at a very wide range of temporal and spatial scales, the topology of distributary channel networks is a result of two fundamental mechanisms, namely mouth-bar deposition and channel avulsion (*Jerolmack*, 2009). Mouth-bar distributary lengths scale with the width of the parent channel, producing relatively small (compact) channel networks with typical fractal branching patterns (*Edmonds and Slingerland*, 2007). Avulsive distributary lengths scale with the backwater length, typically resulting in few but long distributaries (*Jerolmack and Swenson*, 2007). Each of the competing processes or a combination thereof can therefore determine the topology of a network by suppressing any of the two fundamental mechanisms of delta evolution.

Being regarded as a classic example of mixed tide and river dominated delta (*Galloway*, 1975; *Orton and Reading*, 1993; *Storms et al.*, 2005), the Mahakam delta channel network in East Kalimantan, Indonesia, shows a clear distinction between fluvial and tidal distributary domains (*Allen et al.*, 1977). Two active fluvial distributary systems directed towards the northeast and the southwest and a tide-dominated inter-distributary zone promptly depict the morphology of the delta (Figure 1.2). At first glance, the Mahakam delta corresponds to a mouth-bar distributary channel network, which is supported by the lack of channel avulsions (*Allen et al.*,
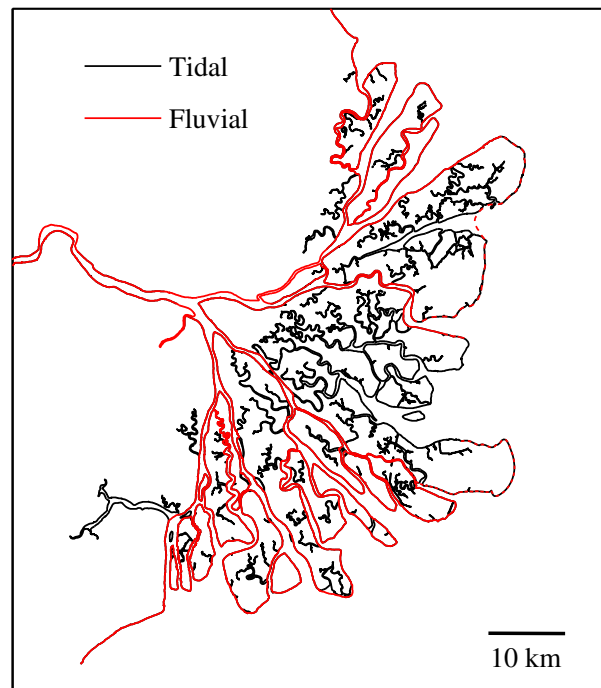
Figure 1.2: The Mahakam delta channel network showing distinct fluvial and tidal distributary domains (modified after *Allen et al.* (1977)).

1977; *Storms et al.*, 2005). Distributary channel lengths, however, do not seem to decrease systematically towards the shore, whereas channel widths clearly depict an increasing trend. Tidally-influenced deltas generally show a distinct channel network when compared to their purely fluvial counterparts. Tidally-influenced deltas can have many tidal channels attached to the fluvial distributary network, with one or two active fluvial distributary channels that may be stable for thousands of years (*Tanabe et al.*, 2003; *Olariu and Bhattacharya*, 2006). The relative stability and elongated planform shape of tidally-influenced distributaries (*Olariu and Bhattacharya*, 2006) suggests that tides can be influential on the progradation patterns.

1.2 Motivation

The River Mahakam runs across a relatively flat subsiding basin characterized by a very mild slope. During normal river flow conditions, semidiurnal and diurnal water level fluctuations induced by the tide can be measurable up to the lakes region, which is located about 200 km from the river mouth. It has been suggested that tidal processes may have a dampening effect on the fluvial dynamics of the delta region (*Allen et al.*, 1977), leading to the characteristic progradation pattern, void of channel avulsions. This has been later ascribed to the characteristic non-flooding discharge regime of the lower Mahakam catchment area (*Storms et al.*, 2005). During high-flow discharge conditions, the lakes upstream buffer the flood peaks, resulting in a relatively constant discharge regime in the lower reaches of the River Mahakam (*Hidayat et al.*,

INTRODUCTION

2011). The depositional pattern in the Mahakam delta is very complex, ranging from fluvial sandy bars to tidally-induced mud deposits (*Gastaldo*, 1992; *Lambert*, 2003). Although tidal and fluvial dominance have changed throughout time, affecting the tidal or fluvial character of some of the channels, the presence of characteristic sand-mud couplets indicates that deposition in the Mahakam delta is mainly driven by the spring-neap tidal cycle instead of the semidiurnal or diurnal tidal cycle (*Storms et al.*, 2005).

Since volumetric estimates of sediment quantities infilled by the river during the past five thousand years suggest that present day sediment-loads are too low to have resulted in the formation of the late-Holocene (or modern) Mahakam delta (*Storms et al.*, 2005), one may argue the lakes upstream have been absent during progradation. The buffering effect of the lakes has a large effect on fine sediment retention and its absence may imply a much higher sediment load issued to the delta. In turn, the tidal influence is expected to have increased steadily with sea-level rise over the past thousands of years, which drives an increased sedimentation rate due to the supply of fine sediments to the delta plain. This scenario, however, cannot explain the lack of channel avulsions or the presence of sand-mud couplets in the stratigraphic record, since all fluvial instability that is hypothetically buffered by the lakes can distort the observed progradation and depositional patterns.

The influence tides may have on river discharge is difficult to explain solely on the basis of their own contribution. Tides can induce flow variations on the timescale of hours that have limited or non-existent intervention in the discharge regimes. However, tides interacting with the river discharge can induce flow and water level variations typically in the order of days or weeks (*Buschman et al.*, 2009). In tidal rivers such as the Mahakam, the incoming tide interacts with the river discharge and creates a fortnightly oscillation in water level (*LeBlond*, 1979). The fortnightly tide could have a modulating effect on the drainage of the lakes region in the River Mahakam: flood peaks may be admitted during neap tides, while being counteracted during spring tides.

Sediment transport may also be affected by the river-tide interaction mechanism, thus exerting influence on the sediment yield in the delta region. Besides flows being modulated at specific frequencies, the variation of water and sediment discharge throughout the network may be largely affected by the tide and its interaction with river discharge. River discharge division at bifurcations leads to the division of sediment transport (*Wang et al.*, 1995), which has profound implications for delta morphology. In river deltas, asymmetrical bifurcations are prevalent because they are stable to a wider range of perturbations than symmetrical bifurcations (*Edmonds and Slingerland*, 2008). In tidally-influenced bifurcations, tides can enhance or reduce asymmetry in the division of river discharge (*Buschman et al.*, 2010), thus affecting their stability. The long-term stability of tidally-influenced bifurcations could eventually explain the relative stability and characteristic progradation patterns of tidally-influenced deltas.

This thesis aims at exploring how fluvial discharge and tides lead to mechanisms that may shape the morphology of the Mahakam distributary channel network. I will investigate several aspects of tidal hydrodynamics and sediment transport in fluvial environments, in relation to scaling and stability of the Mahakam delta. These aspects include how river-tide interaction induce flow variations in the tidal river and delta channels, how water and sediment discharge is divided in the tidally-influenced bifurcations in the delta, and how fluvial and tidal discharges are accommodated by the channel network. Besides understanding physical processes that may

be relevant to tidally-influenced deltas, this thesis aims to improve measurement methods in research focusing on rivers and tidal channels.

1.3 Research Questions

1.3.1 Tidal Rivers

Rivers debouching into the sea are subjected to tidal variation at the river mouth. In lowland regions, farther away from the estuarine environment where fresh and saline waters meet, tides have a significant impact on the river flow by means of subtidal (averaged over a diurnal period) water level variations controlled by river-tide interaction (*Buschman et al.*, 2009). The tidal wave propagating up-river experiences distortion and damping induced by bottom friction (*Godin*, 1999) and river discharge (*Horrevoets et al.*, 2004). Bottom friction leads to the creation of overtides (*LeBlond*, 1978), which typically affect the amplitude and timing of high and low water (*Godin*, 1985, 1991a), and compound tides (*LeBlond*, 1979) that are the cause of fortnightly variation in water level. During spring tides, bottom friction is higher and the water level increases; the opposite occurs during neap tides. As a consequence, river stage undergoes subtidal modulation over a fortnight (*LeBlond*, 1979). Besides this apparent oscillatory effect, river-tide interaction creates a steady gradient in the water surface, which steepens the surface profile of the river up to the point of tidal extinction (*LeBlond*, 1979; *Godin and Martinez*, 1994). The influence of this long-term water level setup may reach much further inland than the tidal motion itself (*Godin and Martinez*, 1994), potentially intervening in the discharge regimes of tidal rivers. In this context, this thesis aims to provide answers to the following research questions:

- Can tides modulate floods and low flows?

- If so, which are the underlying mechanisms?

- Which are the implications of river-tide interaction to sediment transport?

1.3.2 River Bifurcations

Channel junctions are key elements in tidally-influenced delta channel networks, and control the division of water and sediment discharge over downstream channels. Suspended sediment dispersal, which has effects on the morphology and on the ecology of the delta, is controlled by these junctions, which can be regarded as river bifurcations fed by alluvial flows under the influence of tides. Bifurcating channels are ubiquitous in anabranching rivers (e.g. *Burge*, 2006), in braided rivers (e.g. *Richardson and Thorne*, 2001), and particularly in river deltas. The processes occurring at bifurcations have been investigated theoretically (e.g. *Wang et al.*, 1995; *Bolla-Pitaluga et al.*, 2003), with numerical models (e.g. *Lane and Richards*, 1998; *Dargahi*, 2004), with physical models (e.g. *Zanichelli et al.*, 2004; *Islam et al.*, 2006) and in experimental flumes (e.g. *Federici and Paola*, 2003; *Bertoldi and Tubino*, 2005). In general, discharge division at river bifurcations is characterized by local hydraulic conditions and by the discharge capacity of the branches, determining preferential directions of water and sediment pathways. In tidal

regions, tides that intrude from the mouths of distributaries and tidal channels can exert a strong influence on water and sediment discharge division (*Buschman et al.*, 2010). At present, predicting such partitioning under different discharge and tidal regimes is concealed by the poor understanding of the processes occurring in tidally-influenced river bifurcations. Hence, this thesis aims to provide answers to the following research questions:

- How is water and sediment discharge divided at the main bifurcations in the Mahakam delta?

- What is the effect of tides on water and sediment discharge division?

- Which factors ultimately control sediment transport processes at these bifurcations?

1.3.3   Delta Channel Networks

The channel network is the skeleton of a delta as it maintains the flux of sediments necessary for the delta to prograde. In distributary mouth-bar river deltas, channel geometry scales according to a power-law relation between the channel cross-sectional area and the water discharge conveyed by the channel. The exponent in this relation typically lies in between 0.8 and 1.2 (*Edmonds and Slingerland*, 2007). In tidal channel networks without river influences, this exponent often shows the same range of variation, but the tidal prism or peak tidal discharge is used instead of a discharge with a constant frequency of exceedance (e.g. *D'Alpaos et al.*, 2010). Channel geometry in tidally-influenced river deltas can show a mixed scaling behavior of fluvial and tidal channel networks, as the channel forming discharge is both of river and tidal origin. As a consequence, tidal processes play a prominent role in the morphological evolution of tidally-influenced river deltas (*Geleynse et al.*, 2011), which may also have an impact on the response of the delta to changes in river discharge (*Edmonds et al.*, 2010) and ultimately on its evolutionary structure (*Wolinsky et al.*, 2010). Here I will focus on the following research questions:

- Does the topology of the Mahakam channel network show a mixed scaling behavior and if so, how is the scaling behavior related to the tides?

- Which are the implications of river-tide interaction to tidally-influenced river deltas?

1.4   Approach

The River Mahakam and its delta can be regarded as a land-sea continuum. The system is constrained by forces of a much different nature, acting at very different spatial and temporal scales. Landwards, the dynamical interplay between the climatic forcing and the topography results in precipitation patterns acting at the catchment scale. These patterns ultimately impose the discharge regimes in the upstream areas of the river (*Hidayat et al.*, 2011). Seawards, water levels in the river and delta are mainly controlled by sea-level and the oceanic tides which act at several time-scales. Therefore, discharge regimes in the Mahakam land-sea continuum are characterized by temporal scales typically spanning from hourly to seasonal (*Sassi et al.*,

2011a). When tides propagate through the delta channels, they induce flows in either direction of the channel. These flows acting on different channels of the network are being combined and split at junctions and interact with the incoming river discharge. Understanding the Mahakam land-sea continuum necessarily requires a multi-scale approach, both in space and in time.

The approach in this thesis is a mixture of field-based observations and hydrodynamical modeling. Model tools can help exploring environmental flow variables at times and locations where measurements were not available and to perform sensitivity studies. Until recently, hydrodynamical models were not able to simulate multi-scale processes in a parsimonious way (*Deleersnijder et al.*, 2010). Achieving geometrical flexibility with numerical schemes based on the traditional finite differences requires complex model structures such as domain decomposition or grid nesting (*Deleersnijder and Lermusiaux*, 2008). Finite element methods, in turn, allow to represent complex geometries such as those imposed by the Mahakam delta channel network in a simple way. Here I employ the finite-element hydrodynamical model SLIM[1], to simulate the complex flows driven by river discharge and tides in the Mahakam delta channel network.

Sampling of environmental flow variables with traditional monitoring techniques cannot cope with a multi-scaling approach either. Monitoring water discharge and sediment transport typically requires a significant amount of man power, which makes sampling these variables at widely different temporal and spatial scales less efficient and more costly (*Wren et al.*, 2000; *Gray and Gartner*, 2009). Technological advances in acoustic instrumentation, however, have lead to increased possibilities in multi-scale monitoring of environmental flows. Acoustic Doppler current profilers (ADCPs) mounted on a vessel have been employed for nearly two decades to quantify flows in marine, estuarine and fluvial environments because of the ability of ADCPs to resolve spatial and temporal heterogeneities in the flow field. The use of ADCPs to regularly monitor water discharge in rivers is becoming more common because ADCPs can easily replace arrays of single-point flow-meters and can be deployed in any cross-section along the river. The trade off between spatial and temporal coverage and measurement accuracy, however, still requires caution when designing fieldwork campaigns. Here I employ ADCPs to continuously monitor river discharge for a period of nearly a year and a half, to quantify the flow division at two main river bifurcations in the delta, and to quantify mass concentration of sediments in suspension at several locations.

1.5   Thesis Outline

This thesis is organized in seven chapters (see Figure 1.3), besides this introduction. **Chapter 2** is concerned with discharge regimes in the River Mahakam by introducing a novel method to accurately monitor river discharge continuously with a Horizontal acoustic Doppler current profiler (H-ADCP). **Chapter 3** explores in detail the mechanism of river-tide interaction based on observations of water levels along the river and flow velocities obtained at the discharge station. Based on a numerical model that simulates the flows driven by river discharge and tides in the delta, **Chapter 4** shows that tides have an impact on the division of river discharge at bifurcations of the Mahakam delta. **Chapter 5** is devoted to the quantification of suspended

---

[1]Second-generation Louvain-la-Neuve Ice-ocean Model (SLIM, www.climate.be/slim)

Chapter 2
Discharge regimes

Chapter 4
Water discharge
division

Chapter 3
River-tide interaction

Chapter 5
Suspended sediments

Chapter 7
Hydraulic geometry

Chapter 6
Sediment discharge
division
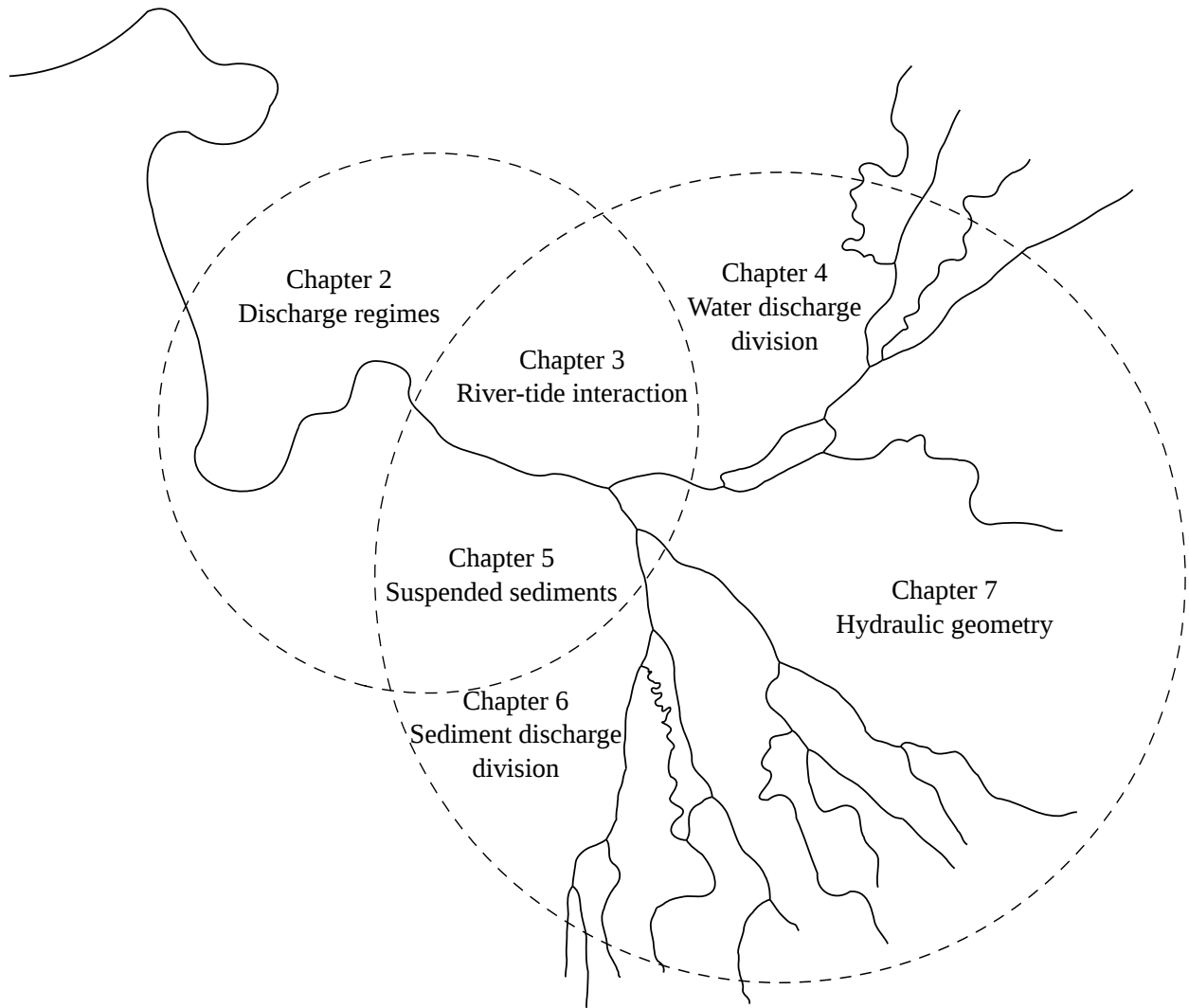
Figure 1.3: How this thesis is organized: focus area per chapter.

sediments in the River Mahakam and its delta by proposing a new strategy for ADCP backscatter calibrations. The proposed approach is applied at two tidally-influenced bifurcations in the Mahakam delta to quantify flow and sediment transport division (**Chapter 6**). **Chapter 7** investigates the scaling behavior of the Mahakam delta channel network by developing downstream Hydraulic Geometry (HG) relations. Finally, the synthesis in **Chapter 8** answers the research questions posed in the introduction, and offers an outlook.

INTRODUCTION

Chapter 2

Discharge Regimes

Abstract: Horizontal acoustic Doppler current profilers (H-ADCPs) can be employed to estimate river discharge based on water level measurements and flow velocity array data across a river transect. A new method is presented that accounts for the dip in velocity near the water surface, which is caused by sidewall effects that decrease with the width to depth ratio of a channel. A boundary layer model is introduced to convert single depth velocity data from the H-ADCP to specific discharge. The parameters of the model include the local roughness length and a dip correction factor, which accounts for the sidewall effects. A regression model is employed to translate specific discharge to total discharge. The method was tested in the River Mahakam, representing a large river of complex bathymetry, where part of the flow is intrinsically three-dimensional and discharge rates exceed 8000 m^{3}s^{-1}. Results from five moving boat ADCP surveys covering separate semi-diurnal tidal cycles are presented, three of which are used for calibration purposes whereas the remaining two served for validation of the method. The dip correction factor showed a significant correlation with distance to the wall, and bears a strong relation to secondary currents. The sidewall effects appeared to remain relatively constant throughout the tidal cycles under study. Bed roughness length is estimated at periods of maximum velocity, showing more variation at sub-tidal than at intratidal time scales. Intratidal variations were particularly obvious during bi-directional flow conditions, which occurred only during conditions of low river discharge. The new method was shown to outperform the widely used index velocity method, by systematically reducing the relative error in the discharge estimates.

2.1   Introduction

Continuous series of river discharge are crucial in studies of water resources. Rainfall-runoff models generally depend on water discharge series both for calibration and for validation of model concepts (*McMillan et al.*, 2010). Hydrodynamical models often rely on discharge series as boundary conditions (*Liu et al.*, 2007). Conventional methods to estimate water discharge series include a number of uncertainties which are dependent on flow conditions (*Di Baldassarre and Montanari*, 2009). In large rivers, the relation between stage and discharge is often ambiguous (*Petersen-Overleir*, 2006). Hysteresis effects often inhibit extrapolation of a rating curve beyond the range of measurements used for its derivation (*Dottori et al.*, 2009). In tidal rivers, the rating curve concept fails to describe the relation between water level and discharge because water level is not solely a function of river flow (*El-Jabi et al.*, 1992). Tides induce flows at time scales ranging from hours to days, invalidating the steady flow assumption. Time-lags associated with these rapidly varying flows produce complex flow patterns across river channels. Horizontally deployed Acoustic Doppler Current Profilers (H-ADCPs) can measure water level and flow velocity across the river section, which in combination with moving-boat ADCP measurements provide a promising alternative to conventional methods.

Over the past decade, several methods to infer river discharge from H-ADCP measurement have been reported. *Nihei and Kimizu* (2008) developed a dynamic interpolation and extrapolation method, assimilating H-ADCP data with numerical simulations. *Le Coz et al.* (2008) compared the Index Velocity Method (IVM, see *Simpson and Bland* (2000)) and the Velocity Profile Method (VPM) with several far-field extrapolation techniques. The IVM is widely being used, and consists of regressing section-averaged velocity with an index velocity from the H-ADCP. The VPM computes discharge over the cross section (total discharge) from theoretical vertical velocity profiles made dimensional with the H-ADCP velocity measurements and integrated over the cross section. Recently, *Hoitink et al.* (2009) combined the IVM and VPM approaches in a semi-deterministic, semi-stochastic method to convert H-ADCP measurements to water discharge. The deterministic part relied on the validity of the law of the wall, to calculate discharge per unit width (or specific discharge) from single depth H-ADCP velocity data. The obtained specific discharge is then regressed against time-shifted total discharge, which constitutes the stochastic part of the method. The method takes into account the time lag between specific and total discharge, which is relevant especially in tidal areas or wide inland rivers.

Crucial in the deterministic part of the approach by *Hoitink et al.* (2009) is the determination of the effective hydraulic roughness length (z_0), parameterizing river bed roughness. Throughout a single semi-diurnal tidal cycle, they found that z_0 remains relatively constant during periods of ebb and flood. Constancy of z_0 assures the validity of the law of the wall, which allows to estimate depth-mean velocity from measured single-depth velocity. In an alluvial channel, bed roughness depends on the nature of bed material and its spatial variations, and on the dynamics of bed forms for a given bed material (*Yen*, 2002). Although the former is linked to sediment grain properties such as its grain size, the latter depends on flow depth and velocity. Changes in bed roughness due to bed forms can be substantial in flow over a sand bed (*van Rijn*, 1984a, 2007). In tidal environments, z_0 exhibits variations between ebb and flood which are more likely to be caused by flow conditions than by bed composition (*Dinehart*,

2002). Values of z_0 may also vary over a spring-neap cycle (*Cheng et al.*, 1999) and possibly over the long-term runoff fluctuations. Although the properties of bed material at a given cross section may be constant in time, the dynamic interplay of bedforms with flow conditions renders constancy of z_0 questionable. Here, we present data from five separate semi-diurnal tidal cycles, providing insight into the spatio-temporal development of z_0.

H-ADCPs are typically being deployed at a river bank, which implies that the highest quality flow measurements are obtained near the river bank. In open channels, the lateral wall is known to influence the shear stress distribution which may impact the cross-section averaged bed shear stress both in inbank flows (*Vanoni and Brooks*, 1957; *Cheng and Chua*, 2005) and in compound channels (*Shiono and Knight*, 1991; *Papanicolaou et al.*, 2007). Sidewalls not only affect the lateral shear stress distribution, but also the velocity field in their proximity (*Tominaga and Nezu*, 1991). In rivers, the position of maximum velocity in the water column generally appears below the surface, as opposed to the situation in tidal channels, where logarithmic velocity profiles prevail (*Lueck and Lu*, 1997; *Sime et al.*, 2007). The dip in the velocity profile is generally attributed to the generation of weak secondary flows (*Cardoso et al.*, 1989; *Nezu et al.*, 1993). Whether these are driven by turbulence anisotropy or by channel geometry, secondary flows affect streamwise velocity profiles by redistributing momentum. Although the velocity dip is most pronounced in open channels having a width to depth ratio less than 5, wide open channels can also show this effect near the riverbank (*Nezu and Nakagawa*, 1993; *Sukhodolov et al.*, 1998). Based on an analysis of the Reynolds equations, *Yang* (2005) showed that the energy from the main flow is transported toward the nearest boundary through a minimum relative distance, or normal distance to the boundary. Accordingly, the flow region near the riverbank can 'feel' the presence of the sidewall, resulting in a velocity distribution with the maximum velocity below the surface. In the present chapter we adopt a boundary layer model based on results from *Yang et al.* (2004b) and *Yang et al.* (2004a), to account for sidewall effects in upscaling H-ADCP data.

Discharge measurements obtained with a boat-mounted ADCP are affected by several sources of error (*Gonzalez-Castro and Muste*, 2007). Errors in estimates of boat velocity, used to convert velocity data in instrument coordinates to earth coordinates, can significantly bias discharge estimates. Boat velocity is measured with respect to a fixed reference by acoustic Bottom Tracking (BT) or by a Differential Global Positioning System (D-GPS). BT-estimated velocities are biased by sediment transport and high sediment concentration near the bottom (*Rennie et al.*, 2002). In turn, D-GPS velocity estimates are affected by boat operation, D-GPS precision and signal multi-path artifacts related to riverbank vegetation (*Rennie and Rainville*, 2006). Combining both systems, *Rennie and Millar* (2004) obtained spatial distributions of fluvial bed-load sediment transport by linking the bias in boat velocity estimated with D-GPS and BT, and the apparent bed-load velocity. In addition to the reference velocity, discharge measurements can be biased by heading errors (*Kolb*, 1995). Heading errors can cause a bias in boat track and thus also in velocity measurements. *Trump and Marmorino* (1997) compared two independent estimates of boat velocity with BT in combination with a gyrocompass, and a D-GPS system. Results showed that boat speed estimates agreed while direction estimates were strongly correlated to the boat heading from the gyrocompass. Here we present a correction method using a multi-antenna system, which can minimize the errors posed by gyro-compasses and D-GPS derived headings after proper calibration and determination of the

alignment between the ADCP and the compass.

The structure of this chapter is as follows. Section 2.2 introduces the boundary layer model accounting for sidewall effects, briefly repeating the work of *Yang et al.* (2004b). Section 2.3 introduces the study area, data collection and data processing methods. Section 2.4 describes the river bed composition, its morphology and data referencing techniques. Section 2.5 presents an analysis of the flow structure, focusing on the H-ADCP measurement range. In Section 2.6, the discharge estimation methodology is described and Section 2.7 presents the validation of the method. Sections 2.8 and 2.9 present a discussion and the conclusions, respectively.

2.2 Boundary Layer Model

In a steady, uniform and fully developed turbulent channel flow, the momentum equation in the streamwise direction can be written as:

$$\frac{\partial \left(\rho u w - \tau_{sz} \right)}{\partial z} + \frac{\partial \left(\rho u v - \tau_{sn} \right)}{\partial n} = \rho g S, \tag{2.1}$$

where s is defined as the streamwise direction, n is spanwise direction, z is normal distance from the bed, u,v,w are mean velocity components in the s, n and z directions, respectively, $\tau_{sz} \approx -\rho \overline{u'w'}$, $\tau_{sn} \approx -\rho \overline{u'v'}$, where u',v',w' are turbulent velocity fluctuations, ρ is fluid density, g is gravity acceleration and S denotes energy slope.

Near the bed, the first term on the left hand side of equation 2.1 is much greater than the second term (*Yang et al.*, 2004b). Integration along the vertical direction yields

$$-\overline{u'w'} = u_{*,b}^2 - gzS + uw, \tag{2.2}$$

where $u_{*,b}$ is shear velocity at the bottom. Equation 2.2 can be rewritten after the global shear velocity u_* is introduced:

$$\frac{-\overline{u'w'}}{u_*^2} = \left(1 - \frac{z}{H} \right) - \alpha_1 \frac{z}{H} + \frac{uw}{u_*^2} + c_1, \tag{2.3}$$

where $\alpha_1 = (gHS - u_*^2)/u_*^2$, H water depth and $c_1 = (u_{*,b}^2 - u_*^2)/u_*^2$. Measured profiles of Reynolds shear stress in open channel from the centerline to the sidewall show that $-\overline{u'w'}/u_*^2$ approaches 1 as z/H approaches 0 (*Immamoto and Ishigaki*, 1988), indicating that c_1 can be neglected.

The third term on the right-hand side of equation 2.3, reflecting the influence of secondary currents, can be approximated by the linear relation (*Yang et al.*, 2004b)

$$\frac{uw}{u_*^2} \approx -\alpha_2 \frac{z}{H}, \tag{2.4}$$

where $\alpha_2 > 0$. Therefore, an approximate relation for the Reynolds shear stress profile in open channel flow can be obtained as

$$\frac{-\overline{u'w'}}{u_*^2} = \left(1 - \frac{z}{H} \right) - \alpha \frac{z}{H}, \tag{2.5}$$

where $\alpha = \alpha_1 + \alpha_2 > 0$. The cross exchange of momentum by secondary flows is empirically modeled by steepening the dimensionless Reynolds shear stress profiles, because generally, secondary currents near the surface act in the downward direction and near the bed in the upward direction (*Nezu and Nakagawa*, 1993; *Yang et al.*, 2004b).

Mean velocity profiles can be obtained assuming that

$$-\overline{u'w'} = \nu_t \frac{du}{dz},$$

(2.6)

in which the turbulent eddy viscosity ν_t can be expressed as

$$\nu_t = \kappa u_* z \left(1 - \frac{z}{H}\right),$$

(2.7)

where $\kappa \approx 0.4$. Substituting equation 2.6 and 2.7 into equation 2.5, we obtain

$$\frac{du}{dz} = \frac{u_*}{\kappa z} - \frac{\alpha \frac{u_*}{\kappa H}}{\left(1 - \frac{z}{H}\right)},$$

(2.8)

which, after integration, yields the following expression for the velocity profile affected by sidewall effects:

$$u\left(z\right) = \frac{u_*}{\kappa} \ln\left(\frac{z}{z_0}\right) + \frac{u_*}{\kappa} \alpha \ln\left(1 - \frac{z}{H}\right),$$

(2.9)

where z_0 is the roughness length.

The second term on the right hand side of equation 2.9 decreases with depth, thus creating the velocity dip at the surface. The parameter α can be directly related to the relative height above the bottom of the maximum velocity according to:

$$\frac{z_{max}}{H} = \frac{1}{1 + \alpha}.$$

(2.10)

Results from experiments including a wide range of channel aspect ratios (*Yang et al.*, 2004b) indicate that α increases toward the banks, where the velocity dip becomes most pronounced. The dip-correction factor α can be approximated with the expression

$$\alpha = 1.3 \exp(-\frac{n}{H}),$$

(2.11)

where n is the spanwise coordinate or distance from the bank.

2.3   Study Area and Data Collection

Measurements were carried out in a 420 m wide cross section in the River Mahakam, East Kalimantan, Indonesia (Figure 2.1). Salinity intrusion generally reaches to about 10 km seaward the delta apex. Only during extremely low flows, such as the El Niño-related drought in 1997, salinity intrusion can reach beyond the delta apex. The study area is therefore generally subject to freshwater conditions. Due to the mild slope of the river, the tidal wave can propagate up to 190 km from the river mouth, depending on the river discharge. A 600 kHz H-ADCP
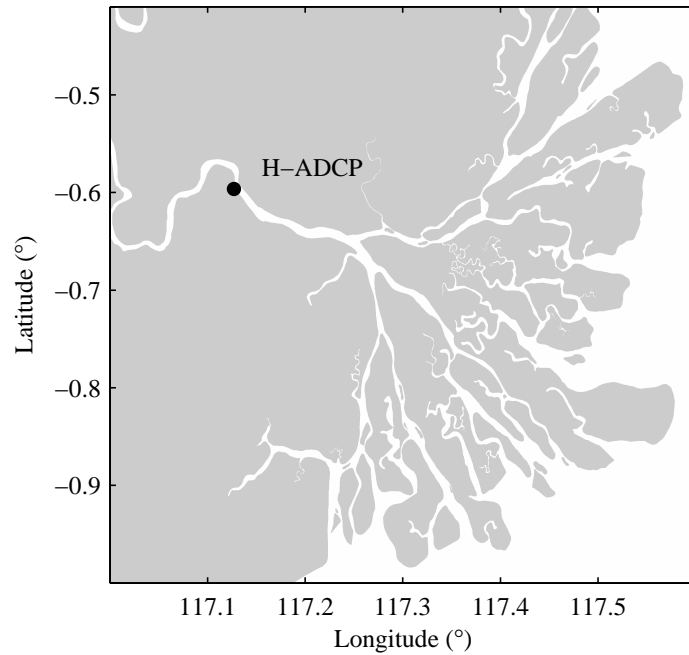
Figure 2.1: Location map showing the position of the H-ADCP in the River Mahakam. Salinity intrusion generally reaches to about 10 km seaward from the delta apex.

manufactured by RD Instruments was mounted for 525 days on a solid wooden jetty in a straight reach of the river, between two bends. This location was selected because of its relatively narrow cross section, maximizing the fraction of the river width covered by the H-ADCP (about one third). In addition, riverbanks at this particular location seem to be virtually fixed because they are naturally protected by the outcrops of a tertiary system citepbemmelen. The H-ADCP was mounted at 1.5 m below the lowest recorded water level and about 5 m from the bottom. Pitch and roll of the instrument remained constant during the measuring period, amounting to 0.06° and 0.55°, respectively. Because mean water depth rapidly increases to about 20 m, main and side-lobe beam interference due to bottom reflections was not expected because at 100 m range the vertical displacement of the beams would be 0.1 and 4 m, respectively. The measurement protocol for the H-ADCP consisted in 10 minute bursts at 1 Hz, every 30 minutes. An ensemble was an average over 600 pings and the horizontal cell size was 1 m. The range to the first cell center was 1.96 m.

Conventional boat-mounted ADCP discharge measurements were periodically taken in front of the H-ADCP. The research boat was equipped with a 1.2 MHz RDI Broadband ADCP measuring in mode 12, a multi-antenna Global Positioning System compass operating in differential mode (D-GPS) and a single-beam echo-sounder. The ADCP measured a single ping ensemble at approximately 1 Hz with a depth cell size of 0.35 m. Each ping was composed of 6 sub-pings separated by 0.04 s. The range to the first cell center was 0.865 m. The boat speed ranged between 1-3 m s^{-1}.

Along-channel (s) and cross-channel (n) coordinates for each ADCP campaign were defined on the basis of bed morphology following *Hoitink et al.* (2009). Easting and northing coordinates
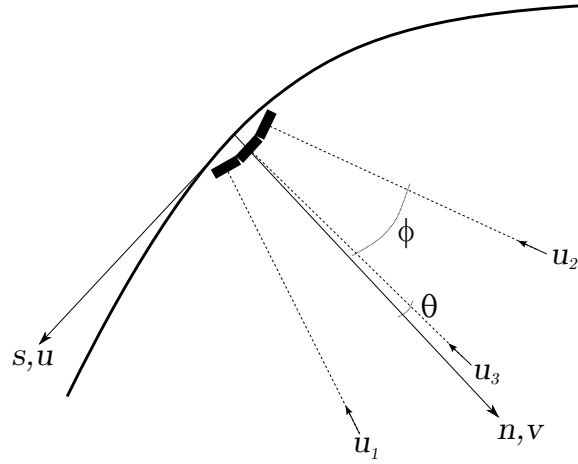
Figure 2.2: Definition sketch (top view), where u is velocity in the flood direction, coinciding with the s axis; v is across channel velocity toward the inner bend along the n axis; ϕ is the H-ADCP beam separation angle; θ is the angular difference between the n axis and the axis of the central acoustic beam of the H-ADCP, measured positive as indicated; u_1, u_2, and u_3 are the radial velocities along the three acoustic H-ADCP beams.

of the depth map were rotated systematically in steps of 0.5 degrees. For each rotation step, the root-mean-square deviations from mean values in the potential s direction were averaged. Depth variation along the s coordinate was found to be minimal when it deviated 165° from the North. Therefore, the positive s-coordinate is defined 165° with respect to the North. The n-coordinate points perpendicular to the s-coordinate, counterclockwise with its origin at the riverbank where the H-ADCP was deployed (Figure 2.2). The z-coordinate was defined pointing upward with its origin at mean water level. Mean water level was defined as the mean over the 525 days of observations. The variation around the mean water level, η, ranging roughly from -1 to 1 m, was caused by the combination of tidal and subtidal fluctuations.

The H-ADCP measures along three beams in a horizontal plane, with $\phi = 25°$ angles between the beams (Figure 2.2). In the current deployment, the pitch of the H-ADCP was nearly zero degrees and the central beam axis was rotated by an angle $\theta = 1.8°$ relative to the n-coordinate, in anti-clockwise direction. The along-beam velocities, denoted by u_1, u_2 and u_3, are positive toward the transducers and relate to the $\hat{u}$ and $\hat{v}$ velocity components according to

$$u_1 = -\hat{v}\cos(\phi - \theta) - \hat{u}\sin(\phi - \theta), \tag{2.12}$$

$$u_2 = -\hat{v}\cos(\phi + \theta) - \hat{u}\sin(\phi + \theta), \tag{2.13}$$

$$u_3 = -\hat{v}\cos(\theta) - \hat{u}\sin(\theta), \tag{2.14}$$

where the hat symbol is used to indicate that the velocity components can be considered a volume average over an acoustic target cell. Two of the three equations (2.12)-(2.14) suffice to calculate $\hat{u}$ and $\hat{v}$. The redundant beam is included in the instrument for error estimation. Because the n-axis falls between the centerlines of beams 1 and 3, we chose to calculate $\hat{u}$ and

17
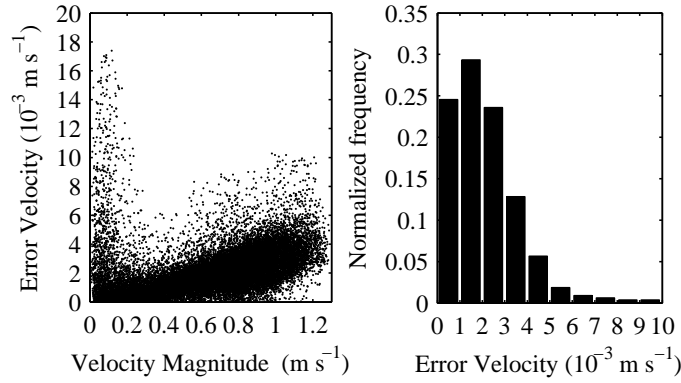
Figure 2.3: Left: absolute difference between velocity estimates obtained using equations (2.12) and (2.14) and corresponding estimates using equations (2.13) and (2.14), as a function of velocity magnitude, computed as the average of both estimates. Right: normalized frequency distribution of error velocity values lower than 0.01 m s^{-1}. Bin centers are spaced by 0.001 m s^{-1}.

Table 2.1: Summary of the boat mounted ADCP surveys with tidally averaged quantities.

Name	Date	Flow	Tide	$W\,(m)$	$A\,(m^2)$	η (m)	$U\,(ms^{-1})$	$Q\,(m^3s^{-1})$
Cal1	30-Nov-2008	High	Spring	420	8650	0.36	0.80	6760
Val1	17-Jan-2009	High	Spring	420	8610	0.27	0.75	6420
Cal2	12-Mar-2009	High	Spring	420	8620	0.29	0.56	4780
Val2	24-May-2009	Low	Mean	400	8110	0.04	0.52	4410
Cal3	06-Aug-2009	Low	Neap	410	8140	-0.38	0.10	740

$\hat{v}$ from equations (2.12) and (2.14), limiting the maximum beam separation to about 60 m at $n = 150$ m. Figure 2.3 shows the absolute difference between velocity estimates obtained using equations (2.12) and (2.14) and corresponding estimates using equations (2.13) and (2.14), as a function of velocity magnitude, computed as the average of both estimations. The error velocity is relatively large when the velocity magnitude is small (<0.2), which may be related to a reduction of flow homogeneity during weak flows. A minor systematic error increases with velocity magnitude, amounting to about 5 10^{-3} m s^{-1} at flows of 1.2 m s^{-1}. The normalized frequency distribution for error velocities in the range between 0 and 0.01 m s^{-1} shows that 90 % of the error is concentrated in the range 0-0.005 m s^{-1}, confirming inhomogeneity between the beams to be negligible.

To categorize flow conditions at each of the moving-boat ADCP surveys, we computed an index velocity (u_I) as the space-time average of the H-ADCP velocity components in the s-direction. The mean and the linear drift were removed from water level time-series recorded by the H-ADCP. Time-series of water level elevation and index velocity were subjected to a linear low-pass filter with cutoff frequency corresponding to 4 days, to yield the subtidal fluctuations. Subtidal fluctuations were subsequently filtered with a cutoff frequency corresponding to 56 days, to yield seasonal fluctuations (Figure 2.4).

The mean index velocity amounted to 0.61 m s^{-1} in downstream direction. High- (low-)
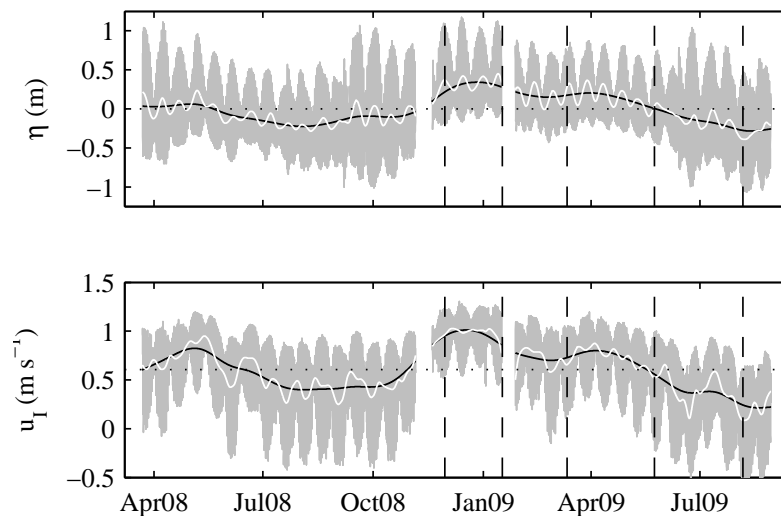
Figure 2.4: Water level elevation (top panel) and index velocity (bottom panel) from H-ADCP velocity profiles in gray lines. The phase difference between water level and index velocity is approximately 1.5 h. White and black lines show sub-tidal and seasonal fluctuations (respectively). Thin dotted lines indicate mean values. Vertical dashed lines indicate the date of each moving boat ADCP campaign.

flow conditions were defined as periods above (below) the mean index velocity. Spring (neap) conditions were defined as those periods when the difference between subtidal and seasonal fluctuations was positive (negative). Some ADCP surveys fall close to the intersection between the subtidal and the seasonal fluctuation curves, which therefore represent mean tide conditions. Five 13-h ADCP surveys were carried out spanning high- and low-flow conditions during spring and neap tides. A summary of the tidally averaged quantities during the moving-boat ADCP surveys is presented in Table 2.1. During low-flow conditions, tidally averaged discharge reaches well below 1000 $\mathrm{m}^3\,\mathrm{s}^{-1}$, with instantaneous flow in downstream as well as in upstream directions. During high-flow conditions, tidally averaged discharge attains values ranging between 4000 and 7000 $\mathrm{m}^3\,\mathrm{s}^{-1}$, with instantaneous flow in downstream direction only. We used three ADCP surveys for calibration purposes and the remaining two for validation of the method.

2.4   Bed Composition and Data Referencing

Transect data across the river with a single-beam echosounder were projected on a curvilinear grid based on linear interpolation (*Legleiter and Kyriakidis*, 2007) to produce the bathymetric map of the river (Figure 2.5). The bathymetry downstream of the H-ADCP location depicts a relatively shallow reach of about 12 m depth, while at the measurement section and upstream, very deep areas of up to 35 m occur. These deep trenches are most likely caused by confinement of the flow by non-erodible banks. The depth of these trenches is two to three times the mean water depth. Bed samples were obtained with a Van Veen grabber at locations nearby the H-ADCP. Samples from ten transects consisting of five bed samples each were sieved into eleven
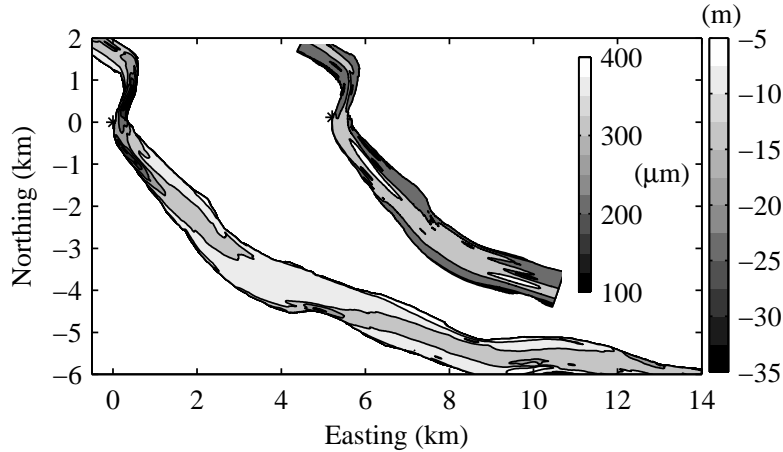
Figure 2.5: Bathymetry of the River Mahakam, Easting and Northing coordinates correspond to UTM (zone 50M) with respect to the position of the H-ADCP (denoted with the asterisk). Inset: map of median grain size D_{50} in μm in the surroundings of the H-ADCP location.

size classes to obtain a grain size distribution. Figure 2.5 also shows a map of the median grain size D_{50}, based on interpolation of the samples. The spatial distribution of D_{50} indicates that the river bed is mainly composed of fine to medium sands ($D_{50} = 200$-300 μm). Riverbanks comprise fine sands and large amounts of silt and clay. It is interesting to note the presence of some patches of coarser sand in the middle of the section, at irregular parts of the bathymetry.

To construct a local depth map, range estimates from acoustic bottom tracking were corrected for pitch and roll of the instrument, and referenced to the mean water level. The depth estimates were projected on a rectangular grid with a mesh size of about 2 m, which is slightly larger than a typical footprint of the ADCP beams, covering 1.5 m². Considering each beam of the ADCP as an independent depth estimator, we computed the root-mean-square-difference (RMSD) between depth estimates from the four beams. Figure 2.6 shows the spatial distribution of RMSD for a particular ADCP campaign, where values above 2 m were discarded. It shows an increase in regions where the slope is higher (towards the bank and in the deeper section), highlighting the inaccuracy of the ADCP depth estimates due to errors primarily from pitch and roll angles. RMSD values in the region in front of the H-ADCP remain within one meter, averaging to about 0.2 m. The coefficient of variation of the RMSD distribution, defined as the ratio of RMSD to the mean, indicates an overall error below 0.05, showing that the inaccuracy in bed topography estimates in the region in front of the H-ADCP with the bottom tracking system of the ADCP is acceptable.

Conversion from single point velocity to depth-mean velocity requires an accurate, time dependent description of bed topography along the measurement range of the H-ADCP. There-
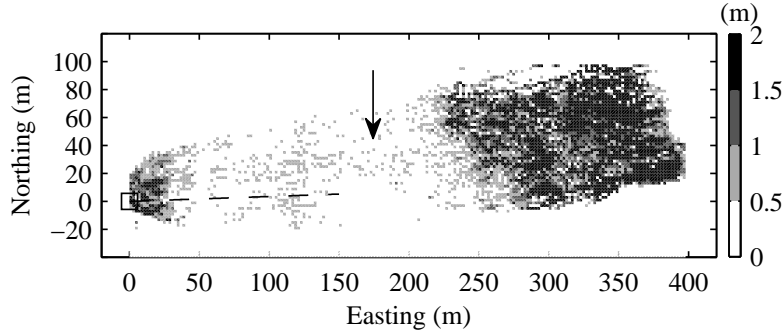
Figure 2.6: Spatial distribution of RMSD between depth estimates from the four beams of the ADCP, each averaged over a rectangular grid of 2 m spacing. The dashed line shows the 150 m range of the H-ADCP. The arrow points in the downstream flow direction.

fore, we computed the bathymetric map from each ADCP campaign over the area that covers the measurement range of the H-ADCP. Figure 2.7 shows a series of depth maps produced with each of the ADCP surveys, in which depth levels were confined to the range between 15 and 25 m. The local morphology shows a relatively flat bottom, gradually deepening toward the Northeast of the cross section. A relatively large transverse bottom slope up to 6% can be found at about 100-150 m from the H-ADCP. A bed feature located at midrange of the H-ADCP appears to evolve in time, as suggested by the contour lines on the maps. The bathymetric data in earth coordinates were transformed to local s-n-coordinates, and normalized with the width, computed as the length between the intersections of the n coordinate with the shorelines from a topographic map. Before normalization, we computed width, mean depth and area of each transect. Mean and standard deviation of the width to depth ratios from all moving boat ADCP surveys amounted to 22 and 2, respectively.

To compute flow velocity with respect to a fixed reference frame, boat speed must be subtracted first. Boat speed was computed for each ensemble with the Bottom Tracking (BT) and the D-GPS compass system. BT-derived boat speed estimates were biased by sediment transport during high-flow conditions because the moving bed creates an apparent velocity in the same direction as the flow (*Rennie et al.*, 2002). Therefore, flow speed and discharge were biased low when using the BT system during high-flow conditions. Denoting the boat velocity vector as $\vec{b}$, composed of a streamwise component b_s and a normal component b_n, we computed the difference between the boat speed vector from acoustic BT and from the D-GPS compass, resulting in the bias vector:

$$\vec{b}_{bias} = \vec{b}_{BT} - \vec{b}_{DGPS}. \tag{2.15}$$

Figure 2.8 shows width-averaged values of $b_{bias,s}$ as a function of width-averaged u_I. The error bars indicate the standard deviation computed from the boat speed estimates from individual width cells. Focusing on the streamwise direction, the velocity bias correlates with flow speed during each of the five moving boat ADCP surveys, which can be attributed to sediment transport. We transformed the flow velocity data in instrument coordinates to earth coordinates
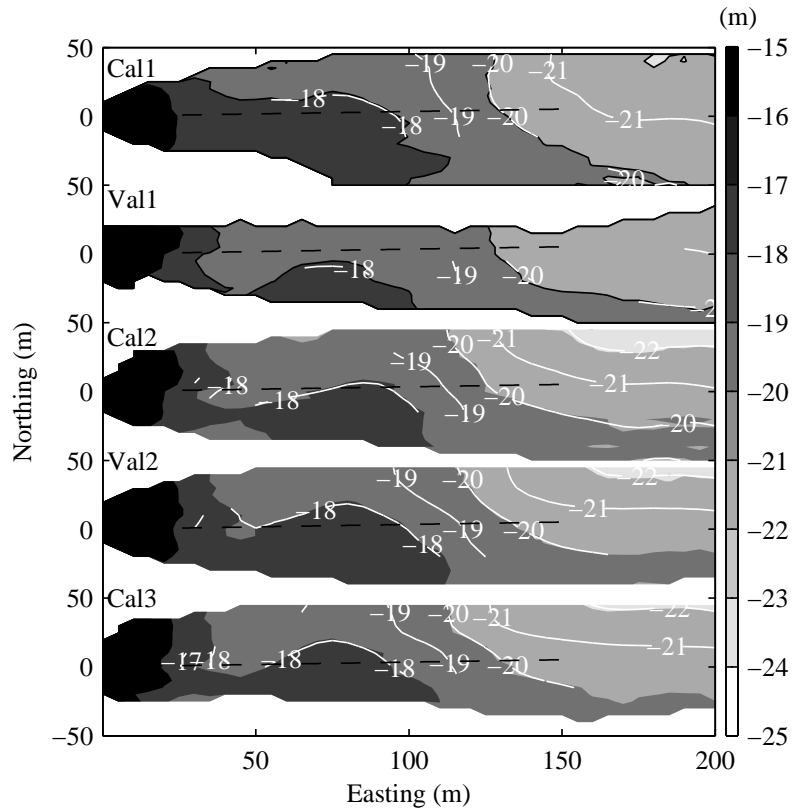
Figure 2.7: Evolution of bed morphology in the area in front of the H-ADCP, produced from local bathymetric maps obtained during each of the moving boat ADCP surveys. The dashed line shows the 150 m range of the H-ADCP. A bed feature at about half of the range of H-ADCP evolves in response to flow conditions.
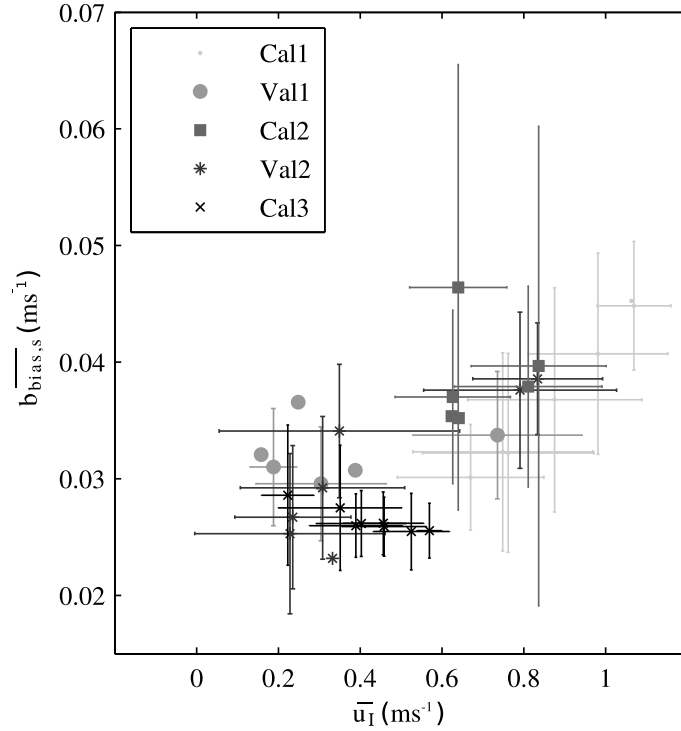
Figure 2.8: Scatter plot of $\overline{b_{bias,s}}$ versus $\bar{u}_I$, showing the ship velocity bias as a function of flow speed in the streamwise direction. The overbar denotes the width-averaged values.

with the D-GPS system during high-flows. During low flows ($u_I < 0.5$), the BT estimate of the boat speed was used, for its smaller scatter.

2.5   Flow Structure

The horizontal flow velocity vector $\vec{u}$ is composed of components u and v, defined in the s and n directions, respectively. Positive values of u coincide with downstream flow. Vertical profiles were transformed to relative height above the bottom according to:

$$\sigma = \frac{H + z}{H + \eta},\tag{2.16}$$

where η is water level variation. We normalized all transects within each ADCP campaign with the maximum width within that campaign, to yield a normalized spanwise n-coordinate, β. We followed the same normalization procedure for the horizontal velocity profiles obtained with the H-ADCP. This way, all velocity measurements were consistently referenced in time and space, projected onto a uniform grid in (σ,β) coordinates. The grid spacing is typically 0.5 and 5 m in the vertical and spanwise directions, respectively. ADCP velocity measurements have contributions of mean flow, turbulence and error components. To isolate the mean flow component from repeated transect measurements, we assumed the mass flux through (σ,β) grid

23

cells to be constant in the streamwise direction within the measurement range. Therefore, the product of u and $H + \eta$ is independent of s. The resulting time series were filtered with a cutoff frequency corresponding to 1.5 h, and the filtered values were divided by $H + \eta$ and averaged in the s direction over the range that was covered during the measurements. Hereinafter, u denotes the mean flow component in the s-direction.

2.5.1 Three-dimensional Velocity Pattern

Velocity profiles obtained from moving boat ADCP measurements were averaged over depth according to:

$$U\left(\beta, t\right) = \int_0^1 u\left(\sigma, \beta, t\right) \mathrm{d}\sigma, \; V\left(\beta, t\right) = \int_0^1 v\left(\sigma, \beta, t\right) \mathrm{d}\sigma. \tag{2.17}$$

Figure 2.9 shows the spatiotemporal distribution of U and V for each of the five moving boat ADCP surveys. The velocity patterns during the different surveys feature similar spatial characteristics. A well defined velocity core is centered at about $\beta = 0.7$. The magnitude and extension of the velocity core can be related to flow conditions. In Cal3, the velocity core becomes slightly shifted toward the center of the channel, because the bathymetry downstream of the cross-section has its thalweg in the middle of the river. Toward the opposite bank, U rapidly decreases to a zone of null velocity at about $\beta = 0.8$, and reverses for $\beta > 0.8$. Apparently, a recirculation cell in the horizontal plane is present, which may be the result of the sudden widening of the cross section (see Fig. 4). The intensity of the recirculating flow is positively correlated with flow strength, suggesting that during high-flows more momentum is withdrawn from the main flow in the form of a horizontal eddy. During low-flows, however, the horizontal eddy persists even during flood tide, when the direction of depth-mean flow reverses.

Values of V contain contributions from the mean flow. A region where $V = 0$ is found in all surveys at about $\beta = 0.65$ and in Cal1 at $\beta = 0.7$, which suggests that the along channel direction obtained from the bathymetry coincides approximately with the mean flow over the deep trench.

The three-dimensional velocity structure can be further understood from the tidally-averaged flow field. For this purpose a velocity component u' is defined which is aligned with the depth mean flow vector, according to:

$$\langle u' \rangle = \frac{1}{T} \int_T \left(u \frac{U}{\sqrt{U^2 + V^2}} + v \frac{V}{\sqrt{U^2 + V^2}} \right) \mathrm{dt}, \tag{2.18}$$

where the angular brackets denote averaging over a tidal cycle. Similarly, a zero-mean tidally-averaged spanwise component reads as:

$$\langle v' \rangle = \frac{1}{T} \int_T \left(u \frac{V}{\sqrt{U^2 + V^2}} - v \frac{U}{\sqrt{U^2 + V^2}} \right) \mathrm{dt}. \tag{2.19}$$

Figure 2.10 shows patterns of $\langle u' \rangle$ and $\langle v' \rangle$ for each of the ADCP surveys. The velocity core, located at about 280 m from the H-ADCP ($\beta = 0.7$), is located between mid-depth and the
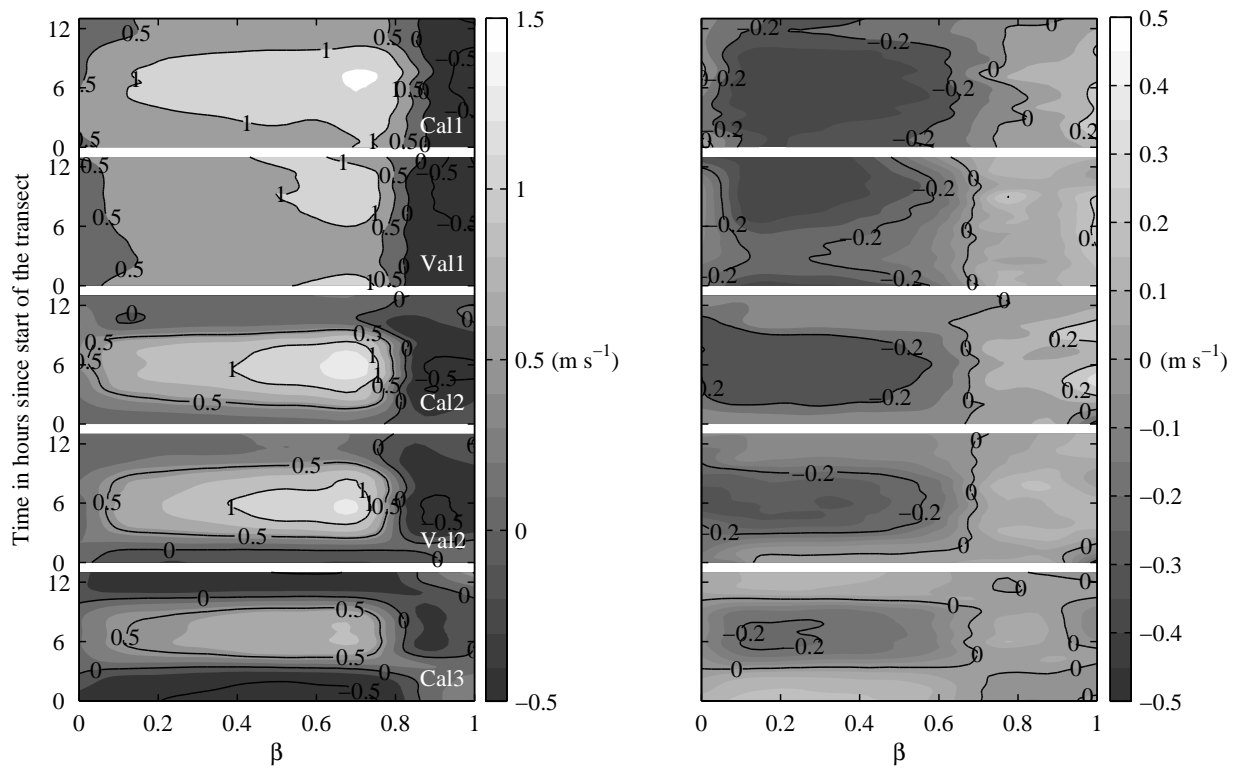
Figure 2.9: Depth averaged streamwise velocity U (left) and spanwise velocity V (right), as a function of normalized width and time, for each of the moving boat ADCP surveys.
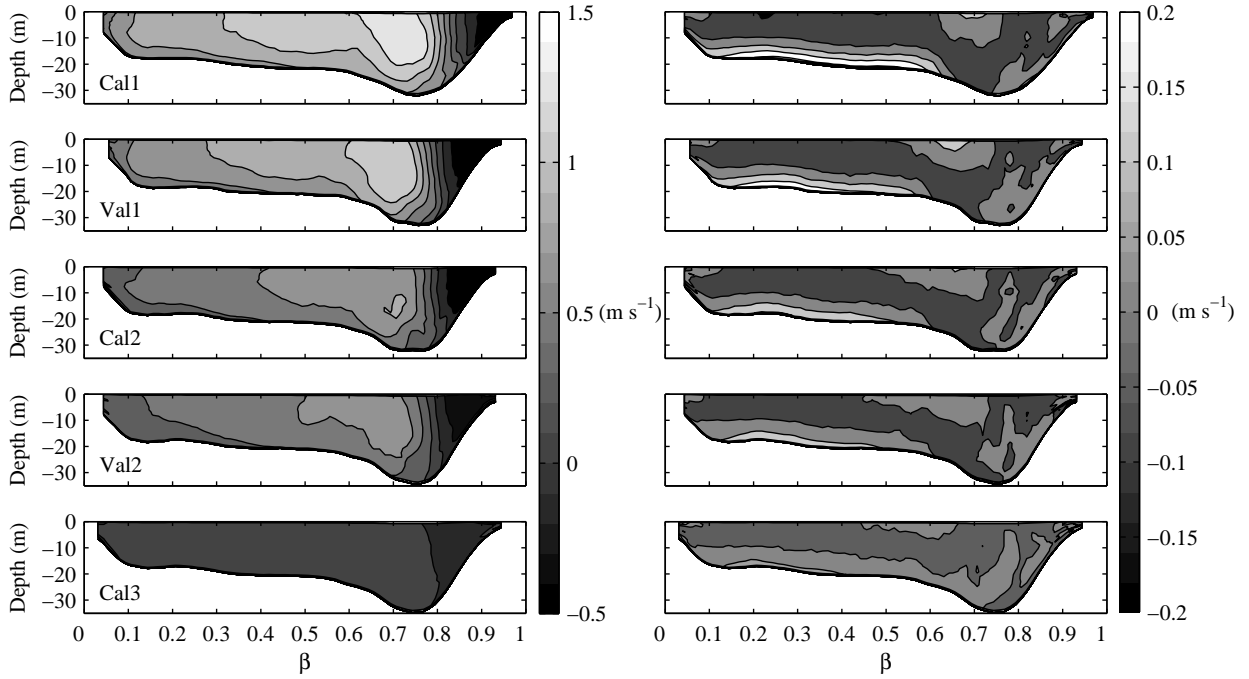
Figure 2.10: Spatial structure of $\langle u' \rangle$ (left) and $\langle v' \rangle$ (right) over the cross-section during each of the moving boat ADCP surveys. The vertical axes indicate depth in meters.

surface. Lines of equal velocity tend to compress much more over this portion of the section than in the region in front of the H-ADCP ($\beta < 0.5$ m). Close to the H-ADCP ($\beta < 0.2$ m), near surface velocities tend to decrease, becoming small in comparison with the depth-averaged flow. This behavior can be related to the normal flows created by secondary circulation cells in the proximity of the bank (*Nezu et al.*, 1993). The tidally-averaged flow field shows persisting secondary circulation cells across the section. The larger cell occupies half of the cross section and is likely triggered by curvature of the flow. The deeper part shows a more complex secondary circulation distribution which may be linked to the three dimensional flow pattern associated to the large bottom slopes in the deep trench.

The velocity field above the trench is intrinsically three-dimensional. Deterministic modeling of the flow would require a three-dimensional approach, as the flow cannot be assumed to be uniform in the along channel direction. The flow structure shows that the shape of the eddy varies systematically with flow strength in the velocity core, which suggests that the discharge through the eddying section can be predicted stochastically. The flow across the transect under study features two distinct zones. A section between $\beta = 0$ and 0.6 features a gradual increase of the flow strength with β and a strong secondary circulation that peaks in strength at $\beta = 0.22$. The second zone is between $\beta = 0.6$ and 1 and accommodates a complex three-dimensional eddy-type of motion, which enhances the flow passing the trench and reverses the flow near the bank opposite to the H-ADCP. The measuring range of the H-ADCP is within the region $\beta < 0.6$, where the boundary layer model described in section 2 can be applied to convert H-ADCP data to specific discharge $q = U(H + \eta)$.
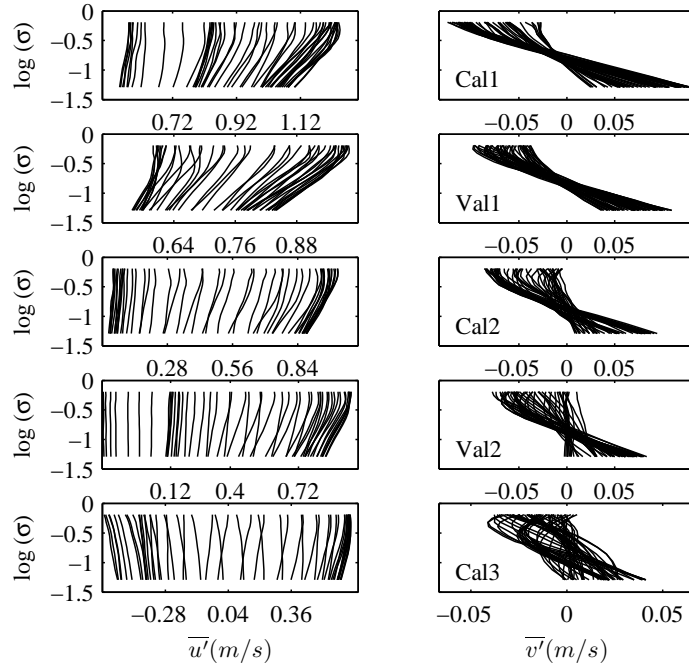
Figure 2.11: Width-averaged profiles of $\overline{u'}$ (left) and $\overline{v'}$ (right) as a function of normalized depth. Note the different velocity scale between each ADCP campaign.

2.5.2 Vertical Profiles of Streamwise Velocity in the H-ADCP Range

Figure 2.11 presents vertical profiles of streamwise velocity $\overline{u}$ and spanwise velocity $\overline{v}$, where the over line indicates width averaging over the range $0 < \beta < 0.6$. Velocity profiles clearly deviate from the logarithmic distribution at about mid-depth and above. During the Cal3 campaign, velocity profiles show a pronounced peak near the surface during flood tide. Spanwise velocity fluctuations attain values up to 0.15 m s^{-1}, with maximum spanwise velocities close to the bed and above mid-depth, suggesting curvature-induced secondary circulation.

Equation 2.9 can be rewritten in terms of σ, yielding:

$$u\left(\sigma, \beta, t\right) = \frac{u_*}{\kappa}\left(\ln\left(\sigma\right) + 1 + \alpha + \alpha \ln\left(1 - \sigma\right)\right) + U, \tag{2.20}$$

where u_* is shear velocity and $\kappa \approx 0.4$. The dip-correction factor can be estimated as

$$\alpha = \frac{1}{\sigma_{max}} - 1, \tag{2.21}$$

where σ_{max} is the relative height where the maximum velocity occurs. The degree in which the observed velocity profiles can be captured in the proposed boundary layer model was investigated in two steps. First, values of α were calculated by determining the relative depth of maximum velocity, σ_{max}, for instantaneous velocity profiles. Since those velocity profiles are influenced by turbulence and noise, the relative depth where the mean flow velocity peaks is not readily obtained. To estimate σ_{max}, we repeatedly fitted a logarithmic profile starting with

27
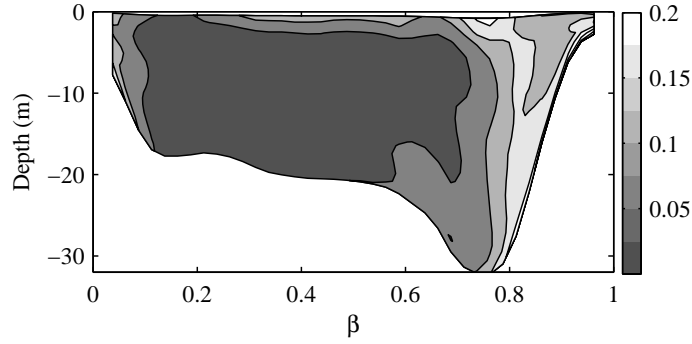
Figure 2.12: Goodness of fit of the data to the adopted velocity profile function, based on the normalized, mean absolute difference.

the lowermost three ADCP cells, adding a velocity cell from bottom to top for each subsequent fit. The value of σ_{max} is then established from the development of the goodness of fit, which decreases once that cells above σ_{max} are included in the fitting procedure. Figure 2.12 shows the goodness of fit of the data to the adopted velocity profile function, based on the mean absolute difference normalized with the mean velocity magnitude. The goodness of fit is consistently high in the range $0.1 < \beta < 0.55$. In that range, it is typically below 2.5%, except for a small layer near the surface where it attains values up to 7.5%. This leads us to conclude that the model used to establish depth-mean velocity is appropriate.

In the second step, u_* and U were derived from the linear regression of u against $(\ln(\sigma) + 1 + \alpha + \alpha \ln(1 - \sigma))/\kappa$. The top two panels in Figure 2.13 present the tidally-averaged estimates of u_* and U, obtained from the regression analysis. The profiles of both $\langle u_* \rangle$ and $\langle U \rangle$ show to be highly consistent, i.e. neighboring independent estimates are very similar. The bottom panel in Figure 2.13 shows the Root Mean Square Deviation (RMSD) between the estimated values of depth-mean velocity from the regression, $\hat{U}$, and direct estimates of U obtained from the observed velocity profiles, which were extrapolated to the bottom and bed. In the range of the H-ADCP ($\beta < 0.6$), the RMSD is below 0.06 m s^{-1} at all times, whereas in the trench zone the RMSD can reach up to 0.10 m s^{-1}.

2.5.3   Roughness Length and Dip Correction Factor

The estimates of $\hat{U}$ and u_* can be used to estimate roughness length (z_0), which proceeds from:

$$z_0 = \frac{H + \eta}{\exp\left(\frac{\kappa U}{u_*} + 1 + \alpha\right)}. \tag{2.22}$$

Figure 2.14 shows time series of the z_0, geometrically averaged over the range $0 < \beta < 0.6$, and α, as a function of time since the start of the ebb in each of the moving boat ADCP surveys. Herein, we apply High Water Slack (HWS) and Low Water Slack (LWS) definitions to unidirectional flows with an appreciable semi-diurnal tidal modulation, by considering slack water to occur when $U - \langle U \rangle = 0$. The start of the ebb is defined at HWS. During the period of
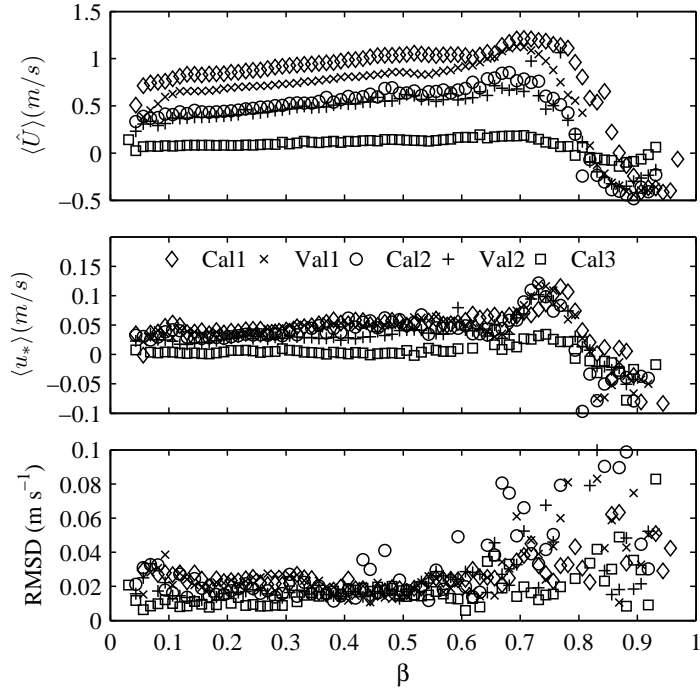
Figure 2.13: Tidally averaged estimates of U (top) and u_* (middle) computed from the regression based on equation 2.20. Bottom: Root Mean Square Deviation between the direct estimates of U from the velocity profiles, and estimates from the regression analysis.

maximum velocities, which lasts for 2 to 3 hours, z_0 and α estimates remain relatively constant in time during the ADCP surveys. Substantial intratidal variations of z_0 during Cal3 and Val2 can be primarily attributed to flow reversal, which renders velocity profiles unstable. Focusing on estimates of z_0 during periods of maximum velocity, it shows that sub-tidal variations in roughness length are significantly larger than the intratidal variations. Roughness variations within a tidal cycle are only relevant during low-flow conditions, when bi-directional flows occur.

Elaboration of Eq. 2.20 results in the following expression:

$$g\left(\sigma, \beta\right) = \alpha\left(I\left(\sigma, \beta\right) + J\left(\sigma, \beta\right)\right) + \left(1 + \ln\left(z_0\right)\right) J\left(\sigma, \beta\right), \tag{2.23}$$

where

$$g\left(\sigma, \beta\right) = \int \left(\frac{u\left(\sigma, \beta, t\right) - U\left(\beta, t\right)}{U\left(\beta, t\right)} \ln\left(H + \eta\left(t\right)\right) - \ln\left(\sigma\right) - 1\right) \mathrm{dt}, \tag{2.24}$$

$$I\left(\sigma, \beta\right) = \int \frac{u\left(\sigma, \beta, t\right) - U\left(\beta, t\right)}{U\left(\beta, t\right)} \mathrm{dt}, \tag{2.25}$$

$$J\left(\sigma, \beta\right) = \int \left(1 + \ln\left(1 - \sigma\right)\right) \mathrm{dt}. \tag{2.26}$$

29

Local values of z_0 and α can be obtained from the bi-linear regression with zero intercept through calculated values of g versus $I + J$ and J. Figure 2.15 shows cross-river profiles of z_0 and α over half of the channel width. Spatial variations in z_0 are highest during bi-directional flows, and increase systematically toward the bank. Cross-river profiles of α are consistent within transects featuring a minimum around $\beta = 0.2$ and an increment toward the center of the channel. In the vicinity of the riverbank ($\beta < 0.2$), width profiles of α according to Eq. (2.11) can be approximated with a Taylor expansion according to $\alpha \approx A - B\beta$, where $A = 1.3$, and $B = 1.3W/H$. A linear fit yields $A = 1.00, 1.24, 1.38$, and $B = 5.23, 4.41, 6.02$, for each of the three calibration surveys, respectively. These figures are consistent with $A = 1.3$ reported by *Yang et al.* (2004b). However, the values of B are about three times smaller than the value obtained with the local aspect ratio of the river ($\frac{W}{H} \sim 22$). This may relate to the fact that the velocity dip does not extend over the full river width.

Figure 2.16 investigates the stage dependence of $\langle z_0 \rangle$, showing in the top panel a linear relation between $\langle \eta \rangle$ and the geometric mean over $0 < \beta < 0.6$ of z_0. The bottom two panels explore if the stage dependence of z_0 varies over width, by splitting the region of interest in two. In the region $0.3 < \beta < 0.6$ the relation shows a reduced linearity, whereas in the region $0 < \beta < 0.3$ the stage-roughness relation agrees with one obtained for the region $0 < \beta < 0.6$.

2.6 Discharge Estimation Methodology

2.6.1 Deterministic Part

Single-point H-ADCP velocity measurements u_c can be translated to depth-mean velocity U according to:

$$U = Fu_c \tag{2.27}$$

$$F = \frac{\ln\left(\frac{H+\eta}{\exp(1+\alpha)}\right) - \ln(z_0)}{\ln(\sigma_c(H+\eta)) + \alpha\ln(1-\sigma_c) - \ln(z_0)}, \tag{2.28}$$

where u_c is the flow velocity array at normalized depth σ_c. Close to the riverbank, σ_c is typically in the range between 0.8 and 0.9, and $\alpha = 0.4$ to 0.8. Within these ranges of variation, F takes values between 0.9 and 1.

The following approach was followed to obtain continuous series of z_0 and α over the range of the H-ADCP:

1. Values of z_0 were predicted from the tidally averaged water level according to: $\log_{10}(z_0) = 2.5\langle\eta\rangle - 2.32$ (see top panel in Figure 2.16). Variation of z_0 over width is ignored.

2. Values of α were predicted from a bilinear relation with β: $\alpha = 1.2 - 6\beta$ for $0 < \beta < 0.16$ and $\alpha = 0.24$ for $\beta > 0.16$. Variation of α in time is ignored.

2.6.2 Stochastic Part

Using depth-mean velocity estimates, specific discharge $q = \hat{U}(H + \eta)$ can be obtained from the H-ADCP velocity measurements. A stochastic model is adopted to relate q to the total discharge Q:
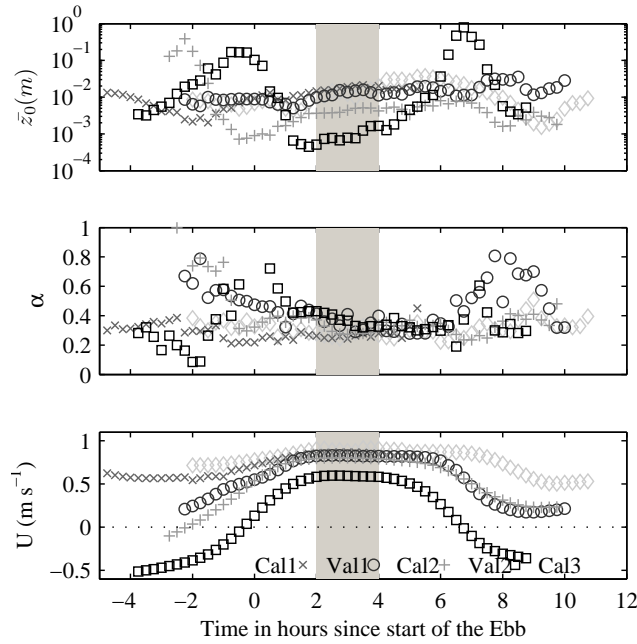
Figure 2.14: Geometric mean ($\beta < 0.6$) of z_0 (top), α (middle) and U (bottom) as a function of time. Time series for each moving boat ADCP campaign commence at the start of the ebb period. Gray areas indicate the periods that are supposed to be void of slack water effects, during which z_0 is relatively constant.
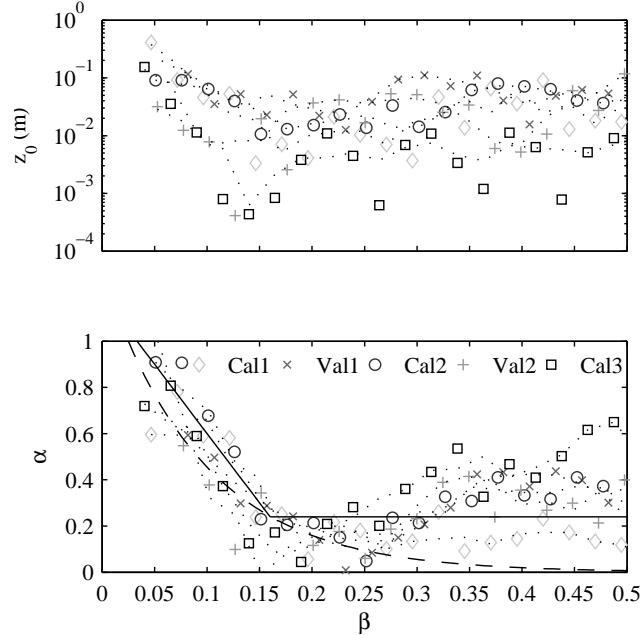
Figure 2.15: Cross-river profiles of z_0 and α. Dotted lines remove spatial variations with wave lengths smaller than 50 m. The solid line is the best fit given by $\alpha = 1.2 - 6\beta$ for $0 < \beta < 0.16$ and $\alpha = 0.24$ for $\beta > 0.16$. The dotted line is given by equation 2.11.

31
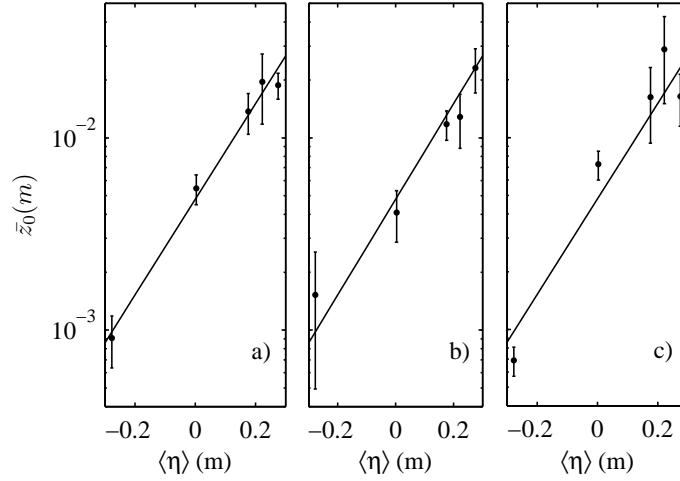
Figure 2.16: Geometric mean of z_0 as a function of tidally averaged water level for a) $0 < \beta < 0.6$, b) $0 < \beta < 0.3$, and c) $0.3 < \beta < 0.6$. Error bars indicate the standard deviation. Best fit lines represent $\log_{10}(\bar{z}_0) = a\langle\eta\rangle - b$ with $a = 2.5, 2.065, 2.75$, and $b = 2.32, 2.3, 2.3$, for a), b), c), respectively.

$$Q(t) = f(\beta)\,W q(\beta, t + \tau(\beta)), \tag{2.29}$$

where W is the river width, $f(\beta)$ is a constant amplification factor and $\tau(\beta)$ is a time lag function to take inertial effects into account (*Hoitink et al.*, 2009). The time lag τ as a function of β was obtained by establishing the time difference between the occurrence of $Q - \langle Q\rangle = 0$ and $q - \langle q\rangle = 0$. The width dependent amplification factor was obtained from a linear regression.

Figure 2.17 shows width profiles of τ and f for the transition between ebb and flood (LWS) and vice-versa (HWS), for each of the moving boat ADCP surveys. Values of τ become remarkably large near the banks ($\beta < 0.15$). In the region $\beta > 0.15$ the agreement between values of τ and f from the different moving boat ADCP surveys is high. In the region $\beta > 0.7$, τ exceeds half an hour. For $\beta > 0.8$, specific discharge does not follow total discharge anymore because of the flow reversals induced by the eddy. Profiles of f remain constant between the surveys in the range $0.15 < \beta < 0.75$. Discrepancies near the bank can be attributed to subtidal variations in flow strength, impacting the redistribution of specific discharge. Figure 2.17 also shows the relative Root-Mean-Square Error in modeled values of Q, defined as the ratio of the RMSE in the modeled values of Q and the tidally averaged discharge $\langle Q\rangle$. Within $0.15 < \beta < 0.75$, values of rRMSE remain below 0.1. Based on the rRMSE results in Figure 2.17 it can be concluded that the conversion of specific discharge to total discharge can best be based on H-ADCP measurements in the range $\beta > 0.15$. To calculate Q at any moment in time from estimates of q in that range, we use best-fit lines of τ and f using the results from the three calibration surveys, which read:

1. $\tau = 8.9 - 4\sin^{-0.9}(1.25\pi\beta)$ (see top panel in Figure 2.17).

2. $\log(f) = -0.5 - 0.4\log(\beta) - 0.33\beta$ (see mid panel in Figure 2.17).
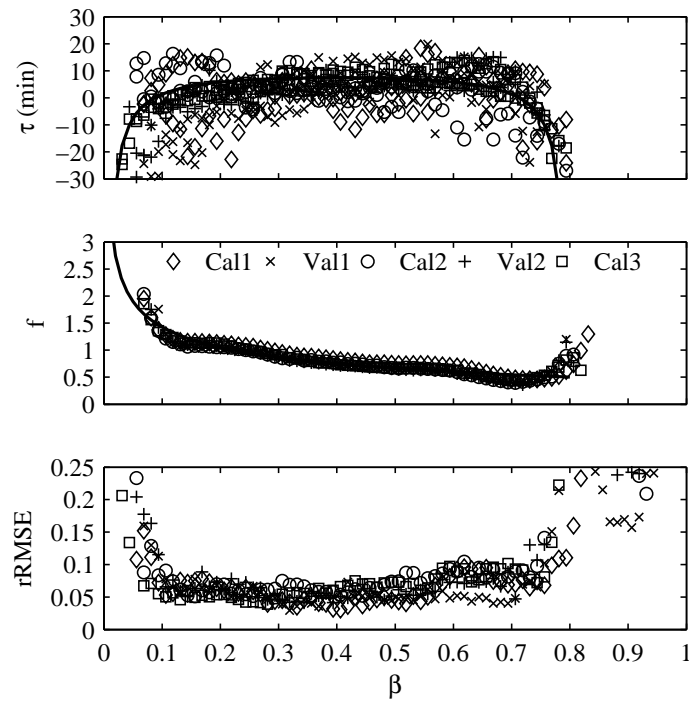
Figure 2.17: Top: time difference between the occurrence of $q - \langle q \rangle = 0$ and $Q - \langle Q \rangle = 0$, in case of the transition from flood to ebb (HWS) and vice-versa (LWS). Middle: amplification factor f in equation 2.29. Bottom: relative root-mean-square error in modeled values of Q.

2.7   Validation

Nine months of velocity data obtained with the H-ADCP spanning a wide range of flow conditions were used to produce a continuous series of water discharge. Following the approach described in the previous section, mutually independent estimates were obtained from each horizontal cell. Improved estimates of Q were obtained by averaging over $0.15 < \beta < 0.35$. The validation was realized using data from two moving boat ADCP surveys which were not used for the estimation of the model parameters z_0, α, f and τ. The first validation dataset represents high-flow conditions during spring tide and the second was during conditions of low river flow and a mean tidal range.

Figure 2.18 shows the correspondence between discharge computed with the boat-mounted ADCP (Q_{trans}) and the present method ($Q_{\text{H-ADCP}}$). Peak discharges exceed 8000 m³ s⁻¹. The RMSD between $Q_{\text{H-ADCP}}$ and Q_{trans} amounted to 330 and 460 m³ s⁻¹ for high- (Val1) and low-flow (Val2) conditions. The relative difference remains below 10% during the periods of validation and is highest during low discharges. Figure 2.18 also shows estimates of discharge obtained using the widely used Index Velocity Method (e.g. *Le Coz et al.*, 2008), and the relative difference with the boat-mounted ADCP campaign. Both during high-flows and during low-flows, the relative difference between modeled and measured discharges is larger using the IVM. During high-flow, peak values of the relative difference reduce from 0.16 for the IVM to 0.11 for the present method. The comparison during Val1 seems to be better than during Val2. However, part of this relates to the difference in vertical scale, which was necessary because Val2 includes slack water, when relative errors become large. During slack water, the errors involved in the discharge estimates from shipborne velocity data, which are considered to be the 'truth', become of the same order of magnitude as the discharges derived from H-ADCP data.

2.8   Discussion

Studies quantifying uncertainties in estimates of roughness length from velocity profiles have generally focused on rigid deployments (e.g. *Wilcock*, 1996). Adopting an approach in which a shipborne ADCP is employed to estimate roughness length from velocity profiles is generally considered to be prone to errors (*Sime et al.*, 2007). Slight variations in the vertical placement of the profiles may cause significant variability in the results (*Biron et al.*, 1998). Poorly resolved velocity gradients, lack of knowledge of the extension of the bottom boundary layer and measurement noise introduced by the moving vessel, all may play a role in the determination of roughness length and shear velocity. The crucial argument we have to conclude that our estimates of roughness length and shear velocity can be accurate, is that neighboring estimates of depth-mean and shear velocity in Fig. 2.13 are similar, while they have been obtained in a mutually independent way. We cannot think of a systematic error that would cause the neighboring measurements to be consistent, but wrong. Our filtering in the time domain based on equations 23 through 26 filters out the errors in vertical positioning, which can be expected to be different each time the boat passes by a location. Individual ADCP velocity ensembles are an average over 6 sub-pings of 0.04 s, which coincides with about 0.5 m when the boat speed is 2 m s⁻¹. Therefore, the velocity profiles can be considered a spatial average over about 0.5 m
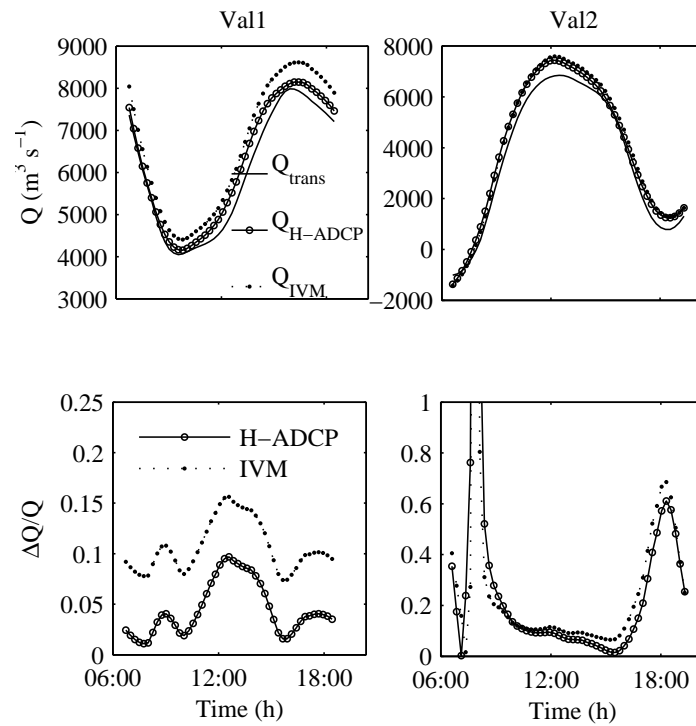
Figure 2.18: Top: discharge as a function of time computed from the moving boat ADCP data (Q_{trans}), from H-ADCP data processed with the present method ($Q_{\text{H-ADCP}}$) and with the Index Velocity Method Q_{IVM} for the two validation datasets. Bottom: relative error in discharge measurements as a function of time for the present method and for the IVM.

in the boat direction, which reduces the effect of spatial variation of the reference height. The difference between smoothed lines of z_0 during the different surveys and the original estimates indicates the error, which is in the order of a decade.

Converting H-ADCP velocity data to specific discharge crucially depends on the determination of the effective roughness length z_0, parameterizing bottom roughness. The results presented in Figures 2.14 and 2.15 confirm conclusions by *Hoitink et al.* (2009), who claim that consistent estimates of z_0 can be obtained from moving boat ADCP measurements when a large number of ADCP transects is available to filter out the contributions of noise and turbulence. It was shown that z_0 was particularly dependent on the river stage (Figure 2.16), which may relate to changes in bedforms. During high-flows, when the 18-m isobath migrates downstream, z_0 is largest. Conversely, during low-flows, when the 18-m isobath evolves upstream, z_0 is lowest. Bed morphology in the River Mahakam is strongly influenced by the width confinement, and is much more complex than in many other alluvial environments where morphodynamics are more predictable. The bed dynamics in the River Mahakam may be in response to the details of the three-dimensional flow patterns, which are stage dependent. It can be shown that the conversion factor F becomes more dependent on roughness when σ_c decreases, i.e. when the velocity dip becomes more pronounced. The effective influence of bed dynamics on the discharge estimates is thus dependent on the occurrence of sidewall effects.

An essential assumption made in the analysis of sidewall effects is that the Reynolds equation in the bed region holds over the entire water depth. This assumption allowed *Lueck and Lu* (1997) and *Cheng et al.* (1999) to successfully use the logarithmic velocity profile over the entire water column, to compute bed shear and roughness in contrasting environments. In the same spirit, we applied the modified velocity profile with velocity dip to our observations to estimate hydraulic parameters, yielding consistent results that hold for measuring surveys that took place months apart. Whereas the aim in the present chapter is to obtain accurate, continuous estimates of discharge, the iterative method to fit the velocity profile with a velocity dip to moving boat ADCP measurements can be readily used to estimate bed shear stress.

Bedload sediment transport jeopardizes the use of acoustic bottom tracking for the transformation of flow velocity data from instrument coordinates to earth coordinates. Flow velocity obtained accordingly is biased low, resulting in underestimation of discharge estimates. Figure 2.19 shows a comparison between the error in boat-mounted ADCP velocity measurements transformed to earth coordinates using acoustic bottom tracking and using dual-antenna GPS measurements, considering H-ADCP velocity measurements as a reference of reality. It shows that the effect of the moving bed is progressively better noticeable for higher flow velocities, which may result from the nonlinear response of sediment transport to flow velocity. Sediment transport, in turn, can affect boundary layer processes, increasing z_0. Hence, part of the stage dependency of z_0 could be caused by higher sediment transport rates during high river stages. Better understanding of alluvial bed roughness will allow to improve the accuracy of discharge estimates from H-ADCP measurements. In turn, regular calibration surveys offer possibilities to perform such analyses, if the domain where bathymetry measurements are taken is made wider than merely the region where the H-ADCP is located. Surveys combining multi-beam echo soundings and ADCP measurements would allow to link the roughness lengths inferred from ADCP velocity profiles to morphodynamic processes.
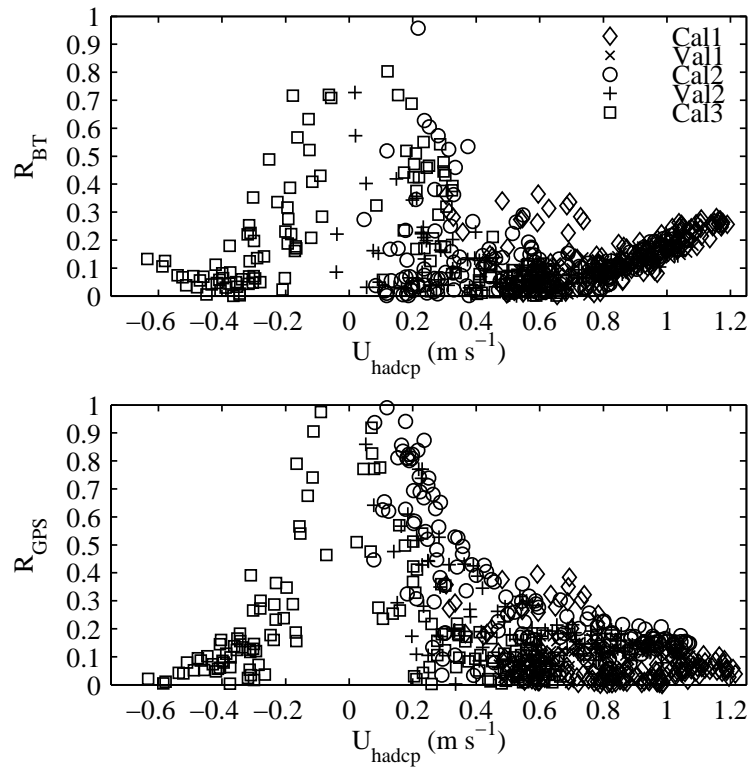
Figure 2.19: Scatter plot of the relative difference $R = |U_{trans} - U_{hadcp}|/|U_{hadcp}|$ versus U_{hadcp} in the range $0.15 < \beta < 0.35$, where U_{trans} and U_{hadcp} are depth-mean velocity estimates from the transect boat and the H-ADCP (respectively), indicating the relative difference between U_{trans} and U_b as a function of flow strength for U_{trans} computed with the BT (upper) and the GPS (lower).

2.9 Conclusions

A new method to convert H-ADCP velocity measurements into continuous time-series of water discharge is presented, which can be applied to large rivers with discharges exceeding 8000 $m^3 s^{-1}$. It extends an existing semi-deterministic, semi-stochastic approach developed for rivers of rapidly varied flows, adopting a boundary layer model that accounts for sidewall effects resulting in a dip in flow velocity near the surface. The method was applied to H-ADCP measurements taken at a site in the River Mahakam, where the flow is intrinsically three-dimensional. Data-series covering five moving-boat ADCP surveys were used. Each campaign covered a semidiurnal tidal cycle, three of which were used for calibration, whereas the remaining two served for validation. The method includes four parameters: (1) a stage-dependent value of the bed roughness z_0, which is geometrically averaged over the H-ADCP range; (2) a sidewall correction factor α that is assumed constant in time, but varies over width according to a bi-linear profile that fitted best to the calibration data; (3) a steady, but width-dependent time-lag τ between variation in specific and total discharge and (4) a constant, but width dependent amplification factor f. With z_0 and α, H-ADCP velocity measurements can be converted to specific discharge, using the boundary layer model. Specific discharge is being translated to total discharge using a regression model with parameters τ and f. The best estimate of total discharge is finally obtained by averaging over the width range where the linear correlation between specific and total discharge was highest. Further progress depends primarily on the predictability of z_0, which depends on studies of alluvial bed morphology.

Chapter 3

River-Tide Interaction

Abstract: River-tide interaction creates oscillatory and steady gradients in the water surface that can potentially drive discharge variations in tidal rivers. Here we show tidal and subtidal water level measurements at stations along the River Mahakam suggest river-tide interaction is responsible for the admittance of river discharge waves into the downstream reaches of the tidal river. Time-series of tidal amplitude at five gauge stations along the river, and flow velocity amplitude at a discharge station were obtained applying wavelet analysis. Tidal amplitudes along the river were employed to estimate the temporal variation in tidal damping coefficients for quaterdiurnal, semidiurnal and diurnal tidal species. Estimated damping coefficients indicate a strong dependence on river flow. A wavelet cross-correlation with the gauge at sea yielded the wavenumbers, which remained constant throughout the measuring period. The subtidal, regional along-channel pressure gradient is balanced by subtidal friction, which can be decomposed into contributions from the river flow (S_r), from river-tide interaction (S_{rt}) and from tidal asymmetry (S_t). An empirical relation between tidal damping and river discharge was employed to derive the along-channel variation of the subtidal friction components in an idealized tidal river resembling the Mahakam. The magnitude of S_{rt} and S_t strongly depends on the magnitude of S_r. The relative importance of these, however, depends on the choice of the maximum velocity used to make all amplitudes dimensionless. Our results suggest that even for high river flow and low tidal velocity amplitude, river discharge enhances river-tide interaction, causing subtidal water level setup. A simple multi-linear regression model using S_r and S_{rt} is employed to predict subtidal water levels at locations upstream, with a relatively good agreement between predictions and observations.

---

[1]This chapter is largely based on the manuscript: Sassi, M.G., and A.J.F. Hoitink, *Subtidal water levels in a tidal river*, submitted to Journal of Geophysical Research-Oceans

3.1 Introduction

Rivers debouching into the sea are subjected to tidal variation at the river mouth. In lowland regions, farther away from the estuarine environment where fresh and saline waters meet, tides have a significant impact on the river flow by means of subtidal (averaged over a lunar day) water level variations controlled by river-tide interaction (*Buschman et al.*, 2009). River-tide interaction refers to a frictional effect that is induced by tidal amplitudes varying in the presence of a net current (*Dronkers*, 1964; *LeBlond*, 1979; *Godin*, 1991b). Since tidal amplitudes are generally governed by the spring-neap cycle, the water surface of the river features a fortnightly variation. Besides this oscillatory effect, river-tide interaction creates a steady gradient in the water surface that steepens the surface profile of the river up to the point of tidal extinction (*LeBlond*, 1979; *Godin and Martinez*, 1994). Results by *Godin and Martinez* (1994) suggest that the influence of this long-term water level setup may reach much further inland than the tidal motion. Here we investigate consequences of subtidal water level setup for river discharge regimes in tidal rivers.

The tidal wave propagating up-river experiences distortion and damping induced by bottom friction (e.g *Godin*, 1999) and river discharge (e.g. *Horrevoets et al.*, 2004). Bottom friction can lead to the creation of sub and super harmonics (e.g. *Friedrichs and Aubrey*, 1988), affecting the amplitude and timing of high and low water (e.g. *Savenije*, 2001; *Savenije and Veling*, 2005). *LeBlond* (1978) described tidal propagation as a diffusion problem by pointing out that frictional forces in tidal channels typically exceed inertial accelerations. Fortnightly modulation in water levels is caused by fortnightly variation in bottom friction over a spring-neap cycle (*LeBlond*, 1979). *LeBlond* (1979) concluded that the effect on surface level is cumulative up-river, such that it accounts for the gradual up-river depression of mean low water levels during spring tide relative to neap tide. *Godin* (1985) observed that the tidal range is reduced by the increase in river discharge towards the upstream regions of the river, whereas friction is increased (decreased) during ebb (flood) in the downstream regions. In both cases, high and low water timings were distorted. In a subsequent contribution, *Godin* (1991a) observed that periodic retention of some of the fresh water during spring tides caused long period oscillations at 14 and 28 days. In addition, he pointed out that the coincidence of a peak in river discharge with extreme tidal ranges could create unusually high levels upstream. In this chapter we show that besides forcing water levels at specific tidal frequencies, river-tide interaction can drive discharge variations in tidal rivers by imposing a steady gradient in water level. In a sense, this can be understood as a backwater effect.

Frictional effects in tidal rivers are represented by the bottom friction term in the momentum equation (*Dronkers*, 1964). Traditionally, the focus has been on approximating the non-linear behavior of bottom friction to quantify its impact on the incoming tide. *Godin* (1991b) presented compact approximations to the bottom friction term valid for upstream (no flow reversal) and downstream (flow reversal) regions of a river, showing that in the upstream region the damping of the incoming tide is controlled exclusively by the river discharge. *Jay* (1991) sought for analytical solutions to tidal propagation in channels with strong topographic convergence. He pointed out that friction, topography, the presence of tidal flat areas, finite wave amplitude and river flow, all influence the wavenumber and damping coefficient of the tidal wave. *Godin and Martinez* (1994) conducted numerical experiments to investigate the

effects of quadratic bottom friction by neglecting the contributions of advective accelerations; they found a dependence of damping with tidal amplitude and a strong contribution of the net current to bottom friction. *Jay* (1997) obtained analytical expressions relating the variation of the logarithm of tidal amplitudes (i.e. damping coefficient) with the square root of river discharge. *Godin* (1999) concluded that the tidal damping coefficient varies in a non-linear fashion with the river flow, which can be mainly approximated by a quadratic dependence. Here we argue that temporal variations in river discharge create mutual feedbacks between river stage and the tidal motion, via the mechanism of river-tide interaction. This is a complex feedback mechanism that has not been described before, because so far the analyses reasoned from a constant river discharge.

Due to the deterministic nature of the tides, understanding the subtle adaptation of subtidal water levels to variations in river discharge and tides may yield a tool to forecast river stages in tidal rivers. *Godin and Martinez* (1994) showed that in the presence of a net current flowing downstream, the surface slope is steepened in the downstream region while it asymptotically approaches the value given by the traditional Chézy law in the upstream region of the river. *Jay* (1997) emphasized that river stage depends on the square of river flow, as in a uniform flow in which the effect of tides is accounted for by an effective friction coefficient. *Godin* (1999) elaborated on the harmonic solutions to the momentum equation, concluding that the surface profile is given by contributions due to river flow and due to the interaction of the river flow with tides. *Kukulka and Jay* (2003a) developed a one-dimensional subtidal river stage model which accounts for variable river discharge and tidal discharge, showing that both water levels and the damping coefficient depend on river discharge and tidal discharge amplitude. *Buschman et al.* (2009) presented a modified version of the subtidal momentum balance by proposing a method of analysis that decomposes subtidal friction into contributions by the river flow, river-tide interaction and tides only. They proposed a simple linear regression model to predict changes in subtidal water level with changes in subtidal friction. Here we build on the model of *Buschman et al.* (2009), to explore the degree in which upstream subtidal water levels in a tidal river can be explained from a limited number of input conditions.

This chapter is organized as follows. We describe the field setting and measurements in Section 3.3. The time-frequency representation of the observations is presented in Section 3.4. Section 3.5 introduces the subtidal friction decomposition method. Contributions due to river flow, river-tide interaction and tidal asymmetry are modeled along the river, incorporating the tidal damping coefficient into the friction representation. We finalize this chapter with a summary and conclusions in Section 3.6.

3.2   Background

In a seminal study on river-tide interaction, *LeBlond* (1979) performed a dimensional scaling analysis of the shallow water equations applied to the case of a tidal river forced with semidiurnal tides and a constant river outflow. The analysis showed the subtidal variation in water level is solely a function of the fortnightly fluctuation in tidal velocity amplitude driven by the spring-neap cycle. The latter arises from the unequivocal balance between the subtidal pressure gradient and bottom friction in the along-channel momentum equation (e.g. *LeBlond*, 1978;

Buschman et al., 2009), which in LeBlond's formalism is given by:

$$\frac{\partial \Psi\left(\eta\right)}{\partial s} \propto \Psi\left(u''^2\right) - 2\epsilon\Psi\left(u\right)u_R + \epsilon^2\Psi\left(\Psi^2\left(u\right)\right). \tag{3.1}$$

The double primes denote fluctuations within a day and the subscript R denotes a fortnightly averaged component. Ψ denotes the mathematical operation that can be seen as a band-pass filter to remove tidal variation and oscillations with a period larger than two weeks; η represents the surface water level, u the flow velocity, and s the along-channel coordinate; ϵ is a scaling factor that is smaller than one.

Since tidal amplitudes invariably decay up-river, because of friction and the river outflow, the amplitude of the forced fortnightly tide that results from neglecting terms of order ϵ and smaller, increases up-river up to a point at which it remains constant (*LeBlond*, 1979). In fact, beyond that point, the fortnightly tide is also damped by friction and the river outflow along with the main tidal constituents, though at a lower rate (*Godin and Martinez*, 1994). The observed behavior is captured in the second term in Eq. (3.1), which is given by the product of the fortnightly velocity amplitude and the river outflow. Despite being scaled by ϵ, $2\epsilon\Psi\left(u\right)u_R$ can be greater than $\Psi\left(u''^2\right)$ in the upstream reaches of the river, which leads to the expected damping of the fortnightly tide.

The analysis above offers a solid argument that the forced fortnightly tide depends both on tidal amplitudes and river discharge, and indicates that the damping up-river may be entirely controlled by the river flow. Although the assumption of a constant river discharge leads to a relatively easy mathematical treatment of the equations, real rivers feature variations in discharge that can range from hours to months (e.g. *Sassi et al.*, 2011a; *Hidayat et al.*, 2011; *Buschman et al.*, 2012), masking the subtidal band in which the forced fortnightly tide occurs.

Approximations to the non-linear behavior of bottom friction include expansions of the square of the velocity with Chebyshev polynomials (*Dronkers*, 1964; *Godin*, 1991b), typically using the velocity normalised with some choice of maximum velocity. The method of decomposition proposed by *Buschman et al.* (2009) introduces an expansion in terms of tidal species, which represent a group of tidal constituents with similar frequencies. In their approach, contributions to subtidal friction by the river flow, by river-tide interaction and by tidal asymmetry are given by

$$S_r = a\tilde{u}_0 + b\tilde{u}_0^3, \tag{3.2}$$

$$S_{rt} = \frac{3}{2}b\tilde{u}_0\left(\tilde{U}_1^2 + \tilde{U}_2^2 + \tilde{U}_4^2\right), \tag{3.3}$$

$$S_t = \frac{3}{4}b\left(\tilde{U}_2\tilde{U}_1^2\cos(2\phi_1 - \phi_2) + \tilde{U}_4\tilde{U}_2^2\cos(2\phi_2 - \phi_4)\right), \tag{3.4}$$

where a and b are two constant coefficients that arise from the Chebyshev polynomial approximation, and $\tilde{U}$ is the tidal velocity amplitude made non-dimensional with the maximum velocity (*Godin*, 1991b); the subscripts 1, 2 and 4 represent the tidal velocity amplitudes corresponding to diurnal, semidiurnal and quaterdiurnal tidal species, respectively; u_0 is the subtidal velocity, ϕ_1 and ϕ_2 are the phase differences between diurnal and semidiurnal tidal species, and between semidiurnal and quaterdiurnal tidal species, respectively; and subscripts r, rt and t denote river, river-tide interaction and tidal asymmetry, respectively.
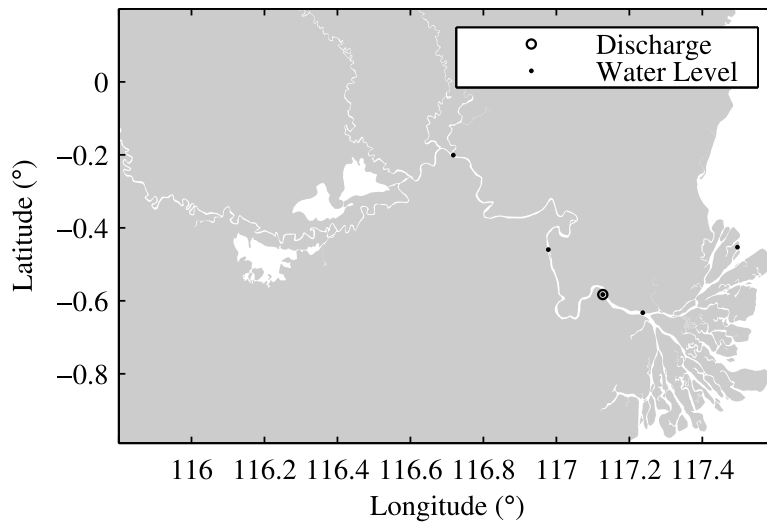
Figure 3.1: Map of the River Mahakam in Indonesia with locations of discharge and water level stations (modified after *Sassi et al.* (2011b)). The lakes are located at about 200 km from the coast.

3.3 Discharge Regimes and Tides

3.3.1 Study Area and Instrumentation

The River Mahakam in Indonesia is a tropical lowland river with significant tidal influence due to its very mild bottom slope (*Allen et al.*, 1977). The upper reaches of the river are separated by a system of interconnected lakes that buffers flood peaks and results in a relatively constant discharge in the lower reaches of the river (*Storms et al.*, 2005; *Hidayat et al.*, 2011). The relatively slow fluctuation of the river discharge, at time scales longer than a fortnight, allows the system to adjust to subsequent quasi-equilibrium states.

We deployed an observational network for a period of about 18 months along the lower 200 km of the river (Figure 3.1). This measuring setup consisted of five water level gauges distributed along the river and in the delta, and a horizontally deployed acoustic Doppler current profiler (H-ADCP), which was located near the delta apex. The water level gauges recorded one minute averages of surface level fluctuations every 15 minutes, while the H-ADCP was programmed to yield 10 minutes average array data of flow velocity, every 30 minutes. Both instruments recorded at 1 Hz. Velocity measured with the H-ADCP was converted to river discharge using conventional shipborne ADCP discharge measurements. In total, seven 13-h ADCP surveys were carried out spanning high- and low-flow conditions, during spring tide and neap tide (*Sassi et al.*, 2011a).

3.3.2 Subtidal Variability

Water surface elevation with respect to a reference level is written as

$$\zeta = Z + H + \eta, \tag{3.5}$$

where H is the width-averaged depth, Z is the height of the width-averaged bottom and η is the water surface variation. Water surface variation is decomposed as

$$\eta = \eta_0 + \eta'' = \eta_R + \eta' + \eta'', \tag{3.6}$$

where the double prime denotes the tidal variation and the subscript 0 denotes the subtidal variation. The subtidal variation can be further decomposed into a fortnightly average (subscript R) and a remainder denoted by the prime. Similarly, the river discharge Q can be written as

$$Q = Q_0 + Q''. \tag{3.7}$$

Subtidal variations were determined by averaging the time-series over one day. The difference in mean water level $H + Z$ was obtained by setting up a regional subtidal momentum balance over the lower reaches of the river, in between the discharge station and the delta apex (*Buschman et al.*, 2009). Accordingly, the Chézy coefficient and the bottom slope of the river yielded 58 $\text{m}^{1/2}\text{s}^{-1}$ and 1.058×10^{-5}, respectively.

River-tide interaction drives the co-oscillation of the subtidal water level with varying tidal amplitudes. The tidal regime in the River Mahakam is mixed mainly semidiurnal, therefore, the spring-neap cycle has contributions due to tropical and synodic months (*Kvale*, 2006; *Hoitink*, 2008), complicating the periodicities in the tidal amplitudes. On top of this frequent oscillation, the tidal damping induced by river discharge also drives variations in tidal amplitudes, and therefore in subtidal water levels.

Figure 3.2 shows time-series of η, η_0, Q and Q_0 over approximately six months. The discharge station coincides with the level gauge 60 km from the coast. Tidal amplitudes systematically decrease up-river, whereas subtidal variations increase up-river only in the first four gauges. These results are consistent with the results of numerical simulations performed by *Godin and Martinez* (1994). At the most upstream gauge (at 160 km), however, subtidal variations in water level better resemble variations in subtidal discharge farther downstream than subtidal water levels at the neighboring gauge. In the inland region, subtidal variations induced by river-tide interaction are thus less important than the actual variations induced by the river flow. The latter observation can be quantified by the spectral coherence between the semidiurnal tidal amplitude and the corresponding subtidal variation, which typically peaks in the fortnightly band for both the discharge series and the water level series, except for the water level time-series at 160 km from the river mouth.

Note that at the discharge station, variations in Q_0 are nearly in anti-phase with variations in η_0. Both at the discharge station and at the most upstream level gauge, the lows often occur during spring tides whereas the transition to the peaks regularly coincides with the occurrence of neap tides (indicated by arrows in Fig. 3.2). During spring tide, the elevated levels of friction by the tidal currents hinder the admittance of discharge waves through the downstream reaches

of the river. During neap tides, a river discharge wave can develop. The latter development is characterized by a rise in water level in the upstream reaches that is promoted by the effect of river-tide interaction. This general view can be blurred by variation in runoff, which, if strong enough, can force discharge through a tidal river at spring tide.

3.4 Time-Frequency Representation

In this section, the temporal variations in tidal amplitudes, tidal velocity amplitudes and phases along the river are analysed, which are extracted from water level and water discharge time-series using the Continuous Wavelet Transform with a Morlet mother wavelet (*Jay*, 1997; *Flinchem and Jay*, 2000; *Jay and Kukulka*, 2003). The temporal analysis will serve for estimating the temporal variations in subtidal bottom friction using Eqs. (3.2).

3.4.1 Water Level

The scale resolution used in the wavelet transform allows us to distinguish only between main tidal species and not among tidal constituents (*Jay and Flinchem*, 1999). Wavelet amplitudes corresponding to quarterdiurnal (D_4), semidiurnal (D_2) and diurnal (D_1) fluctuations were obtained from the spectrograms and averaged over one day to obtain the subtidal variation in tidal amplitude of each tidal species.

The tide is represented as a damped wave traveling up-river (*LeBlond*, 1979; *Godin*, 1999) such that the tidal water level fluctuation η'' can be written as

$$\eta'' = \sum_l \eta_l, \tag{3.8}$$

$$\eta_l(s,t) = D_{0,l}(t) \exp(r_l(t)s) \operatorname{Re}\{\exp(ik_l(t)s - il\omega t)\},$$

where r_l and k_l are the damping coefficient and the wavenumber of each tidal species ($l = 1,2,4$), respectively, ω is the angular frequency corresponding to a diurnal tide with a period of a lunar day, i is the imaginary unit, s is the along-channel coordinate, and $D_{0,l}$ is the corresponding tidal amplitude at sea. Denoting with D_l the tidal amplitudes at locations upstream, the damping coefficient r_l of each tidal species can be computed as (*Kukulka and Jay*, 2003b)

$$\ln|D_l| = \ln|D_{0,l}| + r_l s, \tag{3.9}$$

where r_l is given in km^{-1}.

Figure 3.3 shows diurnal and semidiurnal water level amplitudes resulting from wavelet analysis at stations along the river for approximately one year of measurements, as well as the estimated damping coefficient for each tidal species. The amplitude of the spring-neap cycle of the semidiurnal species is largely modulated by seasonal variation, whereas that of the diurnal species is fixed to the equatorial passage of the Moon (*Kvale*, 2006). Both diurnal and semidiurnal species attenuate as a result of friction along the river over most of the observation period (as indicated by the lighter colors). Damping coefficients were estimated using all available gauges for a particular time. The magnitude of the damping coefficient increases with increasing frequency (*Godin and Martinez*, 1994; *Godin*, 1999). During a high discharge period
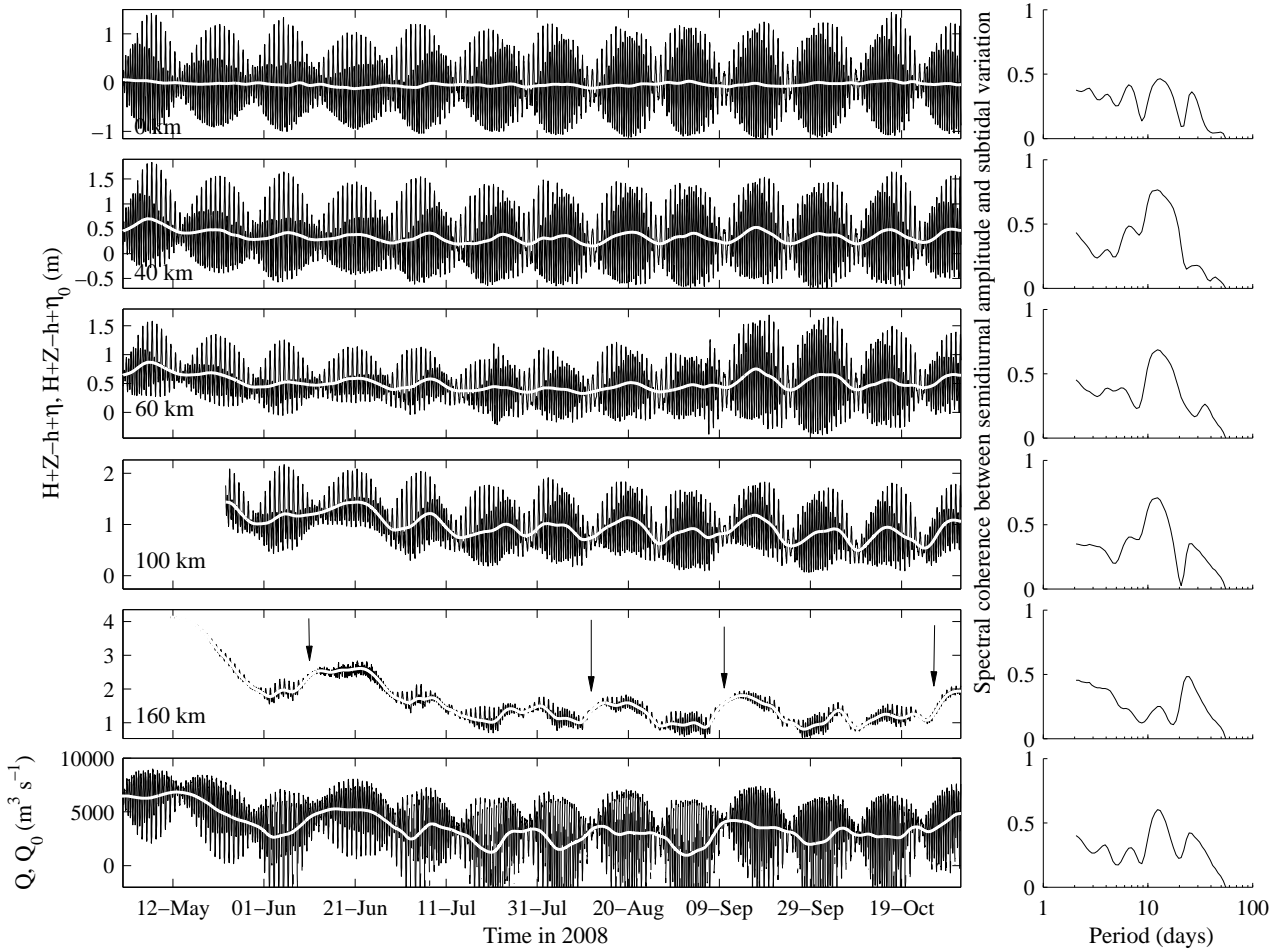
Figure 3.2: Time-series of water level (black) and subtidal water level (white) at stations along the river. The difference in mean water level $H + Z$ was obtained by setting a regional momentum balance over the lower reach of the river. For simplicity, we subtracted a mean depth h such that $H + Z + \eta_0 - h$ at the most seaward station is zero. Bottom: discharge (black) and subtidal discharge (white) at the discharge station. The right panels show the spectral coherence between the semidiurnal tidal amplitude and the corresponding subtidal variation.

46
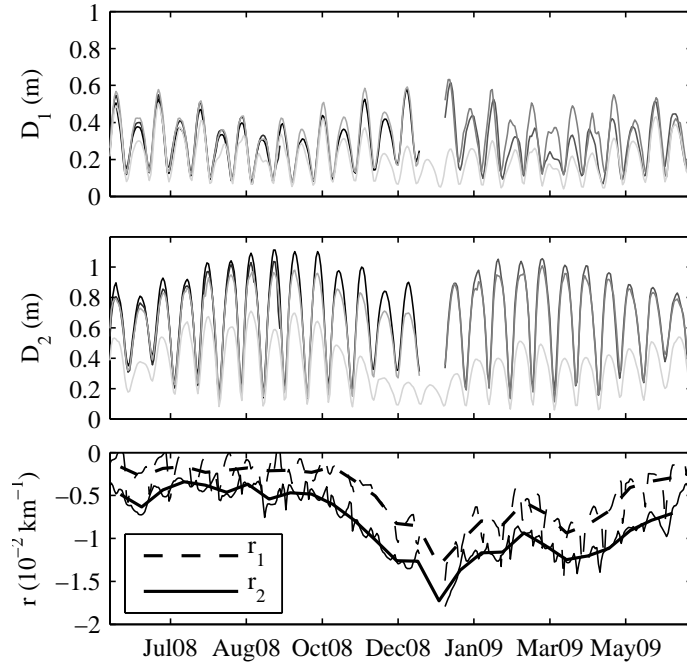
Figure 3.3: Time-series of diurnal (D_1) and semidiurnal (D_2) water level amplitudes resulting from wavelet analysis at stations along the river (lighter colors are more up-river). Bottom: damping coefficient r (10^{-2} km^{-1}) for each of the tidal species. The thick line removes temporal oscillations with periods below 14 days.

that lasted from November 2008 to April 2009, damping rates increased up to four times with respect to those observed during low-flow periods. Values of D_4 covary with D_2 (not shown); the damping of the quarterdiurnal tidal species follows the same temporal evolution as for the diurnal and semidiurnal species.

Phase differences of tidal species along the river are obtained from wavelet cross correlation with the station at the sea (*Grinsted et al.*, 2004). The phase difference for each tidal species $\Delta\phi_l$ is related to the wavenumber k_l as (*Kukulka and Jay*, 2003b)

$$\Delta\phi_l = k_l s, \tag{3.10}$$

where $\Delta\phi_l$ is given in radians and k_l is given in rad km^{-1}. Figure 3.4 shows the phase difference with respect to the station at sea of the diurnal, semidiurnal, and quarterdiurnal tidal species, and the estimated wavenumber of each tidal species. Phase differences were computed using the gauges at 40 km and 100 km from the sea. $\Delta\phi_l$ remains relatively constant in time, depicting variations that mimic those of the spring-neap cycle. Phase differences along the river clearly increase with increasing frequency (*Godin and Martinez*, 1994; *Godin*, 1999). Wavenumbers are nearly unaffected by river discharge, remaining relatively constant during the measuring period. The mean of the wavenumber over the available six months of data is 2.43 10^{-2}, 1.57 10^{-2}, and 0.96 10^{-2} rad km^{-1}, for quarterdiurnal, semidiurnal and diurnal tidal species, respectively.
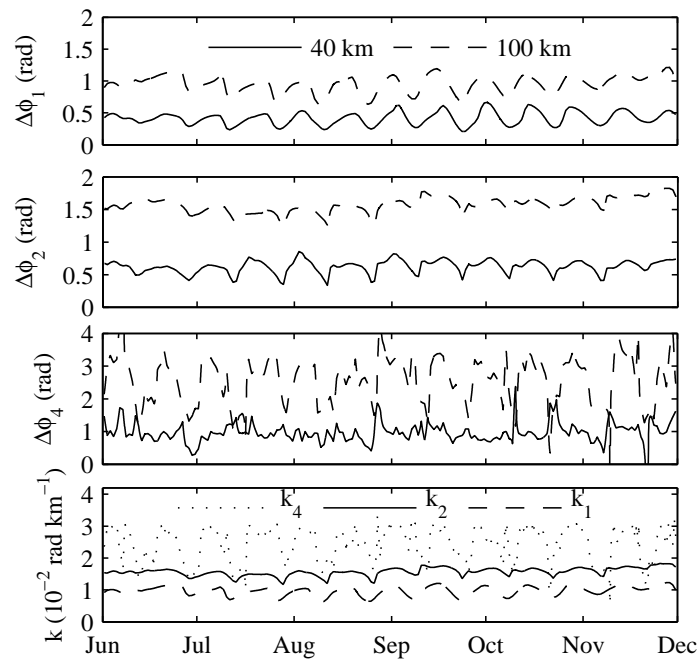
Figure 3.4: Times-series of diurnal ($\Delta\phi_1$), semidiurnal ($\Delta\phi_2$), and quarterdiurnal ($\Delta\phi_4$) phase difference with respect to the station at sea, obtained with cross wavelet analysis at stations along the river. Bottom: wavenumber k (10^{-2} rad km^{-1}) for each of the tidal species.

3.4.2 Flow Velocity

Flow velocity was obtained as the ratio between water discharge and cross-sectional area, assuming a constant width and accounting for water level variation. Time-series of mean flow velocity at the discharge station were subjected to wavelet analysis to yield velocity amplitudes corresponding to quarterdiurnal (U_4), semidiurnal (U_2) and diurnal (U_1) tidal species. Velocity series were also averaged over one day to obtain u_0, the subtidal velocity, and again averaged over 14 days to obtain u_R, the river flow. Figure 3.5 shows time-series of u_R, u_0, U_1, U_2 and U_4 at the discharge station from approximately 1.5 year of H-ADCP data. u_0 fluctuates between about 0.4 and 1.2 m s^{-1}. The semidiurnal species dominate the velocity fluctuations, featuring more variation in amplitude maxima than in amplitude minima. The spring-neap variation of U_2 is largely modulated by the river flow while that of U_1 does not show such a response. Values of U_4 clearly covary with U_2, with a mean phase difference of approximately 180°. The phase difference between diurnal and semidiurnal tidal species has a mean value of about 155°. Some variation in U_2 is also attributed to tidal damping due to the river discharge. The discharge peak during May 2008 to July 2008 shows a decrease in both U_1 and U_2, which is also apparent during the other, much longer high-discharge period lasting from October 2008 to January 2009.

3.5 Subtidal Friction

Building on the information from the previous section, the present section investigates the degree in which subtidal water levels at locations upstream can be predicted with discharge information, and knowledge of the propagation and damping of the tidal species. First, the subtidal friction components in Eq. (3.2) are shown to correlate well with subtidal water levels at the discharge station. Then, we model the contributions of subtidal friction along the river, using a quasi-empirical expression for the tidal damping coefficient that controls the amount of tidal damping as a function of river discharge. Finally, we validate the model, which captures the main mechanism of river-tide interaction, by showing the degree of agreement between the simple river-tide interaction model and the observations.

3.5.1 Decomposition

Aiming to understand the relation between the subtidal water levels at the discharge station and the measured flow velocity (*Kukulka and Jay*, 2003a; *Buschman et al.*, 2009), we decompose subtidal friction in contributions due to river flow, river-tide interaction and tidal asymmetry (Eq. 3.2). Here, the maximum velocity is chosen as

$$U_{max} = \max\left(u_0 + \sum_{l=1,2,4} U_l\right) \tag{3.11}$$

where 'max' denotes the maximum value of the expression in between brackets. Typically, the actual current at a certain moment in time will have a smaller value than U_{max} (*Godin*, 1991a). Figure 3.6 shows the contributions to subtidal friction at the discharge station from the river
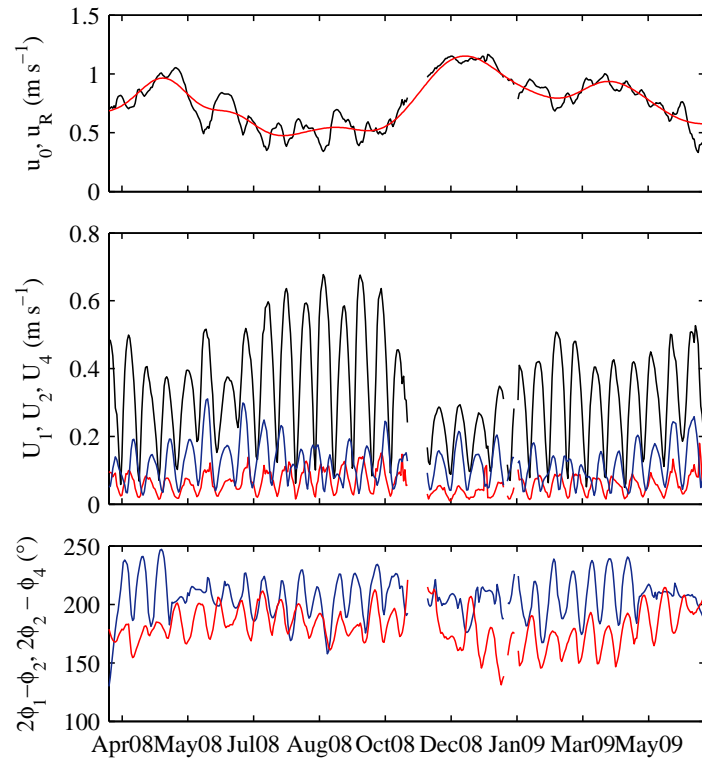
Figure 3.5: Top: time-series of subtidal velocity u_0 and river flow u_R. Middle: time-series of velocity amplitudes of diurnal (U_1, blue line), semidiurnal (U_2, black line) and quarterdiurnal (U_4, red line) tidal species obtained from wavelet analysis. Bottom: phase differences between diurnal and semidiurnal tidal species (blue line) and between semidiurnal and quarterdiurnal tidal species (red line).

Figure 3.6: Top panel: contributions to subtidal friction at the discharge station from the river flow (S_r), from river-tide interaction (S_{rt}) and from tidal asymmetry (S_t). Lower panel: comparison between subtidal water level (black solid line) and predictions (red dashed line) from a multi-linear regression with S_r and S_{rt}.

flow (S_r), from river-tide interaction (S_{rt}) and from tidal asymmetry (S_t). The amplitude in the variation of S_{rt} is likely modulated by S_r, but S_{rt} shows a stronger dependence on the squared tidal velocity amplitude (*Buschman et al.*, 2009). S_t co-varies with S_{rt} and is always negative. The non-zero mean in S_{rt} causes the rise in surface elevation due to river-tide interaction.

The comparison between water level and predictions from a multi-linear regression with S_r and S_{rt} yields a coefficient of determination $R^2 = 0.87$ and error variance $\epsilon = 0.0039~m^2$, with all other combinations yielding a lower degree of agreement. These results are very much in-line with those of *Buschman et al.* (2009) obtained in the River Berau, although they used only the S_{rt} term to predict the subtidal water levels. The relative magnitude of S_r and S_{rt} depends on the choice of the maximum velocity U_{max}, which is accounted for by the relative magnitude of the regression coefficients in the multi-linear regression.

The subtidal pressure gradient can be decomposed according to:

$$\frac{\partial \eta_0}{\partial s} = \frac{\partial \eta_R}{\partial s} + \frac{\partial \eta'}{\partial s}. \tag{3.12}$$
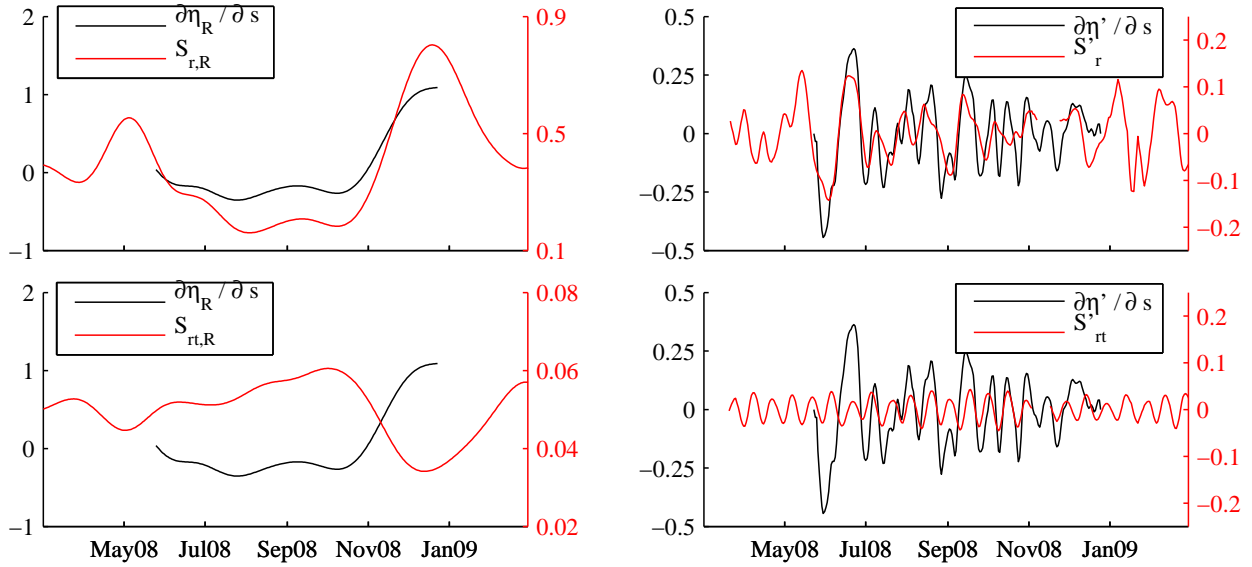
Figure 3.7: Subtidal momentum balance as a function of time between regional surface slope $\partial\eta/\partial s$ and bottom friction S (Eq. 3.13) for the fortnightly averaged (subscript R) and the fluctuating (denoted with the prime) components. The magnitude of the surface slope was scaled by a factor $C^2 H/U_{max}^2$.

Accordingly, the regional subtidal momentum balance can be written as

$$\frac{\partial\eta_R}{\partial s} \propto S_{r,R} + S_{rt,R} \tag{3.13}$$

$$\frac{\partial\eta'}{\partial s} \propto S'_r + S'_{rt}. \tag{3.14}$$

where the prime denotes the fluctuating component, the subscript R denotes the fortnightly averaged component, and the constant of proportionality is given by $U_{max}^2/C^2 H$. Fig. 3.7 shows the terms in Eq. (3.13) as a function of time. The surface slope was obtained by fitting a linear function through the available water levels at a given time. The dynamics in the fortnightly averaged component of the surface slope are mimicked by the $S_{r,R}$ term. The magnitude of $S_{rt,R}$ is smaller, and clearly depicts a strong negative correlation with $S_{r,R}$. The fluctuating component of the surface slope is more complicatedly described by a combination of S'_r and S'_{rt}, both showing variations in the same range.

3.5.2 Contributions Along the River

To relate subtidal water levels along the river to the the discharge station in a simple model, the spatial distributions of the different contributions to subtidal friction were derived using the results from Section 3.4. From the linearized continuity equation of the tidal species, the tidal velocity amplitude may be represented in a similar fashion as the water level:

$$U_l(s) = U_{0,l} \exp(r_l s), \tag{3.15}$$

52

where r_l is the damping coefficient of the tidal species $l = 1,2,4$, which were previously estimated, and $U_{0,l}$ is the tidal velocity amplitude at the discharge station. The non-dimensional tidal velocity along the river can now be readily simulated. Since we exclude the tributaries from our analysis, river discharge is assumed constant along the River Mahakam. Assuming a constant cross-section along the river reach which spans the locations of all water level sensors up to the delta apex, the subtidal velocity u_0 remains constant along the river, too. Since the maximum velocity can be computed as

$$U_{max}(s) = \max \left(u_0 + \sum_{l=1,2,4} U_{0,l} \exp \left(r_l s \right) \right),$$ (3.16)

all velocities along the river can be made dimensionless. Phase differences and wavenumbers in the tidal asymmetry term are assumed constant.

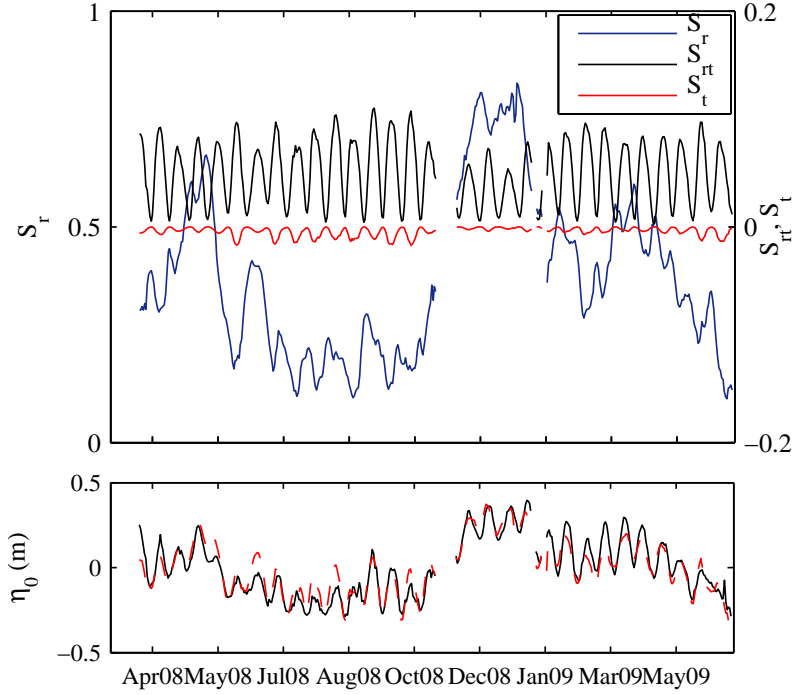Figure 3.8 shows contributions to subtidal friction along the river from the river flow (S_r), from river-tide interaction (S_{rt}) and from tidal asymmetry (S_t). S_r shows the largest range of variation, with S_{rt} and S_t being subordinates. Note that for convenience we have plotted -S_t instead of S_t. The damped character of the tidal wave is visible. Moreover, during low-flows, S_{rt} and S_t remain relatively constant along the river, whereas during high-discharge they become almost negligible. It is interesting that the spatial extent to which S_{rt} and S_t are non-negligible is much dependent on the magnitude of S_r. On the other hand, the spatial variation of S_r depends on the tidal velocity amplitude along the river. Hence, predicting subtidal water levels along the river with a multi-linear regression model such as the one proposed before results in regression coefficients that vary in space and in time, limiting the general applicability of such a model.

3.5.3 Tidal Damping

The dynamic interplay between S_r and S_{rt} is probably best explained in terms of the gradual adaptation of the water surface to the variable discharge. *Godin* (1999) showed that the damping coefficient depends in a complex manner on river flow velocity. In solving the equations of motion, he assumed a constant river flow. Figure 3.9 shows that r depends nonlinearly on $\tilde{u}_0$ for quaterdiurnal, semidiurnal and diurnal tidal species. r_4 is positive for low-flows, which indicates amplification rather than damping. Amplification of the quarterdiurnal and fortnightly components take place along the lower reach of the river until a point where it starts to be damped along with the main components (*Godin and Martinez*, 1994; *Gallo and Vinzon*, 2005). The r versus $\tilde{u}_0$ diagrams feature a number of loops at different time-scales. Averaging over a period of 14 days reveals a single large loop. It takes less time for r to increase with $\tilde{u}_0$ than vice versa, which indicates that under a discharge wave, tides are damped relatively faster during the rising limb than during the recession part.

The damping coefficient can be related to river flow as in:

$$r_l\left(t \right) = \beta_l \tilde{u}_0 \left(t + \tau_l \right)^{\alpha_l},$$ (3.17)

where τ_l denotes the time-lag, $l = 1,2,4$. Table 3.1 shows a summary of the parameters obtained with a lagged, linear regression of the log-transformed variables. For the quarterdiurnal species,
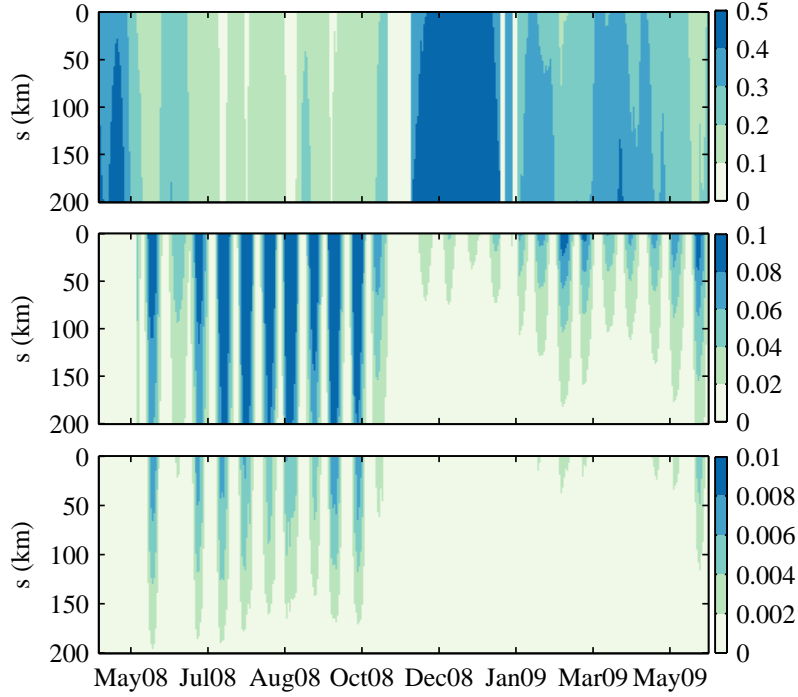
Figure 3.8: Contributions to subtidal friction along the river from the river flow (S_r, top panel), river-tide interaction (S_{rt}, middle panel) and tidal asymmetry (S_t, lower panel). For convenience, we have plotted $-S_t$ since S_t is always negative.
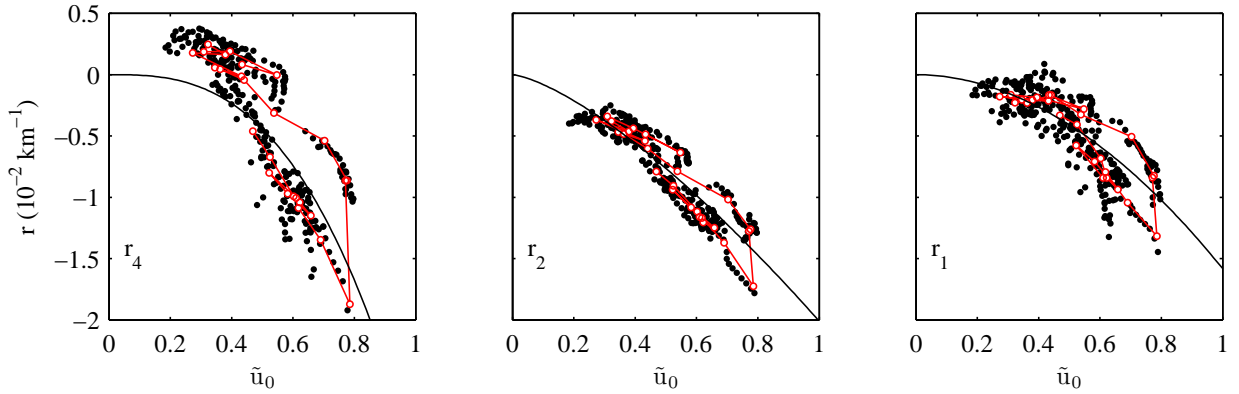
Figure 3.9: Damping coefficient r (10^{-2} km^{-1}) as a function of non-dimensional subtidal velocity $\tilde{u}_0$ for quaterdiurnal (r_4), semidiurnal (r_2) and diurnal (r_1) tidal species. The red lines remove temporal variations of the order of 14 days. The solid line is the best-fit line based on equation (3.17).

Table 3.1: Summary of regression parameters in Eq. (3.17). The variability is given by the standard error in the linear regression. The goodness of fit is represented by the coefficient of determination R^2.

r_l	$\alpha_l \pm \delta\alpha_l$	$\beta_l \pm \delta\beta_l$	τ_l (days)	R^2
r_4	2.2 ± 0.6	-2.3 ± 1.3	-10	0.77
r_2	1.5 ± 0.1	-2.2 ± 1.1	-3	0.91
r_1	2.1 ± 0.2	-1.8 ± 1.1	-6	0.86

we performed the regression with r values corresponding to tidal damping only. For each tidal species, we computed the regressions for time-lags varying from -30 to 30 days. The time-lag τ_l corresponds to the best-fit value, which was based on the coefficient of determination R^2. The estimated exponent α_l varies between 1.5 and 2, which is consistent with the value derived by *Jay* (1997) and by *Godin* (1999). The proportionality coefficient β_l remains relatively constant, albeit with a larger variability. All time-lags are within a fortnight. Note that since $\tilde{u}_0$ is dimensionless, β_l has units of 10^{-2} km^{-1}. Regressing r with u_0 yields similar exponents α, for each of the tidal species.

The subtidal friction contribution due to river-tide interaction can be written as

$$S_{rt}(s) = \frac{3}{2} b \tilde{u}_0 \sum_{l=1,2,4} \tilde{U}_{0,l}^2 \exp\left(2\beta_l \tilde{u}_0^{\alpha_l} s\right), \tag{3.18}$$

where $\beta_l = \beta = -2$, and $\alpha_l = 2, 1.5$ and 2 for $l = 1,2$ and 4, respectively. The ratio between $\tilde{U}_{0,1}^2$ and $\tilde{U}_{0,2}^2$ and the ratio between $\tilde{U}_{0,4}^2$ and $\tilde{U}_{0,2}^2$ yield an overall mean of 0.784 and 0.35, respectively. Neglecting the small variations around these mean ratios and neglecting the time-lags in equation (3.17), subtidal friction due to river-tide interaction can then be modeled as

$$S_{rt}(s) \approx \frac{3}{2} b \tilde{U}_{0,2}^2 \tilde{u}_0 \exp\left(-4\tilde{u}_0^2 s\right) \left\{ 0.74 + \exp\left(-4\left(\tilde{u}_0^2 - \tilde{u}_0^{1.5}\right) s\right) \right\}. \tag{3.19}$$

Eq. (3.19) models the contribution of river-tide interaction to the friction term in the momentum equation, quantifying the resistance a river discharge wave experiences when traveling through the tidal river. It shows the additional friction is directly proportional to the tidal amplitude squared, but a much more complex nonlinear function of the river flow. Figure 3.10 shows the logarithm to base ten of the ratio between S_{rt} and S_r as a function of river flow u_0 and semidiurnal tidal velocity amplitude at the mouth $U_{0,2}$, for three locations along the idealized river ($s = 0, 100, 200$ km). The parameter range for which the ratio of S_{rt} to S_r falls between nearly one third and three is considerable, and remains relatively broad up-river. For a river flow of 0.5 m s^{-1} and semidiurnal tidal amplitudes at the mouth of about 0.7 m s^{-1}, we find $S_{rt} \sim S_r$ at 200 km from the river mouth. This explains why during June-October 2008 river discharge features a strong fortnightly oscillation all along the downstream reaches of the River Mahakam. Moreover, at lower flow rates S_{rt} can still be greater than S_r, which also explains why river discharge division in the terminal distributaries of the Mahakam delta is highly impacted by river-tide interaction (*Sassi et al.*, 2011b, 2012a).
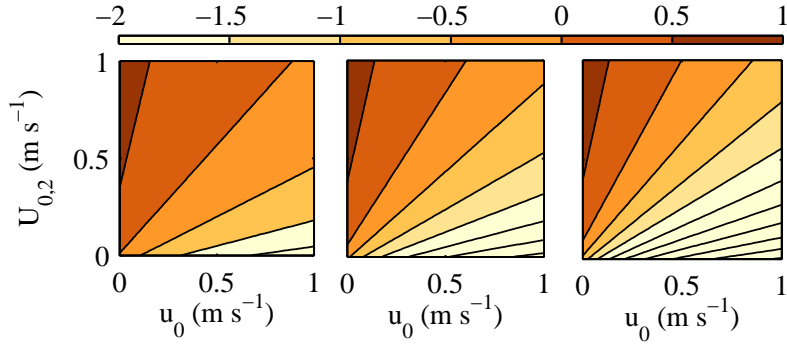
Figure 3.10: Logarithm to base ten of the ratio between S_{rt} and S_r as a function of river flow u_0 and semidiurnal tidal velocity amplitude at the mouth $U_{0,2}$ for three locations along the river ($s = 0$, 100, 200 km).

3.5.4 Validation

Using the semidiurnal tidal velocity amplitude $U_{0,2}$ and river flow velocity u_0 obtained at the discharge station, we investigate the extent to which subtidal water levels measured upstream can be pedicted from S_{rt} using equation (3.19) and S_r. Figure 3.11 shows subtidal water levels η_0 at four locations along the river, and the predictions using a multi-linear regression with S_r and S_{rt}. For each of the four stations, 50% of the data was used for calibration, to establish the two regression coefficients per site. The remaining 50% of the data is used for validation, which shows a good agreement between predictions and observations ($r_{corr} > 0.8$). This confirms Eq. (3.19) captures the essence of additional friction by river-tide interaction.

3.6 Summary and Conclusion

River-tide interaction refers to a frictional effect driven by variable tidal amplitudes in the presence of a net river flow, causing a co-oscillation of the river water surface with the tidal forcing. Since tidal amplitudes at a given location mainly vary with the spring-neap cycle, the water surface oscillates at specific and well-defined tidal frequencies. For steady flow conditions, tidal amplitudes along the river may depend on a number of factors yielding tidal damping or amplification. At locations far enough up-river, however, all tidal constituents vanish due to the effect of bottom friction. This vanishing contribution of the forced fortnightly tide leads to a non-zero mean contribution to the water surface profile. Since tidal amplitudes vary with changes in river discharge in time and space, river discharge fluctuations create an additional source of friction that drive tidal damping or tidal amplification. Therefore, river-tide interaction results in fortnightly contributions to the water surface profile with highly-variable amplitudes. This contribution shows the quasi-steady pressure gradient can drive fortnightly averaged discharge variations in a tidal river. The feedback between river discharge and the tidal motion, and the variation in runoff limit the predictability of subtidal water levels in tidal rivers.

In this study we have investigated the mechanism of river-tide interaction in relation to
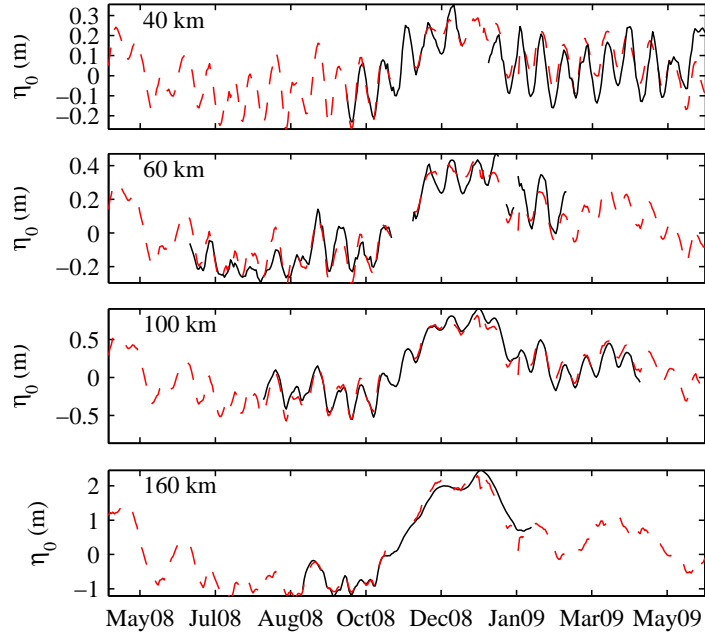
Figure 3.11: Comparison between subtidal water level at stations along the river (black solid line) and predictions (red dashed line) with S_{rt} using equation (3.19) and S_r, obtained by calibration with 50% of the data. The remaining 50% of the data serve as validation.

variations in river discharge, which was based on field observations undertaken in the River Mahakam, Indonesia. A network of pressure sensors and a discharge station was set up along the lower reaches of the tidal river. Tidal amplitudes decrease up-river whereas subtidal variations amplify. Subtidal variations in water level measured upstream resemble more those variations in subtidal discharge measured downstream than the subtidal water level measured at the closemost gauge. Since the subtidal water level is driven by a combination of river discharge and river-tide interaction, these observations suggest that river-tide interaction controls the admittance of river discharge waves into the downstream reaches of the River Mahakam.

Wavelet analysis was applied to water level and water discharge data, to obtain time-series of amplitudes from the tidal surface levels and from the mean flow velocities. Tidal surface level amplitudes along the river allowed us to estimate the temporal variation in tidal damping coefficients. A wavelet cross correlation with the gauged levels at the sea yielded wavenumbers. Damping coefficients strongly depend on the river discharge, showing a dynamic behavior within a fortnight. Wavenumbers remained relatively constant during the measuring period. Contributions to subtidal friction due to river flow (S_r), river-tide interaction (S_{rt}) and tidal asymmetry (S_t) were estimated. The relation between tidal damping and river discharge was employed to derive the along-channel variation of the subtidal friction components. The magnitudes of S_{rt} and S_t strongly depend on the magnitude of S_r. The relative importance of these, however, depend on the choice of the maximum velocity used to make all amplitudes dimensionless. Our results show that even for high river flow and low tidal velocity amplitudes, river-tide interaction adds significantly to subtidal friction, since S_{rt} depends non-linearly on

57

the river flow. Finally, a simple model was proposed revealing the dependence of subtidal friction from river-tide interaction on tidal amplitude and river flow velocity. Subtidal water levels were predicted at locations upstream, calibrated with 50% of the data, using S_r and the derived expression for S_{rt}. The remaining 50% of the data, used for validation, shows a good agreement between predictions and observations.

Chapter 4

Discharge Division

Abstract: Bifurcations in tidally-influenced deltas distribute river discharge over downstream channels, asserting a strong control over terrestrial runoff to the coastal ocean. Whereas the mechanics of river bifurcations is well-understood, junctions in tidal channels have received comparatively little attention in the literature. This chapter aims to quantify the tidal impact on subtidal discharge distribution at the bifurcations in the Mahakam Delta, East Kalimantan, Indonesia. The Mahakam Delta is a regular fan-shaped delta, composed of a quasi-symmetric network of rectilinear distributaries and sinuous tidal channels. A depth-averaged version of the unstructured mesh, finite-element model SLIM (Second-generation Louvain-la-Neuve Ice-ocean Model) has been used to simulate the hydrodynamics driven by river discharge and tides in the delta channel network. The model was forced with tides at open sea boundaries and with measured and modeled river discharge at upstream locations. Calibration was performed with water level time-series and flow measurements, both spanning a simulation period. Validation was performed by comparing the model results with discharge measurements at the two principal bifurcations in the delta. Results indicate that within 10 to 15 km from the delta apex, the tides alter the river discharge division by about 10% in all bifurcations. The tidal impact increases seaward, with a maximum value of the order of 30%. In general, the effect of tides is to hamper the discharge division that would occur in the case without tides.

4.1   Introduction

Most of the world's large rivers debouch in deltas prograding on continental shelves. Flow division in delta channel networks may affect the occurrence of natural resources in coastal areas, as river discharges carry terrestrial sediments, nutrients and contaminants to the coastal zone. Discharge division at bifurcations may assert a strong control over the morphological evolution of river deltas (*Wolinsky et al.*, 2010), as the flow brings the material needed for delta progradation (*Edmonds and Slingerland*, 2007). Coastal ecosystems may depend on the organic matter brought by the river, whose main pathways are controlled by flow processes at bifurcations in the delta. The processes governing flow division at river bifurcations have been investigated theoretically (*Wang et al.*, 1995; *Bolla-Pitaluga et al.*, 2003), with numerical models (*Lane and Richards*, 1998; *Dargahi*, 2004; *Zanichelli et al.*, 2004), and in experimental flumes (*Bertoldi and Tubino*, 2007). These studies generally do not consider the influence of tides, which intrude from the mouths of distributaries and complicate the processes governing flow division (*Buschman et al.*, 2010). The aim of this chapter is to investigate the tidal impact on the distribution of river discharge over the distributary channels of a tidally-influenced delta.

In shallow rivers, frictional forces generally exceed forces associated with inertial accelerations. Therefore, fortnightly fluctuations in water level arise as a consequence of fortnightly variation in friction (*LeBlond*, 1979; *Godin*, 1991b). *Buschman et al.* (2009) decomposed the tidally averaged friction term (herein subtidal friction) into contributions due to (1) river discharge, (2) river-tide interaction and (3) tidal asymmetry inherent to the sum of tidal harmonics. Subtidal friction is mainly balanced by the pressure gradient, which leads to the characteristic subtidal variation in water level. *Buschman et al.* (2009) used their analysis of the subtidal momentum balance to explain subtidal water level dynamics in the Berau River, East Kalimantan, Indonesia. Motivated by observations at the apex of the Berau Delta, *Buschman et al.* (2010) investigated the sensitivity of subtidal flow division to tidal modulation. An idealized numerical model was setup of a river that bifurcates in two sea-connected branches, with parameters resembling those in the real case. Numerical experiments were conducted to investigate the sensitivity of subtidal flow division to variations in depth, length, width and bed roughness of one of the bifurcating branches. *Buschman et al.* (2010) highlighted the importance of tides in enhancing the inequality in subtidal flow division when one of the sea-connected branches was deeper or shorter, whereas bed roughness differences resulted in an opposing effect. The aforementioned idealized study awaits confirmation from studies of delta distributary networks based on full-complexity models, such as presented herein.

A tidal wave that propagates upriver as a progressive wave induces a landward mass transport known as Stokes flux. The Stokes flux is maximal when water surface level and flow velocity are in phase, and reduces when the phase difference approaches 90 degrees. Stokes fluxes in tidal channels therefore may be negligible when the effect of friction balances the effect of width convergence, such that the tidal wave resembles a standing wave (*Friedrichs and Aubrey*, 1994). In a single channel, the Stokes flux is compensated by a seaward directed flux (hereinafter return flux), induced by a subtidal pressure gradient. When two channels join at a bifurcation, the system is constrained by one water surface level, although flow velocity amplitudes and phases may differ. The landward Stokes flux at each of the channels induces a return flow that does not necessarily balance in each individual channel. The asymmetry in

the return flow therefore enhances a tidal mean discharge into one of the downstream channels.

Studies on tidal distributary networks often address problems with numerical models, owing to the complexity of the systems and the impossibility to monitor relevant spatial and temporal scales comprehensively. The insights from the existing literature is therefore fragmented. In the Columbia River estuary, *Lutz et al.* (1975) observed that for low river discharge, tides caused an asymmetrical flow distribution during the ebb. *Hill and Souza* (2006) showed that continuity and momentum equations may be linearized for a network of deep channels. They successfully represented tidal propagation in a fjord region. In a channel network forced by tides at entrances on opposite sides *Warner et al.* (2003) showed that subtidal flows are controlled by the temporal phasing and spatial asymmetry of the two forcing tides. *Buijsman and Ridderinkhof* (2007) showed that subtidal flows in the shallow Wadden Sea occur between the inlet channels that have a large tidal range and inlets with lower tidal range, reflecting the effect of nonlinearities in the shallow water equations.

The tidal motion in delta channel networks is characterized by a wide range of temporal and spatial scales, which becomes even wider when river dynamics and the transient interactions with the tidal motion are taken into account. Unstructured-mesh modeling is a promising option to deal with multi-scale physics in space and time (e.g. *Deleersnijder et al.*, 2010). The main advantage is the spatial flexibility with a possible refinement in small channels, in shallow areas or across inclined bottoms. The Second-generation Louvain-la-Neuve Ice-ocean Model (SLIM, www.climate.be/slim) is able to cope with highly multi-scale applications (*Deleersnijder and Lermusiaux*, 2008; *Lambrechts et al.*, 2008a) such as the Great Barrier Reef (*Lambrechts et al.*, 2008b) or the Scheldt River Basin (*de Brye et al.*, 2010). Therefore, a finite-element approach is preferred over the traditional finite-difference approach, as unstructured meshes allow to refine the computational grid in the narrow channels of the delta. In addition, as local conditions at bifurcations may play a fundamental role in discharge division, boundaries can be better represented with an increased resolution.

Calibration and validation of coastal hydrodynamic models usually rely on the correct representation of water levels and flow velocities at tidal frequencies. Although the tidal motion may account for a large amount of the variability in the dynamics of the system, it only accounts for a limited portion of the frequency domain. Studies dealing with tides and river discharge should also capture the portion of the spectrum corresponding to subtidal variations. In this context, continuous time-series of water levels are readily obtained, but particularly in large river systems, discharge measurements require a substantial effort. Repeated surveys with Acoustic Doppler Current Profilers (ADCPs) mounted on a boat are increasingly being used to understand complex flows at cross-sections in natural environments (*Dinehart and Burau*, 2005a,b). Discharge measurements can then be obtained at a bifurcation spanning the major tidal frequencies and can be repeated at neap tide and spring tide. Several of such discharge surveys were acquired as validation data for this chapter.

This chapter continues as follows. Section 4.2 introduces the Mahakam Delta channel network and measuring network. Section 4.3 presents discharge measurements at the principal bifurcations in the delta. Section 4.4 briefly describes the implementation of SLIM to the Mahakam case. Section 4.5 shows the calibration and validation of the numerical model with fieldwork measurements. Section 4.6 investigates the effect of tides on discharge division. Finally, Section 4.7 presents a summary and the conclusions.

4.2   Field Site and Instrumentation

The River Mahakam is located in the East Kalimantan province, Indonesia (Figure 4.1). The catchment area is approximately 75.000 km^2 and the total river length is about 900 km, of which three quarters are navigable. The annual mean river discharge has been estimated in the order of 3000 m^{3}s^{-1} (*Allen and Chambers*, 1998). East Kalimantan province is characterized by a tropical rain forest climate with a dry (May to September) and a wet (October to April) season, governed by the Monsoons. The river mouth is separated from the upper reaches of the catchment by an alluvial plain located about 150 km upstream. During periods of heavy rainfall, strong floods up to 5000 m^{3}s^{-1} can rise the mean water level more than five meters. A system of interconnected lakes with a total area of about 400 km^2 creates a buffer capacity damping flood surges and resulting in a relatively constant discharge in the lower reaches of the river.

At the delta apex, the River Mahakam drains into a regular fan-shaped delta composed of a quasi-symmetric network of rectilinear distributaries and sinuous tidal channels. The Mahakam delta encompasses two fluvial distributary systems directed SE and NE, comprising eight and four outlets debouching into the sea, respectively. The inter-distributary zone is tide-dominated and allocates many tidal channels, which are only occasionally connected to the fluvial system. Salinity intrusion generally reaches to about 10 km seaward from the delta apex (or 30 km landward from the coast). Only during extremely low flows, such as the El Niño-related drought in 1997, salinity intrusion can reach beyond the delta apex. The study area is therefore generally subject to freshwater conditions. Due to the mild slope of the river, the tidal wave can propagate up to 190 km from the river mouth, depending on the river discharge.

A measuring network was setup along the lower 400 km of the river, for a period of about 18 months. It consisted of several water level gauges distributed along the river and in the delta. Two horizontally deployed acoustic Doppler current profilers (H-ADCPs) were installed upstream of the lakes region, and near the delta apex, respectively (see Figure 4.1). The measuring protocol of the water level gauges was set to yield a one minute average every 15 minutes, while that of the H-ADCPs was set to yield a 10 minute average every 30 minutes. Both instruments recording at 1 Hz. Table 4.1 displays amplitudes and phases of the main tidal constituents obtained from a harmonic analysis of surface elevation, measured at an outlet in the northern part of the delta. Velocity measured with the H-ADCP was converted to river discharge using conventional shipborne ADCP discharge measurements. At the downstream discharge station, where tides dominate, seven 13-h ADCP campaigns were carried out spanning high- and low- flow conditions, during spring tide and neap tide. Upstream of the lakes, where the tidal influence is negligible, eight 6h ADCP campaigns also covered a wide range of flow conditions. Details of the procedures to convert flow velocity across the river section into water discharge can be found in *Sassi et al.* (2011a), who present an adaptation to the method described in *Hoitink et al.* (2009).

An intensive bathymetric survey with a single-beam echo-sounder was conducted covering the main part of the river, its tributaries, the three lakes and the delta region. Transect data of bed elevation were projected on a curvilinear grid based on linear interpolation (*Legleiter and Kyriakidis*, 2007) to produce the bathymetric map of the channels. Figure 4.2 shows the bathymetry of the delta, which has been simplified by omitting tidal channels not connected to
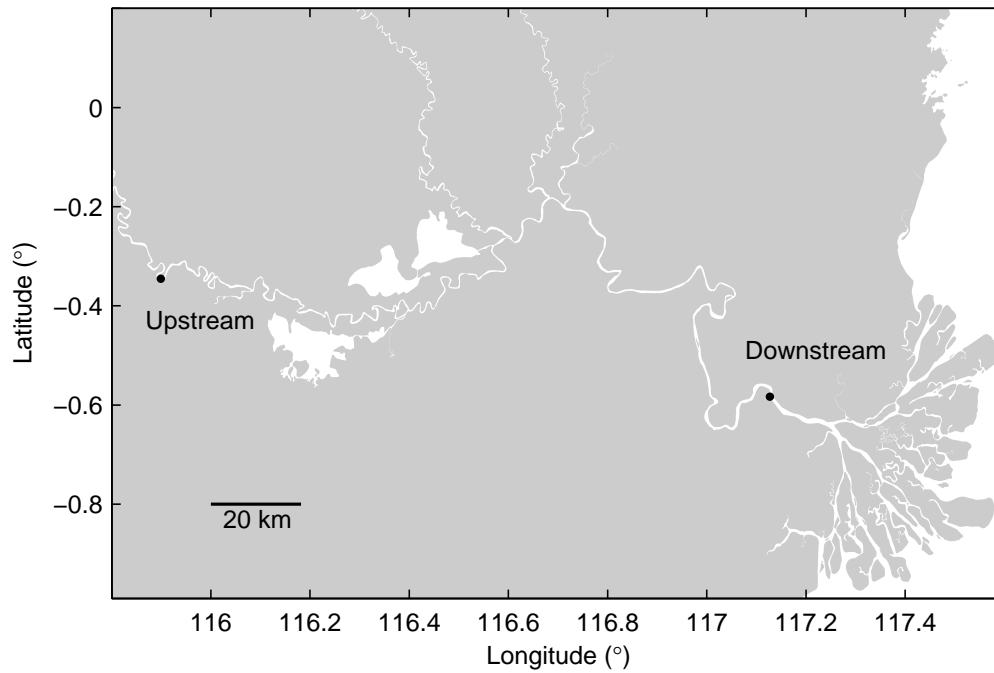
Figure 4.1: Location map of the River Mahakam in East Kalimantan, Indonesia. Black dots denote H-ADCP discharge stations, separated by about 300 km.

Table 4.1: Overview of main tidal constituents, obtained from a harmonic analysis of water level gauges at an outlet in the northern part of the delta.

Constituent	Amplitude (cm)	Phase (°)
Q1	4	263.07
O1	19	254.36
P1	7	315.38
K1	24	256.01
N2	7	165.44
M2	55	146.69
S2	40	263.30
K2	15	354.23
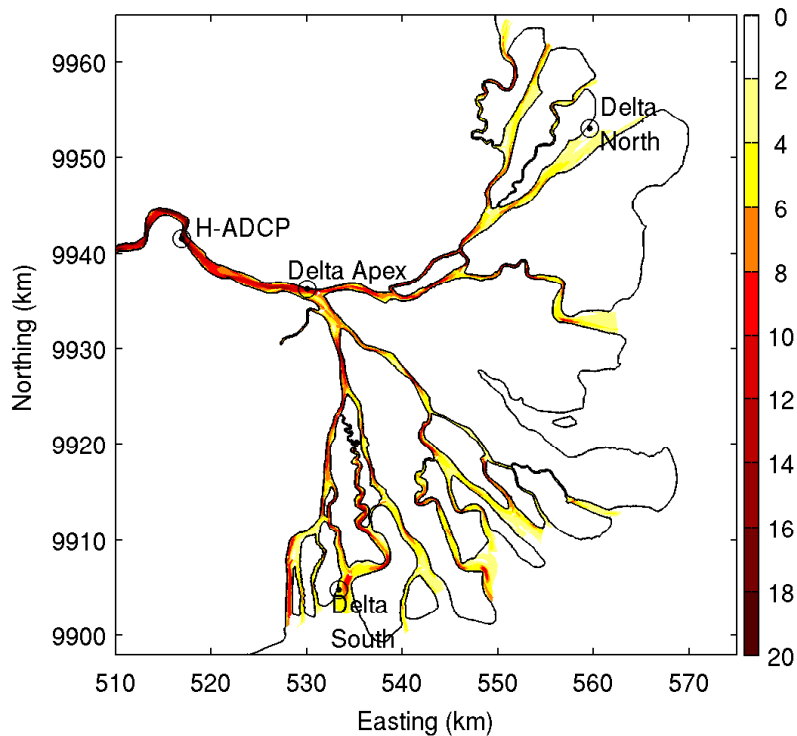
Figure 4.2: Bathymetry (in meters below mean sea level) of the Mahakam Delta channel network. Easting and Northing coordinates correspond to UTM50M. Depths are in meters below mean sea level. The discharge station, indicated by H-ADCP, is located upstream of the delta apex. Water level stations are located just before the delta apex and at the seaside of the northern and southern distributaries.

the fluvial network. All channels in the delta have variable depth, generally ranging between 5 and 15 m. The distributaries become shallower seawards; the river is consistently deeper, with an average depth of 15 m. Noteworthy are several deep spots located at bends, junctions and constrictions.

4.3 Surveys to Establish Discharge Distribution

Discharge measurements were carried out at the principal bifurcating branches in the delta (Figure 4.3). The bathymetry of the river, upstream of the delta apex, features a meandering thalweg which continues through the northern branch. At the southern branch, an elongated depositional area in the middle of the channel, extending about 4 km, divides the channel in two well-defined water courses. The southernmost of these water courses cuts through the elongated bank, leading to the northern branch of the first bifurcation. It is interesting to note the shallow area at the confluence of a small tributary and the southern branch, which defines another water course leading to the southern branch of the first bifurcation.

With a boat-mounted ADCP 13-h transects were navigated to collect velocity profiles at
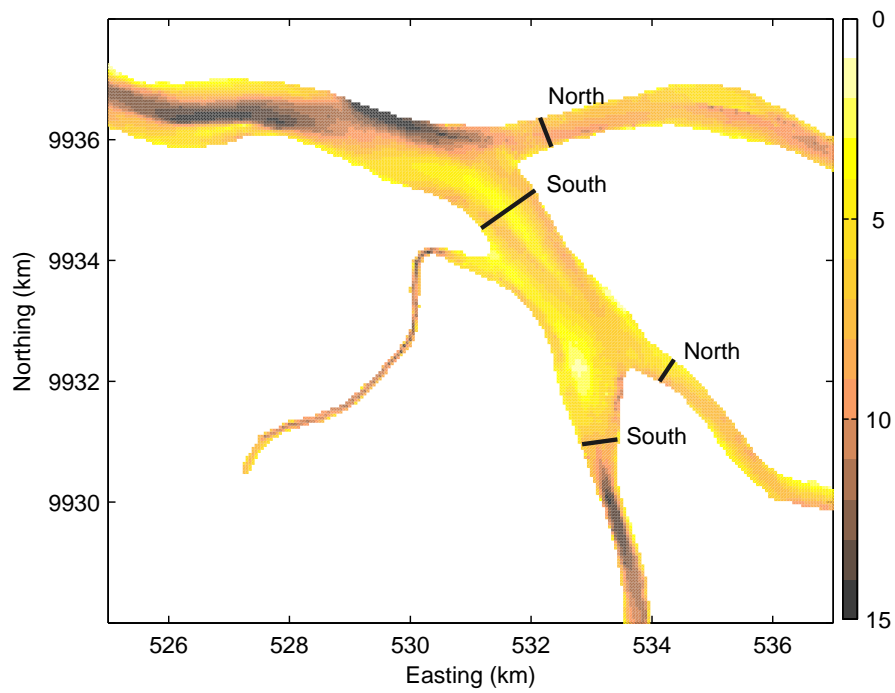
Figure 4.3: Bathymetry (in meters below mean sea level) of the delta apex and the first bifurcation. Black lines indicate the cross-river transects navigated to obtain discharge estimates in the northern and southern channels of the two principal bifurcations.

the two principal bifurcations of the delta, hereinafter Delta Apex (DA) and First Bifurcation (Bif). Navigated transects during spring tide and neap tide covered the same path. The research boat was equipped with a 1.2 MHz RDI Broadband ADCP measuring in mode 12, a multi-antenna Global Positioning System compass operating in differential mode (D-GPS) and a single-beam echo-sounder. The ADCP measured a single ping ensemble at approximately 1 Hz with a depth cell size of 0.35 m. Each ping was composed of 6 sub-pings separated by 0.04 s. The range to the first cell center was 0.86 m from the surface. The boat speed ranged between 1-3 m s^{-1}. To compute flow velocity with respect to a fixed reference frame, the boat speed vector was subtracted from the measured velocity vector. Boat speed was computed for each ensemble using Bottom Tracking (BT) and the D-GPS compass system. BT-derived boat speed estimates are known to be biased by sediment transport during strong currents, because the moving bed creates an apparent velocity in the same direction as the flow (*Rennie et al.*, 2002). Therefore, when available, we corrected flow velocity with the D-GPS compass system.

Each ADCP ensemble represents a vertical profile of the three flow velocity components. A transect can be defined as the path in between two opposing riverbanks. Within a transect and within the measuring range of the ADCP, discharge was computed as (*Simpson*, 2001)

$$Q(t) = \int_0^T \int_0^H (\vec{v_S} \times \vec{v_F}) \cdot \hat{k} \, dz \, dt', \tag{4.1}$$

where Q is water discharge (m^3 s^{-1}), t is time, $\vec{v_S}$ is boat velocity vector as determined with the BT or D-GPS systems (m s^{-1}), $\vec{v_F}$ is water velocity vector from each ADCP ensemble (m s^{-1}), $\hat{k}$ is a unit vector in the vertical direction, dz is vertical differential depth, t' is time within a transect during which Q is assumed independent of T, H is total water depth (m), and T is total transect time (s). T is typically about 5 minutes for a channel width of 500 m. The integrand can be written as

$$X = (\vec{v_S} \times \vec{v_F}) \cdot \hat{k} = v_{Fx} v_{Sy} - v_{Sx} v_{Fy}, \tag{4.2}$$

where X has units of discharge per unit width per unit time, and x and y are the two horizontal coordinates. Discharge near the bottom and near the surface was estimated by computing the slope of the three uppermost valid bins to extrapolate X up to the surface, and by fitting a constant power law to the 20% lowermost valid bins to extrapolate X down to the bottom. Discharge near the banks was obtained by linearly extrapolating X to zero at the banks.

ADCP campaigns took place during spring tide and neap tide, at both locations during the rising limb of a discharge wave. Figure 4.4 shows time-series of measured discharge over a semidiurnal tidal cycle, obtained at the bifurcating branches of Delta Apex (top) and First Bifurcation (bottom) during neap (left) and spring tide (right). Discharge fluctuates due to the modulation effect of the tides, which is stronger during spring tide than during neap tide. Intratidal discharge fluctuations are particularly asymmetrical during spring tides, with a long-lasting ebb and comparatively shorter flood. At the northern branch at Delta Apex, during spring tides, the flood period leads to a landward flow for approximately 30% of the tidal cycle. It is interesting to note that this does not occur at the northern branch of First Bifurcation, despite that this junction is closer to the sea.

A synoptic overview of the tidally averaged quantities summarizing the moving-boat ADCP campaigns is presented in Table 4.2. The combined North and South discharge at First Bifurcation may expected to be similar to the discharge measured at the southern branch of Delta
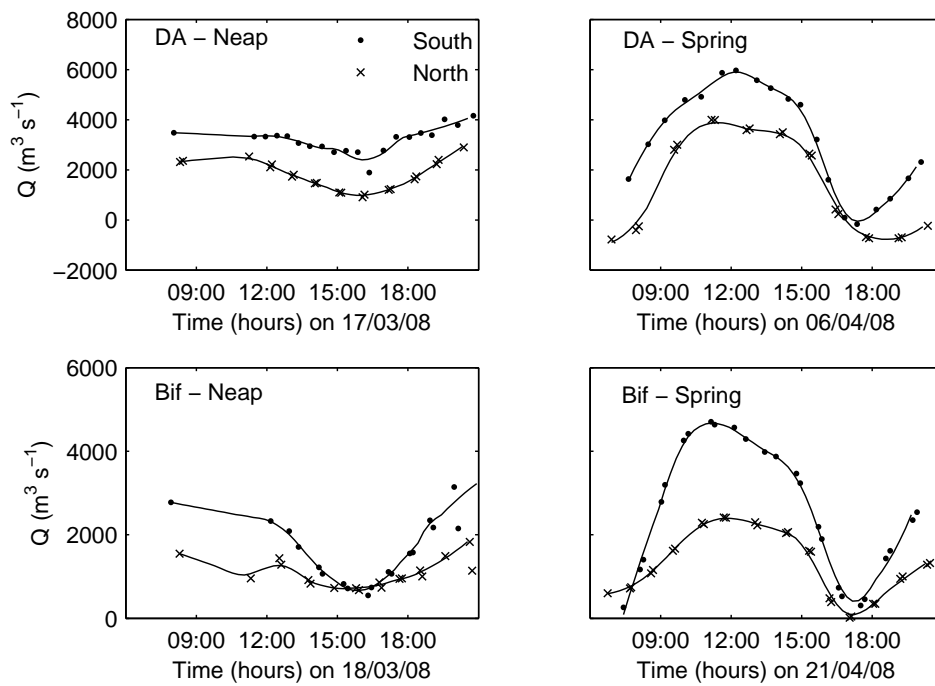
Figure 4.4: Measured discharge obtained at bifurcating branches in Delta Apex (top) and First Bifurcation (bottom) over neap (left) and spring (right) tidal conditions. Positive discharges correspond to a seaward flow direction. Solid lines smooth out temporal variations in discharge below 1.5 h.

67

Table 4.2: Summary of tidally averaged quantities during the hydrographic campaigns, where DA stands for Delta Apex, Bif stands for First Bifurcation.

Location	Date	Tide	Branch	$W\,(m)$	$A\,(m^2)$	$Q\,(m^3 s^{-1})$
DA	17-Mar-2008	Neap	North	530	4080	1920
			South	910	5980	3480
DA	06-Apr-2008	Spring	North	500	3960	1430
			South	1010	6580	3240
Bif	18-Mar-2008	Neap	North	400	2650	1150
			South	600	4720	2140
Bif	21-Apr-2008	Spring	North	450	3080	1330
			South	750	5470	2650

Apex. Regarding neap tide, the difference is indeed merely 6%. During spring tide, the difference reaches 20%, but the spring tide measurements at Delta Apex were taken two weeks earlier then the ones at First Bifurcation. Besides measurement errors, there are three other reasons why the discharge averaged over a semidiurnal tidal cycle is not necessarily identical for successive spring-neap cycles. First of all, the river discharge changes significantly in two weeks time (see Figure 4.6). Secondly, with a 13-h measurement series, diurnal tides cannot be properly isolated from the subtidal discharge. Diurnal tides feature a spring-neap cycle synchronized with the 27.32-day orbital cycle of the Moon (*Kvale*, 2006; *Hoitink*, 2008), which has a slightly different period than the familiar spring-neap cycles induced by the 29.52-day cycle of lunar phases. Finally, the difference can partly be caused by the small tributary debouching in between Delta Apex and First Bifurcation.

4.4 Numerical Model

A depth-averaged version of SLIM was used. Two 2D computational domains were defined to cover the Mahakam delta and the lakes, which were connected to a 1D representation of the river and parts of its tributaries. Bathymetry was obtained from measurements in all domains, except for the outer delta and continental shelf, where GEBCO (www.gebco.net) database information was used. Figure 4.5 shows the computational mesh of the numerical model. Over 70% of the elements represent the delta. Details of the model implementation can be found in *de Brye et al.* (2011).

The model was forced with tides from the global ocean tidal model TPXO7.1 at open boundaries located far away from the delta, stretching over the entire Makassar Strait (Figure 4.5). The 2D shallow-water equations succeed in representing the propagation of the tides through the strait and onto the continental shelf, up to the outlets of the delta. Although strong wind conditions may hamper the 2D approach, the impact of wind in the Makassar Strait is limited. Baroclinic effects associated to 3D flows were assumed to have negligible

interaction with the delta.

At the upstream boundary, the model was forced with a discharge series derived from H-ADCP measurements. At the tributaries connected to downstream modeling domain, discharge series were obtained from a rainfall-runoff model, calibrated with the measured discharge series of the principal subcatchment (Figure 4.6). The slope of the river was set to 1×10^{-5}. This value was inferred from an analysis of the subtidal momentum balance following *Buschman et al.* (2009), using flow measurements from the H-ADCP near Samarinda and surface elevation from the level gauge at Delta Apex. Bottom friction, represented by a Manning coefficient n, was obtained from the following calibration procedure, in which the computational domain is split in three parts. A constant Manning coefficient ($n = 0.023$) was assumed in the deepest part of the domain beyond the slope break of the continental shelf, since it was found to be a good choice for the continental shelf in another application of the SLIM model (*de Brye et al.*, 2010). A different constant Manning coefficient represented bottom roughness in the fluvial part of the domain, upstream of the mouths of the distributaries. In the continental shelf part in between the latter two regions of constant bottom roughness, a linear transition between the deep water part of the model and the distributaries was assumed. We have varied the Manning coefficient in the inner region from 0.017 to 0.029 and we have tested five cases, of which $n = 0.026$ in the inner region resulted in the best match with our measurements. Those test cases were simulated over a time-span of two weeks. The numerical simulations for calibration of the model were carried out with water levels obtained at the three stations depicted in Figure 4.2, and discharge estimates from the monitoring station located in Samarinda (*Sassi et al.*, 2011a). The calibration presented herein is slightly different from a previous approach described by *de Brye et al.* (2011), who calibrated the model with water levels only. The following section presents the results of simulations with the optimized bottom roughness configuration. Model runs spanned from March through April 2008.

4.5 Results

Time-series of water levels from the model and the observations were subjected to a Continuous Wavelet Transform, using a Morlet mother wavelet. Wavelet analysis was preferred over traditional harmonic analysis because of its ability to deal with non-stationary signals (*Jay*, 1997). The scale resolution used in the wavelet transform allowed us to distinguish between main tidal species, instead of between tidal constituents. The wavelet spectrograms yielded amplitudes of quarterdiurnal (D_4), semidiurnal (D_2) and diurnal (D_1) fluctuations. Time-series of water levels and discharge were averaged over a 24-h period to obtain subtidal water levels and discharges (respectively).

Spectrograms generally show a well-defined gap between the tidal band, where the main tidal species occur, and the subtidal band, where river discharge fluctuations and associated interactions with the tidal motion dominate (see Figure 4.7). The frequencies at which wavelet power is resolved is an array of powers of 2, which is chosen such that D_1, D_2 and D_4 are resolved (*Buschman et al.*, 2009). With that choice, it is not possible to sharply distinguish between fortnightly fluctuations and monthly or seasonal fluctuations. Nevertheless, we isolated the fortnightly variation by delimiting the fortnightly frequency domain in the normalized global wavelet power spectrum. This procedure yields fortnightly power concentrated in a
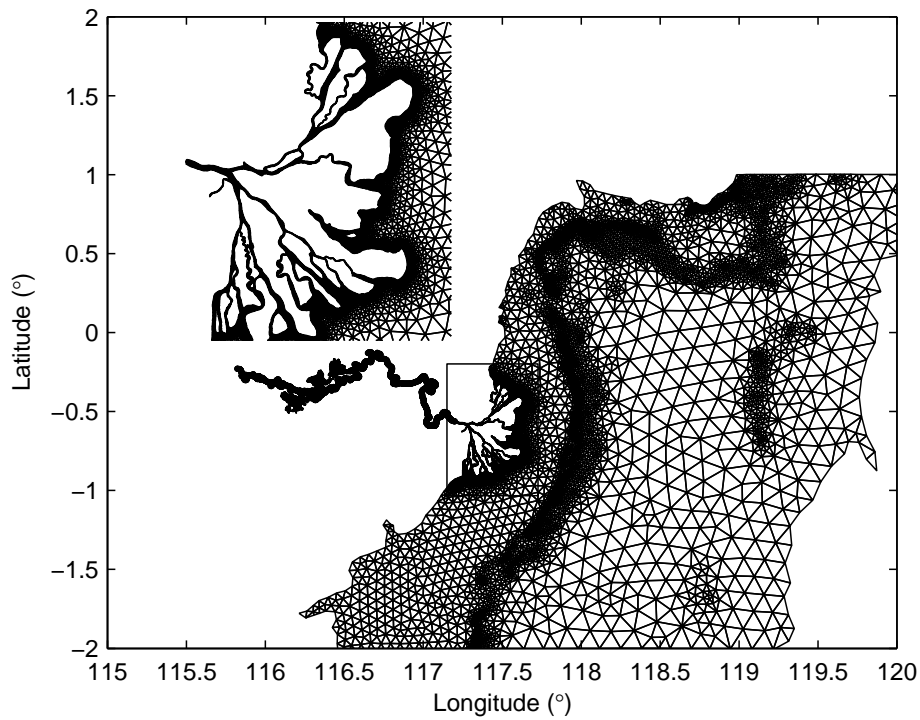
Figure 4.5: Mesh of the computational domain. The 2D domain is connected to a 1D river and tributaries network.
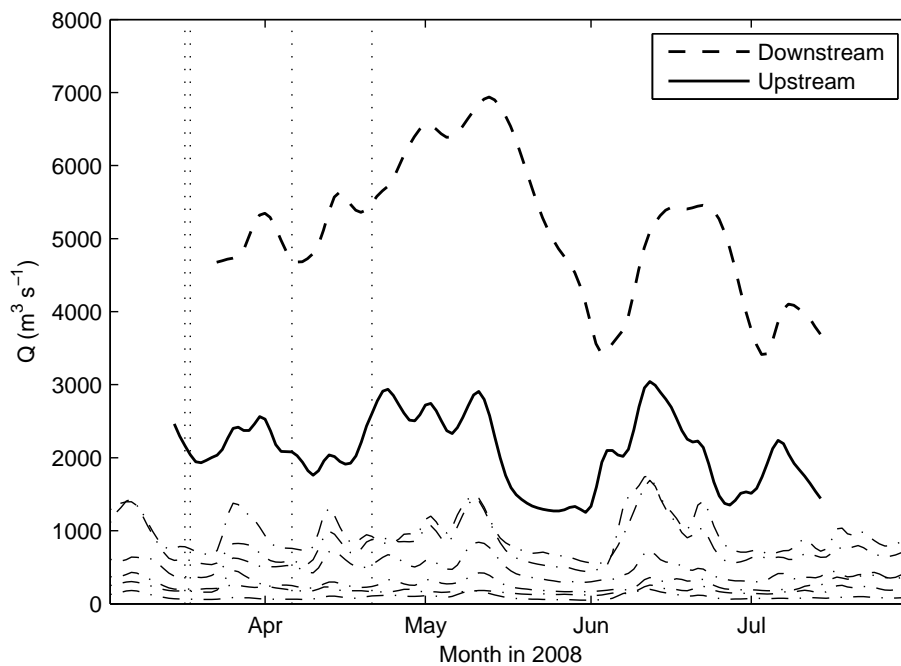
Figure 4.6: Measured discharge series at upstream and downstream locations. Dash-dotted lines indicate discharge series in the tributaries as obtained from the rainfall-runoff model. Dotted lines denote the date of discharge measurements at the bifurcations.
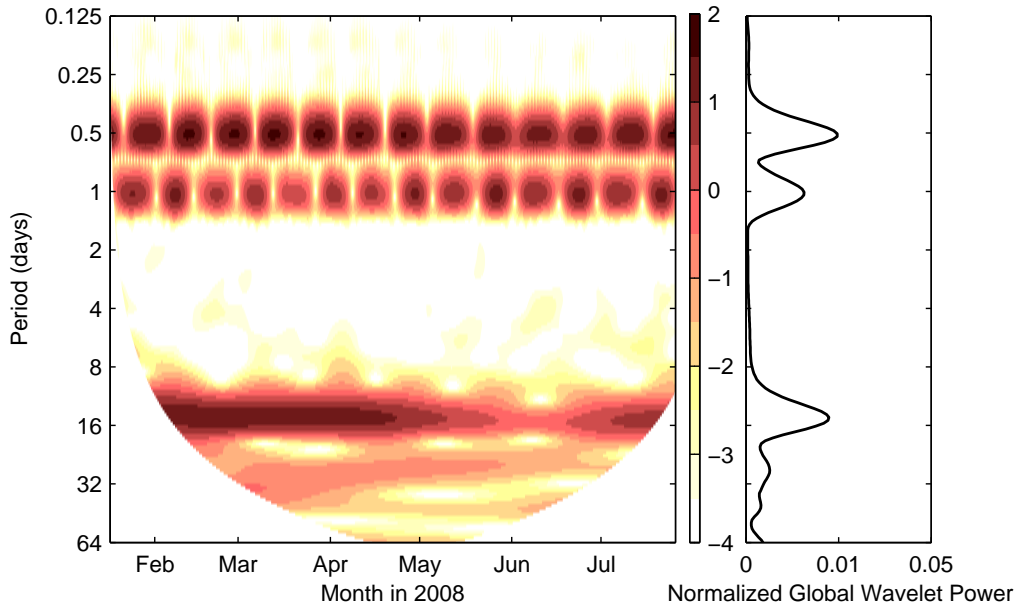
Figure 4.7: Wavelet spectrogram (left) and normalized global wavelet power spectrum (right) for water level time-series at Delta Apex station.

band corresponding roughly to 10-20 days. Fortnightly amplitudes of water levels obtained accordingly are denoted by $D_{1/14}$. It is noted that, to some degree, power from adjacent regions in the spectrogram, such as that associated to weekly and monthly fluctuations, may have leaked into the selected window.

4.5.1 Validation of Modeled Water Levels and Flow

Figure 4.8 shows time-series of subtidal water level and amplitudes of D_4, D_2, D_1 and $D_{1/14}$ from observations at Delta North, and corresponding model results after calibration. Diurnal and semidiurnal amplitudes show a fortnightly periodicity associated with the tropical and synodic spring-neap cycles, i.e. 13.6 and 14.8 days, respectively. Quarter diurnal amplitudes covary with semidiurnal amplitudes, indicating that most of the variation in D_4 is driven by nonlinear interaction of D_2 with itself. Variations in $D_{1/14}$ are the result of frictional forces induced by a combination of D_1, D_2 and river flow (*Godin*, 1999; *Buschman et al.*, 2009).

At Delta North, a good agreement between the model and observations is obtained for the D_1 and D_2 tidal species (Figure 4.8). Amplitudes of $D_{1/14}$ are underestimated, but are not important for the overall dynamics at this location. Amplitudes of D_4 are well represented, although some underestimation can be observed. The latter discrepancy can partly be explained by the idealization of the coastlines and riverbanks, which have a significant control over the nonlinear terms in the equations of motion. At Delta South, the agreement between the model and observations is high both for the main tidal species and for the fortnightly amplitude (Figure 4.9). We expect water levels in Delta South to be better represented than in Delta North, because the bathymetry of the southern distributary system shows deeper channels than in the northern one. Shallower sections are likely to amplify water levels, if the bathymetry or

71
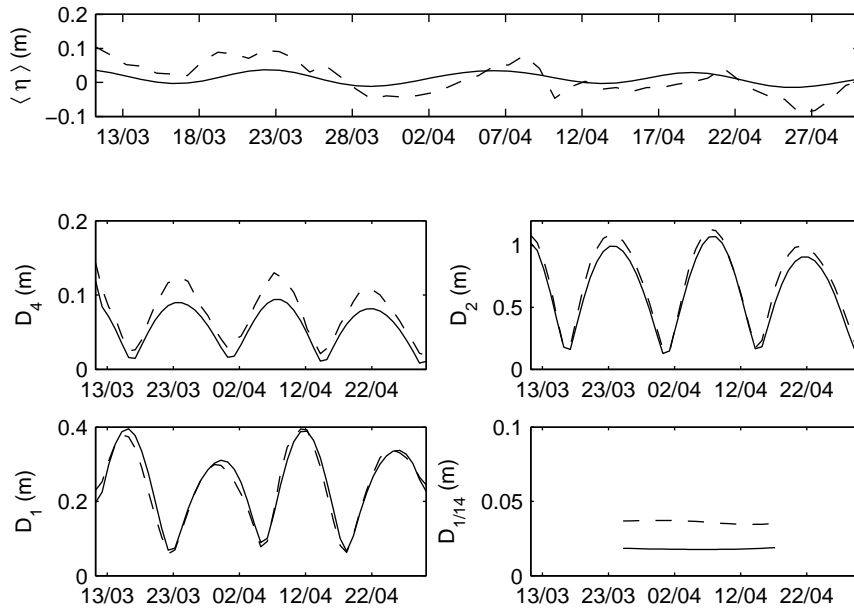
Figure 4.8: Subtidal water level $\langle\eta\rangle$ and water level amplitude obtained from a wavelet decomposition, isolating the three main tidal species (D_1, D_2 and D_4) and the fortnightly amplitude $D_{1/14}$ from observations at the Delta North station (dashed line), and from the corresponding model results (solid line).
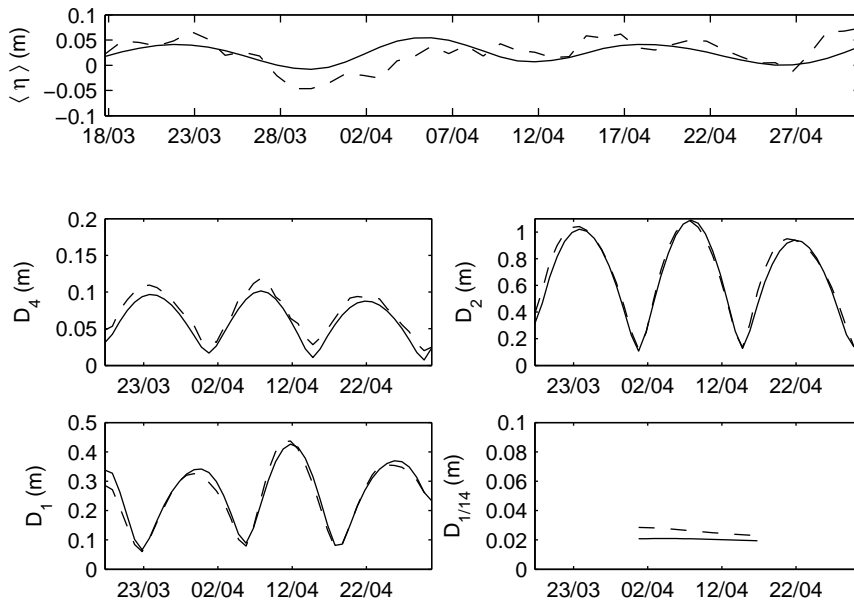
Figure 4.9: Subtidal water level $\langle\eta\rangle$ and water level amplitude obtained from a wavelet decomposition, isolating the three main tidal species (D_1, D_2 and D_4) and the fortnightly amplitude $D_{1/14}$ from observations at the Delta South station (dashed line), and from the corresponding model results (solid line).

the model geometry are inaccurate. Other reasons may be the accuracy of GEBCO database in shallow areas, especially in the vicinity of the outlets.

Figure 4.10 shows the comparison between model and observation at Delta Apex, located approximately 40 km from the outlets. At this location tidal waves have undergone transformations while propagating through the main branches of the delta. Amplitudes of D_1 and D_2 are here slightly underestimated, whereas D_4 is well represented. Amplitudes of $D_{1/14}$ are larger than in coastal locations, increasing upriver to a point where tides are significantly damped by the river discharge (*LeBlond*, 1979; *Godin*, 1999; *Buschman et al.*, 2009). Disagreement of diurnal and semidiurnal species are likely related to the exclusion of tidal channels.

Time-series of mean flow velocity obtained from the downstream H-ADCP discharge station was also subjected to the wavelet analysis previously described. Figure 4.11 compares model and observations at the H-ADCP discharge station. The agreement for the U_1, U_2 and $U_{1/14}$ tidal species is high. The fortnightly amplitudes of flow velocity are significant, exceeding 0.05 m s^{-1}. The model overestimates the quarter-diurnal flow variation, which may be related to spatial variations in bed roughness that were not accounted for.

4.5.2   Validation of Modeled Discharge Division

To validate the numerical model, we compare model results with measured discharges at DA and Bif stations. Figure 4.12 shows the discharges in the northern (left) and southern (right) branches of DA station during neap tide (top) and spring tide (bottom), both for model results and for the observations. The model correctly represents the observed intra-tidal discharge variation in both bifurcations during spring tide and neap tide conditions. During spring tides in the southern branch, model results show a landward flow which is not present in the observations. The difference in tidally averaged discharge between model and observation in the northern branch is negligible, both during spring tide and during neap tide. The model underestimates the subtidal discharge in the southern branch by roughly 500 m^3 s^{-1} (approximately 15%), in both tidal periods considered. Figure 4.13 compares discharge from the model and the observations at Bif station, showing that differences in subtidal discharge are within 10%. Figure 4.14 investigates the variation in discharge division over the downstream branches both at DA and Bif stations. To some extent, the discharge division in the model is too asymmetrical, especially at DA station during spring tide.

We attribute the minor discrepancies between model results and observations to the limited degree in which spatial variations of bed roughness are accounted for. Differences in bed roughness between distributaries may be explained by sediment sorting at the apex (*Frings and Kleinhans*, 2008), which leads to variation in bed material and in the occurrence of bed forms. Other possible causes of discrepancies are the representation of the river banks in the model, which does not capture the geometric complexity of lateral channels, and the limited number of tidal constituents used to force the model.
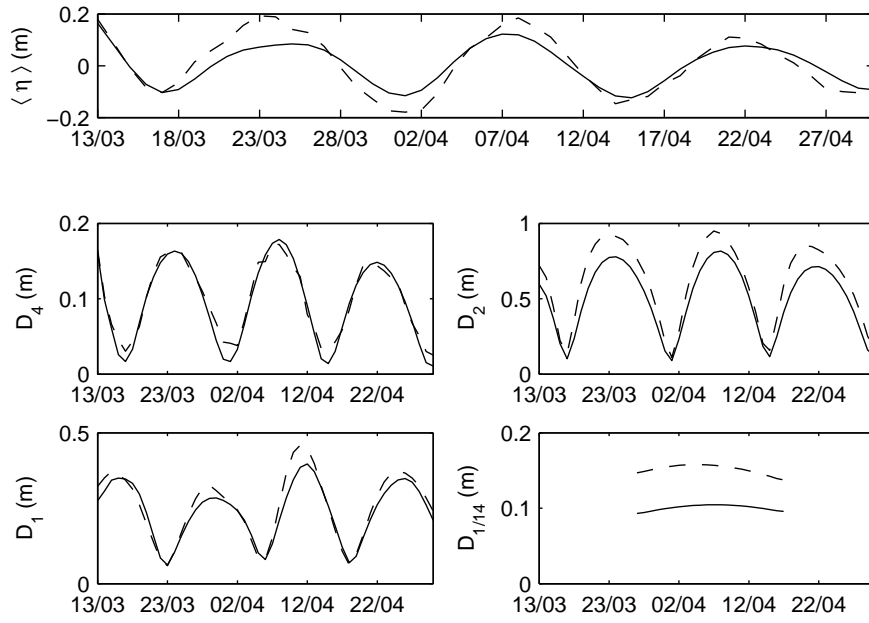
Figure 4.10: Subtidal water level $\langle\eta\rangle$ and water level amplitude obtained from a wavelet decomposition, isolating the three main tidal species (D_1, D_2 and D_4) and the fortnightly amplitude $D_{1/14}$ from observations at the Delta Apex station (dashed line), and from the corresponding model results (solid line).
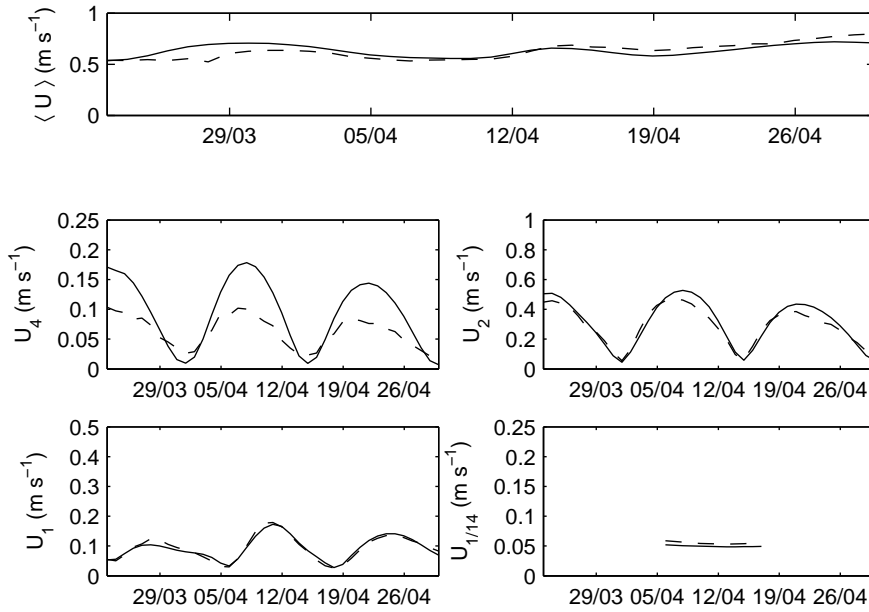
Figure 4.11: Subtidal flow velocity $\langle U\rangle$ and velocity amplitude obtained from a wavelet decomposition, isolating the three main tidal species (U_1, U_2 and U_4) and the fortnightly amplitude $U_{1/14}$ from observations at the H-ADCP discharge station (dashed line), and from the corresponding model results (solid line).
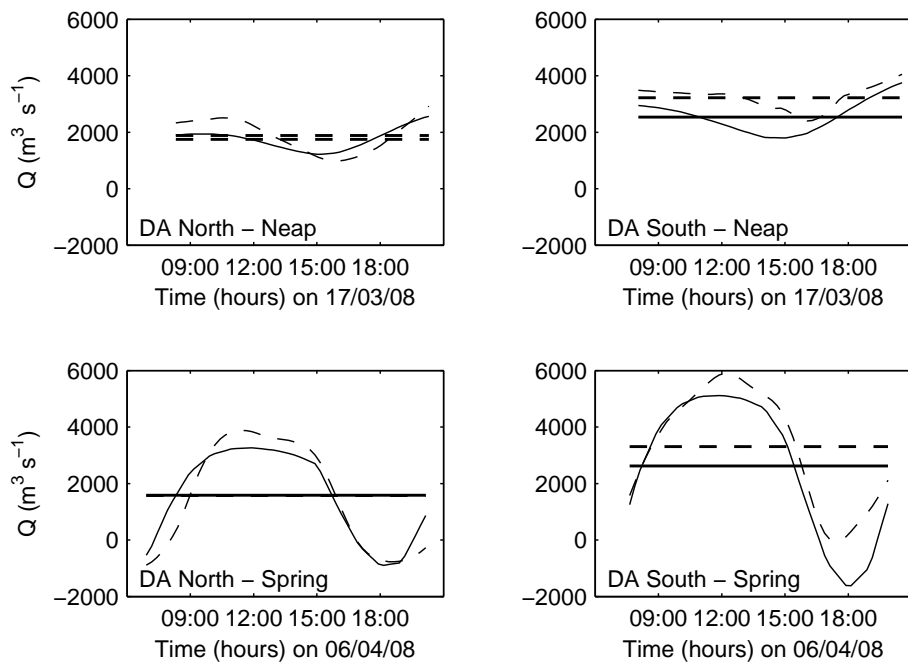
Figure 4.12: Time-series of water discharge from model results (solid line) and observations (dashed line) at the northern (left) and southern (right) branches during neap tide (top) and spring tide (bottom) at DA station. Positive discharge coincides with seaward flow.
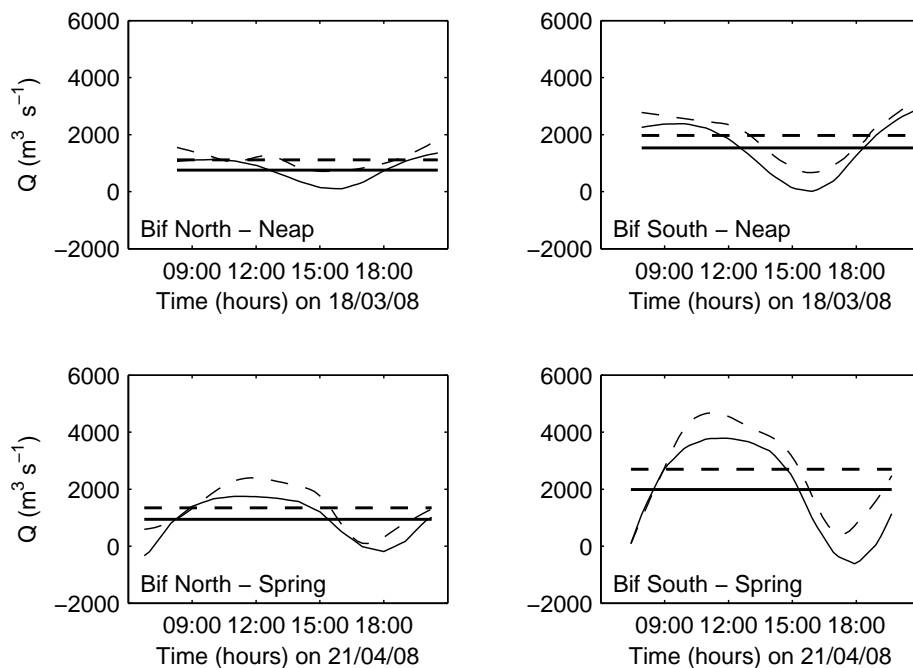
Figure 4.13: Time-series of water discharge from model results (solid line) and observations (dashed line) at the northern (left) and southern (right) branches during neap tide (top) and spring tide (bottom) at Bif station. Positive discharge coincides with seaward flow.
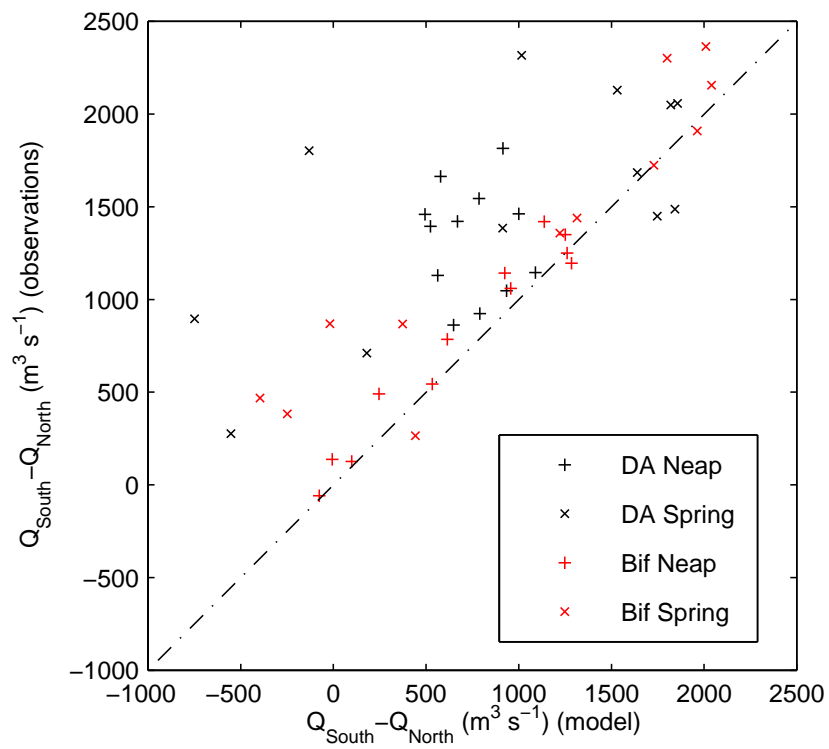
Figure 4.14: Discharge difference between branches obtained with the model and with observations.

4.6   Subtidal Discharge Division

The subtidal discharge division at a bifurcation is here quantified as (*Buschman et al.*, 2010)

$$\Psi = \frac{\langle Q_1 \rangle - \langle Q_2 \rangle}{\langle Q_1 \rangle + \langle Q_2 \rangle}, \tag{4.3}$$

where brackets indicate tidal average, and suffixes 1 and 2 stand for the southern and northern branches, respectively. The discharge asymmetry index (Ψ) is zero for an equal discharge division; it is positive when subtidal discharge in the southern channel is larger, attaining a value of one when all subtidal discharge is carried by the southern channel, and minus one for the reverse case. Figure 4.15 shows Ψ and subtidal water level $\langle \eta \rangle$ for DA and Bif stations, obtained from the model. The subtidal water level variation features a spring-neap oscillation directly in response to the strength of the forcing. The subtidal discharge division covaries with subtidal water level, although it lags behind the spring-neap cycle, and peaks at the transition between neap tide and spring tide. The discharge division at both bifurcations is particularly asymmetrical at the onset of spring tide, tending to be more equally distributed at the peak of spring tides.

To distinguish between effects of tides, river discharge and river-tide interactions on subtidal discharge division, subtidal discharges were decomposed using the method of factor separation (*Stein and Alpert*, 1993). The model was run for three forcing conditions:

- Tides only: the model is forced with tides at the downstream boundary, whereas a radiative boundary condition is imposed at a suitable upstream location.

- River discharge only: the model is forced with river discharge at the upstream boundary and set to equilibrium water level at the marine boundary.

- Tides and river discharge: the model is configured as described in Section 4.4.

Noting that neither for tidal nor river discharge forcing $\langle Q_1 \rangle + \langle Q_2 \rangle$ is zero (*Buschman et al.*, 2010), the subtidal discharge forced by both river flow and tides ($\langle Q \rangle$) can be decomposed as

$$\langle Q \rangle = Q_r + \langle Q_t \rangle + \langle Q_{rt} \rangle, \tag{4.4}$$

where Q_r denotes the contribution solely due to river flow, Q_t is the contribution due to tides alone and Q_{rt} is the contribution due to river-tide interaction.

4.6.1   Response to Tidal Forcing Only

To understand the effect of tides on subtidal discharge division, the contribution from simulations forced with tides only (Q_t) is split in three components. To do so, the cross-section averaged flow velocity is decomposed according to $U = \langle U \rangle + U'$, where the prime denotes the variation during a diurnal tidal cycle. Depth can be written as $d = h + \eta$. Assuming a time-invariant channel width (W), subtidal discharge can be rewritten as

$$\langle Q_t \rangle = W \langle U' \eta \rangle + W h \langle U \rangle + W \langle U \rangle \langle \eta \rangle, \tag{4.5}$$

77

where the first term denotes the Stokes transport Q_S, the second term is the return discharge Q_R and the third term is a residual term that is small as $\langle \eta \rangle$ is near-zero. In general, Q_S is directed landward, generating a water level gradient that forces a net compensating return discharge seaward. The magnitudes of Q_R and Q_S can be highly nonuniform in convergent channels, being largest close to the sea and decreasing landward. In single channels, having constant width or being convergent, the water storage is limited and Q_S and Q_R balance. Therefore, $\langle Q_t \rangle$ is small or zero. In a network channel, Q_S and Q_R do not necessarily balance, implying that $\langle Q_t \rangle$ in the bifurcating channels may have nonzero values (*Buschman et al.*, 2010).

Figure 4.16 shows the decomposition of $\langle Q_t \rangle$ into contributions of the Stokes transport Q_S, return discharge Q_R and the residual term at bifurcating branches in DA station. Q_S is landward and increases during spring tides. The component due to the residual term is negligible. Values of Q_S in the southern branch are about 1.5 times larger than in the northern branch. In the northern branch, the net transport ($\langle Q_t \rangle$) increases toward neap tides. In the southern branch, Q_S and Q_R balance during spring tide, whereas during neap tide a transfer from the southern branch to the northern branch and back to the southern branch is observed. Then, the transfer from the northern to the southern branch takes place. When averaged over several spring-neap cycles, the net transport is nearly zero. The behavior at Bif station is similar (not shown).

The limited impact of the tides on the discharge division at DA and Bif stations relates to the large distance to the coast, which is about 40 km from the delta apex. The interplay between Q_S and Q_R at bifurcating branches explains the spring-neap variability in the discharge asymmetry ratio Ψ. During spring tides, Q_S and Q_R balance at each bifurcating branch, leading to an equal discharge division. During neap tides, the transfer from the southern to the northern branches driven by the Stokes flux leads to a more unequal discharge distribution, temporarily favoring the southern branch.

4.6.2   Tidal Impact on Discharge Division

To carry out a systematic analysis of the causes of asymmetry in the subtidal discharge division at each of the bifurcation in the Mahakam Delta, the discharge asymmetry index Ψ (eq. 4.3) was split up in three components

$$\Psi = \Psi_r + \Psi_t + \Psi_{rt}, \tag{4.6}$$

where Ψ_r denotes the asymmetry in the discharge division from simulations with river flow, Ψ_t is obtained from the tides only simulations and Ψ_{rt} can be obtained by subtracting Ψ_r and Ψ_t from Ψ. By convention (see eq. 4.3), 1 and 2 denote herein further the right and left bifurcating channel when approaching the bifurcation while moving upstream, respectively. The result of this convention is that except for the southernmost bifurcation, southerly channels have the subscript 1 and the northerly channels subscript 2.

Figure 4.17 shows Ψ, Ψ_r and the relative difference $(\Psi - \Psi_r)/\Psi_r$ expressed as a percentage (0-100) for each bifurcation in the Mahakam delta, computed by averaging the subtidal discharge over several spring-neap cycles. Values of Ψ range from -0.4 to 0.6, which reflects the large variation of flow dynamics at bifurcations of the channel network. The relative difference
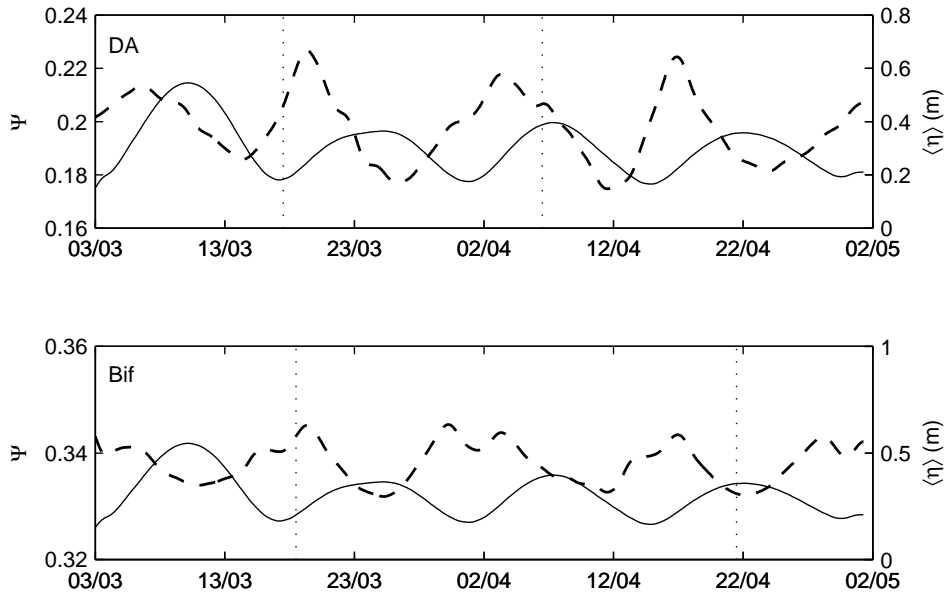
Figure 4.15: Discharge asymmetry index Ψ (dashed line) and subtidal water level $\langle\eta\rangle$ (solid line) as a function of time at Delta Apex (top) and First Bifurcation (bottom). Dotted lines denote the date of discharge measurements at the bifurcations.
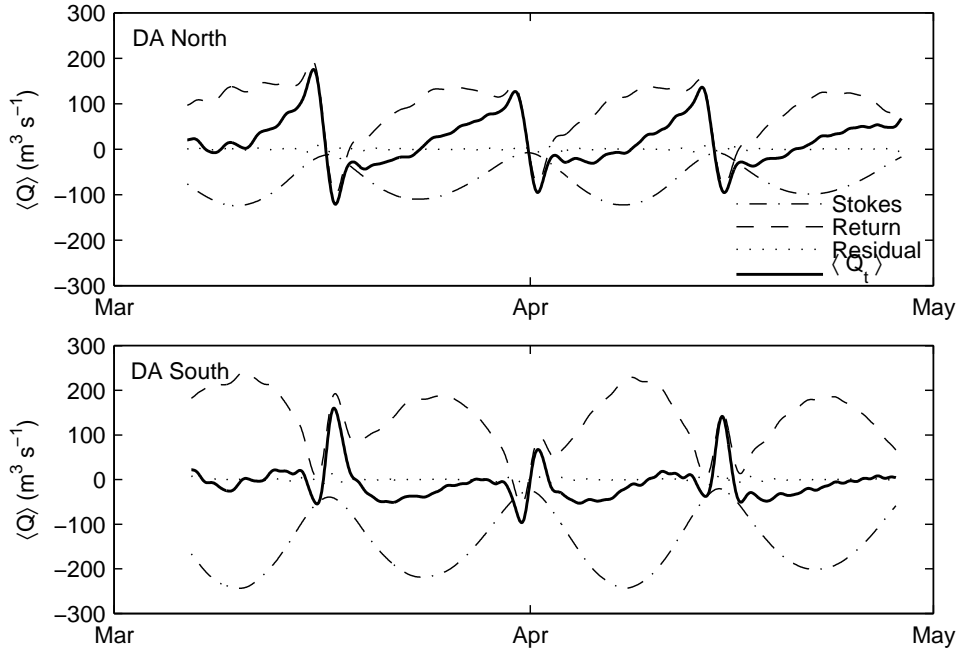
Figure 4.16: Decomposition of subtidal discharge induced by tidal motion only $\langle Q_t \rangle$ into contributions of the Stokes transport Q_S, return discharge Q_R and the residual term in Eq. 5, at bifurcating branches in DA station. The Stokes transport is landward whereas the return discharge is seaward.

79
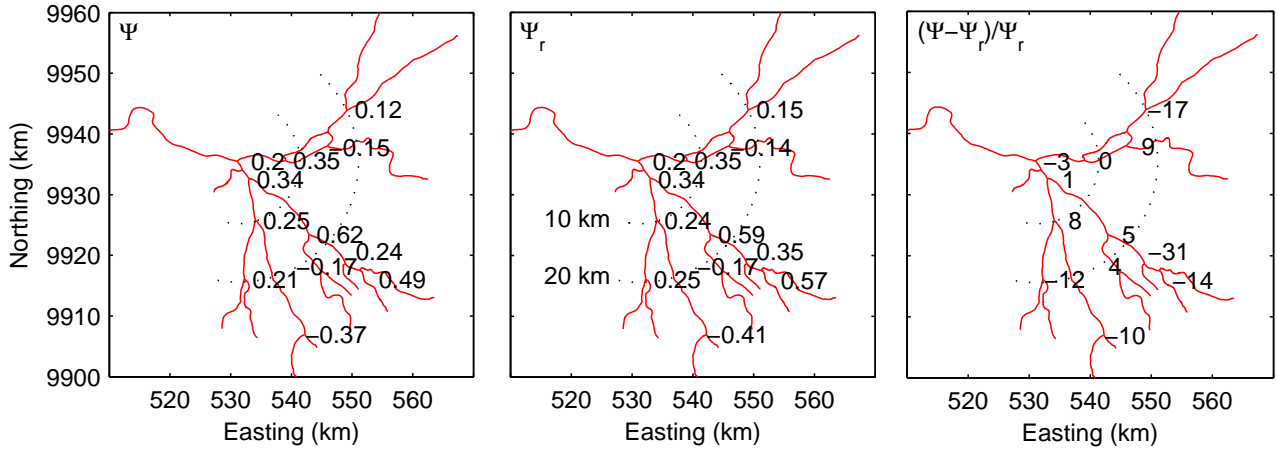
Figure 4.17: Centerlines of the channels in the Mahakam delta showing the bifurcations. Black dotted lines indicate radial distance in km from the delta apex. Numbers indicate Ψ values at each of the bifurcations analysed. r stands for simulations forced with river flow. The relative difference is expressed as a percentage.

indicates the tidal impact on subtidal discharge distribution, as it increases with the contributions from tides and river-tide interaction. Within 10 to 15 km from DA station, the tidal impact on river discharge division is within 10% in all bifurcations. Tidal impact increases seaward with a maximum value of the order of 30%. It is interesting to note that in general, the effect of tides is to hamper the discharge division that would occur in the case without tides.

Buschman et al. (2010) found that the tidal motion favors the allocation of river discharge to shorter and deeper channels, enhancing the inequality in the discharge division over two downstream channels connected to the sea. In many instances, the results presented herein do not confirm these findings, which suggests that simplifying the geomorphological complexity as performed by *Buschman et al.* (2010) may change the subtle processes governing the tidal-averaged distribution of discharge over distributaries. In the Mahakam Delta, the channels feature a very distinct bed morphology and the junction angles of the bifurcations show a large variability. In the study by *Buschman et al.* (2010), both downstream channels diverged with the same angle from the upstream channel. Besides the issue of geomorphological complexity, processes occurring at a single nodal point cannot be readily translated to a network in which nodes and branches interact, which may result in chaotic behavior.

At the bifurcation that is most markedly in contrast with the results by *Buschman et al.* (2010), tides modify the discharge distribution by 31% (see Figure 4.17). That junction connects a very deep and short sea-connected southern branch to a much smaller northern branch, which bifurcates once more in two equally long branches. The large tidal impact observed may relate to water level setup caused by river-tide interaction in the channels (*Godin and Martinez*, 1994; *Buschman et al.*, 2009). The southern channel conveys a larger share of the river discharge, resulting in a tendency to generate a subtidal water level setup, as shown in Figure 4.18. At the junction, the subtidal water level is constrained by the subtidal water level in the northern
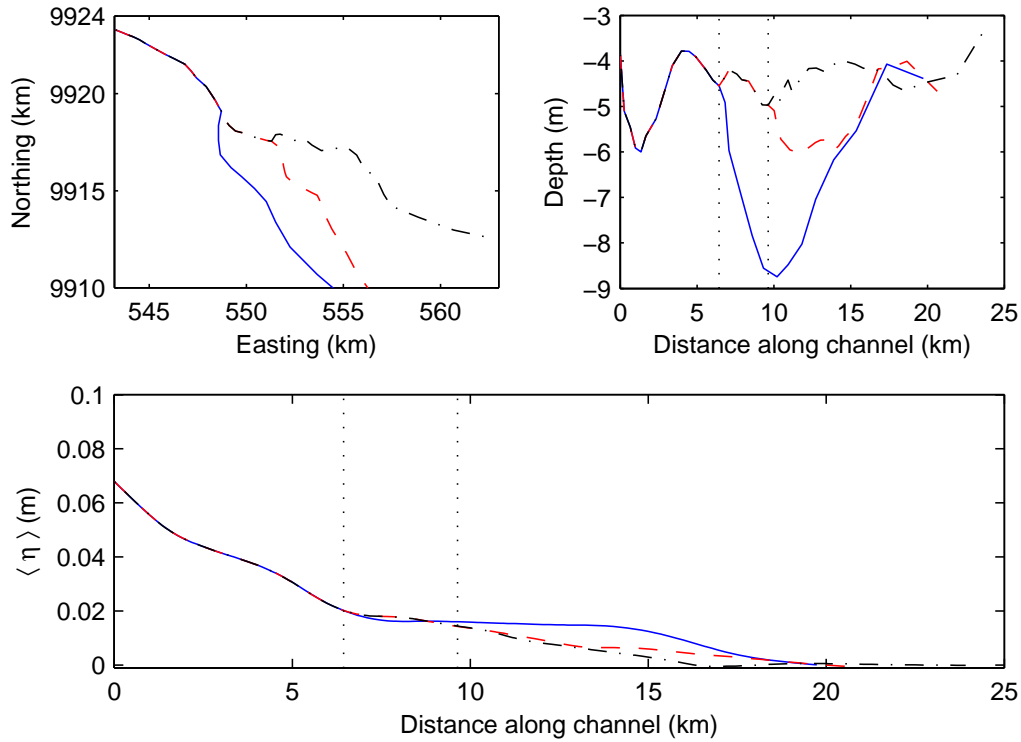
Figure 4.18: Subtidal water level profiles in the part of the Mahakam delta where the tidal impact on river discharge division is largest (bottom). The top left panel shows the geographical location and the top right panel the depth profiles along the channels.

channel, which is elevated by the river-tide interaction in the southern channel. The subtidal water level setup in the southern channel thus increases the subtidal water level gradient at the junction towards the northern channel, reducing the allocation of river discharge to the southern channel. We propose the term *differential water level setup* to describe this phenomenon, which is dominant in the seaward part of the Mahakam channel network. Differential water level setup may occur in many other channel networks in the world, where junctions connect large branches conveying both river and tidal discharges, to smaller branches where the tidal motion is dominant.

4.7   Summary and Conclusion

A depth-averaged version of the unstructured mesh, finite-element model SLIM (Second-generation Louvain-la-Neuve Ice-ocean Model) has been used to simulate the hydrodynamics driven by river discharge and tides in the Mahakam delta channel network, East Kalimantan, Indonesia. The aim of the chapter was to establish and understand the tidal impact on river discharge division at the bifurcations in the delta. Two 2D computational domains were defined to cover the Mahakam delta and the lakes region, which were interconnected by a 1D computational domain representing the river and several tributaries. Measured bathymetry was used in all

domains except for the continental shelf and Makassar Strait, where GEBCO database information was used. The model was forced with tides from the global ocean tidal model TPXO7.1 at open boundaries, located far away from the delta, stretching across the entire Makassar Strait. At the upstream boundary, the model was forced with measured discharge series. At the tributaries, discharge series were obtained from a rainfall-runoff model from the main subcatchment, calibrated with the measured discharge series. The slope of the river was estimated from an analysis of the subtidal momentum balance inferred from data. Bottom friction was obtained from model calibration, decomposing the model domain in three regions. Model runs spanned from March to April 2008. Calibration was performed with water level time-series, measured at three locations in the delta, and flow measurements at a discharge station located near the river mouth, both spanning the simulation period. Validation was performed by comparing model results with discharge distribution measurements at the two principal bifurcations in the delta.

To distinguish between effects of tides, river discharge and their interaction, subtidal discharge was decomposed using a method of factor separation. Apart from the calibration and validation simulations, the model was run in two more configurations: imposing tides only and imposing river flow. The discharge asymmetry index Ψ, computed as the ratio between the difference in discharge between two branches to their sum, was computed for each case. Results from the simulations forced with tides only indicate that at the delta apex Ψ features a fortnightly oscillation, which is driven by the imbalance in the return discharges induced by the Stokes fluxes. When averaged over several spring-neap cycles, the net transport is nearly zero, revealing that in absence of a river discharge no residual circulation occurs. The discharge asymmetry index for simulations forced with river discharge and tides was then split up in three components ($\Psi = \Psi_r + \Psi_t + \Psi_{rt}$, where Ψ_r denotes the contribution solely due to river flow, Ψ_t the contribution due to tides alone and Ψ_{rt} the contribution due to river-tide interaction). Values of Ψ ranged from -0.4 to 0.6, reflecting the geomorphological complexity of the Mahakam Delta. Maps of the relative difference $(\Psi - \Psi_r)/\Psi_r$, expressed as a percentage, showed that within 10-15 km from the delta apex, tides were found to alter the relative difference $(\Psi - \Psi_r)/\Psi_r$ by less than 10% at all bifurcations. Tidal impact increases seaward with a maximum value of the order of 30%. In general, the effect of tides is to hamper the discharge division that would occur in the case without tides. At the bifurcation where the tidal impact was largest, steepening of the tidal-averaged water level profile in the deepest and shortest channel by river-tide interaction enhanced the gradient in the longer and shallower channel. The enhanced subtidal water level gradient favored the allocation of river discharge to the longer and shallower channel.

Chapter 5

Suspended Sediment Retrieval

Abstract: Although designed for velocity measurements, acoustic Doppler current profilers (ADCPs) are widely being used to monitor suspended particulate matter in rivers and in marine environments. To quantify mass concentrations of suspended matter, ADCP backscatter is generally calibrated with in situ measurements. ADCP backscatter calibrations are often highly site-specific and season-dependent, which is typically attributed to the sensitivity of the acoustic response to the number of scatterers and their size. Besides being a joint function of the concentration and the size of the scatterers, the acoustic backscatter can be heavily affected by the attenuation due to suspended matter along the two-way path to the target volume. We aim to show that accounting for sound attenuation in ADCP backscatter calibrations may broaden the range of application of ADCPs in natural environments. The trade-off between the applicability and the accuracy of a certain calibration depends on the variation in size distribution and concentration along the sound path. We propose a simple approach to derive the attenuation constant per unit concentration or specific attenuation, based on two water samples collected along the sound path of the ADCP. A single calibration was successfully applied at five locations along the River Mahakam, located up to 200 km apart. ADCP-derived estimates of suspended mass concentration were shown to be unbiased, even far away from the transducer.

5.1   Introduction

Quantifying mass concentration of suspended particulates in natural environments is typically accomplished using surrogate measurements, since direct analysis of samples is too labor intensive to capture large-scale dynamics in time and in space (*Wren et al.*, 2000; *Gray and Gartner*, 2009). Acoustic profilers can yield non-intrusive, collocated, and simultaneous measurements of mass concentration of suspended particulate matter (*Young et al.*, 1982; *Thorne and Hanes*, 2002). Acoustic Doppler current profilers (ADCPs) were originally designed for flow measurement. While manufacturers store ADCP backscatter for quality checking of the velocity measurements, many researchers have adopted the ADCP backscatter as a surrogate measure of suspended mass concentration (e.g. *Dinehart and Burau*, 2005b,a). Over the past decade, a variety of studies on geophysical surface flows have relied on the use of ADCPs to quantify variation of mass concentration of suspended matter, in the context of sediment transport research (e.g. *Souza et al.*, 2004; *Kostaschuk et al.*, 2005; *Wargo and Styles*, 2007; *Wall et al.*, 2008; *Bartholoma et al.*, 2009; *Defendi et al.*, 2010) and environmental monitoring (e.g. *Hoitink*, 2004).

ADCP backscatter calibrations have been found to be highly site-specific and season dependent (e.g. *Gartner*, 2004; *Hoitink and Hoekstra*, 2005), which can be attributed to the sensitivity of the acoustic response to particle size, density, shape and composition of scatterers in the target volume. *Reichel and Nachtnebel* (1994) were among the first to investigate the relation between ADCP backscatter and suspended sediment concentration in a fluvial environment; they concluded that a mono-frequency instrument such as the ADCP cannot separate effects due to particle concentration from those due to size distribution. In effect, when density, shape and composition of the suspended particles can be assumed constant, the acoustic backscatter mainly depends on the number of scatterers and their size (e.g. *Medwin and Clay*, 1998; *Vincent*, 2007; *Marttila et al.*, 2010).

The acoustic backscatter measured by the ADCP transducer, however, can be strongly influenced by the attenuation caused by suspended matter along the sound path (e.g. *Thorne et al.*, 1993; *Lee and Hanes*, 1995). Sound attenuation by suspended matter depends on the mass concentration of the suspension and comprises contributions due to scattering and due to viscous absorption (*Urick*, 1948). For the working frequencies of commonly used ADCPs, viscous absorption is typically greater when the mud fraction dominates, whereas with sandy material both viscous absorption and scattering may contribute to sound attenuation. *Gartner* (2004) accounted for sound attenuation due to scattering and viscous absorption when inverting acoustic backscatter profiles measured with a downward-looking ADCP, deployed at about two meters from the bed. Using as reference concentration the calibrated signal of an Optical Backscatter Sensor (OBS), which was deployed at about one meter from the bed, the approach provides a single value of attenuation for the profile. That approach can be justified only over a short profiling range where variations in mass concentration with depth can be neglected. For longer profiling ranges and when a systematic gradient in concentration exists, the approach will result in a bias in the estimates of mass concentration, which may increase with distance from the position where the reference concentration is obtained to correct for attenuation. *Holdaway et al.* (1999) and *Hoitink and Hoekstra* (2005) considered sound attenuation due to viscous absorption in the inversion of ADCP backscatter profiles. While *Hoitink and Hoekstra* (2005)

found negligible attenuation, mainly due to low concentrations, *Holdaway et al.* (1999) found a 26% increase in the estimate of concentration when accounting for sediment attenuation. The studies mentioned above have considered only rigid deployments, where water samples are typically collocated with the ADCP target volume. In this chapter we extend the applicability to moving-boat deployments.

The determination of sound attenuation due to suspended sediments is complicated by gradients in the concentration profile and variations in the size distribution of the suspended particles. *Moore et al.* (2011) accounted for acoustic attenuation in their approach to obtain suspended mass concentration of fine material using Horizontal ADCPs. Their determination of sound attenuation, however, assumes the concentration field along the sound path to be constant. *Hurther et al.* (2011) proposed a novel dual-frequency inversion method to account for sound attenuation of acoustic backscatter profiles measured in the bottom boundary layer, where the high concentrations contribute significantly to errors in the inversion of acoustic profiles using the standard inversion methods (*Thorne et al.*, 2011). The method is however limited to the near-bed flow region where no sediment sorting occurs along the acoustic path.

Variations in the size distribution of suspended particles along the sound path produce opposing effects on the resulting backscatter. For instance, the upward fining of suspended sediment causes the acoustic backscatter obtained with boat-mounted ADCPs to increase with range from the transducer, whereas the attenuation due to scattering reduces the observed backscatter. *Topping et al.* (2007) exploited the sensitivity to these two mechanisms. They used ADCPs working at different frequencies to discriminate between variations in suspended sediment concentration from variations in sediment size. Later, *Wright et al.* (2010) applied a similar approach to discriminate the mass concentrations due to silt and clay and those due to sand only. If size distribution does not change along the sound path and sound attenuation is negligible, backscatter profiles may reflect the sediment concentration profile. When attenuation is not negligible but still the size distribution is constant along the sound path, backscatter profiles can show significant departures from sediment concentration profiles. The degree of departure makes it necessary to apply a positive correction in the measured backscatter which increases with range from the transducer.

The effect the size distribution has on the backscatter and attenuation functions, given an instrument's working frequency, is complex. *Thorne and Meral* (2008) showed that for a normal distribution of a moderately sorted sediment suspension, the width of the size distribution may enhance the scattering part of the attenuation by a factor three, compared to the value which is obtained by using the mean particle size only. The potential impact of the sediment size distribution on the backscatter function increases with the width of the distribution. *Moate and Thorne* (2009) showed that the distribution type also affects the attenuation, because the details of the form function may enhance or weaken the backscatter strength up to one order of magnitude. In the Rayleigh regime, for the same mean particle size and sorting, a log-normal distribution yields larger estimates of the acoustical parameters than a normal or a bi-modal distribution. We are not aware of similar studies done on the viscous absorption part of the attenuation. In field conditions, size distributions are often noisy and open-ended, that is, the sampled size range cannot cover the entire distribution of suspended particles sizes. This easily introduces errors and motivates the use of an empirical approach to determine the effect of attenuation in ADCP backscatter calibrations. Here we introduce a simple approach

that relies on at least two water samples along the sound path of the ADCP to obtain an empirically derived attenuation constant per unit concentration. This is particularly needed when backscatter profiles progressively diverge from mass concentration profiles with distance from the transducers.

This chapter is structured as follows. Section 5.2 describes the theoretical background of the acoustic backscatter problem. Section 5.3 introduces the calibration strategy along with an empirical method to derive attenuation. In Section 5.4, the data collection methods and deployment locations are presented. Section 5.5 presents the results of the measurements with the optical instruments. The conversion to mass concentration of suspended sediments using the ADCP backscatter is presented in Section 5.6. Section 5.7 finalizes this chapter with the conclusions.

5.2 Acoustic Formulation

Volume backscatter strength S_v is related to the number of scatterers per unit volume n_b and the mean backscattering cross-section $\langle \sigma_{bs} \rangle$ as

$$S_v = 10 \log_{10} \left(n_b \langle \sigma_{bs} \rangle \right), \tag{5.1}$$

where a reference of 1 m^{-2} is used in the expression between brackets. For spherical scatterers, n_b relates to the mass concentration of suspended particles M_s as

$$M_s = \frac{4}{3} \pi \rho_s n_b \langle a_s^3 \rangle, \tag{5.2}$$

where a_s and ρ_s are the radius and density of the particles, respectively, and the angular brackets denote the operation

$$\langle g \rangle = \int_0^\infty g\left(a_s\right) n\left(a_s\right) \, \mathrm{d}a_s, \tag{5.3}$$

where $n(a_s)$ represents the size distribution of particles in suspension and $g\left(a_s\right)$ any function of the particle size. Hence, knowledge of $n(a_s)$ allows the estimation of the mean particle size $\langle a_s \rangle$, the standard deviation and higher order moments of the distribution. The mean backscattering cross-section can be written as (*Medwin and Clay*, 1998)

$$\langle \sigma_{bs} \rangle = \frac{1}{4} \langle a_s^2 f^2 \rangle, \tag{5.4}$$

where f denotes a backscatter form function which describes the backscatter intensity of the particles in suspension (see *Thorne and Meral*, 2008). Combining equations (5.1)-(5.4), the volume backscatter strength becomes

$$S_v = 10 \log_{10} \left(k_s^2 M_s \right), \tag{5.5}$$

where

$$k_s^2 = \frac{3}{16\pi\rho_s} \frac{\langle a_s^2 f^2 \rangle}{\langle a_s^3 \rangle}. \tag{5.6}$$

Echo intensity profiles recorded by an ADCP transducer can be transformed into volume backscattering strength S$_v$ (*Deines*, 1999). Recently, *Gostiaux and van Haren* (2010) introduced a correction to the equation proposed by *Deines* (1999) for echo intensity approaching the noise level. Accordingly, volume backscattering strength is written as

$$S_v = K_c E + 2 \left(\alpha_w + \alpha_s \right) R + 10 \log_{10} \left(\frac{T_T R^2 \psi^2}{L P_T} \right) + C, \qquad (5.7)$$

where S$_v$ is in dB. α_w represents sound attenuation due to the absorption by water and α_s is attenuation due to the absorption and scattering by particles (both in dB m^{-1}), R is the range along the central axis of the beam (m), ψ is a function that accounts for the departure from spherical spreading within the near-field of the transducer (*Downing et al.*, 1995), E echo intensity (counts), T_T is the transducer temperature (°C), L is the transmit pulse length (m), P_T is the transmit power (W), and K_c (dB count^{-1}) and C (dB) are instrument dependent constants. The ADCP records T_T, P_T, and E, and computes R from the time span between emission and reception of the acoustic pings and the speed of sound. For our ADCP configuration $L =$ 0.5 m. K_c is beam-specific and can be determined from a calibration with special acoustic instrumentation. Typical values of K_c and C for our 1200 kHz broadband ADCP are 0.45 dB count^{-1} and -129.1 dB, respectively, (*Deines*, 1999). The first term in equation (5.7) represents the backscatter signal and the ambient noise received by the transducer. Several factors are conveniently grouped in the third term, including thermal noise and spherical spreading in the far- and the near-field of the transducer.

Values of α_w depend primarily on the temperature and salinity of water (0.25-0.29 dB m^{-1} in this study), whereas α_s, the attenuation coefficient due to suspended sediments, having neglected viscous absorption, is given by

$$\alpha_s = \frac{1}{R} \int_0^R \xi_s \left(r \right) M_s \left(r \right) \, \mathrm{d}r, \qquad (5.8)$$

Herein, ξ_s is the attenuation per unit concentration (or specific attenuation) due to scattering (*Urick*, 1948; *Richards et al.*, 1996; *Ha et al.*, 2011)

$$\xi_s = \frac{3}{4 \rho_s} \frac{\langle a_s^2 \chi \rangle}{\langle a_s^3 \rangle}, \qquad (5.9)$$

where χ denotes the normalized total scattering cross section (*Thorne and Meral*, 2008). Although ξ_s and k_s^2 can sometimes be successfully derived from the mean particle size (*Holdaway et al.*, 1999), both parameters are very sensitive to the size distribution function and can be erroneously estimated by an order of magnitude (*Thorne and Meral*, 2008; *Moate and Thorne*, 2009). Eq. (5.8) may also include the attenuation per unit concentration due to viscous absorption ξ_v (*Urick*, 1948; *Richards et al.*, 1996; *Ha et al.*, 2011), which in this study is not considered because $\xi_v << \xi_s$, due to the size of the scatterers in suspension and the frequency of the ADCP. The term $2\alpha_s R$ in Eq. (5.7) is then mainly dependent on the shape of ξ_s and M_s profiles.

The mutual dependency of M_s, S$_v$ and α_s complicates ADCP backscatter calibrations because to estimate M_s, profiles of S$_v$ have to be corrected for sound attenuation, which in turn

depends on M_s (see *Thorne and Hanes*, 2002). To account for sound attenuation due to the sediments in suspension, the acoustic backscatter equation reads

$$S_{v,\alpha_s=0} + 2 \int_0^R \xi_s(r) \, M_s(r) \, \mathrm{dr} = 10 \log_{10}\left(k_s^2 M_s\right), \tag{5.10}$$

where $S_{v,\alpha_s=0}$ denotes S_v computed with equation (5.7) but neglecting attenuation due to the sediments. The solution M_s involves either an implicit approach (*Thorne et al.*, 1993), an explicit approach (*Lee and Hanes*, 1995), or a combination of both approaches (*Thorne and Hanes*, 2002). Here, we employ the explicit approach combined with a calibration strategy and an empirically derived specific attenuation constant.

5.3   Calibration Method

An explicit solution to equation (5.10) is given by (see *Lee and Hanes*, 1995; *Thorne and Hanes*, 2002)

$$M_s(R) = \frac{\beta(R)/k_s^2(R)}{K(R_{ref})/k_s^2(R_{ref}) - \int_{R_{ref}}^R \gamma(r) \frac{\beta(r)}{k_s^2(r)} \, \mathrm{dr}}, \tag{5.11}$$

where

$$\beta = 10^{\frac{S_{v,\alpha_s=0}}{10}}, \quad K(R_{ref}) = \frac{\beta(R_{ref})}{M_{ref}}, \quad \gamma = \frac{\ln(10)}{5}\xi_s. \tag{5.12}$$

Equation (5.11) yields the concentration profile over the entire range R, provided a reference mass concentration M_{ref} is known at a distance R_{ref} from the transducer, and both k_s^2 and γ are available. By applying equation (5.11) in field conditions, uncertainties in the reference concentration, in the specific attenuation ξ_s or in the backscatter function k_s^2, have an impact on the estimated concentration profile. If the particle size distribution does not change significantly over depth, the parameters k_s^2 and ξ_s can be assumed constant over depth, and Eq. (5.11) reduces to (see *Thorne and Hanes*, 2002)

$$M_s(R) = \frac{\beta(R)}{K(R_{ref}) - \gamma \int_{R_{ref}}^R \beta(r) \, \mathrm{dr}}. \tag{5.13}$$

A calibration procedure is needed to translate ADCP backscatter to concentration profiles without a reference concentration. By collecting water samples at a single range R_{ref}, *Holdaway et al.* (1999) developed a calibration in which $K(R_{ref})$ was obtained as the average over all measurements corresponding to the times when bottle samples were collected. This approach is well-suited for rigid deployments where the ADCP is fixed at a known distance above the bottom. Although R_{ref} can be chosen close to the ADCP transducers, the calibration also reflects the attenuation of the acoustic signal due to sediments along the range up to R_{ref}. Since suspended mass concentrations near the bed are relatively high, this cause of attenuation may be substantial. In moving boat deployments, water samples are never exactly collocated

to ADCP target volume, so R_{ref} is not constant. However, reference concentrations near the surface will show relatively little spatial-temporal variation and are typically low, reducing significantly the attenuation effects. Close to the ADCP transducer, we assume

$$K\left(R_{ref}\right) = a\beta(\tilde{R}_{ref})^b, \tag{5.14}$$

where a is equal to unity, with units corresponding to the inverse of mass concentration, b is a calibration coefficient and the range $\tilde{R}_{ref}$ is chosen to coincide with the mean range where near-surface water samples are taken. Ignoring slight differences between $\tilde{R}_{ref}$ and the exact range R_{ref} where the water samples and the ADCP measurements are taken, the samples provide pairs of M_{ref} and $\beta(R_{ref})$ for which $K(R_{ref})$ is computed. The coefficient b can then be obtained from a linear regression forced through the origin between $10\log_{10}(K(R_{ref}))$ and $\mathrm{S}_{v,\alpha_s=0}(\tilde{R}_{ref})$. This approach was inspired by methods of rainfall retrieval from radar described in *Berne and Uijlenhoet* (2007) and *Uijlenhoet and Berne* (2008).

Theoretically, ξ_s can be estimated based on field estimates of particle size distribution functions. Such estimates, however, may be highly uncertain in field conditions. For instance, overestimating ξ_s may lead to values of the denominator in Eq. (5.13) very close to zero, compromising concentration estimates. The specific attenuation can be estimated by collecting another water sample at a known distance from the ADCP transducer. Evaluating Eq. (5.13) at R_2, the range to the second water sample, the empirically derived, depth-averaged attenuation γ_e reads

$$\gamma_e = \frac{\ln(10)}{5}\xi_{s,e} = \frac{K(R_1) - \frac{\beta(R_2)}{M_s(R_2)}}{\int_{R_1}^{R_2}\beta\left(r\right)\,\mathrm{d}r}, \tag{5.15}$$

where R_1 and R_2 are the ranges to the two water samples, which are to be chosen far apart. The reference range close to the surface R_{ref} may coincide with R_1, and R_2 is chosen close to the bed. If additional samples are taken at mid-depth, these can be used to further refine the estimate of $\xi_{s,e}$ in the form of a profile. Here, additional samples taken at mid-depth are used for validation of the proposed approach.

5.4   Data Collection

ADCP measurements and collocated water samples were taken at several locations along the River Mahakam, Indonesia (Figure 5.1), during two months when river discharge was high (*Sassi et al.*, 2011a). All locations were subject to freshwater conditions during data collection. At the sites SMD and MLK, we chose an anchor location at about 50 m from the riverbank. At SMD, measurements were carried out during spring tides (SMDSp), and during neap tides (SMDNp). At DA and FB we performed the measurements by navigating between anchored stations representative of each bifurcating branch. We have indicated with the letter N, C or S, the station's name corresponding to northern, central and southern channels, respectively. At the southern branch at site FB, and in MK, measurements were carried out at two locations close to the riverbanks. These two locations were further denoted with numbers 1 and 2 in the corresponding names. At MK, we chose two more stations close to the riverbank, one station
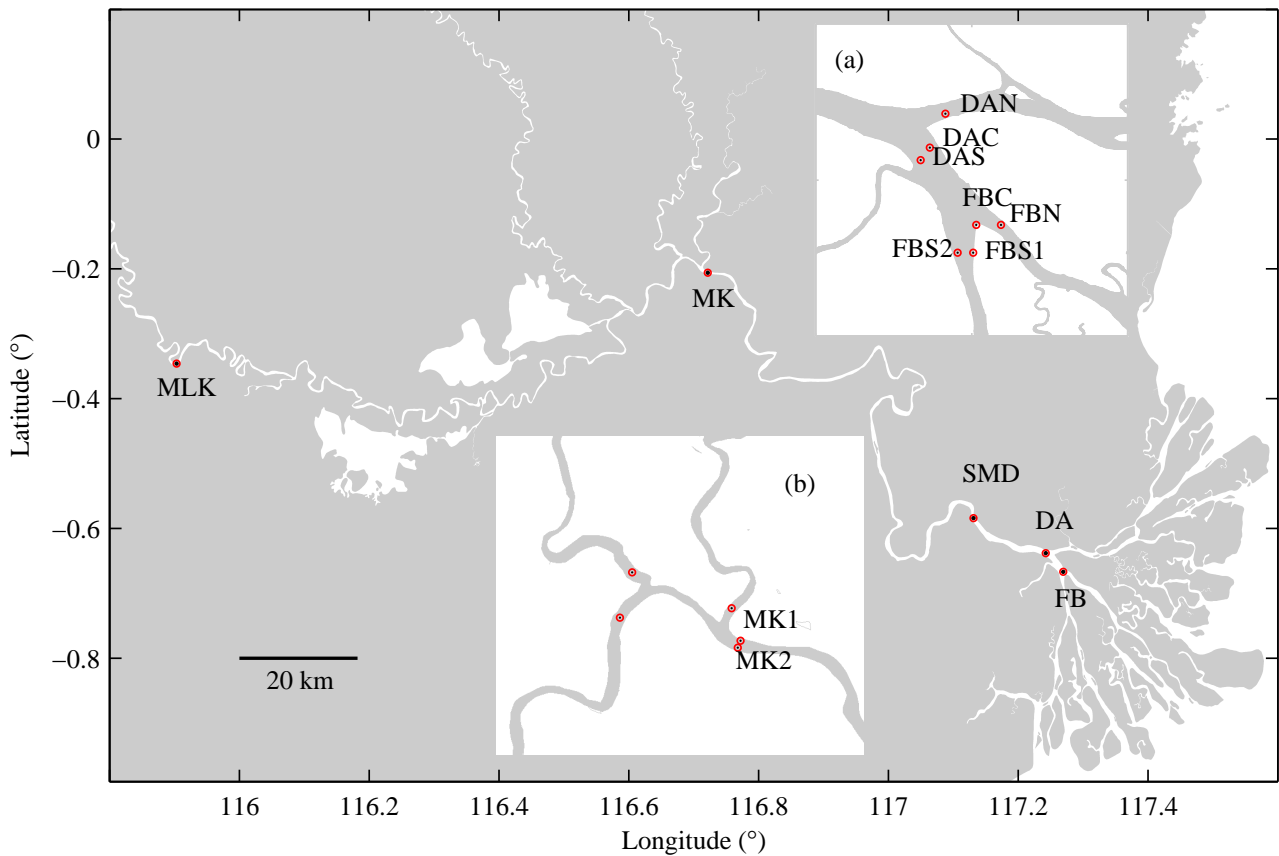
Figure 5.1: Map of the River Mahakam in Indonesia indicating the locations of the deployments (modified after *Sassi et al.* (2011b)). Inset (a) depicts the locations corresponding to DA and FB; inset (b) depicts the locations corresponding to MK. SMD and MLK correspond to single locations. See Table 5.1 for details.
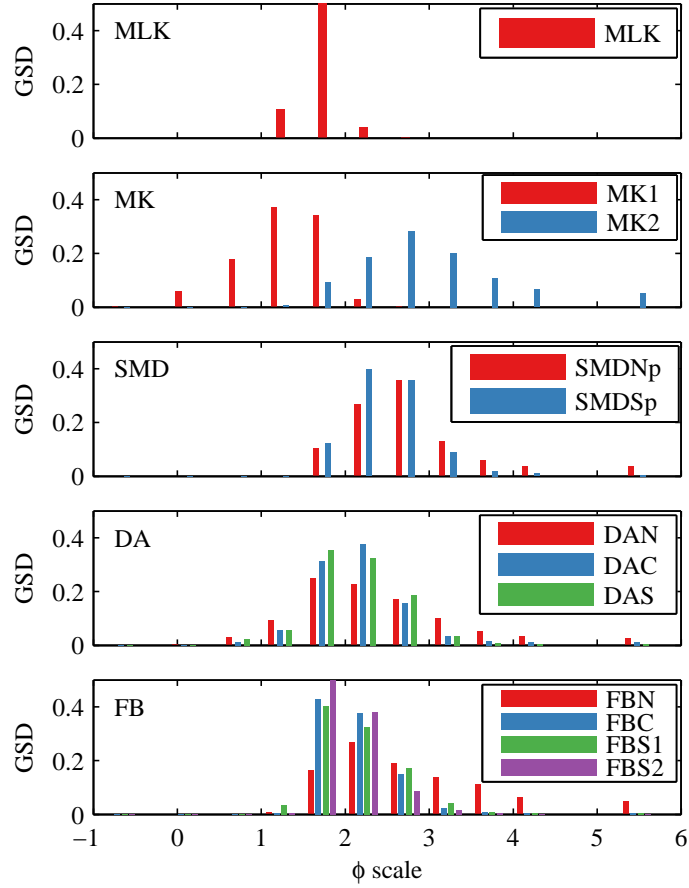
Figure 5.2: Grain size distribution from bed samples obtained at each of the measurement locations in ϕ-scale ($\phi = -\log_2(D/D_0)$ where D is the size class and D_0 corresponds to 1 mm). See Figure 5.1 and Table 5.1 for details of the locations.

in the middle of the river but at some distance upstream and one station in the middle of two nearby tributaries (Figure 5.1).

Bed sediments collected with a Van Veen grabber were sieved into eleven size classes to obtain grain size distributions (GSD). Figure 5.2 shows the obtained GSD of bed samples at the deployment locations. All distributions are centered in the medium to fine sand fraction, although there is a clear shift towards finer fractions in the samples obtained in SMD. Wider distributions with a large content of very fine sand and silt are obtained from samples from DAN and FBN. The GSD obtained at SMDNp also shows a large content of very fine sand and silt. Samples from MK1 and MK2 correspond to opposite locations across the channel. Bed samples collected at this particular location indicated a clear distinction in the composition of bed sediments at the opposite riverbanks. This difference may be related to sorting processes related to the confluence with a tributary nearby. Cumulative distributions yielded the median grain size D_{50} and the Interquartile Range IQR = D_{75} - D_{25}, a measure of the statistical dispersion of the distribution. Table 5.1 offers a summary of the deployment locations along with median grain size D_{50} and IQR values.

91

~0.5 m

H
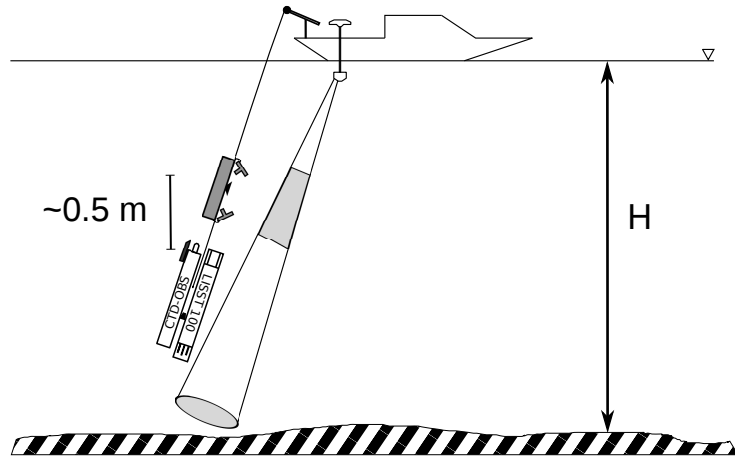
Figure 5.3: Sketch of deployment strategy in the calibration campaigns, showing the sound path of one ADCP beam and the position of the instrument array. H represents the water depth.

Calibration surveys consisted of shipboard measurements with an Optical Backscatter Sensor (OBS) which was attached to a Conductivity-Temperature-Depth (CTD) probe, a Laser In Situ Scattering and Transmissometry meter (LISST-100 type C) and a Niskin Bottle (Figure 5.3). The OBS attached to the CTD sampled turbidity at 2 Hz. Turbidity was expressed in Formazin Turbidity Units, which are related to instrument response (in mV) by a constant factor and a gain. The gain was set such that the sensitivity of the instrument was 10 mV per FTU in the range between 0 and 500 FTU. The LISST-100 sampled optical transmission and forward scattering within a set of 32 logarithmically spaced ring detectors, also at 2 Hz. The ring detectors correspond to particle size classes which approximately span the range between 5 and 500 μm (*Agrawal et al.*, 2008). The scattering distribution was corrected using a background scatter distribution from a sample of bi-distilled water, obtained before deployment, and further corrected for the non-ideal response of the detectors (*Agrawal and Pottsmith*, 2000). By an iterative inversion procedure (*Pedocchi and Garcia*, 2006), areal distributions over the 32 size classes were inferred. Multiplication by the corresponding size class and dividing by an instrument dependent and calibration-derived volume conversion factor (*Gartner et al.*, 2001) yields volume concentration (in μl l^{-1}), distributed over the 32 size classes. From the volume concentration per size class, the total volume concentration is readily computed. The particle size distribution $n(a_s)$ is obtained by assuming independence between density and particle radius, and the presence of spherical particles only. Suspended mass content in water samples was measured by vacuum filtration of 250 ml of sampled water on preweighed polycarbonate filters with a pore size of 0.4 μm. After filtration, the containers were cleaned with bi-distilled water to remove salts and remaining material. Filters were dried in an oven at 105° and weighed. Also, a fixed amount of bi-distilled water was filtered to correct for variations in filter weight after the cleaning procedure.

The research boat was equipped with a downward-looking 1200 kHz broadband ADCP. The ADCP measured a single ping ensemble at approximately 1 Hz with a depth cell size of 0.35 m. Each ping was composed of 6 sub-pings separated by 0.04 s. The range to the first cell center

was 0.865 m. The ADCP collected velocity and echo intensity data using four transducers, while the OBS, the LISST and the Niskin Bottle were winched down to a certain level, where they measured for approximately 2-3 minutes. Within that period, a water sample was taken. This procedure was repeated for different levels, at different periods of time and at different locations. In the tidal areas the procedure was repeated to cover a full semidiurnal tidal cycle. The OBS sampling volume was located roughly 0.25 m from the LISST sampling volume. The Niskin bottle was attached about 0.5 m away from the OBS and the LISST sampling volumes. We averaged all measured variables over the 2-3 minute measuring interval to minimize the differences in sampling volumes and inexact collocation. The horizontal distance between the instrument array and the closest bin of the ADCP was not entirely constant, due to drifting of the instrument array and inaccuracy of the ADCP positioning.

A total of 110 water samples were collected to calibrate the optical response of the OBS and the optical attenuation of the LISST. The total collocated measurements of the OBS, LISST and ADCP amounted to 220, spread over 60 profiles. The ADCP measured continuous profiles of acoustic backscatter and the LISST and OBS sampled on three to six levels for each profile, depending on the water depth.

5.5   Optical Measurements

5.5.1   Particle Size Distributions

Figure 5.4 shows particle size distributions $n(a_s)$ at the deployment locations. Most of the observations depict a well defined peak at around $\phi = 3\text{-}4$. The mean particle diameter, as determined with the LISST, ranges from 70 to 220 μm, corresponding to a very fine to fine sand fraction. At SMD, two types of distribution are present: one distribution is well-sorted, with a clear peak in the finer fraction; the other distribution is poorly-sorted with a shift towards the coarser fractions. These observations stem from one particular tidal cycle (SMDSp), since the LISST was not used during the deployment at SMDNp. The variations may be related to tidal resuspension events. At this particular location, the cross-section is characterized by a sudden narrowing (*Sassi et al.*, 2011a), which may enhance acceleration effects induced by the tide. Size distributions from locations in DA are consistent within and between locations. Distributions from locations in FB show some variability, in particular within the range between $\phi = 1$ and 5, with a subtle peak at $\phi > 8$. Variations at the low and high-end of the distribution may be explained by particles outside the measurable range that scatter light into the nearest size classes within the range of measurement of the instrument (*Agrawal and Pottsmith*, 2000; *Traykovski et al.*, 1999). Observations in MK show a large variability at the low-end of the distribution and some minor variability around $\phi = 3\text{-}4$, which may lead to significant changes in the mean particle size. Finally, observations in MLK show that all measured distributions are consistent with each other and that they show a clear open-ended distribution, most likely related to the presence of coarse material found in the bed samples.

Table 5.1: Summary of the ADCP deployments and corresponding calibration information. The median grain size D_{50} and the Interquartile Range IQR correspond to the grain size distributions obtained from bed samples.

Name	Location	Date	H (m)	OBS Readings	LISST Readings	Water Sample	Bed Sample	D_{50} (μm)	IQR (μm)
MLK	Melak (MLK)	22-Jan-09	20	x	x	-	x	370	80
MK	Kaman 1 Neap (MK1)	19-Dec-08	17	x	x	x	x	480	220
MK	Kaman 2 Neap (MK2)	19-Dec-08	15	x	x	x	x	170	120
MK	Kaman 1 Spring	25-Jan-09	16	x	x	-	-	-	-
MK	Kaman 2 Spring	25-Jan-09	15	x	x	-	-	-	-
MK	Kaman Upstream	24-Jan-09	17	x	x	-	-	-	-
MK	Tributary East	24-Jan-09	12	x	x	-	-	-	-
MK	Tributary West	24-Jan-09	13	x	x	-	-	-	-
SMD	Samarinda Neap (SMDNp)	22-Nov-08	18	x	-	x	x	190	100
SMD	Samarinda Spring (SMDSp)	29-Nov-08	18	x	x	x	x	220	100
DA	Delta Apex Center (DAC)	04-Jan-09	8	x	x	x	x	280	140
DA	North Branch (DAN)	04-Jan-09	8	x	x	x	x	260	200
DA	South Branch (DAS)	04-Jan-09	9	x	x	x	x	290	160
FB	First Bifurcation Center (FBC)	03-Jan-09	4	x	x	x	x	290	120
FB	North Branch (FBN)	03-Jan-09	7	x	x	x	x	200	160
FB	South Branch 1 (FBS1)	03-Jan-09	5	x	x	x	x	290	140
FB	South Branch 2 (FBS2)	03-Jan-09	10	x	x	x	x	300	120
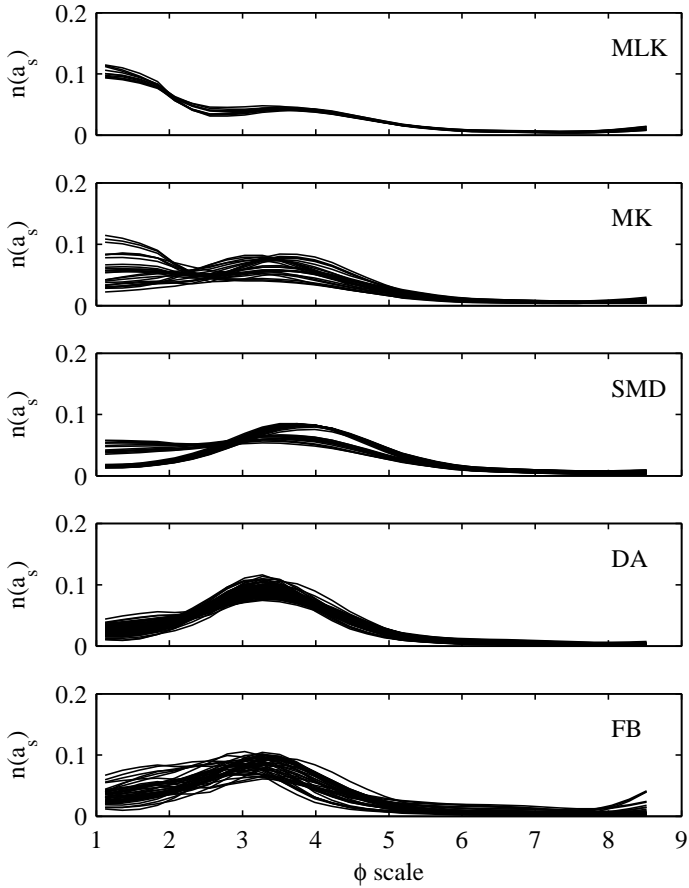
Figure 5.4: Particle size distribution $n(a_s)$ measured with the LISST, lumped per survey.

5.5.2   OBS and Transmissometer Calibrations

For the OBS and the transmissometer of the LISST we assume a linear relation between instrument reading and in situ mass in water samples

$$\text{Instrument reading} = m \times M_s + c, \qquad (5.16)$$

where the instrument reading represents turbidity (FTU) for the OBS and optical beam attenuation (m^{-1}) for the transmissometer. Accordingly, m is the instrument gain whereas c is the instrument offset. To obtain mass concentration M_s we invert equation (5.16). Confidence limits for M_s values were constructed by computing

$$\delta M_s = \frac{s}{m} \sqrt{\frac{1}{N} + \frac{D_T^2}{\sum D_T^2}} t_{(0.95, N-2)}, \qquad (5.17)$$

where s is the standard deviation of the squared sum of the residuals from the calibration, N is the amount of samples used in the calibration, D_T is the absolute deviation of the instrument reading with respect to the mean, and t is the 95% Student's t-distribution with N - 2 degrees of freedom. Note that these confidence intervals are based on the inverse regression assumption, which leads to a more conservative estimate than simply swapping variables in the linear regression (*Lavagnini and Magno*, 2007).

Figure 5.5 shows the relation between turbidity readings and mass concentration. To investigate the sensitivity of the calibrations, we have clustered the data per location and per sediment size. The percentage of volume concentration above or below 96 μm was used as an indicator of the variations in coarse and fine sediment size. This threshold corresponds to the value in the size distribution which shows the highest degree of variation (see *Fugate and Friedrichs*, 2002). The estimated gains do not feature an apparent dependence on location (Fig. 5.5a). The offsets depict more variation (see Table 5.2). The increased gain shown by calibrations in MK can be attributed to the limited amount of samples, which is confirmed by an increased standard error. When clustering the data per sediment size class, the resulting gains show to be consistent whereas the offset increases for fine sediments (Fig. 5.5b). A fixed instrument offset can be caused by the presence of a constant concentration of fine grains (*Ludwig and Hanes*, 1990; *Green and Boon III*, 1993; *Bunt et al.*, 1999). A linear regression with all the measurements yields a relatively higher gain. We apply a bi-linear relation with a constant gain and variable offset, to account for the presence of fine sediments in suspension. The value at which the relation changes from using one offset to the other was chosen such that it minimizes the Root-Mean-Squared-Deviation (RMSD) of the difference between OBS and transmissomenter estimates.

Optical transmission measured by the LISST is obtained from the ratio between transmitted and received power. The transmitted power is normalized by its value when the background measurement is made using highly filtered pure water (*Agrawal and Pottsmith*, 2000). The optical beam is attenuated by absorption by water, dissolved material, and particles, and attenuation due to scattering by particles according to the Beer-Lambert law. Since the path length of the instrument is known, the beam attenuation coefficient (m^{-1}) is readily computed. Beam attenuation can be linearly related to mass or volume concentration (*Davies-Colley and Smith*, 2001). Figure 5.6 shows that clustering the data either by location or by sediment size

Figure 5.5: OBS calibration using in situ mass in water samples: a) grouped by location, b) grouped by sediment size, c) using all measurements. Error bars indicate the variability over the two minute measurement interval.

causes variation in the instrument gain and offset. The scatter around the best-fit line suggests that variations in beam attenuation may be explained by particle size effects (*Mikkelsen and Pejrup*, 2000). A multi-linear regression approach with several other variables is an unattractive way of handling this issue, as it would complicate the calibration relation significantly. Explaining changes in M_s due to changes in particle size requires information derived from time series (*Fugate and Friedrichs*, 2002) rather than from measurements at a single moment in time.

We chose to use a single calibration for all data since a linear regression with all the measurements yields the lowest standard error of the parameters, and because transmissometer readings are complementary to the OBS measurements. Figure 5.7 compares all estimates of mass concentration M_s derived from the OBS and from the transmissometer of the LISST. Despite the large scatter around the line of perfect agreement for concentrations in the range 100-200 mg l^{-1}, M_s estimates show to be consistent all over the measured range ($r = 0.91$; $N = 220$). The RMSD of the residuals amounts to 22 mg l^{-1}.

5.5.3 Apparent Density

Transmissometer calibrations may be dependent on particle size (*Baker and Lavelle*, 1984; *Bunt et al.*, 1999), especially when changes in particle size from clay to silt classes occur. In general, our measurements indicate the River Mahakam features much coarser material in suspension. Recent observations (*Boss et al.*, 2009; *Hill et al.*, 2011) indicate that in natural environments the aggregated state of particles constrains the sensitivity of optical beam attenuation to particle size significantly. More recently, *Neukermans et al.* (2012) provided strong evidence that the mass-specific beam attenuation coefficient can be very well correlated with the apparent density. In this section we provide estimates of the apparent density, showing that in our measurements this might be the case (see Figure 5.8).

Volume concentration measured by the LISST can be used with mass concentration es-

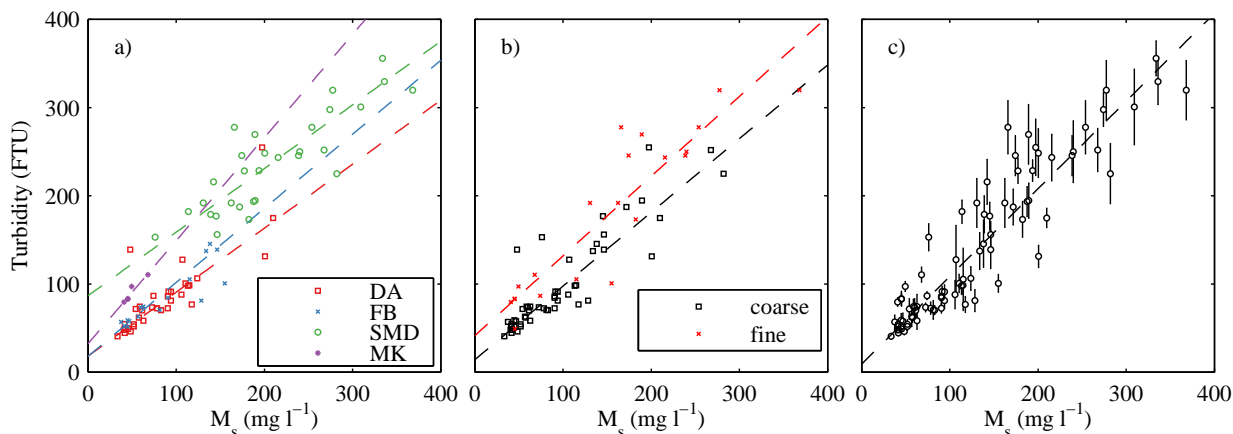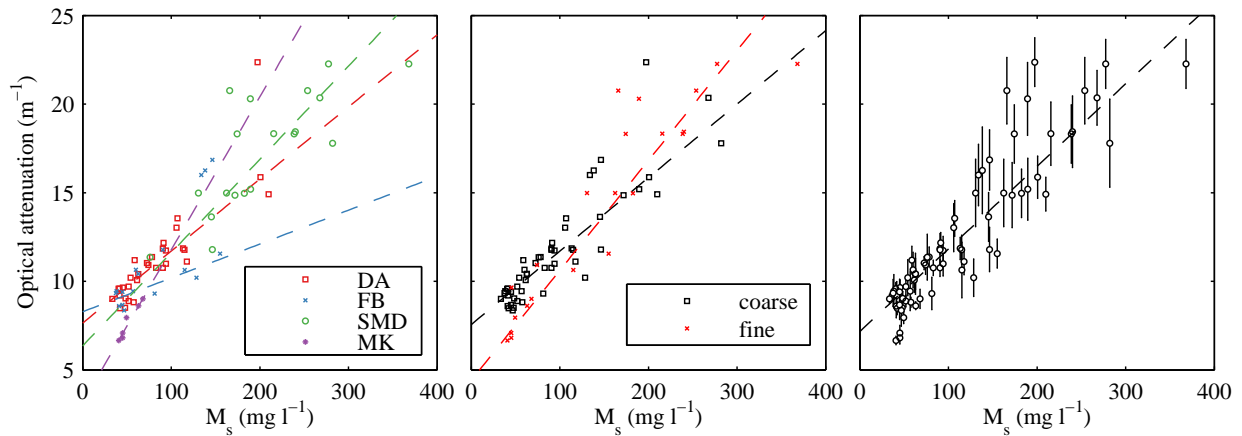Figure 5.6: Transmissometer calibration using in situ mass in water samples: a) grouped by location, b) grouped by sediment size, c) using all measurements. Error bars indicate the variability over the two minute measurement interval.
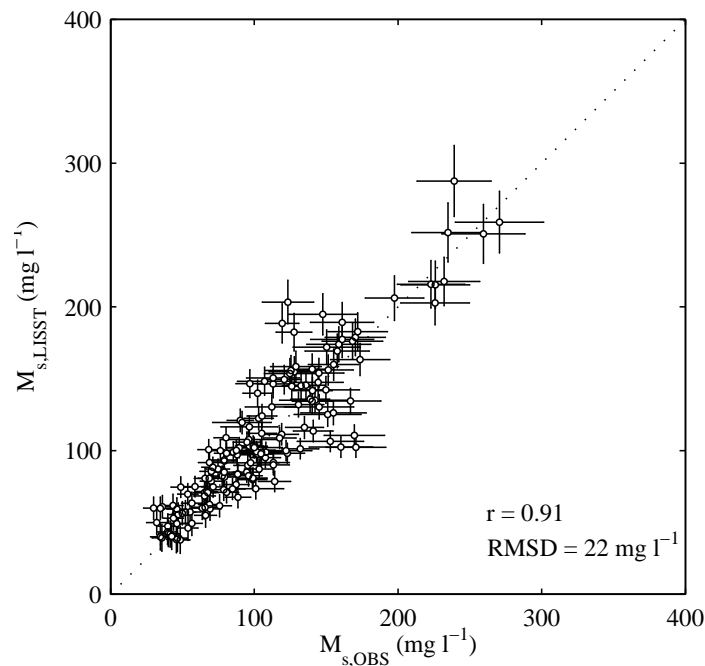
Figure 5.7: Correspondence between mass concentration derived from the OBS and from the LISST. Error bars indicate the uncertainty in the estimates based on the confidence intervals in the inverse regression.
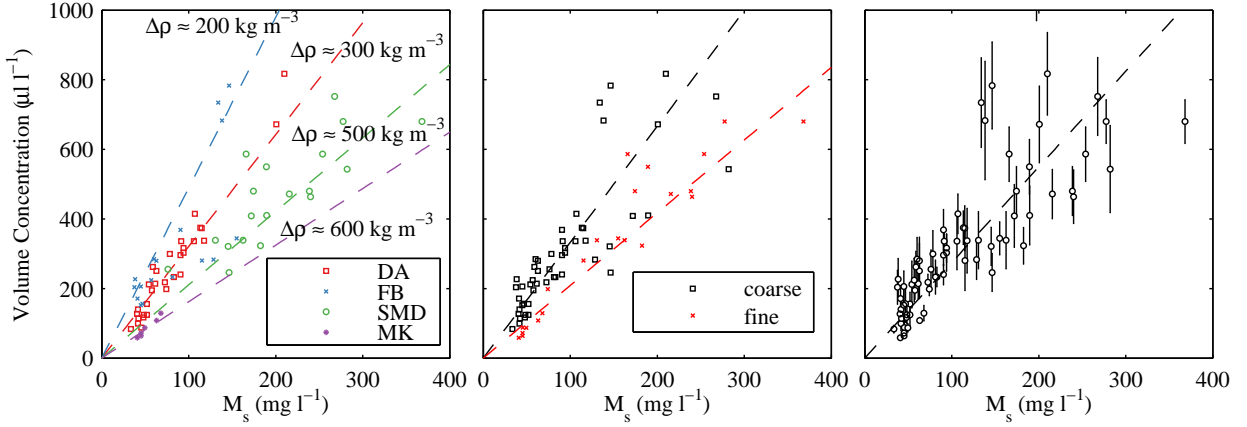
Figure 5.8: Volume concentration as a function of mass concentration in water samples M_s: a) grouped by location, b) grouped by sediment size, c) using all measurements. The inverse of the slope constitutes an estimate of the apparent density. Error bars indicate the variability over the two minute measurement interval.

timates from water samples to compute the apparent density. The apparent density of a suspension can be computed as (*Gartner and Carder*, 1979; *Mikkelsen and Pejrup*, 2001)

$$\Delta\rho = \rho_s - \rho_w = \frac{M_s}{V}, \tag{5.18}$$

where ρ_w is water density, ρ_s is the density of the suspension, M_s is mass concentration in water samples and V is volume concentration as outputted by the LISST. As changes in salinity and temperature are negligible, $\rho_w = 1000\,\mathrm{kg\,m^{-3}}$. *Mikkelsen and Pejrup* (2001) argue that equation (5.18) is an approximation which is valid only when large parts of the suspension consist of flocs. If a substantial amount consists of primary particles, then equation (5.18) approaches the density of primary particles. Figure 5.8 investigates the relation between volume concentration and mass concentration, having assumed a zero intercept. $\Delta\rho$ can be readily estimated from the inverse of the slope in this relation. Accordingly, ρ_s varies between 1200 and 1600 kg m^{-3} (which is accordingly obtained from the inverse of the slope in the Volume Concentration relation in Table 5.2). A linear regression with all the measurements yields $\rho_s \approx 1370$ kg m^{-3}. This value is used in all acoustic calculations. For consistency, mass concentration is converted to its SI equivalent.

The relatively low densities found in our measurements suggest aggregation of particles in suspension. One plausible explanation for these low values is the occurrence of flocs. Apparent density in the ocean is to a large extent controlled by organic matter (*Bowers et al.*, 2009), which generally leads to flocculation. In freshwater systems, elevated particulate organic content and attached bacteria may also lead to flocculation of suspended particles (*Droppo and Ongley*, 1994; *Droppo et al.*, 1997). If flocs are present in our measurements, they may behave as single sized scatterers with a reduced density.

Table 5.2: Summary of the calibrations of the optical instruments using in situ mass in water samples. The variability is given by the standard error in the linear regression.

Clustering		OBS		Transmissometer		Volume Concentration
		$m \pm \delta m$	$c \pm \delta c$	$m \pm \delta m \ (\times 10^{-2})$	$c \pm \delta c$	$m \pm \delta m$
Location	DA	0.73 ± 0.04	18.2 ± 4	4.1 ± 0.5	7.6 ± 0.4	3.21 ± 0.11
	FB	0.84 ± 0.06	17.8 ± 6.2	1.9 ± 0.8	8.3 ± 0.8	4.9 ± 0.23
	SMD	0.72 ± 0.07	86.6 ± 17	5.3 ± 0.8	6.4 ± 1.7	2.11 ± 0.14
	MK	1.17 ± 0.24	32.2 ± 12	8.6 ± 0.7	3.2 ± 0.4	1.62 ± 0.13
Sediment size	Coarse	0.84 ± 0.04	14 ± 4.4	4.1 ± 0.3	7.6 ± 0.3	3.33 ± 0.08
	Fine	0.9 ± 0.1	41.3 ± 17.6	6.2 ± 0.4	4.4 ± 0.6	2.09 ± 0.08
All data		0.99 ± 0.04	9.1 ± 5.7	4.7 ± 0.2	7.2 ± 0.3	2.75 ± 0.1

5.6 Effect of α_s in ADCP Backscatter Conversion

5.6.1 Data Overview

Backscatter profiles can be systematically biased by uncertainty in the determination of K_c since fluctuations of 20% around the commonly used estimates have been observed (*Gostiaux and van Haren*, 2010). In the context of the inversion of backscatter profiles obtained with Acoustic Backscatter Systems (see *Thorne and Hanes*, 2002), this problem has previously been put forward. Due to the long operating range of an ADCP, relative to near-bed observations taken from a bottom-mounted rig, this problem is particularly relevant. To correct for inaccuracies in K_c and C, these coefficients can be empirically derived using the closest available water sample to the ADCP transducer, such that the effect of attenuation due to sediments may be considered negligible. Denoting $\tilde{K}_c$ and $\tilde{C}$ as initial estimates of K_c and C (respectively), Eqs. (5.1) and (5.7) can be used to obtain

$$E_i = \frac{1}{K_c}\left[10\log_{10}\left(n_b\langle\sigma_{bs}\rangle\right) - \tilde{S}_{v,i}\right] - \frac{C}{K_c}, \tag{5.19}$$

$$\tilde{S}_{v,i} = S_{v,\alpha_s=0,i} - \tilde{K}_c E_i - \tilde{C}, \tag{5.20}$$

where the subindex i indicates a specific ADCP beam. With particle size information from the in situ water samples, $n_b\langle\sigma_{bs}\rangle$ can be estimated without recourse to mass concentration estimates, and K_c and C can be inferred from a linear regression. Accordingly, $K_c = 0.40$, 0.44, 0.41, 0.41 dB count^{-1} and C = -83, -90, -85, -85 dB, for the four ADCP beams in our deployment, respectively.

The re-calculated backscatter strength without taking into account sediment attenuation ($\alpha_s = 0$ in Eq. 5.7), is compared with estimates based on equation (5.5), where k_s^2 is computed using size distribution information and M_s has been determined previously. A comparison for all simultaneous measurements (Figure 5.9) shows good agreement (for the best fit line: $R^2 = 0.77$, slope $= 1.04 \pm 0.09$, intercept $= 0.46 \pm 1.63$ dB, intervals given by the standard error in the linear regression). The scatter in Figure 5.9 can be mainly attributed to sediment attenuation and to the size distributions being open-ended, which limits the accuracy of $\langle\sigma_{bs}\rangle$-estimates. When clustering the data based on distance from the transducer, here indicated by the height above the bottom z normalized with water depth H, Figure 5.9a reveals a significant variation in the calibration relation. The slope of the best fit line systematically decreases with distance from the transducer, which provides evidence of the effect of sound attenuation. Attempts to relate collocated ADCP backscatter to mass concentration in water samples, both obtained at different ranges from the ADCP transducer without correcting for sound attenuation, may render ADCP backscatter calibrations highly site-specific because variation in α_s will then be reflected in the calibration as variation in the regression coefficients. Clustering the data based on location (see Figure 5.9b), also yields widely differing calibrations, highlighting the site-specificness of ADCP backscatter calibrations when sound attenuation by suspended sediment is neglected.

Fig. 5.10 shows profiles of ξ_s, k_s^2, M_s, and β, all normalized with the corresponding depth-mean value, as a function of relative height above the bottom for all the measurement locations. k_s^2 and ξ_s were computed with the size distributions functions obtained with the LISST using
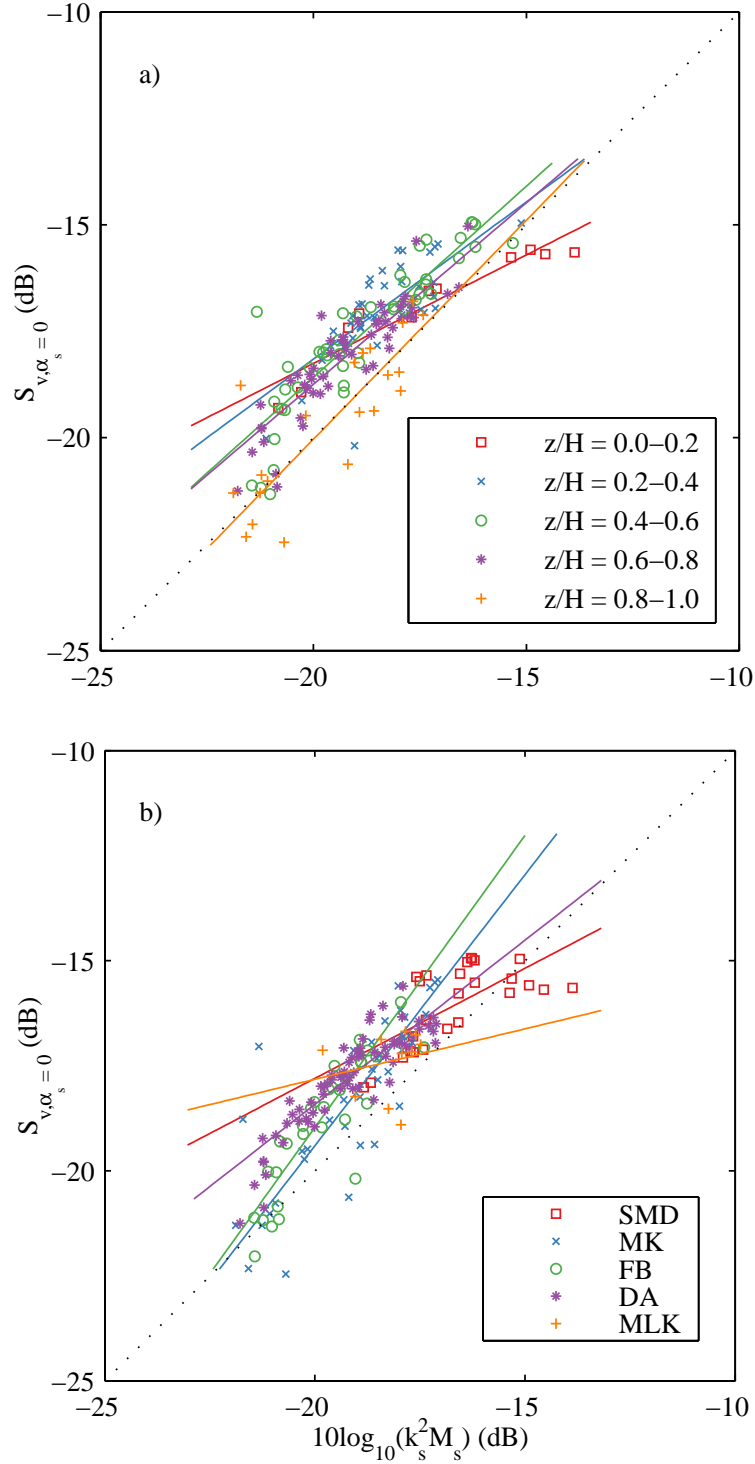
Figure 5.9: Verification of Eq. (5.5) as a function of a) normalized height above the bottom z/H, b) measuring locations. $S_{v,\alpha_s=0}$ is computed without taking into account attenuation by suspended sediment. k_s^2 is computed with the size distribution functions obtained with the LISST.

the expressions in *Thorne and Meral* (2008). Profiles of ξ_s and k_s^2 show minor trends with depth, which differ between the sites. Profiles of $M_s/\overline{M_s}$ show variations spanning over nearly one order of magnitude, typically with lower concentrations near the surface and higher concentrations near the bottom. The observations at MLK suggest the normalized depth profiles to remain nearly constant, which may partly be due to the lack of sufficient measurements near the bottom. In general, the best fit line through clustered values of $M_s/\overline{M_s}$ is approximately exponential. Profiles of $n_b/\overline{n_b}$ (not shown) also show an exponential increase with depth.

Profiles of $\beta/\overline{\beta}$ show a different depth-dependence than profiles of $M_s/\overline{M_s}$. Although both profiles are linear in semi-log space, suggesting an exponential dependence on depth, their slopes differ. When k_s^2 remains constant with depth or sound attenuation by suspended sediment is negligible, depth profiles of $\beta/\overline{\beta}$ are theoretically consistent with depth profiles of $M_s/\overline{M_s}$. Otherwise they diverge because β is impacted by α_s. When k_s^2 varies with depth, profiles of $M_s/\overline{M_s}$ and $\beta/\overline{\beta}$ may diverge, even when sound attenuation is negligible. The significant discordance of profiles of $M_s/\overline{M_s}$ and $\beta/\overline{\beta}$ observed in MLK, SMD and, to some extent, DA, yielding slopes smaller than unity in Fig. 5.9b, is likely related to sound attenuation due to the suspended sediment, which progressively reduces the slope in the calibration relation with distance from the transducer. The divergence observed in FB and MK, which yields slopes greater than one in Fig. 5.9b, may be associated to depth-variations of k_s^2, despite these being subtle. Consequently, the estimates of the empirically derived attenuation coefficient $\xi_{s,e}$ based on the assumption of k_s^2 and ξ_s being depth-independent, may become negative, which is physically not feasible. The quality of the LISST-derived estimates of ξ_s are too poor to evaluate when the estimates of $\xi_{s,e}$ based on Eq. (5.15) are correct, because the LISST only captures part of the particle size distributions. What can be concluded from the LISST data, is that at the sites DA and FB, the particle size distributions feature little variation, suggesting k_s^2 and ξ_s to be depth-independent. At the other sites, the distributions show either much more variation (SMD and MK), or are poorly resolved by the LISST (MLK), which may cause profiles of $M_s/\overline{M_s}$ and $\beta/\overline{\beta}$ to be inconsistent.

Fig. 5.11 shows the validation of the ADCP-derived estimates of M_s using equation (5.13). We tested the sensitivity of M_s estimates to ξ_s, by first assuming $\xi_s = 0$ (panel a), then computing ξ_s using the size distributions measured with the LISST (panel b), and finally using the empirically derived attenuation $\xi_{s,e}$ (Eq. 5.15, panel c). Best-fit lines through data clustered based on the distance from the transducer show that the estimates of ξ_s based on LISST data produce a bias in M_s estimates. M_s estimates neglecting attenuation result in nearly un-biased estimates, but with a large uncertainty. The best correlation between estimated and observed M_s values is obtained by using the empirically derived attenuation.

5.6.2 Proposed Calibration

In Fig. 5.12 we apply the calibration based on Eq. (5.14), for each measurement location separately, including the regression lines to determine the calibration component b and the frequency distributions of $\xi_{s,e}$. Values of b amount to 0.48 ± 0.008, 0.51 ± 0.012, 0.46 ± 0.005, 0.4 ± 0.005, and 0.53 ± 0.028, for SMD, MK, FB, DA and MLK locations, respectively. The estimates of b depict a limited range of variation between locations (a mean value and standard deviation of 0.476 and 0.05, respectively). Values of $\xi_{s,e}$ span over a broad range between -6 and
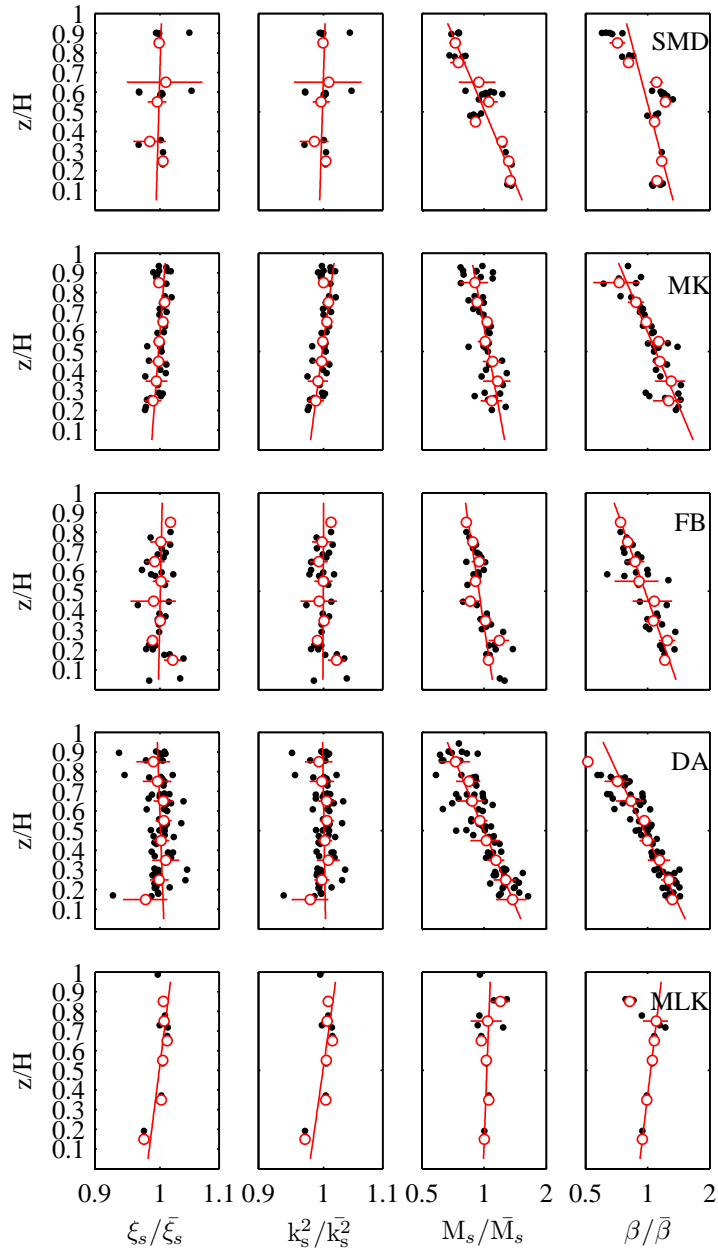
Figure 5.10: Profiles of ξ_s, k_s^2, M_s, and β, normalized with depth-mean values (denoted by the overbar), as a function of normalized height above the bottom z/H. k_s^2 and ξ_s were computed with the size distributions functions obtained with the LISST. White circles indicate clustered values, error bars indicate the standard deviation. Red lines indicate the best fit to clustered values.
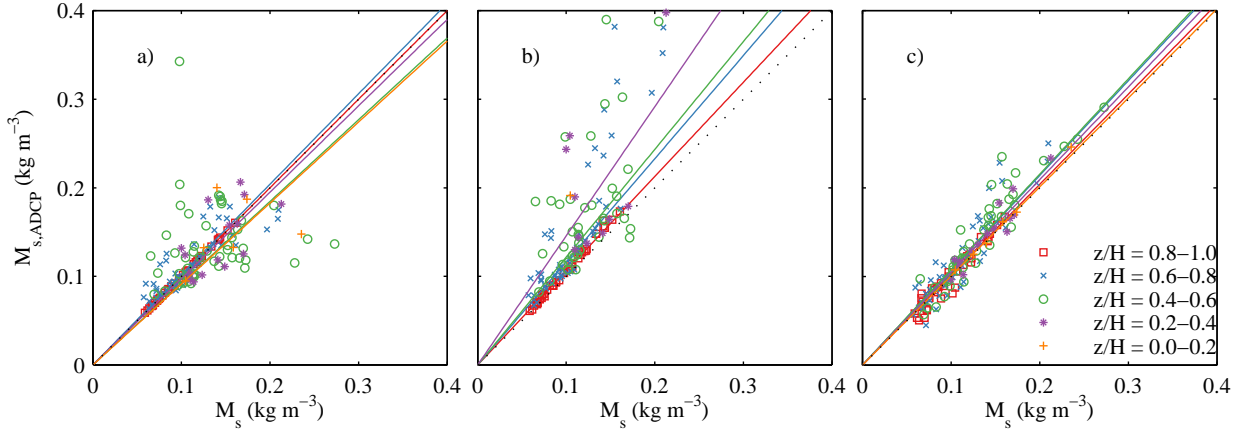
Figure 5.11: Validation of the ADCP-derived estimates of M_s using equation (5.13) as a function of normalized height above the bottom z/H: a) setting $\xi_s = 0$, b) computing ξ_s using size distributions from the LISST, c) with the empirically derived attenuation $\xi_{s,e}$.

2 dB m^2 kg^{-1}, which may be largely attributed to the depth variation of k_s^2 and ξ_s, as discussed in the previous section. The most frequently occurring value of $\xi_{s,e}$ per site amounts to 0.27, -0.12, -2.46, 0.42, and -0.5 dB m^2 kg^{-1}, for sites SMD, MK, FB, DA and MLK, respectively.

Aiming to find a rationale to select a single exponent b and attenuation coefficient $\gamma_{s,e}$ that can be globally applied, we now lump all data from the different sites. The reference range $\tilde{R}_{ref}$ is then 2.4 m from the surface, which is outside the blanking range and within the transition between the near- to far-field range of the ADCP transducers. Fig. 5.13 show the global calibration results. The calibration coefficient b amounts to 0.45 ± 0.008, and will be set at 0.45. The empirically derived specific attenuation $\xi_{s,e}$ now shows a well-defined distribution, with the mode at 0.7 dB m^2 kg^{-1}. We assume the mode of the distribution of $\xi_{s,e}$ can be interpreted as a characteristic value of attenuation. The limited range of the particle size distributions of the LISST do not allow to verify that assumption based on direct estimates, but using the mode can be compared with a statistical optimum. Setting $b = 0.45$ and maximizing the correlation between in situ M_s and ADCP derived concentrations $M_{s,\mathrm{ADCP}}$ yields an optimized value $\xi_{s,o}$ very close to the mode estimated from the frequency distribution (Fig. 5.14). Hence, obtaining a statistical optimized value yields the same attenuation coefficient as taking the mode of the distribution of empirically derived attenuation estimates, based on assumptions of depth independence in k_s^2 and ξ_s. In either of the two approaches, typical concentrations found in the River Mahakam imply $\alpha_s \sim \alpha_w$.

Figure 5.15 compares the values of ADCP derived concentrations $M_{s,\mathrm{ADCP}}$ with corresponding in situ estimates of M_s, for different depth ranges and two calibration strategies. We estimated $M_{s,\mathrm{ADCP}}$ by using the calibration per location (see Fig. 5.12) and the global calibration (see Fig. 5.13), setting b=0.45 and $\xi_{s,e}$ =0.7 dB m^2 kg^{-1}. Linear regressions through the data points for the calibration per location yield slopes amounting to 0.97 ± 0.05, 1.06 ± 0.03, and 0.98 ± 0.03 for groups of observations near the surface, at mid-depth and near the bed, respectively. For the global calibration the slopes amount to 0.98 ± 0.04, 1.1 ± 0.04, and 1.02 ± 0.05 for the same groups of observations. This confirms the ADCP-derived estimates of M_s
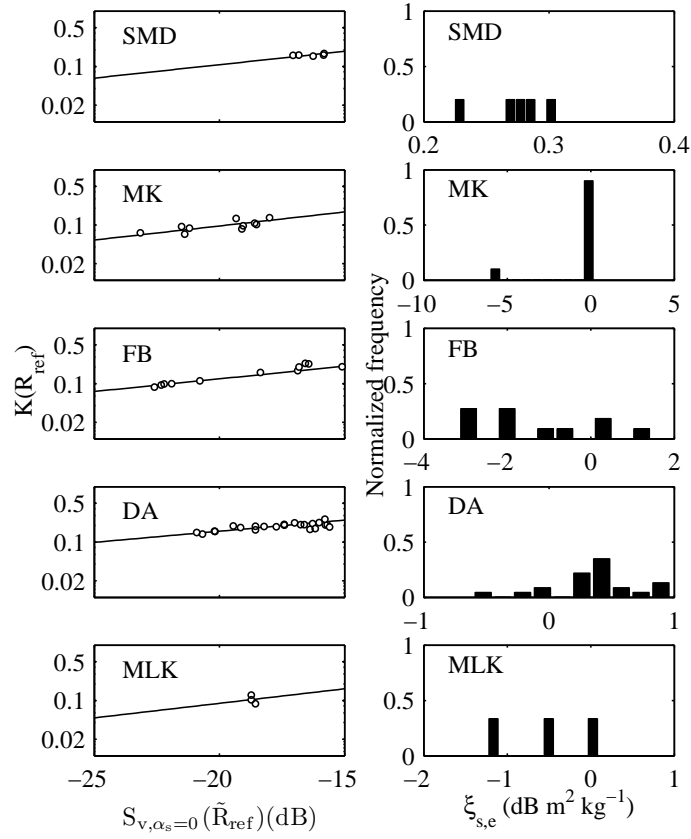
Figure 5.12: Left: calibration results using equation (5.14). The solid line indicates the best fit line, where the slope represents an estimate of the parameter b (Eq. 5.14). Right: normalized frequency distribution of the empirically derived attenuation $\xi_{s,e}$.
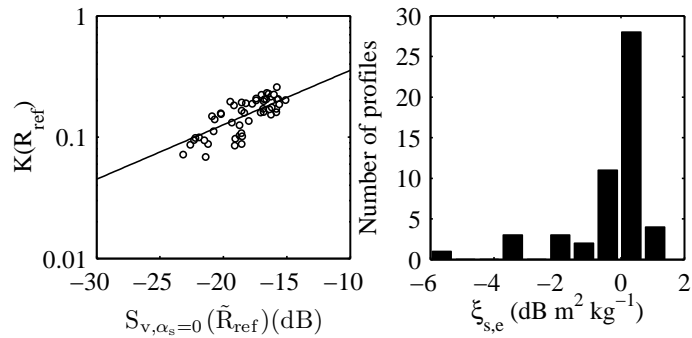
Figure 5.13: Left: calibration using equation (5.14) including data from all sites. The solid line indicates a best fit line with $b = 0.45 \pm 0.008$, where the variability is given by the standard error in the linear regression. Right: frequency distribution of the empirically derived attenuation $\xi_{s,e}$. Bin centers are spaced by 0.7 dB m^2 kg^{-1}. For typical concentrations found in the River Mahakam, the mean value yields $\alpha_s \sim \alpha_w$.

106
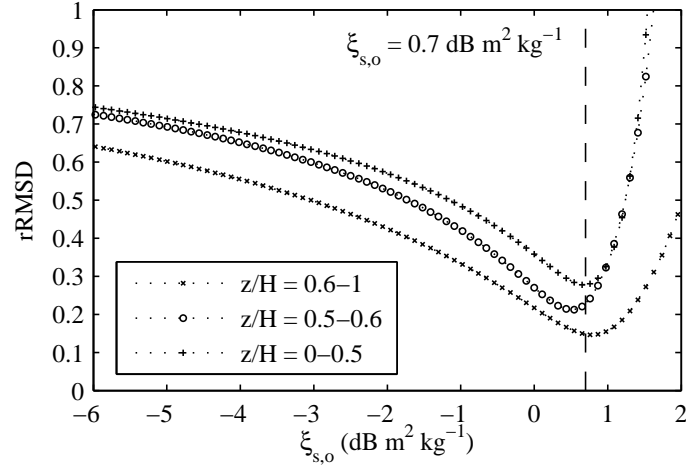
Figure 5.14: Relative root-mean-squared-deviation (rRMSD) of the residuals between in situ M_s and ADCP derived concentrations $M_{s,\mathrm{ADCP}}$ as a function of the specific attenuation ξ_s for groups of samples per depth range, as indicated. Depth ranges where chosen such that the number of observations available for validation is the same for each depth range.

with either calibration are nearly unbiased. The RMSD of the residuals using the calibration per location amounts to 22, 18.5 and 22 mg l^{-1}, for groups of observations near the surface, at mid-depth and near the bed, respectively. For the global calibration the RMSD yields 16, 29 and 34 mg l^{-1}, for the same groups of observations. The differences can be mainly attributed to the different path lengths to the target volume, and higher mass concentrations near the bed, which amplify the effect of assuming k_s^2 and ξ_s to be constant. Overall, the correlation coefficient between in situ and ADCP derived estimates ($r \sim 0.7$) is similar to what other studies report for calibrations at a single site.

5.7 Conclusions

ADCPs can yield non-intrusive, collocated and simultaneous measurements of mass concentration of suspended particulate matter. To quantify mass concentration of suspended matter, ADCP backscatter is calibrated with mass concentration of in situ water samples. ADCP backscatter calibrations are often site-specific, and tend to change in time. Accounting for sound attenuation and size variations along the two-way sound path to the target volume may overcome this deficiency. Re-arranging existing equations, we introduce a calibration method that accounts for sound attenuation, which assumes depth-independence of the particle size distribution function and constancy of sound attenuation per unit concentration of suspended mass. Specific attenuation is obtained by using at least two collocated water samples, one close by and the other remotely from the ADCP transducer. The reference concentration near the transducer is obtained from a power-law regression. Profiles consisting of mass concentration derived from calibrated optical instruments, size distributions inferred from a LISST and acoustic backscatter retrieved from an ADCP obtained at five different locations in the River Mahakam are used to test this approach.
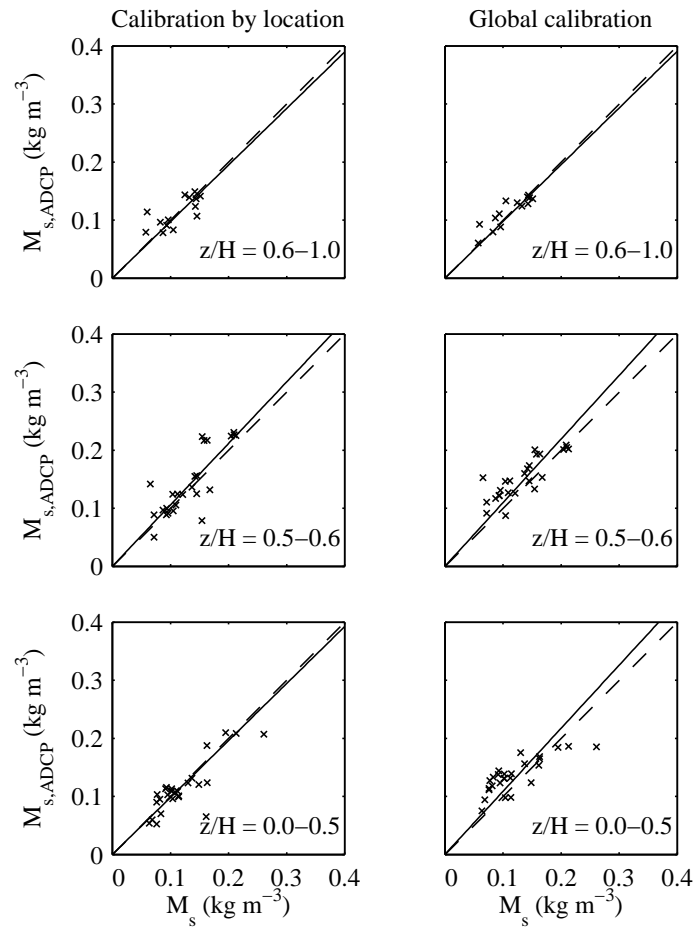
Figure 5.15: Validation of the ADCP-derived estimates of M_s for groups of samples per depth range, as indicated. Left panel: using the calibration per location (see Figure 5.12). Right panel: using the global calibration (see Figure 5.13). The dashed line indicates the line of perfect agreement. The solid line indicates a best fit line. The ADCP-derived estimates of M_s can be considered nearly unbiased.

The two calibration coefficients needed for a global calibration applicable to the entire region covered by the measurements are the exponent b in the power-law regression and an attenuation coefficient $\xi_{s,e}$. The estimation procedure of exponent b is robust, as the calibrated values for each of the different sites is about the same. In a global calibration, which lumps all data from the five locations, $b = 0.45 \pm 0.008$. The attenuation coefficient $\xi_{s,e}$ features a large amount of variation, both in time at a site and between sites. The relatively well-defined part of the frequency distribution can be explained from the degree of consistency between LISST-derived particle size distributions. However, a direct comparison with LISST estimates is hampered by the detection range of the LISST which is too limited to directly estimate the specific attenuation coefficient from field measurements of the particle size distribution. When lumping all data together, a well-defined frequency distribution of $\xi_{s,e}$ emerges. We propose to select the mode of the frequency distribution of $\xi_{s,e}$ for the global calibration, which is nearly equal to the $\xi_{s,e}$ value obtained from a statistical optimization procedure.

ADCP-derived profiles of suspended mass concentration are calculated using the two global calibration coefficients, using independent validation data. The ADCP-based estimates of mass concentration show to be un-biased, even at distance from the transducer. The quality of the estimates deteriorates with depth, which may reflect the importance of sound attenuation by suspended sediment, and amplify the effect of the assumed depth-independence of the particle size distribution. The application of the calibration as proposed depends on the accuracy and resolution of the frequency distribution of $\xi_{s,e}$, which improve when the number of arrays of water samples along the sound path of the ADCP becomes larger.

Chapter 6

Sediment Discharge Division

Abstract: Bifurcations in tidally-influenced delta channel networks control the division of water and sediment discharge over downstream channels, exerting a strong influence on the morphology and the ecology of the delta, and adjacent coastal waters. Flow division at tidally-influenced river bifurcations is complicated by the tides that intrude from the mouths of distributaries and tidal channels, and can affect the division of sediments. Recent studies have pointed out that upstream conditions and secondary circulation may exert a strong control on the division of sediment discharge at river bifurcations. Here, we characterize and quantify the sediment discharge division at two tidally-influenced river bifurcations in response to section averaged flow strength and secondary circulation. We employed a boat-mounted acoustic Doppler current profiler (ADCP), to survey transects at bifurcating branches during a semidiurnal tidal cycle. The ADCP collecting flow velocity and acoustic backscatter data was used to quantify suspended sediment discharge, adopting a recently introduced calibration procedure. Measured profiles of flow velocity and sediment concentration allowed us to compute spatiotemporal distributions of the shear velocity, the roughness length and the Rouse number. Spatiotemporal distributions of the settling velocity were obtained by combining the Rouse number and shear velocity estimates with in-situ determinations of the settling velocity. Bed-load transport rates were estimated from shear velocities. The concentration field shows a direct response to the shear velocity, stressing the alluvial context of the system. The flow in the bifurcating branches is characterized by counter-rotating secondary-flow cells that persist throughout the entire tidal cycle. The pattern of secondary flow suggests the flow approaching the bifurcation is composed of two independent lanes. This two-cell structure inhibits the exchange of sediment that would occur in case the cell would stretch over the full channel width. The division of suspended sediment primarily depends on the upstream transverse profile of the suspended sediment concentration, which is in turn dependent on geometrical factors such as upstream curvature.

---

[1]This chapter is largely based on the manuscript: Sassi, M.G., A.J.F. Hoitink, B.Vermeulen, and Hidayat, *Sediment discharge division at two tidally-influenced river bifurcations*, submitted to Water Resources Research

6.1 Introduction

Bifurcations in delta channel networks control the division of sediments, nutrients and contaminants over downstream channels and the coastal zone, exerting a large impact on the morphology and the ecology of river deltas. In tidal regions, flow division at tidally-influenced bifurcations is complicated by tides that intrude from the mouths of distributaries and tidal channels and can therefore affect the division of sediment transport. At three tidally-influenced bifurcations in the River Rhine, *Frings and Kleinhans* (2008) established a poor correlation between water and sediment discharge. Velocity patterns during ebb and flood can be highly asymmetrical at tidally-influenced bifurcations of the Sacramento River (*Dinehart and Burau*, 2005b). Flow processes in tidally-influenced bifurcations include asymmetry of the tides and tide-induced residual circulations (*Buschman et al.*, 2010; *Sassi et al.*, 2011b). Tides can affect the division of river discharge by imposing differences in Stokes fluxes (*Buschman et al.*, 2010) and in water levels citepsassi2011b, over bifurcating branches. At present, the division of sediment discharge under different discharge and tidal regimes is poorly understood. Here we show existing theory on suspended sediment transport can be readily applied to tidally-influenced bifurcations. Complexity in the relation between water and sediment transport is caused by differences in momentum and sediment diffusivities.

Bed-load transport processes occurring at river bifurcations have been investigated intensively with theoretical models (*Wang et al.*, 1995; *Bolla-Pitaluga et al.*, 2003), with numerical models (*Lane and Richards*, 1998; *Kleinhans et al.*, 2008), and on the basis of flume experiments (*Bertoldi and Tubino*, 2007). A central bar typically develops into a bifurcation, regardless of the hydraulic conditions upstream (e.g. *Federici and Paola*, 2003; *Dargahi*, 2004). The geometry of bifurcations affects the water and sediment discharge division over downstream branches (*Bolla-Pitaluga et al.*, 2003). Local hydraulic conditions at bifurcations are influenced by secondary flow patterns and their relation to local erosion and deposition (*Richardson and Thorne*, 1998). In braided rivers (*Richardson and Thorne*, 2001), the division of the velocity field into multiple threads within a single channel precedes a division in the cross-sectional morphology of the channel, which is a necessary prerequisite for the development of a bifurcation. In a confluence-diffluence unit in the Paraná River (*Parsons et al.*, 2007), the division of flow is initiated close to where the depth of the central scour reduces, well upstream of the downstream diffluence. Although in meandering rivers and in deltas the suspended-load is generally dominant over the bed-load, bed-load transport may determine the long-term morphological evolution of river bifurcations (e.g. *Edmonds and Slingerland*, 2008). Small amounts of bed-load transport can be substantial for the development of bars (*Crosato and Mosselman*, 2009) that affect the morphology of the bifurcations and consequently the division of sediment discharge.

Processes controlling suspended sediment discharge division at bifurcations extend over the full water depth, and may particularly be governed by secondary flows causing transverse exchange of sediment. As a consequence of the curvature induced by the bifurcation, single secondary flow cells occur in each distributary, with water converging at the surface and diverging at the bed (*Thomas et al.*, 2011). *Miori et al.* (2012) showed that when bedforms are not present, counter-rotating secondary circulation cells may develop upstream of the apex of the bifurcation and extend in the downstream channels. When bedforms are prevalent, secondary circulation cells extending over the full water depth may not form (see also *Parsons et al.*, 2007).

Dargahi (2008) found that the existence of multiple secondary flow fields generated upstream, such as in a river bend, may cause deposition in one of the bifurcating branches. *Hardy et al.* (2011) showed that the flow structures generated by the flow in an idealized meander bend upstream of a bifurcation can be larger than those generated by any geometric configuration of the bifurcation tested. In the presence of curvature in the feeding channel, the effects of cuvature-induced secondary flow can overwhelm the effects of local bifurcation characteristics (*Kleinhans et al.*, 2008). These studies suggest that secondary circulation cells upstream of the bifurcation may be an important factor determining sediment discharge partition at bifurcations. A two-cell structure, on the contrary, inhibits the exchange of sediment that would occur in case the cell would extend over the full width of the feeding channel. Then the division of suspended sediment depends on the upstream transverse profile of the suspended sediment concentration, which is controlled by details of the adjacent flow lanes.

To some extent, the division of suspended sediment discharge depends on the details of the vertical distribution of suspended sediment concentration (e.g. *Slingerland and Smith*, 1998). The concentration profile is primarily governed by a balance between diffusive and advective sediment fluxes in the vertical direction (*van Rijn*, 1984b), and follows an exponential distribution in open channel flows known as the Rouse profile. Sediment and momentum diffusivities are closely related, such that the ratio between water and sediment diffusivities (α) is generally unity, and independent of depth (*van Rijn*, 1984b). However, several experiments in flumes (e.g. *Hill et al.*, 1988; *Cellino and Graf*, 1999; *Graf and Cellino*, 2002; *Nikora and Goring*, 2002; *Muste et al.*, 2005) have indicated a wide range of variation around $\alpha = 1$. Field observations in coastal environments (e.g. *Whitehouse*, 1995; *Amos et al.*, 2010) have shown that α may be as low as 0.2 and as high as 3.5, and suggest a positive correlation with sediment size. The proper determination of *alpha* plays a crucial role in suspended sediment transport computations, because settling velocities derived from gradients in sediment concentration are scaled by a factor α, which leads to a systematic source of uncertainty in the calculations. Here we present results from an extensive data set showing that α is systematically greater than unity, indicating that sediment diffusivity generally exceeds momentum diffusivity in sandy environments with a moving bed.

This chapter aims to characterize and understand the spatiotemporal variations of sediment discharge division in response to mean flow and secondary circulation, at two tidally-influenced river bifurcations in the Mahakam delta in East Kalimantan, Indonesia. A description of the field site and instrumentation is presented in Section 6.2. Section 6.3 analyses the flow structure at the bifurcations and provides estimates of the bed-load sediment transport rates. Suspended sediment concentration and settling velocity results are presented in Section 6.4. Section 6.5 shows the division of water and sediment discharge at bifurcating branches of the two bifurcations. Section 6.6 offers a discussion of the main results. We finalize this chapter with the conclusions in Section 6.7.

6.2   Field Site and Instrumentation

Measurements were carried out at two bifurcations in the Mahakam delta, East Kalimantan, Indonesia (Figure 6.1). Salinity intrusion generally reaches to about 10 km seaward from the delta apex. Only during extremely low flows, such as the El Niño-related drought in 1997, can

salinity intrusion reach beyond the delta apex. The study area is therefore generally subject to freshwater conditions. Due to the gentle slope of the river, the tidal wave can propagate up to 190 km from the river mouth, depending on the river discharge. A boat-mounted ADCP surveyed 13-h transects, collecting velocity and backscatter data at the main bifurcations of the delta, labeled Delta Apex and First Bifurcation (see Fig. 6.1). The research boat was equipped with a 1.2 MHz RDI Broadband ADCP measuring in mode 12, a multi-antenna Global Positioning System compass operating in differential mode (D-GPS) and a single-beam echo-sounder. The ADCP measured a single ping ensemble at approximately 1 Hz with a depth cell size of 0.35 m. Each ping was composed of 6 sub-pings separated by 0.04 s. The range to the first cell center was 0.865 m. The boat speed ranged between 1-3 m s^{-1}. ADCP surveys covered spring and neap tidal conditions at both locations, during a flood wave. A summary of the tidally averaged quantities during the moving-boat ADCP surveys is presented in Table 6.1. All surveys lasted for approximately 13 h, to cover a semidiurnal tidal cycle. Due to technical difficulties, the survey at Delta Apex during spring tides lasted for about 7 h, covering the rising tide period only.

To produce the bathymetric map of the region of interest (Figure 6.2), depth data across the river, collected with a single-beam echosounder, were projected on a curvilinear grid using linear interpolation (*Legleiter and Kyriakidis*, 2007). The bathymetry upstream of the Delta Apex location shows a meandering thalweg, which continues in the northern branch. At the southern branch, an elongated depositional area in the middle of the channel extends over four kilometers, dividing the channel in two well defined water courses. About halfway between Delta Apex and First Bifurcation, the southernmost water course splits the elongated bank in two parts, marking the start of the northern branch of First Bifurcation. Transects during spring and neap tides were navigated along a predefined line (see Fig. 6.2).

Prior to the 13-h ADCP surveys, calibration surveys were performed to obtain mass concentration from the echo intensity measured by the boat-mounted ADCP, by collecting co-located measurements with the ADCP, an Optical Backscatter Sensor (OBS) and a Laser In Situ Scattering Transmissometery (LISST). We performed the calibration by navigating between anchor stations representative of each bifurcating branch during neap tides. The deepest location represents the entire cross-section. In the southern branch, two stations were selected corresponding to the main water courses. The calibration procedure consisted of ADCP sampling of echo intensity using the four transducers, while the OBS, the LISST and a Niskin Bottle were winched down to a certain level, where they measured for approximately 2-3 minutes. Within that period, a water sample was taken. This procedure was repeated for different levels at each vertical. An empirical calibration approach was introduced, relying on at least two water samples along the measuring range of the ADCP, that accounts for sound attenuation due to suspended sediments. Details of the calibration procedure can be found in *Sassi et al.* (2012b). After calibration, spatiotemporal distributions of echo intensity measured with the shipborne ADCP were converted into Suspended Sediment Concentration (SSC).

Bed samples were obtained with a Van Veen grabber at locations in Delta Apex and First Bifurcation. Samples from 30 cross transects, consisting of five bed samples each, were sieved into eleven size classes to obtain the Grain Size Distributions (GSD). Figure 6.3 shows an interpolated map of the median grain size D_{50} in μm. The spatial distribution of D_{50} indicates that the river bed is mainly composed of fine to medium sands (D_{50} = 200-400 μm), with
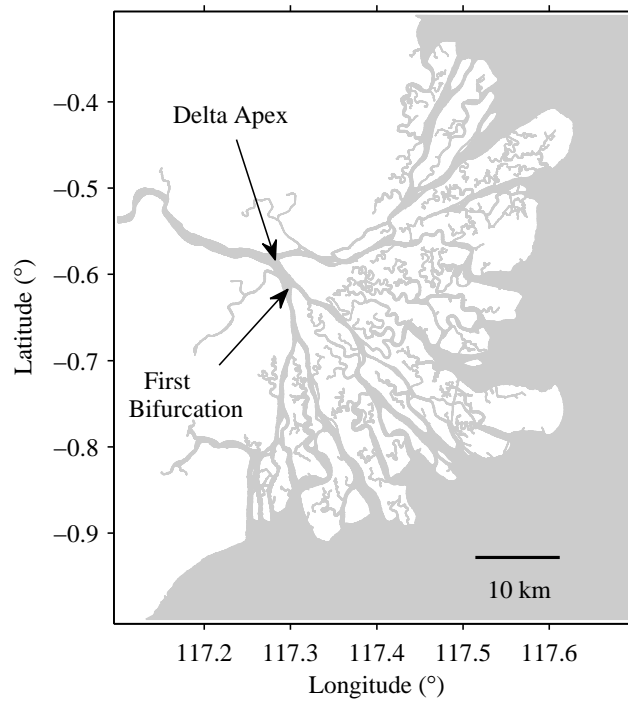
Figure 6.1: Map of the Mahakam delta in East Kalimantan, Indonesia.
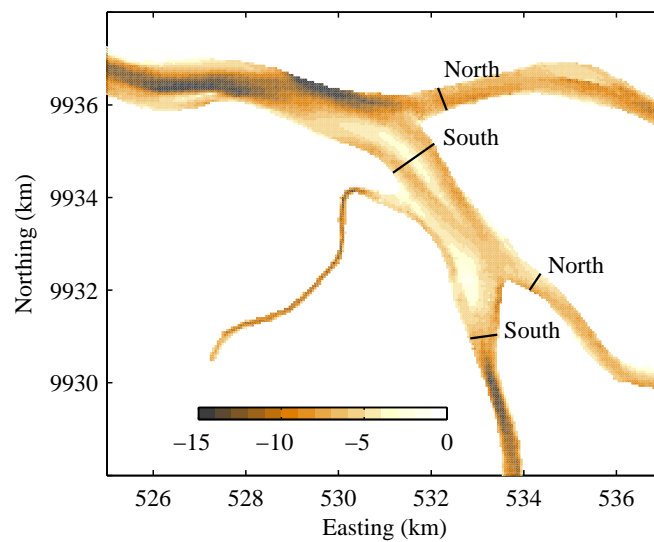
Figure 6.2: Bathymetry (in meters below mean sea level) of Delta Apex and First Bifurcation (modified after *Sassi et al.* (2011b)). Navigated cross-transects to obtain discharge estimates in northern and southern channels of Delta Apex and First Bifurcation, respectively, are depicted with the solid lines.

115

Table 6.1: Summary of the hydrographic surveys. The hat denotes tidal averaging. In italics, the average was computed over a time span smaller than a semidiurnal tidal cycle.

Location	Date	Tide	$W\,(m)$	$\hat{A}\,(m^2)$	$\hat{Q}\,(m^3s^{-1})$
Delta Apex North	04-Jan-2009	Neap	540	4480	3470
Delta Apex South	04-Jan-2009	Neap	1040	7040	4920
Delta Apex North	26-Dec-2008	Spring	560	4610	*2730*
Delta Apex South	26-Dec-2008	Spring	1040	6970	*3550*
First Bifurcation North	03-Jan-2009	Neap	410	2930	1940
First Bifurcation South	03-Jan-2009	Neap	660	5280	3290
First Bifurcation North	27-Dec-2008	Spring	440	3050	1770
First Bifurcation South	27-Dec-2008	Spring	640	5080	2760

medium sands in the main channels ($D_{50} > 250\ \mu$m). Riverbanks comprise fine sands and large amounts of silt and clay. Patches of irregularly distributed coarser sand are present in the middle of the section, whereas some patches of very fine material are found along the elongated bank. The GSD of bed samples collected at the deployment locations indicated in Figure 6.3 are centered in the medium to fine sand fraction (see Figure 6.4). Wider distributions, with a large content of very fine sand and silt, characterize samples from the northern branch of Delta Apex (site DAN) and First Bifurcation (site FBN), respectively. The GSD from a sample taken at DAN is slightly more concentrated in the coarse fraction, indicating significant amounts of medium to coarse sand. No significant difference is found between the samples obtained at the two locations in the southern branches.

Sediment sorting at the upstream bend (*Frings and Kleinhans*, 2008; *Kleinhans et al.*, 2008) may explain the relatively coarse fraction transported towards the northern branch at Delta Apex. Bend sorting typically acts on bed-load transport (*Parker and Andrews*, 1985), which is likely represented by the bottom sediments that we have used to construct the D_{50} map. The GSDs from samples at DAN and FBN confirm this. The GSDs of DAN and FBN samples also suggest that a relatively fine fraction is transported towards the northern branch at Delta Apex and First Bifurcation, respectively. Samples from other locations at the southern branches all feature the same GSD, suggesting a rather uniform along-channel spatial distribution.

6.3   Flow Pattern

6.3.1   Three-dimensional Velocity Field

Vertical profiles of velocity and SSC were transformed to relative height above the bottom according to:

$$\sigma = \frac{z}{H + \eta},\tag{6.1}$$

where H is mean water depth, z is the height above the bottom, and η is water level variation. Water levels were obtained from a pressure sensor located nearby. Mean water level was defined as the mean over each tidal cycle. The variation around mean water level by other causes than
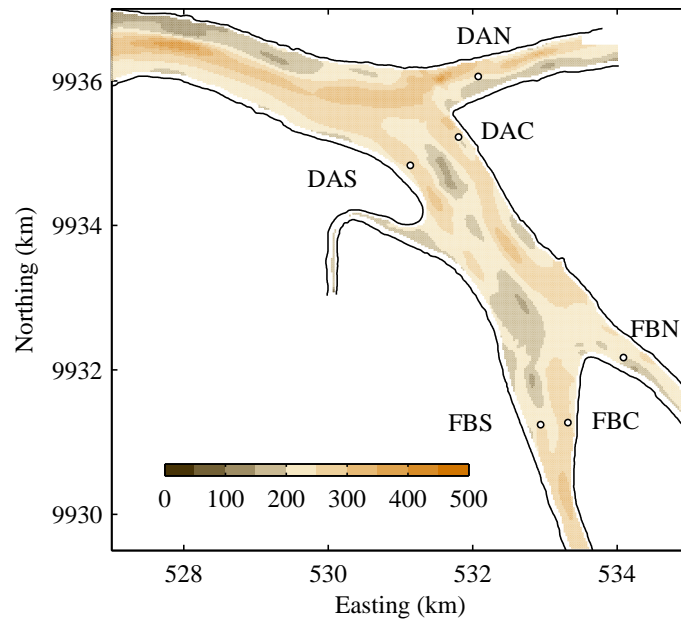
Figure 6.3: Map of median grain size D_{50} (μm) of Delta Apex and First Bifurcation. Deployment locations to perform the ADCP backscatter calibration are depicted with the circles. Full lines represent remotely sensed riverbanks.
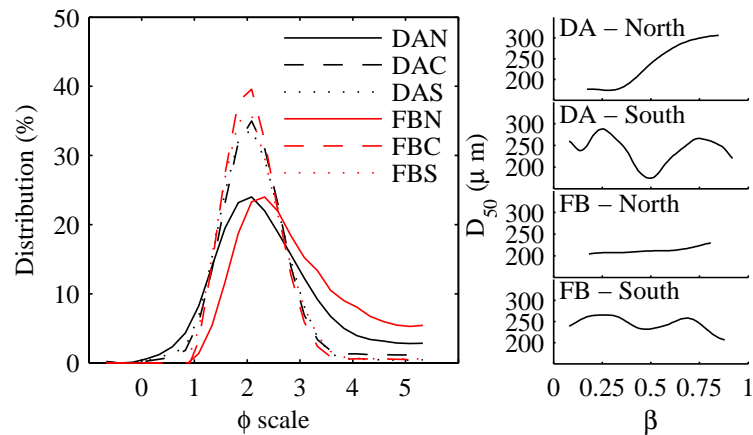
Figure 6.4: Left: Grain Size Distribution (GSD) of bed samples obtained at locations indicated in Figure 6.3, in ϕ-scale ($\phi = -\log_2(D/D_0)$ where D is the size class and D_0 corresponds to 1 mm). Right: D_{50} as a function of normalized width β, along the transects depicted in Fig. 6.2. β varies from zero to one corresponding to the riverbanks in the inner side and the outer side of the bifurcations, respectively (see Section 6.3).

tides (subtidal fluctuations) was negligible (< 0.2 m) in the time-span between ADCP surveys. Along-channel (s) and cross-channel (n) coordinates for each ADCP campaign were defined on the basis of bed morphology following *Hoitink et al.* (2009) and *Sassi et al.* (2011a). Easting and northing coordinates of the depth map were rotated systematically in steps of 0.5 degrees. For each rotation step, the root-mean-square deviations from mean values in the potential s direction were averaged. Depth variation along the s-coordinate in Delta Apex was found to be minimal when it deviated 75° and 140° from the North, for the northern and southern branch, respectively. Similarly, depth variation along the s-coordinate in First Bifurcation was found to be minimal when it deviated 125° and 185° from the North, for the northern branch and southern branch, respectively. The n-coordinate points perpendicular to the s-coordinate, with its origin at the inner side of the bifurcation. We normalized all transects with the total width obtained from the intersection of the n-coordinate with the riverbanks, to yield a normalized spanwise n-coordinate, β.

In general, the orientation of the s-component coincides with the direction of the depth-mean flow. We define a velocity component u' which is aligned with the depth-mean flow vector, according to:

$$u' = u\frac{U}{\sqrt{U^2 + V^2}} + v\frac{V}{\sqrt{U^2 + V^2}}, \qquad (6.2)$$

where

$$U = \int_0^1 u\left(\sigma, \beta, t\right) \mathrm{d}\sigma, \ V = \int_0^1 v\left(\sigma, \beta, t\right) \mathrm{d}\sigma. \qquad (6.3)$$

Similarly, a zero-mean spanwise component v' reads as

$$v' = u\frac{V}{\sqrt{U^2 + V^2}} - v\frac{U}{\sqrt{U^2 + V^2}}. \qquad (6.4)$$

Variations over the depth of the spanwise velocity component can then be considered as the secondary velocity field. For simplicity, hereinafter, we will denote the along-channel and the cross-channel velocity components as u and v, respectively.

Profiles of u and SSC were projected onto a uniform grid in (σ,β) space. The grid spacing is typically 0.5 m and 5 m in the vertical and spanwise directions, respectively. ADCP velocity measurements have contributions of mean flow, turbulence and error components (e.g. *Hoitink et al.*, 2009; *Sassi et al.*, 2011a). SSC profiles derived from backscatter strength have similar contributions. To isolate the mean flow component from repeated transect measurements, we assumed the mass flux through (σ,β) grid cells to be constant in the streamwise direction, within the measurement range. Therefore, the product of u and $H + \eta$, and the product of SSC, u and $H + \eta$, are both independent of s. Although the latter assumption may be hampered by erosion/deposition processes, we assume that the suspended sediment flux remains constant over the limited time-span and along the short span of ADCP measurements in the s coordinate (typically < 50 m). The resulting water mass flux time-series, multiplied by $H + \eta$, were filtered with a cutoff frequency corresponding to 1.5 h, subsequently divided by $H + \eta$, and finally averaged in the s direction over the range that was covered during the measurements. Hereinafter, u denotes the mean flow component in the s-direction, obtained following the latter

procedure. The suspended sediment mass flux time-series were subjected to a similar procedure. On average, one complete transect covering both bifurcations took about 30 minutes. Thus, approximately four transects were navigated every hour at each bifurcating branch.

Figure 6.5 shows the temporal sequence of u with superposed secondary velocity field at bifurcating branches in Delta Apex during spring tides. Each subplot constitutes a one-hour average. The time span of the measurements is roughly from low water to high water. The velocity field shows the maximum velocity at the surface, with the core of the flow typically in the deepest part of the cross-section. In the northern branch, the core is slightly shifted towards the outer side, whereas in the southern branch the core remains above the deepest part of two main watercourses. The secondary velocity fields at each bifurcating branch depict well-defined cells spanning over the entire channel widths, with an opposite sense of rotation between the channels. It is interesting to note the rapid adaptation of the secondary flow field in the northern branch, since the geometry of the upstream bend suggests an opposite sense of rotation, relative to what is observed. The magnitude of cross- channel velocity components is always below 0.1 m s^{-1}. Observations during neap tides (not shown) portray the same pattern in the flow field.

Figure 6.6 shows the flow structure at First Bifurcation during neap tides. The figure covers a time span between two high water moments. The velocity core is located on the surface at both bifurcating branches, however, its position slightly differs between the branches. The secondary velocity field in both bifurcating branches exhibits the same pattern as in Delta Apex. In the southern branch, the secondary velocity field depicts also a zone at about $\beta = 0.2$ with reversed orientation of the flow, and complex velocity profiles, during part of the tidal cycle. This three-dimensional velocity pattern may be associated with the complex morphology along the cross-section. During spring tides (not shown), the flow structure is not significantly different, but a bi-directional flow pattern arises in the southern branch, which lasts for about three hours. At both locations, secondary flow fields are consistent with the curvature of the shorelines. The persistent secondary flow fields in response to local channel curvature may explain the cross-channel bed level profiles, which are deeper in the outer bends.

6.3.2 Vertical Profiles of Along-channel Velocity

The velocity field suggests that vertical profiles of the along-channel velocity component can be approximated with the logarithmic distribution with depth (see *Hoitink et al.*, 2009):

$$u\left(\sigma, \beta, t\right) = \frac{u_*\left(\beta, t\right)}{\kappa}\left(\ln\left(\sigma\right) + 1\right) + U\left(\beta, t\right), \tag{6.5}$$

where u_* is the shear velocity, $\kappa \approx 0.4$, and U is the depth-averaged velocity. Estimates of U and u_* were obtained from the linear regression of u against $\left(\ln\left(\sigma\right) + 1\right)/\kappa$. With these estimates, the roughness length z_0 results in

$$z_0 = \frac{H + \eta}{\exp\left(\frac{\kappa U}{u_*} + 1\right)}. \tag{6.6}$$

Spatial distributions of the tidally averaged shear velocity $\hat{u}_*$ (Figure 6.7) are similar between neap and spring tides at both bifurcating branches, and are consistent with the location of the
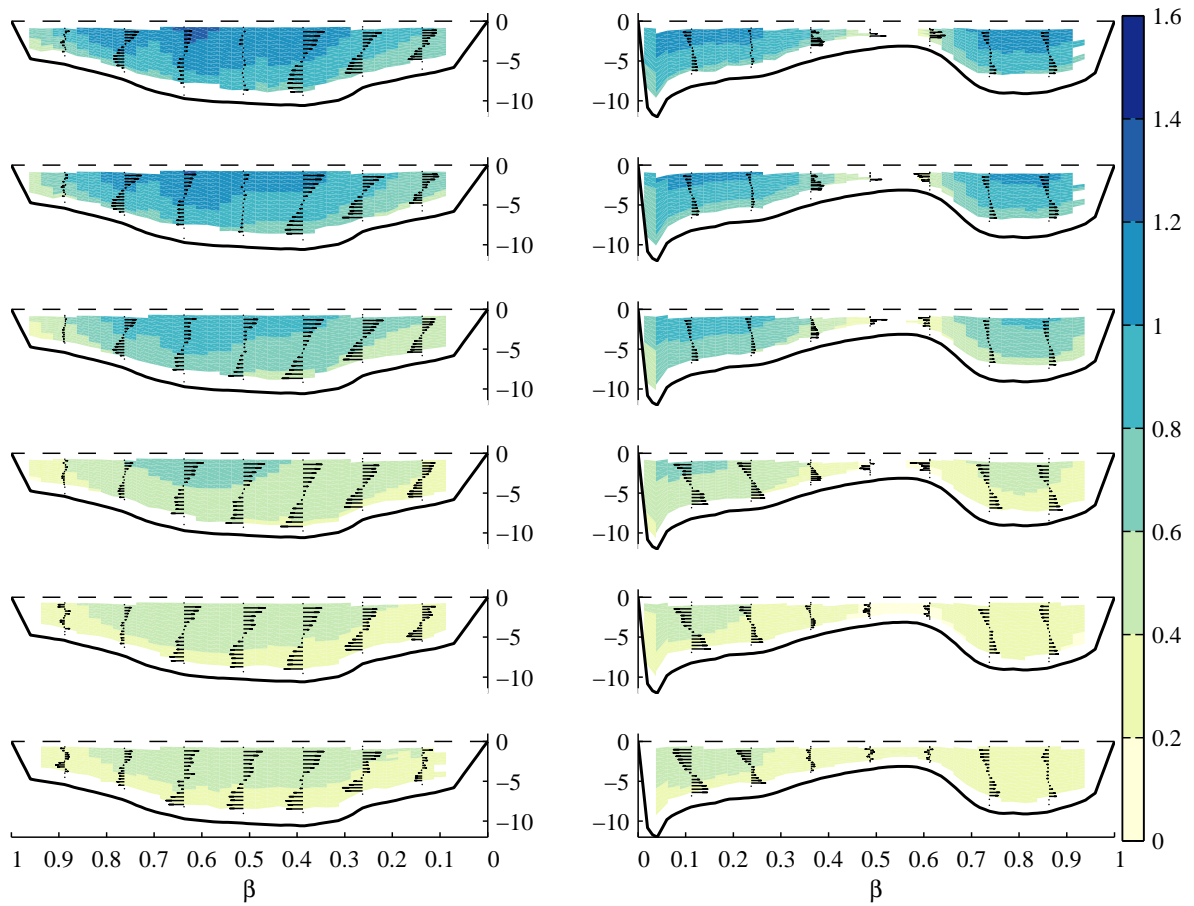
Figure 6.5: Temporal sequence of u (m s^{-1}) with superposed secondary velocity field at North (left) and South (right) transects at Delta Apex during spring tides as a function of depth and normalized width. The downstream flow direction is pointing into the paper. Dashed lines indicate water level whereas solid lines indicate the bottom. Bottom profiles have been linearly extrapolated towards the bank. The vertical coordinates indicate $z - H$ (in m).
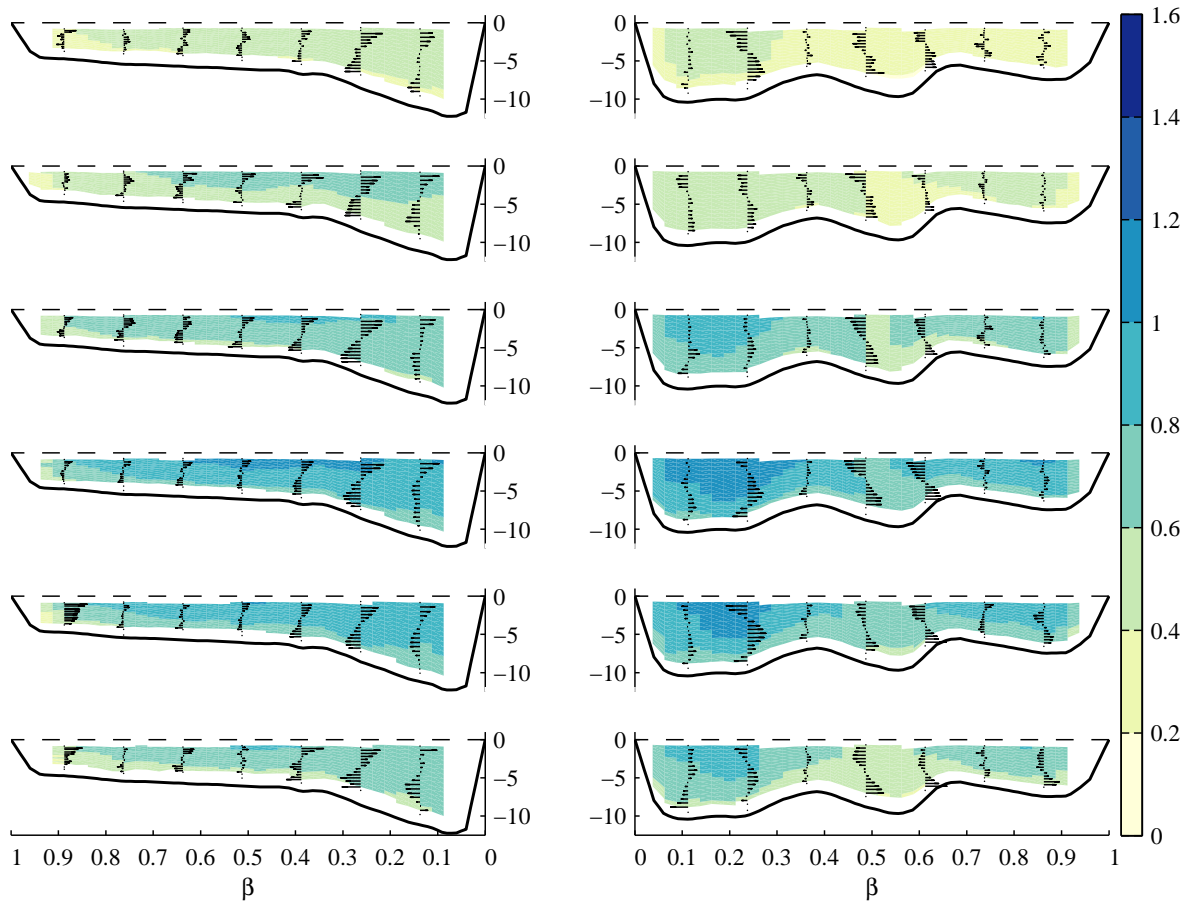
Figure 6.6: Temporal sequence of u (m s^{-1}) with superposed secondary velocity field at North (left) and South (right) transects at First Bifurcation during spring tides as a function of depth and normalized width. The downstream flow direction is pointing into the paper. Dashed lines indicate water level whereas solid lines indicate the bottom. Bottom profiles have been linearly extrapolated towards the bank. The vertical coordinates indicate $z - H$ (in m).
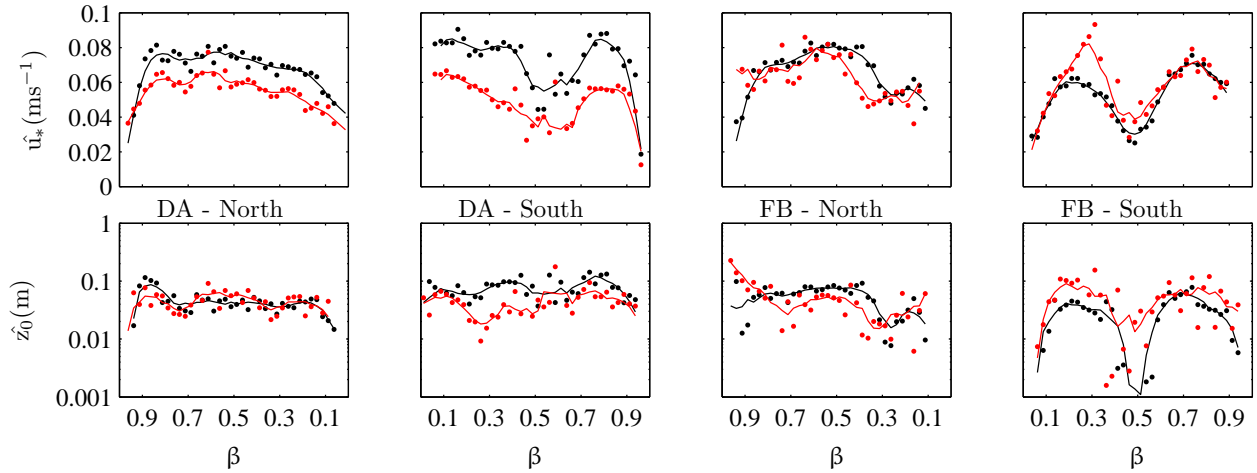
Figure 6.7: Tidally averaged shear velocity $\hat{u}_*$ obtained from the fit to each u profile, and roughness length $\hat{z}_0$ obtained by integrating equation (6.5) over time, both during neap (black) and spring (red) tides, at bifurcating branches in Delta Apex (DA) and First Bifurcation (FB). Smooth lines remove spatial variations of the order of $\beta = 0.1$.

velocity core. The magnitude of the velocity peak is smaller during spring tides, which may be associated to the lack of a sufficiently long averaging period, since this survey lasted for about seven hours. The tidal-mean roughness length $\hat{z}_0$ was obtained by integrating equation (6.5) over time (*Hoitink et al.*, 2009), assuming z_0 does not vary significantly throughout a tidal cycle. This is supported by the fact that flow reversals are limited at the two locations under study. The similarity in spatial distributions of $\hat{z}_0$-profiles between neap tide and spring tide over the northern branch is high. $\hat{z}_0$ profiles also depict an increase towards the outer side of the channel, which resembles the distribution of bed sediments shown in Figure 6.3. In the southern branch, $\hat{z}_0$ in the range $0.2 < \beta < 0.5$ is lower during spring tide than during neap tide, consistent with a decrease in $\hat{u}_*$ from $\beta = 0.1$ to $\beta = 0.5$.

Profiles of the shear velocity at both branches of First Bifurcation are similar at neap tide and spring tide (Figure 6.7). In the northern branch, $\hat{u}_*$ in the region $0.3 < \beta < 0.5$ is lower in magnitude during spring than during neap tide. In the southern branch, values of $\hat{u}_*$ at about $0.1 < \beta < 0.4$ are higher during spring tide than during neap tide. Spatial distributions during neap tide and spring tide reveal a region ($0.1 < \beta < 0.4$) with low magnitudes of $\hat{z}_0$ in the northern branch, which can be related to the grain size distribution of bed sediments (see Figure 6.3). In the southern branch, $\hat{z}_0$ during spring tide is higher than during neap tide. Finally, for $0.4 < \beta < 0.6$, $\hat{z}_0$ during spring tide is one order of magnitude lower than during neap tide, consistent with the decrease in $\hat{u}_*$.

6.3.3 Bed-load Transport Rates

Volumetric bed-load transport rates q_b were estimated based on the bed shear velocity determined above, and using the formulation provided by *van Rijn* (2007):

$$q_b \propto \left(\tau_* - \tau_{*,cr} \right)^{1.5}, \tag{6.7}$$
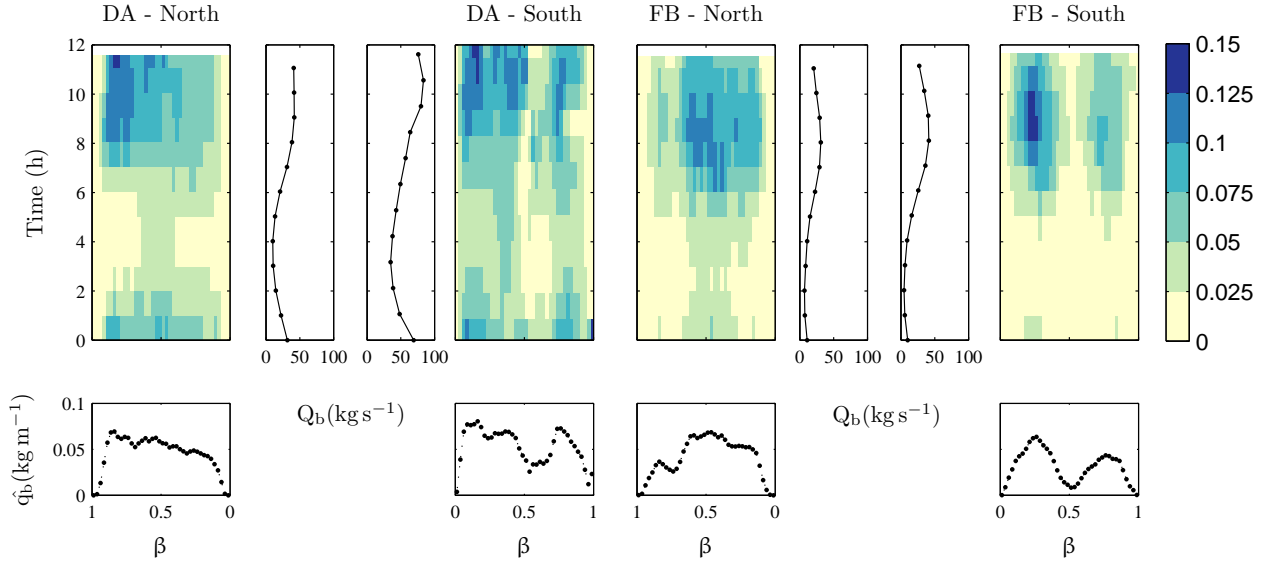
Figure 6.8: Spatiotemporal distribution of estimated bed-load transport rate q_b (kg m^{-1} s^{-1}) at northern (left) and southern (right) branches in Delta Apex (DA) and First Bifurcation (FB) during neap tides. Also shown are the width-integrated bed-load transport Q_b as a function of time, and tidally-averaged bed-load transport $\hat{q}_b$ as a function of normalized width. The vertical coordinate indicates time since the start of the measurements.

where τ_* is the dimensionless bottom shear stress and $\tau_{*,cr}$ is the critical Shields stress at the threshold of motion (*Parker et al.*, 2003), both dependent on D_{50}. Figure 6.8 shows spatiotemporal distributions of q_b (kg m^{-1} s^{-1}) at bifurcating branches at Delta Apex and at First Bifurcation, during neap tide. Temporal variations in q_b are mainly controlled by the semidiurnal tide, with very low transport rates during high water slack, and higher rates during the onset of the tide. The estimated width-integrated bed-load transport rate (Q_b) varies in between nearly zero up to a maximum of about 100 kg s^{-1}. Bedload transport at First Bifurcation is more equally divided over the distributaries than at Delta Apex, as depicted by the difference in magnitude between branches. Spatial distributions of the tidally-averaged bed-load transport rate, $\hat{q}_b$, resemble the spatial distributions of $\hat{u}_*$, despite the spatial variation in D_{50} across the channel.

6.4 Suspended Sediment Concentration

6.4.1 Spatiotemporal Distribution

Figure 6.9 shows spatiotemporal distributions of SSC (in mg l^{-1}) at bifurcating branches at Delta Apex during spring tides. Temporal variations in SSC are primarily controlled by the semidiurnal tide, with concentrations below 20 mg l^{-1} during high water and up to 180 mg l^{-1} during low water. The largest concentrations are typically found near the bottom, and values of SSC decrease towards the surface. The spatial distribution of SSC in the southern branch shows relatively high concentrations near the banks. In the northern branch, high concentrations are
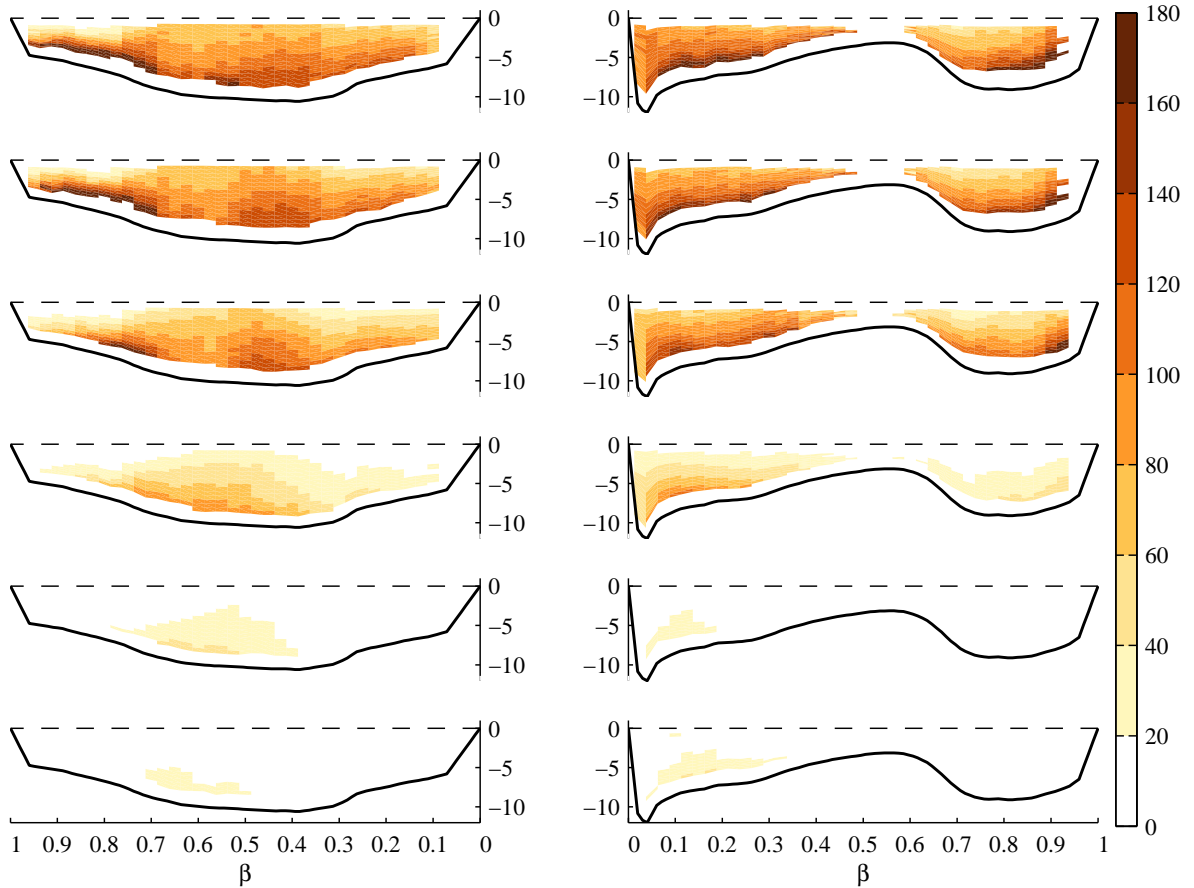
Figure 6.9: Temporal sequence of SSC (mg l^{-1}) at North (left) and South (right) branches in Delta Apex during spring tides as function of depth and normalized width. Dashed lines indicate water level whereas solid lines indicate the bottom. Bottom profiles have been linearly extrapolated towards the bank. The vertical coordinates indicate $z - H$ (m).

also found in the middle and towards the outer side of the channel. The spatial distribution of SSC is linked to the general secondary circulation pattern (see Figure 6.5). During neap tides (not shown), due to the smaller tidal range, the dynamics is highly reduced, with relatively high concentrations (> 50 mg l^{-1}) at high water. The spatial distribution at neap tides remains the same as during spring tides, although in the southern branch it features a nearly uniform high-concentration region near the bottom.

Figure 6.10 shows SSC maps at bifurcating branches for First Bifurcation, during neap tides. The largest concentrations appear towards the inner side of both bifurcating channels. In the southern branch, a region near the outer side of the channel also shows high concentrations near the bottom. The region $0.4 < \beta < 0.6$ shows very low concentrations. During the surveys, at this part of the cross section, we observed a strong decrease in the echo intensity of the ADCP, as well as the presence of oil at the water surface. It appears that the oil, or some other component in the water, may have had a significant influence on the absorption of the ADCP
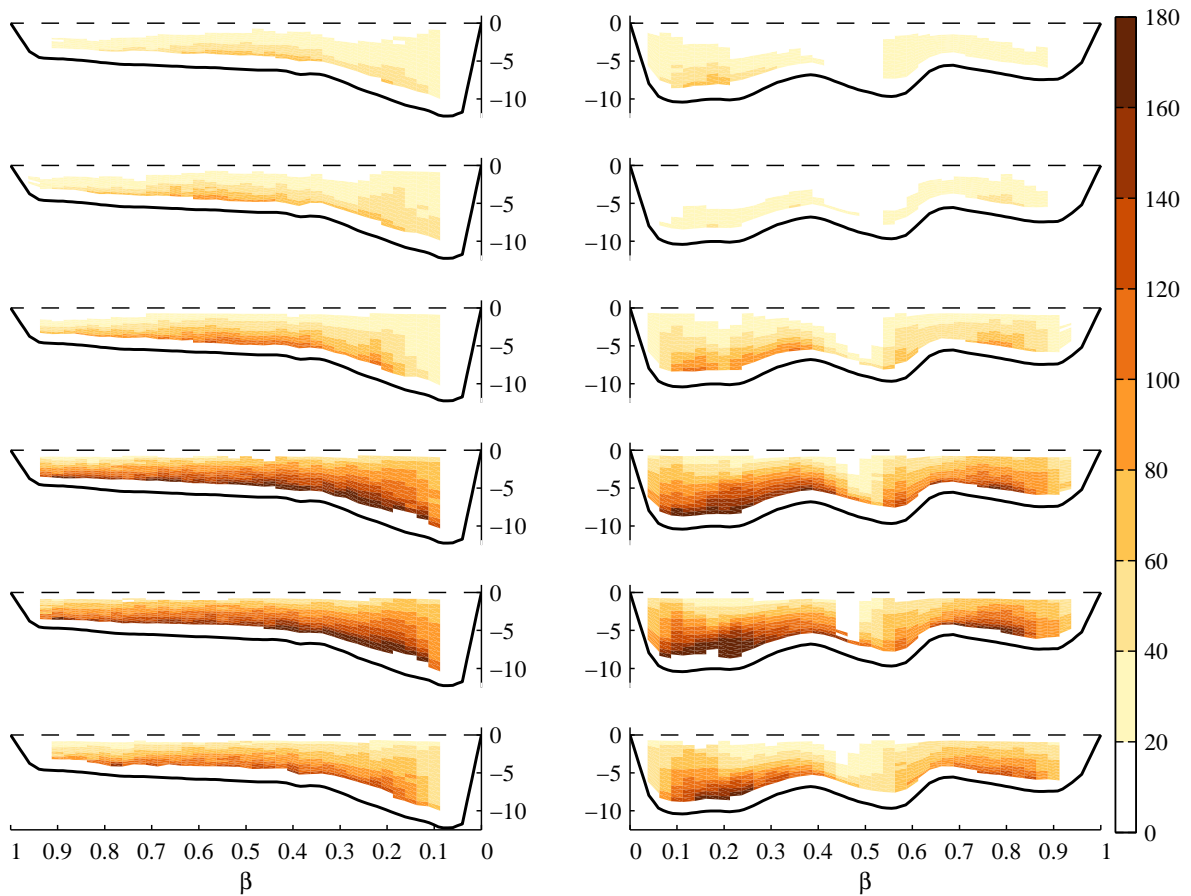
Figure 6.10: Temporal sequence of SSC (mg l^{-1}) at North (left) and South (right) branches in First Bifurcation during neap tides as function of depth and normalized width. Dashed lines indicate water level whereas solid lines indicate the bottom. Bottom profiles have been linearly extrapolated towards the bank. The vertical coordinates indicate $z - H$ (m).

acoustic waves, which has not been accounted for during the computation of the backscatter. Observations during spring tide (not shown) indicate a similar spatial distribution of SSC, except for poorly defined concentration profiles during the three hours that the bi-directional flow lasts.

6.4.2 Concentration Profile Fitting

A Rouse function was fit to the SSC profiles, assuming a balance between the diffusive and advective sediment flux in the vertical direction. This choice is supported by the fact that, in general, we found a strong positive correlation between shear velocity and depth-mean concentration. These relations showed no complex loops related to lag effects, which suggests that the concentration profiles are a direct response to bed shear stress. Accordingly, suspended

sediment concentration (c) profiles can be approximated by the power-law:

$$c\left(z\right) = c_r \left(\frac{z}{H-z}\frac{H-z_r}{z_r}\right)^{-p},\tag{6.8}$$

where c is the mass concentration (kg m^{-3}) at a height z (m) above the bottom, c_r is a reference concentration at z_r, with z_r typically assumed to coincide with the upper boundary of the bed-load layer, and p is the Rouse number. The Rouse number is defined as

$$p = \frac{w_s}{\kappa u_*} = \frac{w_f}{\alpha\kappa u_*},\tag{6.9}$$

where w_s is the settling velocity obtained from the fit (m s^{-1}), w_f is the fall velocity of the particles in suspension (m s^{-1}) and α is the inverse of the turbulent Prandtl-Schmidt number, defined as the ratio of sediment diffusivity k_s to momentum diffusivity k_z. The momentum diffusivity is given here by:

$$k_z = \kappa u_* z \left(1 - \frac{z}{H}\right).\tag{6.10}$$

Equation (6.8) can be rewritten in terms of the normalized depth, such that:

$$\ln\left(c\left(\sigma, \beta, t\right)\right) = -p\left(\beta, t\right)\ln\left(\frac{\sigma}{1-\sigma}\right) + f,\tag{6.11}$$

where f is a function that depends on the reference concentration c_r, the relative reference height σ_r, and p. Estimates of p, the Rouse number, are then obtained from a linear regression of $\ln(c)$ against $\ln(\sigma/1 - \sigma)$.

In the southern branch, $\hat{p}$ remains relatively constant throughout the cross section and decreases towards the outer side of the channel (Figure 6.11). Similar values of $\hat{p}$ are obtained in the northern branch at $0 < \beta < 0.6$, peaking at approximately $\beta = 0.8$, and decreasing towards the outer side of the channel. p-values (not shown) typically lie in the interval between zero and one, which is consistent with the results reported by *van Rijn* (1984b). The tidally averaged relative Root Mean Square Deviation (rRMSD) between the observation and the reconstructed profiles using equation (6.11), indicates that in both channels, on average, the error is 5% to 10% of the depth-averaged value, except for the profiles around $\beta = 0.8$ in the northern branch, where the error may increase up to 20%. At First Bifurcation, $\hat{p}$ values increase towards the outer side of the northern branch, while decreasing towards the banks. At the southern branch, profiles of $hatp$ show variations, which are consistent with variations in the bottom topography. The maximum error at both cross-sections amounts to 15%, but in general, rRMSD values remain below 10%.

6.4.3   Settling Velocity Estimates

From the estimates of p and u_*, spatiotemporal distributions of the settling velocity w_s were readily derived. The magnitude of the settling velocity depends crucially on the value of α. Using data from the ADCP calibration surveys, in-situ determinations of the mean particle
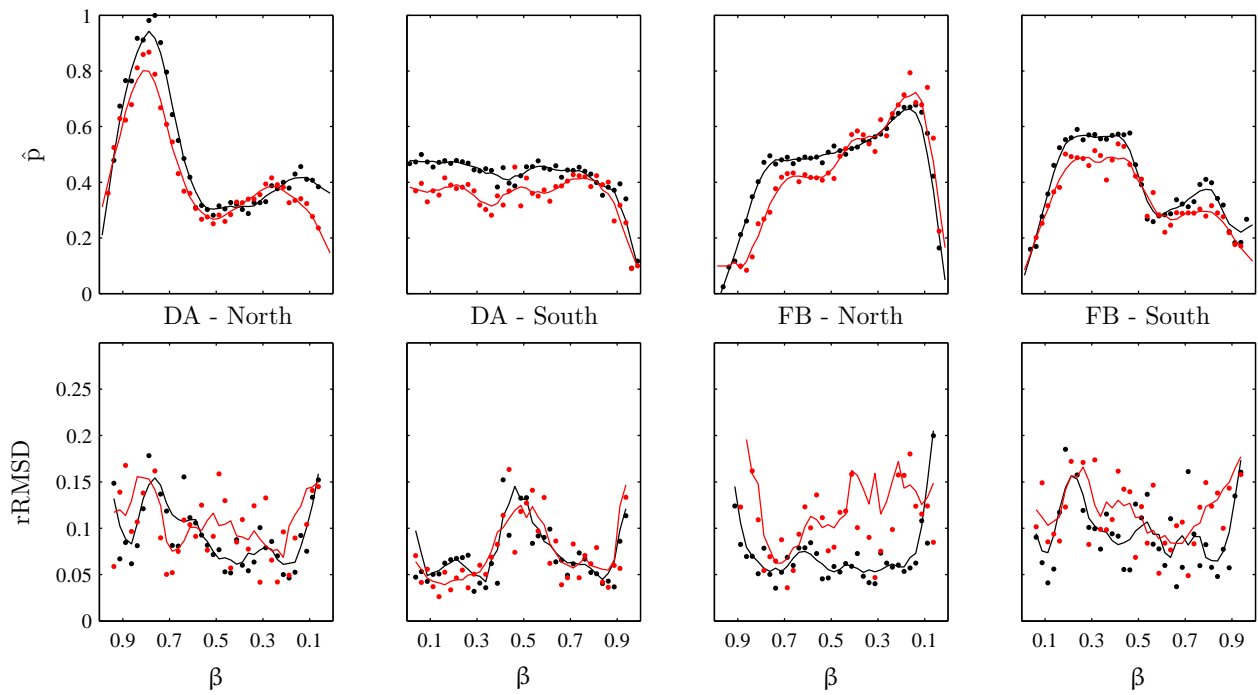
Figure 6.11: Tidally averaged Rouse number $\hat{p}$ obtained from the fit to each profile and relative Root Mean Square Deviation rRMSD between the observation and the reconstructed profile using equation (6.11), both during neap (black) and spring (red) tides. Smooth lines were used to remove spatial variations over β window of about 0.1.

size with the LISST instrument were used to compute the particle fall velocity (*Cheng*, 1997; *Camenen*, 2007):

$$\tilde{w}_f = \frac{\nu}{d} \left[\sqrt{\frac{1}{4}\left(\frac{a}{B}\right)^{2/M} + \left(\frac{4}{3}\frac{d_*^3}{B}\right)^{1/M}} - \frac{1}{2}\left(\frac{a}{B}\right)^{1/M} \right]^M, \qquad (6.12)$$

where ν is the kinematic viscosity of water (10^{-6} m^2 s^{-1}), d is the sediment diameter (m), $a = 32$, $B = 1$, $M = 1.5$, and d_* is the dimensionless particle size. The latter is defined as

$$d_* = \left(\frac{g\Delta\rho}{\rho\nu^2}\right)^{1/3} d, \qquad (6.13)$$

where g is the gravitational acceleration (9.81 m s^{-2}), ρ is the density of water (1000 kg m^{-3}) and $\Delta\rho = \rho_s - \rho$ is the apparent density, with ρ_s the density of the suspended material. Volume concentration V measured by the LISST can be used with in-situ determinations of mass concentration to compute the apparent density (*Gartner and Carder*, 1979; *Mikkelsen and Pejrup*, 2001):

$$\Delta\rho = \rho_s - \rho = \frac{M_s}{V}, \qquad (6.14)$$

where M_s is mass concentration in water samples. Equation (6.12) is based on the two asymptotic functions of the drag coefficient for low and high Reynolds numbers, and is valid for particles of different shape and roundness (*Camenen*, 2007).

Figure 6.12 shows time series of w_f, the depth-averaged $\tilde{w}_f$, computed with in-situ LISST data obtained at three locations at Delta Apex (see Figure 6.2). The mean particle size ranges from 100 to 150 μm and the apparent density ranges from 900 to 1500 kg m^{-3}. Values of w_f show a significant variation in time that is well correlated with the tidal cycle. This confirms that tidal resuspension processes govern the dynamics of suspended sediment transport at the locations under study.

Bulk estimates of α as inferred from the LISST instrument can be obtained from a direct comparison between w_f and the corresponding settling velocity w_s retrieved from the fit to the profiles, using equation (6.9) with $\alpha = 1$. Figure 6.13 shows the bulk estimates of α and time-series of w_f and $\langle w_s \rangle$, obtained by averaging over a suitable width over which the in-situ measurements were taken. Bulk estimates of α yield values greater than one and differ between channels at Delta Apex: 2.36 for the northern branch, and 1.26 and 1.59 for the two locations in the southern branch. We performed the same analysis with the measurements at First Bifurcation (not shown): estimates of α yield 2.69 for the northern branch, and 1.29 and 1.46 for the two locations in the southern branch.

We computed spatiotemporal distributions of settling velocity derived from the concurrent fit to velocity and SSC profiles, using the estimates of α as described above (Figure 6.14). For the southern branches, the two estimates of α were averaged. During neap tides, estimates near the outer side of the northern branch are well correlated with flow strength. Maximum values of w_s reach 30 mm s^{-1}. For $\beta < 0.6$, w_s remains relatively constant throughout the tidal cycle. In the southern branch, spatial variations in w_s depict a zone of relatively low magnitude
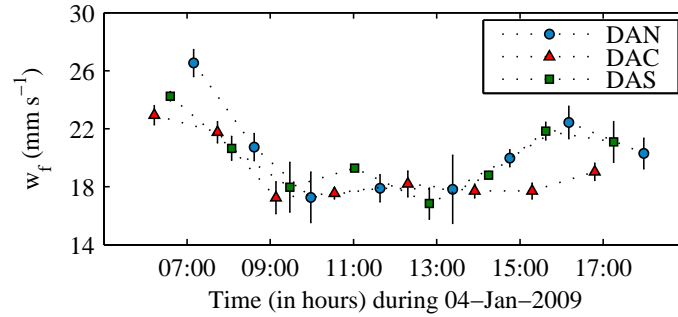
Figure 6.12: Particle fall velocity averaged over depth w_f, computed using equation (6.12) at locations in Delta Apex (see Figure 6.2). Error bars depict one standard deviation around the depth-mean value.
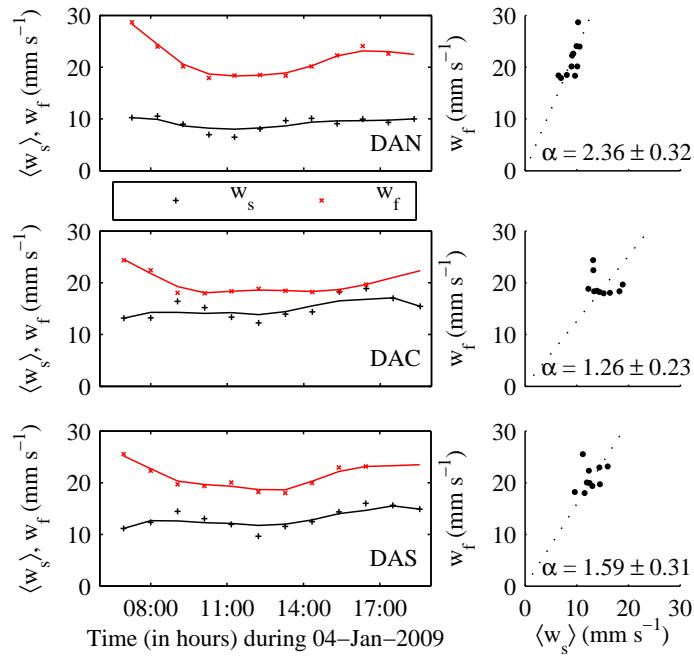
Figure 6.13: Left: time series of w_f derived from LISST measurements and corresponding $\langle w_s \rangle$ derived from the fit to the profiles and averaged over a suitable width that spans the location of the in-situ measurements, for North (top), Center (middle) and South (bottom) locations. Smooth lines were used to remove temporal variations of the order of 1.5 h. Right: bulk estimates of α from a direct comparison between the estimated settling velocities. The dotted line indicates the best-fit line forced through the origin, with a slope given by α.
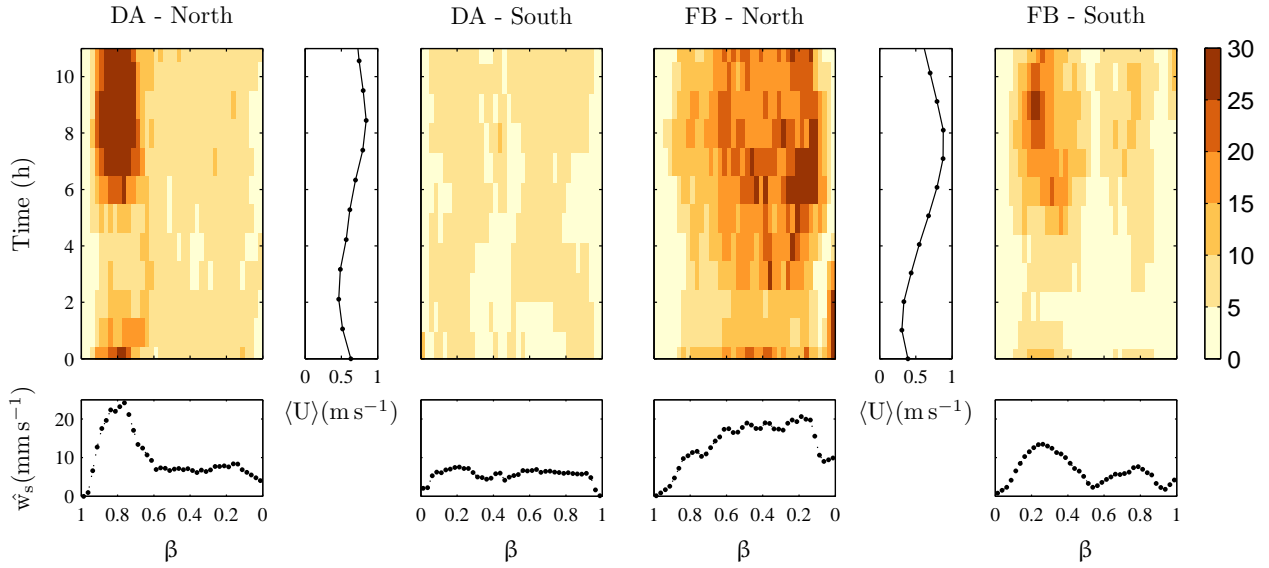
Figure 6.14: Spatiotemporal distribution of settling velocity w_s (in mm s^{-1}) at northern (left) and southern (right) transects at Delta Apex (DA) and First Bifurcation (FB) during neap tides. Also shown the width-averaged depth-mean velocity $\langle U \rangle$ as a function of time, and tidally-averaged settling velocity $\hat{w}_s$ as a function of normalized width. The vertical coordinate indicates time since the start of the measurements.

around $\beta = 0.4$, whereas temporal variations are rather limited. Tidally-averaged values depict contrasting spatial variations between bifurcating branches. At regions of relative constancy through time, w_s averages to about 5-7 mm s^{-1} in both channels, which is in the order of what may be expected for fine sands (*Cheng*, 1997). At First Bifurcation during neap tides, w_s estimates generally show a clear response to flow strength. w_s distributions show relatively large values across the northern branch, whereas at the southern branch, a zone of relatively low values arise at about $\beta = 0.4\text{-}0.5$.

6.5 Sediment Discharge Division

Total sediment discharge Q_s was calculated by adding Q_b to the product of u and c integrated over depth and width. Q_b is typically within 10% of the suspended sediment discharge. Water discharge was computed by integrating u over depth and width. We neglect the unmeasured areas near the surface and the channel boundaries, because extrapolation may introduce error and it is unlikely the blanking areas influence the overall dynamics. Figure 6.15 illustrates the relation between Q_s and Q for northern and southern branches at Delta Apex and First Bifurcation, during neap tides and during spring tides. The nearly closed loop in all discharge relations stems from the semidiurnal tide. During spring tide, the loop is stretched, although the opening of the hysteresis loop seems to remain the same, suggesting that the phase lag between Q_s and Q remain constant between neap tide and spring tide. At First Bifurcation, tidal effects are clearly stronger as both Q and Q_s approach zero during spring tides, in contrast to Delta Apex.

Table 6.2: Summary of parameters using Eq. (6.15). The variability denotes the standard error in the linear regression.

Location	Tide	$b \pm \delta b$		τ (min)	
		North	South	North	South
DA	Neap	2.9 ± 0.08	2.5 ± 0.06	-40	-60
	Spring	3.3 ± 0.05	3.4 ± 0.15	-50	-30
FB	Neap	2.9 ± 0.11	2.7 ± 0.03	-40	-60
	Spring	3.2 ± 0.08	3.1 ± 0.06	-40	-30

The non-linear behavior between Q_s and Q can be captured in the relation (*Bagnold*, 1966):

$$q_s(t) \propto \langle U \rangle (t - \tau)^b, \tag{6.15}$$

where $\langle U \rangle$ stands for the section- and depth-average flow velocity, τ is a time-lag function, and b is an empirically-derived exponent. Specific water discharge q and specific sediment discharge q_s were calculated as Q and Q_s per unit width, respectively. $\langle U \rangle$ was obtained by dividing q by width-averaged H. The time-lag in Eq. (6.15) may be explained by the relaxation model of *Groen* (1967), which states that the rate of increase or decrease of the suspended load at any time is proportional to the deficit or excess of the load with respect to an equilibrium value. Table 6.2 shows a summary of the parameters in Eq. (6.15), determined empirically by fitting a linear regression to the log-transformed variables. We computed the regressions for time-lags varying from -3 to 3 hours. The time-lag τ corresponds to the best-fit, which was based on the coefficient of determination R^2 (greater than 0.95 in all cases). All derived exponents exceed 2.5. b is consistently greater during spring tides, indicating that tides enhance the degree of nonlinearity in the sediment transport relation (Eq. 6.15). The time-lag remains nearly constant in the northern branches, whereas they alternate between neap and spring tides in the southern branches.

Figure 6.16 illustrates the intratidal variation in division of q, q_s and q_b over the bifurcating branches at Delta Apex and at First Bifurcation. At Delta Apex, more water and sediment discharge per unit width is directed towards the northern branch, which is most pronounced during high discharges. The division at First Bifurcation is more symmetrical, and depicts some crossovers regarding the branch that receives the largest specific discharge: for low discharges (high tide) a relatively larger share is directed to the northern branch and for high discharges (low tide) a larger share goes to the southern branch. The division functions of water and suspended sediment are qualitatively similar, being different from the division function of bed-load sediment transport.

The differences between locations cannot simply be explained by the ratio between the areas of the bifurcating channels, which are similar (Table 6.1). Upstream conditions may exert a strong control on the division functions. Delta Apex is subject to flow from a curved channel with a nonuniform depth. A deep section in the northern part of the channel increases the local transport capacity, enhancing the supply of water and sediment to the northern branch. Upstream conditions at First Bifurcation are different, featuring less curvature of the channel and a complex bed topography shaped by the intersected mid-channel bar.

The crossovers in dominance of one branch over the other may be partly related to in-
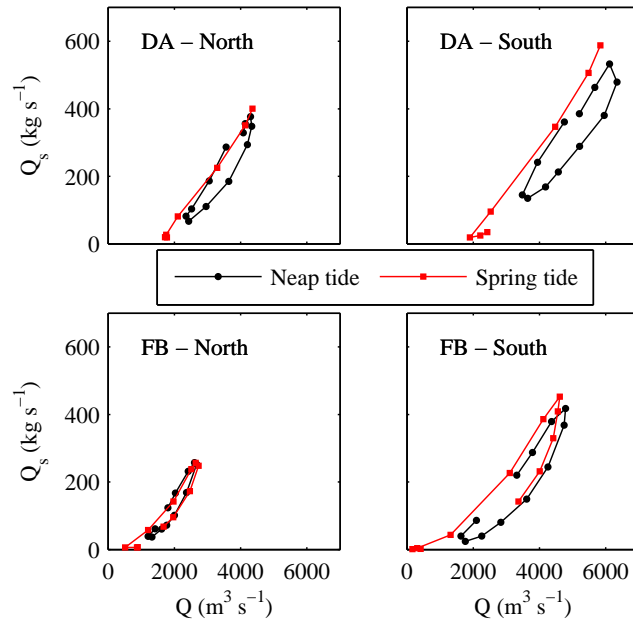
Figure 6.15: Total suspended sediment discharge Q_s as a function of water discharge Q at northern (left) and southern (right) branches at Delta Apex (top) and First Bifurcation (bottom) during neap and spring tides.
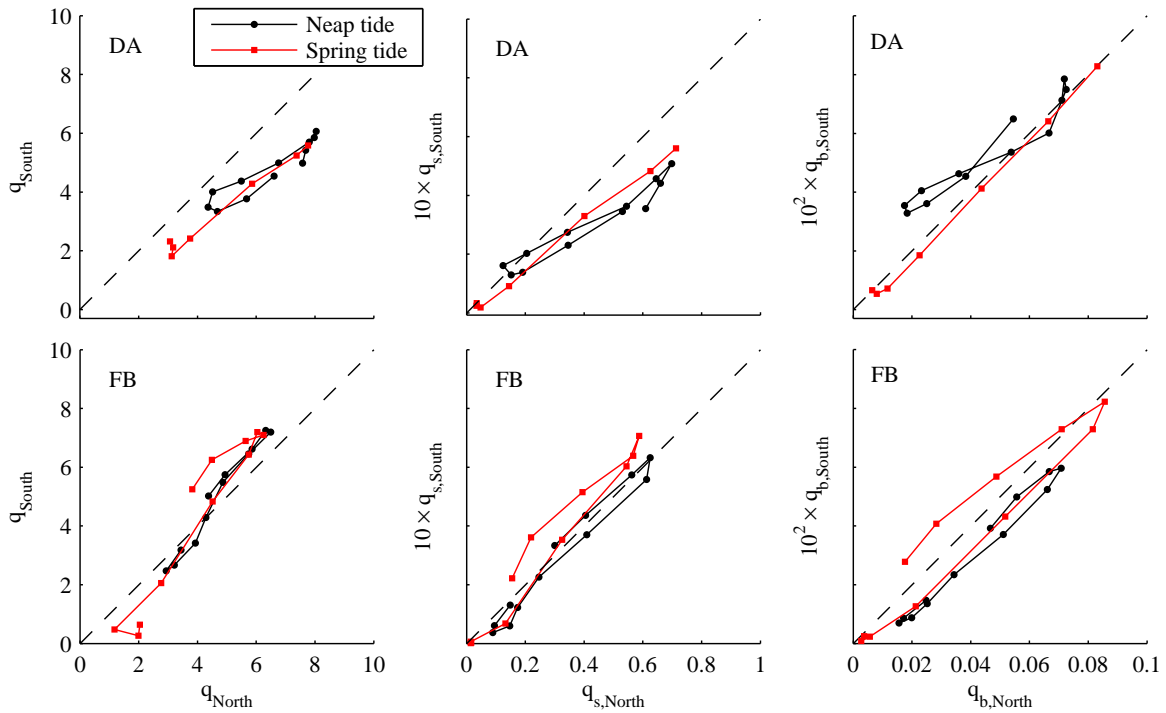
Figure 6.16: Division of specific water discharge q (in m^{2}s^{-1}), total sediment discharge q_s (in kg m^{-1}s^{-1}), and bed-load sediment transport q_b (in kg m^{-1}s^{-1}) between bifurcating branches at Delta Apex (DA) and First Bifurcation (FB) during neap and spring tides. The dashed line indicates the line of perfect agreement.

tratidal variations in water discharge and sediment transport, and small lag effects. Intratidal variations are related to complex non-linear interactions between the flow and the bathymetry, driving tidal asymmetry, which can exist in individual channels. In each branch at a bifurcation, the phase of tidal constituents can be slightly different, which will be manifest as a periodic asymmetry of the sediment discharge distribution. A 13-h period observation is too limited to distinguish between periodic and permanent asymmetries in the sediment discharge distribution, because the period of diurnal and fortnightly tidal constituents is much longer.

6.6   Discussion

The flow in the bifurcations at Delta Apex and First Bifurcation is characterized by counter-rotating, secondary-flow cells, which persist throughout the tidal cycle. The short length over which the secondary flow patterns of the downstream branches develop, which can be inferred from the channel curvature, imply that the parallel flows reaching the bifurcation are largely independent. If the secondary circulation would have the same orientation in both branches, the secondary circulation would cause sediment exchange between the parallel flow lanes. The two-cell structure inhibits such exchange, and causes the division of suspended sediment to be strongly dependent on local flow processes, largely governed by the tide. The adaptation length of the secondary flow, defined as the distance over which the secondary flow develops in response to the driving force due to inertial effects (*Johannesson and Parker*, 1989), appears to be within the range between the onset of the local flow curvature and the bifurcation point. Although laboratory experiments showed that the adaptation lengths for secondary flows are typically within a quarter of the meander length (*Zhou et al.*, 1993), *Johannesson and Parker* (1989) argued that in natural meandering rivers, the adaptation length is significantly reduced to about a tenth of a meander length. This suggests the secondary flow observed in the northern branch at Delta Apex has adapted long before entering the northern branch. It would be interesting to monitor the transition from a one-lane to a two-lane flow structure, which is where an exchange process of suspended sediment may occur. This transition may be gradual, and it is uncertain where this region exactly occurs.

A persistent feature in the bathymetry of the southernmost distributary channel is an elongated depositional area at about the middle of the channel, which separates two water courses along that channel. The map of the D_{50} (see Fig. 6.3) shows that patterns of medium to coarse sands follow the thalweg of the river, advancing through Delta Apex to the North and to the South, and leading to two well-defined sediment pathways along the southern channel. Despite that estimated bed-load transport rates are significantly smaller than the suspended sediment transport rates, these amounts of bed-load transport can be substantial for the development of bars, affecting the morphology of the bifurcations. *Crosato and Mosselman* (2009) developed a simple physics-based predictor to discriminate between river patterns on the basis of the mode m of the wavenumber describing the transversal oscillation of the river bed. Based on the linear model of *Struiksma et al.* (1985), they derive m from the ratio between the adaptation length for perturbations in the transverse profile of depth-averaged streamwise flow velocity and the adaptation length for perturbations in the cross-sectional river bed profile. Theoretically, $m = 1$ represents channels with alternate bars, whereas $m = 2$ indicates the presence of central bars; $m > 3$ would imply more complex transverse bed level profiles. The transverse mode is given

Table 6.3: Summary of transverse modes m obtained using Eq. (6.16). The brackets denote width averaging, the variability is given by one standard deviation around the width-averaged value.

Location	γ		$\langle H \rangle$ (m)		$\langle D_{50} \rangle$ (μm)		$\langle m \rangle \pm \delta\langle m \rangle$	
	North	South	North	South	North	South	North	South
DA	70	150	8.3	6.8	225	240	0.9 ± 0.2	1.8 ± 0.4
FB	60	80	7	8	220	240	0.5 ± 0.2	0.5 ± 0.1

by

$$m^2 = 1.7 \frac{\gamma^2}{\pi^2} \left(b - 3\right) \frac{u_*}{C\sqrt{\Delta D_{50}}}, \qquad (6.16)$$

where γ is the width to depth ratio of the channel, b is the same exponent as in Eq. (6.15), with $b > 3$, and $\Delta = \Delta\rho/\rho$. Using $C = \sqrt{g}\frac{U}{u_*}$ and width-averaged values for H and D_{50}, γ and all other terms in Eq. (6.16) are readily computed, and the results from Section 6.3.2 (cross-profiles of $\hat{z}_0$ and $\hat{u}_*$) can be employed to estimate m. Table 6.3 shows a summary of the results for each location during spring tides ($b > 3$), confirming the theory by *Crosato and Mosselman* (2009) for the location Delta Apex. The discrepancy at First Bifurcation may be partly related to the location of the transect, which is further downstream of the actual section where the mid-channel bar occurs. The non-linear theory by *Blanckaert and de Vriend* (2010) may predict lower values for the adaptation of the flow, consequently affecting the outcome of Eq. (6.16). However, the ratio between channel width and radius of curvature, central in the approach by *Blanckaert and de Vriend* (2010), can be considered too small for non-linear curvature effects as captured in their approach to be of any significance.

Although field estimates of the ratio between sediment to momentum diffusivity are scarce, several studies suggest considerable variation around unity (e.g *Whitehouse*, 1995; *Amos et al.*, 2010). Flume experiments by *Hill et al.* (1998) have shown α may vary between 0.35 and 3. Based on field measurements at two different tidal inlets in the Venice lagoon, *Amos et al.* (2010) found values between 0.3 and 3.5. Their estimations also showed variation between locations, with α consistently different from one. In general, a positive correlation is found between α and suspended sediment size, which critically depends on the flow conditions (*Nielsen and Teakle*, 2004). *van Rijn* (1984b) showed that a functional dependency exists between α and the ratio w_s/u_*, where α always exceeds w_s/u_*. The expression by *van Rijn* (1984b) was later corroborated by *Graf and Cellino* (2002) in experiments with a moving bed and bedforms. *Graf and Cellino* (2002) also showed that for experiments with a flat bed, α was typically lower than unity. Field determinations of the relation between α and the ratio w_s/u_* can be cast in power law relations with a wide range of exponents (e.g *Whitehouse*, 1995; *Kawanisi and Yokosi*, 1997; *Hill et al.*, 1998; *Rose and Thorne*, 2001). Our observations provide field evidence showing α can exceed unity significantly for a moving bed, sandy environment, which is in qualitatively agreement with findings in the existing studies. The correlation between α and the ratio w_f/u_* was, however, only weak ($R^2 = 0.21$ based on six observations). To some extent, our bulk estimates of α can be impacted by the inexact collocation of the measurements. Current research is focusing on rigid deployments with upward looking ADCPs (*Vermeulen et al.*, 2011),

which may provide refined field-estimates of α, as the ADCPs yield simultaneous, co-located estimates of flow velocity and suspended sediment concentration.

Despite the process of suspended sediment transport being intrinsically three-dimensional, modeling this process in rivers and estuaries can be accomplished by depth-integrated, two-dimensional models (e.g *Galappatti and Vreugdenhil*, 1985; *Wang*, 1992). The increased computational cost in adding the vertical dimension is often regarded as too high, in particular when the morphology is allowed to co-evolve with the flow (*Wang and Ribberink*, 1986; *Talmon*, 1992). In river bends and in bifurcations, the increased complexity of the flow due to secondary circulations may call for a fully three-dimensional approach. In the two bifurcations under analysis, we show that even though secondary circulation arises as a consequence of the curvature of the bifurcating branches, the rapid adaptation of the secondary flow causes the parallel flows at the bifurcation to act nearly independently. This flow pattern, inhibiting the exchange of sediment between flow lanes, suggests that in the Mahakam the three-dimensional effects of the suspended sediment are limited, and restricted to an upstream region.

6.7   Conclusions

Transects surveyed with a boat-mounted acoustic Doppler current profiler (ADCP) at bifurcating branches during a semidiurnal tidal cycle were used to characterize and quantify the sediment discharge division at two tidally-influenced river bifurcations. The ADCP collecting flow velocity and acoustic backscatter data was used to quantify bed-load and suspended load transport, adopting a recently introduced calibration procedure to transform acoustic backscatter into mass concentration of suspended sediments. We draw the following conclusions.

1. The concentration field at the bifurcating branches shows a direct response to the bottom shear velocity, indicating that wash-load is subordinate and the system can be considered alluvial. The lack of complex hysteresis loops or phase lags allows to determine spatiotemporal distributions of the settling velocity by combining the Rouse number and the shear velocity, determined from a fit to the concentration and the velocity profiles (respectively). Temporal variations in settling velocity are strongly correlated with the flow strength whereas spatial variations can be readily linked to variations in median grain size of the bottom sediments.

2. Vertical profiles of suspended sediment concentration feature a Rouse distribution. Although the settling velocity is predictable, complexity is introduced by the fact that the ratio between momentum diffusivity and sediment diffusivity is significantly different from unity, which is a common assumption for Rouse profiles. The bulk estimates of the latter quantity qualitatively agreed with results reported in studies focusing on moving bed, sandy environments, which show that the ratio is generally greater than unity, and increases with the ratio between settling velocity and shear velocity.

3. The flow in the bifurcating branches is characterized by counter-rotating, surface-convergent secondary flow cells, which persist throughout the entire tidal cycle. The secondary flow structure suggests the parallel flows approaching the bifurcation act largely independently. This two-cell structure inhibits the exchange of suspended sediment that would occur in

case the cell would stretch over the full width of the feeding channel. The division of suspended sediment primarily depends on the upstream transverse profile of the suspended sediment concentration, which is in turn dependent on geometrical factors such as upstream curvature. Based on our analysis, the three-dimensional effects of the suspended sediment dynamics at the two tidally-influenced bifurcations presented here are shown to be limited.

4. Bed-load transport rates estimated on the basis of the shear velocities and the median grain size remained nearly within 10% of the suspended sediment load. The total suspended load depicts a non-linear relation with the flow, with the degree of nonlinearity increasing during spring tides. Time-lags occur in all cases. The division of total sediment discharge per unit width follows closely the division of specific water discharge, which is different from the division of bed-load sediment. In general, a greater specific discharge was directed towards the northern branch at Delta Apex, whereas the division remained relatively equal at First Bifurcation. These results were attributed to the characteristics of the flow inherited from the upstream region.

Chapter 7

Hydraulic Geometry

Abstract: Channel geometry in tidally-influenced river deltas can show a mixed scaling behavior between that of river and tidal channel networks, as the channel forming discharge is both of river and tidal origin. We present a method of analysis to quantify the tidal signature on delta morphology, by extending the hydraulic geometry concept originally developed for river channel networks to distributary channels subject to tides. Based on results from bathymetric surveys, a systematic analysis is made of the distributary channels in the Mahakam Delta (East Kalimantan, Indonesia). Results from a finite-element numerical model are used to analyze the spatial variation of river and tidal discharges throughout the delta. The channel geometry of the fluvial distributary network scales with bifurcation order, until about halfway the radial distance from the delta apex to the sea. In the seaward part of the delta, distributary channels resemble funnel shaped estuarine channels. The break in morphology, which splits the delta into river- and tide-dominated parts, coincides with a break in the ratio between tidal to fluvial discharges. Downstream hydraulic geometry exponents of the cross-sectional area show a transition from the landward part to the seaward part of the delta. The numerical simulations show that the tidal impact on river discharge division at bifurcations increases with the bifurcation order, and that the variation of river discharge throughout the network is largely affected by the tides. The tidal influence is reflected by the systematic variation of downstream hydraulic geometry exponents.

7.1 Introduction

7.1.1 Hydraulic Geometry Concept Applied to Deltas

Hydraulic geometry (HG) is a set of empirically derived power-law relations between the channels' width, mean depth, and mean flow velocity, and the discharge conveyed by the channel (*Leopold and Maddock*, 1953). In river deltas, channel geometry scales according to the downstream HG relation $\log A \sim \beta \log Q$, where A is channel cross-sectional area, Q is water discharge conveyed by the channel, and β is an exponent typically lying in between 0.8 and 1.2 (*Edmonds and Slingerland*, 2007). In tidal systems, the exponent β often shows the same range of variation, but the tidal prism or peak tidal discharge is used instead of a discharge with a constant frequency of exceedance (*Friedrichs*, 1995; *Rinaldo et al.*, 1999; *D'Alpaos et al.*, 2010). Channel geometry in tidally-influenced river deltas can show a mixed scaling behavior between that of river and tidal channel networks, as the channel forming discharge is both of river and tidal origin. As a consequence, tidal processes play a prominent role in the morphological evolution of tidally influenced river deltas (*Geleynse et al.*, 2011), which may also have an impact on the response of the delta to permanent changes in river discharge (*Edmonds et al.*, 2010) and ultimately on its evolutionary structure (*Wolinsky et al.*, 2010). Although tidal effects on delta morphology can be studied by adopting a process-based morphodynamic modeling approach (*van Der Wegen et al.*, 2011; *Geleynse et al.*, 2011), studies on HG relations may help to acquire a synoptic insight into the morphology of delta channel networks affected by tides, and provide the basis for idealized models of delta evolution (e.g. *Kim et al.*, 2009).

In this chapter we show that the traditional tool of hydraulic geometry can be used to map tidal hydrodynamic processes onto a delta network, which can bridge the gap between physical oceanographic research on tides and the geological literature on river deltas. Traditionally, researchers use tidal amplitude or tidal prism to quantify the tidal influence on a delta (e.g. *Syvitski and Saito*, 2007). However, to asses the degree in which channel morphology is influenced by the tidal motion throughout a delta, which may be used to improve the common classification based on the tripartite division between river-, wave-, and tidally-dominated deltas (*Galloway*, 1975), a more objective and reliable set of metrics is required. Hydraulic geometry provides a set of relations for describing the dominant controls over delta channels synoptically, linking explicitly process and form.

Inside a delta channel network, bifurcations are key elements controlling the division of water and sediment discharge over downstream channels. Flow division at river bifurcations has been investigated intensively with theoretical models (*Wang et al.*, 1995; *Bolla-Pitaluga et al.*, 2003), with numerical models (*Lane and Richards*, 1998; *Dargahi*, 2004; *Zanichelli et al.*, 2004; *Kleinhans et al.*, 2008), and on the basis of flume experiments (*Bertoldi and Tubino*, 2007). In tidally-influenced deltas, however, tides intruding at the mouths of distributaries complicate significantly the processes governing flow division at tidal junctions (*Buschman et al.*, 2010; *Wu et al.*, 2010; *Sassi et al.*, 2011b). *Frings and Kleinhans* (2008) presented a comprehensive dataset on sediment transport and hydrodynamics at three tidal junctions in the River Rhine, showing complex variations in sediment transport during a flood wave. They observed a poor correlation between sediment fluxes and river discharge. In a tidal junction of the Sacramento River, *Dinehart and Burau* (2005b) observed that velocity patterns during ebb and flood can be highly asymmetrical. Asymmetry of the tides and tide-induced residual circulations may

exert a significant impact on the division of river discharge over the distributary channels in tidally-influenced deltas (*Buschman et al.*, 2010; *Sassi et al.*, 2011b). The inclusion of tides in the HG concept and the application to delta channel networks will allow quantification of the degree to which tides influence the variation of river discharge throughout the network (*Singh et al.*, 2003; *Dodov and Foufoula-Georgiou*, 2004; *Eaton and Church*, 2007).

7.1.2 Tidal Processes in River Deltas

Tidal rivers are intrinsically complex, as tidal propagation is influenced by river discharge and vice-versa. Tidal waves propagating upstream become distorted and damped, which is caused both by bottom friction and by the river flow (*Godin*, 1999; *Horrevoets et al.*, 2004; *Buschman et al.*, 2009). Adopting the hydrological perspective, tides impact the river flow by inducing fortnightly variations, which are generated by variation of the tidally-averaged friction over a spring-neap cycle. At spring tide, high levels of tidally-averaged friction act to block the river discharge, increasing water depth and allowing discharge waves to be admitted during neap tide. These effects of the spring-neap cycle can extend far upstream from the estuary (*LeBlond*, 1979; *Godin*, 1991b).

In tidal rivers, the along-channel tidally averaged friction is mainly balanced by a subtidal pressure gradient (*Buschman et al.*, 2009). As a consequence, river-tide interaction induces a water level setup, which becomes progressively larger in the upstream direction (*LeBlond*, 1979; *Godin and Martinez*, 1994). At a bifurcation, a mismatch may occur between the water level setups that would develop in the two channels if they would have been disconnected. The water level setup in the channel where river-tide interaction and the associated propensity for water level setup is largest will promote the allocation of river discharge to the other channel.

Tides can affect river discharge division in one other way. The Stokes transport, which is the drift associated with a traveling wave that can be calculated as the Lagrangian mass transport minus the Eulerian mean, can be different in two adjacent channels that join at a bifurcation. Based on an idealized model, *Buschman et al.* (2010) found that asymmetries in subtidal flow division at the apex of a tidal river splitting over two sea-connected branches were enhanced when one of the sea-connected branches is deeper or shorter. In their study, bed roughness differences resulted in the opposing effect. *Sassi et al.* (2011b) elaborated on the work by *Buschman et al.* (2010), showing that differences in water level setup may play a key role in the division of discharge at tidal junctions. The division of river discharge at tidal junctions leads to variation of the HG exponents, and helps to explain the complexity in HG relations of mixed river-tide dominated deltas.

Studies of estuarine morphology tend to focus on overtide generation to describe the unique geomorphological characteristics of tidal environments (e.g. *Wang et al.*, 1999). This stems from the fact that landscape-forming discharges in tidal systems are highly influenced by peak discharges, which are typically controlled by tidal asymmetry (*Lanzoni and Seminara*, 2002; *Fagherazzi et al.*, 2004). Tidal asymmetry is generally attributed to non-linear interaction of the main semidiurnal tide with itself (*Friedrichs and Aubrey*, 1988). Persistent asymmetrical tides may also be produced by the interaction of diurnal and semidiurnal constituents in tidal regimes where both semidiurnal and diurnal tides contribute significantly to the tidal motion (*Hoitink et al.*, 2003). *Friedrichs* (1995) indicated that in stable channels the minimum shear stress

τ_s necessary to maintain a net zero gradient in the along-channel sediment transport leads to a convergence point, from which τ_s decreases both seaward and landward. Downstream HG relations of the area of such channels will then exhibit exponents (β) greater than unity in flood-dominated systems, and values of β smaller than unity in ebb-dominated systems. *Rinaldo et al.* (1999) suggested that ebb/flood transitions in tidal channels are marked by a break in the slope of the HG relation of the area, which may be interpreted as downstream variation in β. This notwithstanding, we argue that processes such as differential water level setup driven by river-tide interaction (*Sassi et al.*, 2011b), which need weeks to develop rather than days, exert a strong control on the morphological evolution of tidally-influenced river deltas, via the re-distribution of river discharge at bifurcations.

Here we focus on the River Mahakam, which constitutes the major navigable river in East Kalimantan, Indonesia. The River Mahakam flows through a relatively flat basin characterized by a very mild slope. At about 150 km from the river mouth, an alluvial plain marks the transition to the upper reaches of the catchment, where a system of interconnected lakes with a total area of about 400 km^2 is located. Water level fluctuation induced by the tide has been observed upstream of the lakes region (*Hidayat et al.*, 2011). It has been suggested that tidal processes may have a dampening effect on the fluvial dynamics of the delta region, causing a characteristic progradation pattern (*Allen et al.*, 1977). Recently, the absence of discharge peaks was also ascribed to the non-flooding discharge regime resulting from the buffering effect of the lakes (*Storms et al.*, 2005; *Hidayat et al.*, 2011). While flood flows up to 5000 m^3 s^{-1} can cause a rise in water level up to five meters in the upper reaches, flood surges are virtually damped by the buffering effect of the lakes (*Storms et al.*, 2005; *Hidayat et al.*, 2012), which eliminates sudden and large variations in river discharge in the lower reaches of the river. Indeed, the lack of channel migration (*Allen et al.*, 1977) and the absence of channel avulsions (*Storms et al.*, 2005) support these two hypotheses, rendering the Mahakam delta channel network virtually fixed. The relatively constant river discharge in the downstream reaches of the Mahakam allows us to investigate the subtle processes of river-tide interaction, which are often obscured by short-term and high-magnitude tidal processes, and/or fluvial instability. Since the Mahakam river discharge typically fluctuates at time scales longer than a fortnight, the system can adjust to subsequent quasi-equilibrium states (in the order of months), greatly simplifying the complex dynamics that river-tide interactions impose.

7.1.3 Objective and Structure of This Chapter

This chapter aims to develop a method to quantify the tidal signature on delta morphology by applying the hydraulic geometry concept to a delta channel network. We describe the study area, data collection methods and the hydrodynamical model of the delta in Section 7.2. Section 7.3 presents the main results of the geomorphic analysis of the channel network and scaling of the hydrodynamics. Section 7.4 introduces the HG framework for channel networks affected by tides and presents the downstream HG relations based on selected cross-sections in the delta. Section 7.5 describes the mechanisms governing river discharge division, and the impact these mechanisms have on downstream HG relations of the cross-section area, and the mean flow velocity. We finalize this chapter with conclusions in Section 7.6.
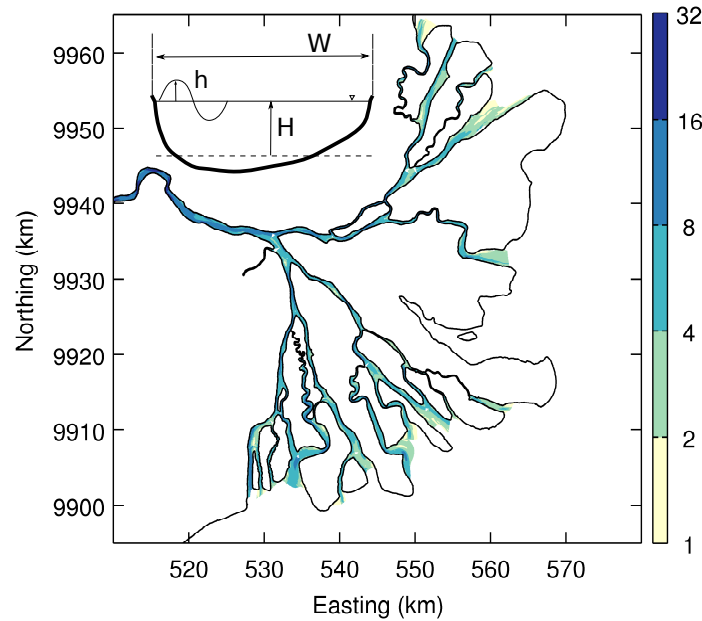
Figure 7.1: Bathymetry of the Mahakam delta channel network (modified after *Sassi et al.* (2011b)) in logarithm to base two scale. Easting and Northing coordinates correspond to UTM50M. Depth is in meters. The inset is a definition sketch of the geometry parameters of the channels in the model. Cross sectional area is represented by a time invariant area WH, where W is channel width and H is the width averaged depth, and a time varying area $W\eta$, where η is the water surface elevation. Water level variation includes fluctuations due to the tides, due to river discharge and due to river-tide interaction.

7.2 Mahakam Delta Channel Network

7.2.1 Site and Data Collection

The River Mahakam debouches into the Makassar Strait, forming a regularly distributed, fan-shaped delta (Figure 7.1). The delta channel network exhibits a quasi-symmetric planform of rectilinear distributaries and sinuous tidal channels. The two main fluvial distributary systems are directed SE and NE, and comprise eight and four outlets to the coastal zone, respectively. The tide-dominated inter-distributary zone allocates many tidal channels, with tidal channels occasionally connected to the fluvial system. Due to the high river discharge, the study area is generally subject to freshwater conditions. During extremely low flows, which may be related to El Niño Southern Oscillation such as during the drought in 1997, salinity intrusion can reach beyond the delta apex. In general, however, salinity intrusion typically reaches to about 10 km seaward from the delta apex (or 30 km from the coast). Depending on the river discharge, the tidal wave can propagate up to 190 km from the river mouth. The tidal regime in the Mahakam delta is mixed, mainly semidiurnal.

Several water level gauges and two horizontally deployed acoustic Doppler current profilers

(H-ADCPs) were operational for about 18 months at locations along the river and in the delta. The two H-ADCPs were deployed upstream of the lakes region and next to the delta apex. The gauges recorded one minute averages of water level fluctuations measured at 1 Hz every 15 minutes, whereas the H-ADCPs yielded a 10 minute average of flow velocity, also at 1 Hz, every 30 minutes. Array data of flow velocity collected with the H-ADCP were converted to river discharge using calibration data from conventional shipborne ADCP discharge measurements. Upstream of the lakes, where tidal influence was found to be negligible, eight 6 h ADCP campaigns covered a wide range of flow conditions (*Hidayat et al.*, 2011). Close to the delta apex, where tides dominate, seven 13 h ADCP campaigns were carried out spanning high- and low- flow conditions, during spring tide and neap tide (*Sassi et al.*, 2011a).

Cross-river depth profiles with an interspacing of about 200 m were obtained with a single-beam echo-sounder at locations spanning the river, its tributaries, the three lakes and the delta region. A bathymetric map of the channels was produced by linear interpolation of the transect data of bed elevation, previously projected onto a curvilinear grid based on the channel centerline (*Legleiter and Kyriakidis*, 2007). The resulting bathymetry has been simplified by omitting all tidal channels that were disconnected from the fluvial network. The bathymetry of the delta (Figure 7.1) shows channels with variable depths, ranging between 5 m and 15 m, with occasional deep spots usually located at bends, junctions and constrictions, and very shallow areas often situated in the regions around bifurcations. The distributaries become increasingly shallow seaward whereas the river has an average depth of around 15 m.

7.2.2 Hydrodynamical Model

The hydrodynamics driven by river discharge and tides was simulated using a depth-averaged version of the unstructured mesh, finite-element model SLIM (Second-generation Louvain-la-Neuve Ice-ocean Model, www.climate.be/slim). The Mahakam delta, the coastal zone and the lakes region were represented by a 2D computational domain, which was connected to a 1D computational domain representing the river and several tributaries. GEBCO (www.gebco.net) database information was used in the continental shelf and the Makassar Strait, whereas measured bathymetry was used in all other domains. Tides from the global ocean tidal model TPXO7.1 (http://volkov.oce.orst.edu/tides) were used to force the model at open boundaries, located far away from the delta and stretching across the entire Makassar Strait. Discharge series obtained from H-ADCP velocity data were used to force the model at the upstream boundary. A rainfall-runoff model calibrated with discharge data from the main subcatchment provided discharge series at the boundaries where tributaries connect to the modeling domain. Extremely small river bed slopes in lowland areas cannot directly be retrieved from a bathymetric survey, because of a lack of an absolute vertical reference with a sufficiently high accuracy. Therefore, the slope of the river was obtained following the approach described in *Buschman et al.* (2009); when concurrent water level and discharge data are available, as in the case of the discharge monitoring station, the river bed slope can be inferred from conservation of momentum. A regional, along-channel momentum balance was set up for a control volume bounding the discharge station and a pressure sensor located further downstream. By collecting additional discharge observations at the downstream point and using the continuous estimates from the discharge station, the bottom slope was readily estimated.

A calibration procedure in which the model domain was decomposed in three regions (*de Brye et al.*, 2011), provided the bottom friction coefficients. Model calibration was performed by comparing model results with water level time-series at three locations in the delta, and with flow measurements obtained at the downstream discharge station. As a form of model validation, we have compared model results with discharge division measurements at the two principal bifurcations in the delta, during spring tide and during neap tide (*Sassi et al.*, 2011b). More details of the model implementation can be found in *de Brye et al.* (2011) and in *Sassi et al.* (2011b).

The computational mesh of the Mahakam delta channel network contains approximately 70% of the elements in the model's computational domain. The model does not include intertidal storage areas such as tidal flats or salt marshes, which may potentially affect the estimation of peak flows. Remote sensing images show the total intertidal area in the Mahakam Delta is very limited. Intertidal areas that once existed, when the system was still natural, have been subjected to land reclamation and are now excluded from the channel network. This ensures that the omission of intertidal areas in the model has limited impact on the model calculations.

7.3   Scaling of the Channel Network

7.3.1   Morphology

Banklines were obtained from remote sensing images, from maps and from the bathymetric survey. Channel center lines were obtained as the mean location line between the bank lines (Figure 7.2) and re-sampled to achieve a constant resolution of 100 m. At each cross-section, the width and mean water depth were computed. Tidal channels attached to the fluvial network were not considered in the analysis. Figure 7.3 shows that mean water depth is inversely correlated to width, for channels in distributary outlets going from North to South. The inverse relation weakens when going to the South, because channels in the South are used for navigation and are subject to continuous dredging activities. Despite some variability across the channels, the distributaries show a clear relationship between depth and width.

A representative channel geometry was computed as the average depth and width over all channels at a given radial distance from the delta apex, and the cross-sectional area and aspect ratio derived from those parameters. Variability across the channels is more apparent near the delta apex than near the coast, because the number of averaged channels increases from the apex to the sea. Figure 7.4 shows the spatial development of the representative channel geometry from the delta apex towards the sea, as a function of the normalized along-channel distance, s/L, where s represents the along-channel distance from the delta apex and L is the distance to the sea along the longest distributary. The representative channel width shows two well-defined regions; a third region arises as the link between these two regions. In the region bounded by an arc with a radius of about 10% of the total radial distance to the apex, the width varies little around a mean value of 1000 m. Within a distance roughly between 10% to 50% of the total radial distance between the apex and the coast, the width oscillates between 400 m and 1000 m. In the remainder of the delta, the width features an increasing trend towards the sea. The representative channel depth oscillates around an average value of about 7 m over the first half of the total radial distance, whereas it shows a decreasing trend
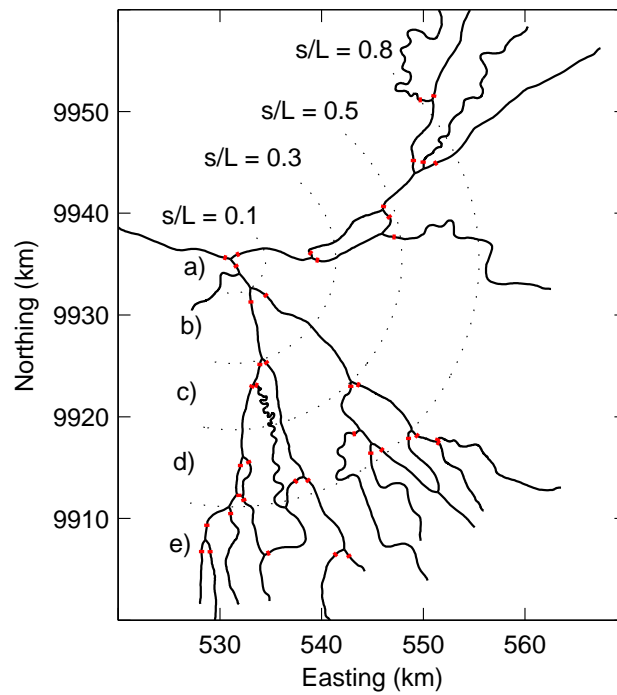
Figure 7.2: Centerlines of the Mahakam delta channel network. Dotted lines indicate arcs through the main bifurcations, with a constant radial distance to the delta apex; a through e label radial segments, s is the channelized distance from the delta apex and L the attained distance to the sea along the longest distributary. Also indicated in red color all cross-sections near each bifurcation for which discharges and water levels obtained with the numerical model were stored. The HG analysis is based on these cross-sections.

144
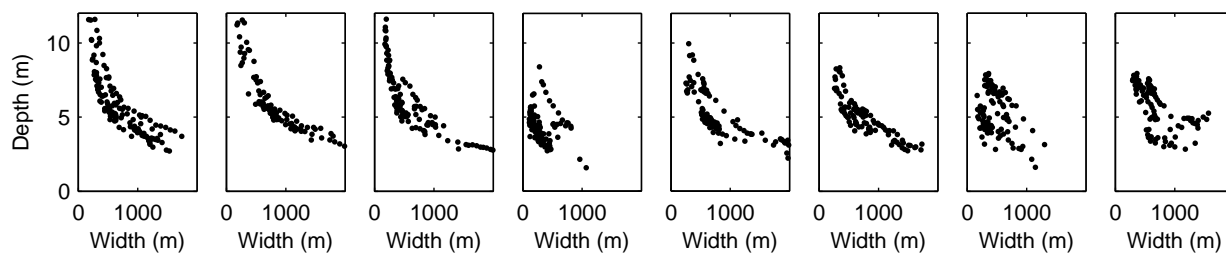
Figure 7.3: Mean depth as a function of channel width for eight distributaries of the Mahakam delta, from North (left) to South (right).

closer to the coast. The representative channel area decreases from the delta apex up to about the central radius in the delta, and increases seaward beyond that arc. The best-fit line to the representative channel area, drawn in the bottom left panel of Fig. 7.4, is obtained from two linear functions in semi-logarithmic space (*Guo*, 2002). The representative aspect ratio oscillates around a constant value in the landward half of the delta, and increases seaward in the remaining part.

In the landward half of the Mahakam delta, the scaling behavior of the representative channel geometry coincides with the scaling observed in river deltas (*Edmonds and Slingerland*, 2007). When made dimensionless, the representative channel area as a function of the bifurcation order follows the same trend as the data presented by *Edmonds and Slingerland* (2007). In the seaward part of the delta, the representative channel geometry resembles that of funnel shaped estuarine channels (*Davies and Woodroffe*, 2010), reflecting the importance of the tidal discharge relative to the river discharge in channel forming processes (*Fagherazzi and Furbish*, 2001). The Mahakam delta reveals a sharp transition between the river-dominated and tide-dominated domains (see Fig. 7.4). This regime change occurs at $s/L = 0.55$, which is based on matching two linear functions in log-space.

7.3.2 Hydrodynamics

A Continuous Wavelet Transform, using a Morlet mother wavelet, was applied to the modeled time-series of water discharge obtained at cross-sections selected in both downstream branches of each bifurcation in the delta (see Fig. 7.2). Amplitudes of quarterdiurnal, semidiurnal and diurnal fluctuations were readily obtained, since spectrograms generally feature a well-defined gap between the tidal and subtidal band (*Sassi et al.*, 2011b). The concept of tidal species is introduced, to denote a group of tidal constituents with frequencies corresponding to a frequency band, as opposed to a unique frequency (*Jay*, 1997). To distinguish between fortnightly fluctuations associated with river-tide interaction (*Buschman et al.*, 2009) and monthly or seasonal fluctuations, we isolated the fortnightly variation by delimiting the fortnightly frequency domain in the normalized global wavelet power spectrum. Hence, fortnightly amplitudes corresponded to wavelet power concentrated in a band with periods roughly in between 10 to 20 days.
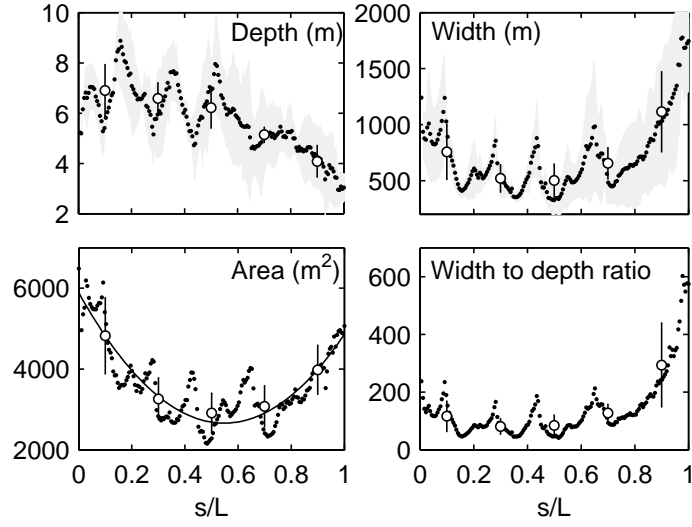
Figure 7.4: Spatial variation of the representative channel geometry from the delta apex to the sea, computed as the mean over all distributaries. The shaded area indicates one standard deviation. Circles denote the cluster means, binned as a function of s/L; error bars denote one standard deviation. Bins are uniformly distributed between 0 and 1 with a bin-size equal to 0.2. The best-fit line through the representative channel area is obtained by matching two linear functions in semi-logarithmic space.

Accordingly, water discharge Q at each cross-section can be decomposed as:

$$Q = Q_r + Q_t, \tag{7.1}$$

where Q_r is the river discharge and Q_t is the tidal discharge. The tidal discharge is defined here as:

$$Q_t(t) = \sum_l Q_l(t), \tag{7.2}$$

$$Q_l(t) = P_l(t)\cos(ilwt + \phi_l), \quad l = 1/14, 1, 2, 4,$$

where i is the imaginary unit, the subscript $1/14$ stands for a fortnightly period of the tide and 1, 2 and 4 denote diurnal, semidiurnal and quarterdiurnal tides, respectively, w is the angular frequency corresponding to a diurnal tide with an exact period of 24 h, ϕ represents the phase and P_l is the tidal discharge amplitude. We define P, the maximum tidal discharge amplitude at a given time, such that

$$P = \sum_{l=1/14,1,2,4} P_l. \tag{7.3}$$

Acknowledging that the tidal discharge at a given point and time is actually smaller, P can be considered to be a surrogate of the maximum astronomical tidal prism. The tidal prism is defined here as the volume of water between mean high tide and mean low tide. All quantities are averaged over the entire simulation period.
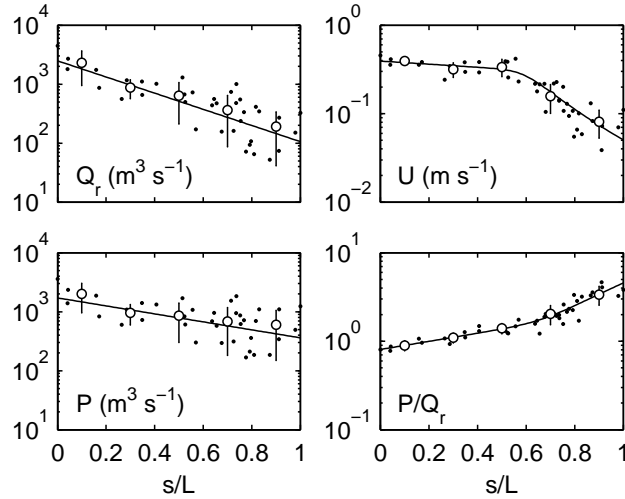
Figure 7.5: Spatial distribution of river discharge Q_r, mean flow velocity U, maximum tidal discharge amplitude P, and the ratio of tidal to fluvial discharge P/Q_r for locations of the selected cross-sections (see Fig. 7.2). Solid lines indicate the best-fit lines. Circles denote the cluster means, binned as a function of s/L; error bars denote one standard deviation. Bins are uniformly distributed between 0 and 1 with a bin-size equal to 0.2. Differences between the slopes computed using the original data and the clustered data remain within 5-10 %. The best-fit lines to U and P/Q_r are obtained by matching two linear functions in semi-logarithmic space.

Both P and Q_r show a seaward decrease in magnitude (Fig. 7.5). The scatter increases seaward because the flow is obtained at a limited number of cross-sections, which span a confined range of the spatial extent of the delta. The decrease in Q_r with distance to the delta apex reflects the partitioning of river discharge at the bifurcations. Conversely, the landward increase in P reflects the combination of tidal discharges at the bifurcations. Q_r decreases with distance to the delta apex faster than P decreases; the exponents in a power-law relation between Q_r and s/L and P and s/L are equal to -3.15 ± 0.53 and -1.56 ± 0.5, respectively, where the variability is given by the standard error in the linear regression. Mean flow velocity U, defined as the ratio between Q and A, and the ratio between tidal discharge and river discharge P/Q_r, remain nearly constant until $s/L = 0.58$ and $s/L = 0.65$, respectively, based on the intersection of two best-fit linear functions in log-space. From that point seaward, U and P/Q_r depict a decrease and increase in magnitude, respectively. Note that the location of the break-point in the hydrodynamics coincides fairly well with the location of a shift in scaling behavior of the channel network, separating the Mahakam delta into a river delta part and a coastal margin featuring funnel-shaped estuaries.

Figures 7.4 and 7.5 also show the cluster means of the data, binned as a function of s/L. Bins were uniformly distributed between 0 and 1 with a bin-size equal to 0.2. The general trend visible in the clustered values was not sensitive to the exact value of the bin size. Increasing the bin size may slightly shift the location of the break in morphology and hydrodynamics, as a result of the reduction of resolution. Decreasing the bin size increases the number of degrees of

freedom in the linear regression, but the number of data points on each bin reduces accordingly. Our choice of bin size coincides with the minimum number of bins that still reproduced the general trend.

7.4   Downstream Hydraulic Geometry

Here we use the numerical model to simulate scenarios for alternative river discharge and tidal forcing conditions. Simulations include a constant river discharge and a tidal time-series in which the diurnal tides and semidiurnal tides amplify each other maximally during spring tide. Simulated scenarios include high and low river discharge input, with and without the tidal forcing. Model runs span two months, and all quantities are averaged over the entire simulation period.

7.4.1   Including Tides in the Hydraulic Geometry Concept

Consider the hydraulic geometry (HG) relation of the area of a channel network in morphological equilibrium that conveys both river and tidal discharge:

$$A = \alpha \left(Q_r + P \right)^\beta, \tag{7.4}$$

where α and β are two coefficients, Q_r denotes the river discharge and P is the maximum tidal discharge amplitude associated with the tidal prism. At-a-site HG refers to the temporal co-variation of A with both Q_r and P at a specific cross-section, whereas downstream HG describes the spatial variation in A for a constant, channel-forming discharge, such as bankfull discharge (Q_{bf}). Here, we are concerned with the latter, and to keep the analysis simple we assume the bankfull discharge in the river is also formative in the channel network.

If $Q_r/P < 1$, retaining the first two terms of the binomial series expansion of A yields:

$$A \approx \alpha \left(1 + \beta \frac{Q_r}{P} \right) P^\beta = \alpha P^\beta + \alpha \beta Q_r P^{\beta - 1}. \tag{7.5}$$

When Q_r and P are correlated, a relation in log-space between A and P will feature limited ambiguity and a well-resolved exponent β can be obtained from the best-fit line. P can be expressed as a power-law of the form

$$P = c Q_r^d, \tag{7.6}$$

where c and d are two coefficients, and $d < 1$ (see Fig. 7.5). The expression is valid only when considering spatial variations in P and Q_r at a constant frequency of exceedance, since at a given cross section these two are typically inversely correlated. The exponent d controls how the tidal prism is accommodated throughout the fluvial network for a given input bankfull discharge. We expect d to remain constant for different values of Q_{bf}, since the channel network is expected to be in morphological equilibrium. Equation (7.5) can be rewritten as:

$$A \approx \alpha c^\beta \left(1 + \frac{\beta}{c} Q_r^{1-d} \right) Q_r^{d\beta}. \tag{7.7}$$
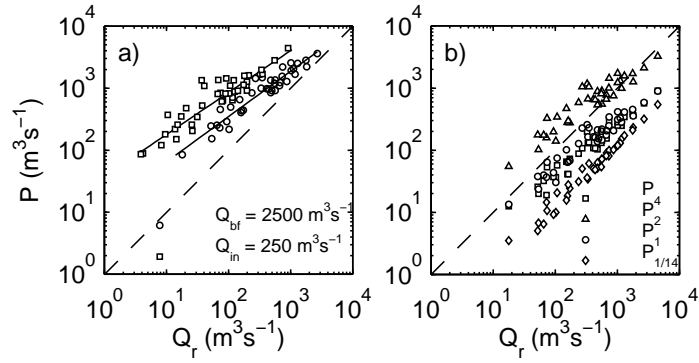
Figure 7.6: a) Maximum tidal discharge amplitude P as a function of river discharge Q_r (see Eq. 7.6). The solid line indicates the best fit line in log space with a slope given by 0.7 ± 0.04, for $Q_{bf} = 2500$ m^{3}s^{-1}, and given by 0.68 ± 0.04, for $Q_{in} = 250$ m^{3}s^{-1}. b) Quarterdiurnal (P_4), semidiurnal (P_2), diurnal (P_1) and fortnightly ($P_{1/14}$) contributions to P as a function of Q_r, for simulations with Q_{bf}. The dashed line indicates the line of perfect agreement.

Eq. (7.7) shows the form of the relation between A and Q_r in tidally-influenced deltas. It provides an explanation why log-log plots of A versus Q_r do not show a linear relation. In addition to the effect of the tidal prism, mechanisms of river-tide interaction cause Q_r to be directly impacted by the tide, provoking mass transport as a result of Stokes drift and differential water level setup (*Buschman et al.*, 2010; *Sassi et al.*, 2011b).

7.4.2   Simplifying Tidal Hydrodynamics

To investigate the downstream HG relations in the delta, we ran the model imposing a constant bankfull river discharge $Q_{bf} = 2500$ m^3 s^{-1} at the upstream boundary. This estimate was obtained from combined flow velocity and water level measurements at the upstream discharge station (*Hidayat et al.*, 2011). Discharge in the tributaries was obtained by applying a rainfall-runoff model calibrated with discharge data from the main river. The contribution of bankfull discharge in the tributaries to the total bankfull discharge in the river was obtained from a lagged non-linear regression between the rainfall-runoff estimates and the discharge measured upstream in the river.

Figure 7.6a shows that channels conveying high river discharge also convey a high tidal discharge. The exponent d in equation (7.6) was estimated to be 0.7 ± 0.04, where the variability is given by the standard error in the linear regression. To assess the applicability of equation (7.6) for varying discharge conditions, we ran the model imposing a very low constant input river discharge at the upstream boundary ($Q_{in} = 250$ m^{3}s^{-1}), yielding $d = 0.68 \pm 0.04$. This indicates that the exponent in equation (7.6) is largely independent of Q_{in}. Contributions to P from the four tidal species are all positively correlated with the river discharge conveyed by the channel (Figure 7.6b), with similar slopes for all species. The semidiurnal species feature the largest tidal prism, followed by the diurnal, quarterdiurnal and fortnightly species.

Figure 7.7a shows the same data as Fig. 7.6a, for simulations with Q_{bf}, but coded for incremental ranges of s/L. The cluster means of P and Q_r (Figure 7.7b), which remove the
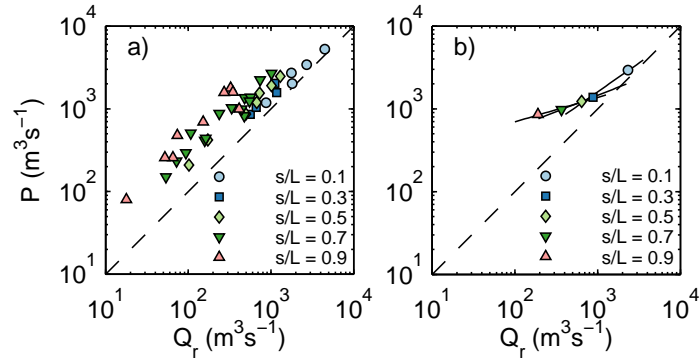
Figure 7.7: a) Maximum tidal discharge amplitude P as a function of river discharge Q_r for simulations with Q_{bf}, but color coded by s/L values, as indicated. b) Same as a) but binned and averaged over s/L. The best-fit line to all data points has a slope of 0.46 ± 0.04. Best-fit lines to the cluster means have slopes of 0.7 ± 0.1, 0.4 ± 0.02 and 0.3 ± 0.07 for the sequence from the delta apex to the shore, respectively. The dashed line indicates the line of perfect agreement.

spreading for a given bin of s/L, suggest a nonlinear relation between P and Q_r. The figure also shows a seaward decrease of the exponent d in Eq. (7.6). The same occurs for the low input river discharge (not shown). The exponent that results from fitting a line through all clustered data points coincides with that derived from a best-fit line through values of P and Q_r ($d = 0.46 \pm 0.04$, see Fig. 7.5). The reduction of d is due to the effect the spreading for a constant value of s/L has on the parameter estimation in a log-log plot (e.g. *Asselman*, 2000; *Packard and Birchard*, 2008). Since the spreading increases seaward, values of P and Q_r typically plot in the lower portion of the log-log plot, becoming influential in the parameter estimation (*Cook and Weisberg*, 1982) and hiding possible structures in the relations. Therefore, the reduction in the exponent d partially reflects the variability across distributary branches rather than the inherent variation along the radial or along-channel dimension. The estimation of the exponents can be performed for cross-sections downstream of each distributary channel, or by binning all information from channels corresponding to equal radial distances. We adopt the latter approach, which allows us to quantify the variation of the downstream HG exponent with radial distance to the delta apex.

The transition between river- to tide- dominated hydrodynamics, as reflected in the downstream variation of the exponent d, may be primarily governed by the increasing number of bifurcations. The number of bifurcation nodes in the radial segments a through e in Fig. 7.2 is 1, 2, 4, 8 and 8, and shows a spatial increase of the number of bifurcations only in the landward section up to $s/L = 0.5$. In the landward part of the delta, discharge is divided over a progressively larger number of channels in the downstream direction, but the absolute number of channels remains relatively small. Downstream changes in Q_r and P occur concomitantly and the exponent d tends to unity. In the seaward part, the number of channels is much larger but the number of bifurcations remains constant. Then the exponent d tends to zero, so that P becomes almost independent of Q_r.

Figure 7.8: Log-log plots of the cross-sectional area A and the discharge conveyed by the channel, using a) Q_r, b) $Q_r + P$, c) P and d) $(\phi + 1)Q_r$. Full lines represent the best-fit line through the data. The dashed line indicates the line of equal values ($\beta = 1$).

7.4.3 Linking Tidal Hydrodynamics to Channel Morphology

Figure 7.8 shows log-log plots of the cross-sectional area A and the discharge conveyed by the channel using (a) river discharge Q_r (Eq. 7.7), (b) the maximum tidal discharge amplitude P (Eq. 7.5), (c) the total discharge $Q_r + P$ (Eq. 7.4) and (d) the river discharge scaled with the bifurcation order $\phi+1$. The bifurcation order $\phi+1$ is defined as the number of bifurcations preceding a particular cross-section. The relation between A and Q_r shows a larger spreading and reduced slope when compared to the relation between A and P. $Q_r + P$ shows a nearly unambiguous relation with A. To arrive at a similarly clear relation between A and Q_r, we multiplied Q_r with $\phi+1$ (Fig. 7.8d). This scaling behavior can be simply explained by the downstream reduction in river discharge when the number of branches increases (see *Edmonds and Slingerland*, 2007). Table 7.1 presents a summary of the exponents obtained by fitting a line in log-log space. The close relation between the exponents found for $Q_r + P$ and $(\phi+1)Q_r$ suggests the ratio of tidal discharge to river discharge scales with bifurcation order:

$$\frac{P}{Q_r} \sim \phi. \tag{7.8}$$

This is in qualitative agreement with the results presented in Fig. 7.5.

The cluster means of A and discharge, binned as a function of s/L, depict a non-linear relation which can be approximated by two linear functions (Figure 7.9a through d). The two linear relations correspond to the landward part of the delta in the domain, up to $s/L = 0.5$,

151

Table 7.1: Summary of parameters in log-log plots of the cross-sectional area A of selected cross-sections and the discharge conveyed by the channel, as indicated. The variability is given by the standard error in the linear regression. The goodness of fit is represented by the coefficient of determination R^2. The exponent β obtained with the best-fit to clustered data is denoted with the subscript *land* and the subscript *sea*.

Discharge	$\alpha \pm \delta\alpha$	$\beta \pm \delta\beta$	R^2	$\beta_{land} \pm \delta\beta_{land}$	$\beta_{sea} \pm \delta\beta_{sea}$
P	1.95 ± 0.38	0.86 ± 0.06	0.84	1.2 ± 0.4	-1.2 $\pm$ 0.1
Q_r	4.22 ± 0.40	0.59 ± 0.07	0.67	0.8 ± 0.1	-0.3 $\pm$ 0.1
$Q_r + P$	2.32 ± 0.43	0.77 ± 0.06	0.80	1 ± 0.2	-0.7 $\pm$ 0.1
$(\phi + 1)Q_r$	2.17 ± 0.53	0.78 ± 0.07	0.74	1.1 ± 0.1	-0.6 $\pm$ 0.2

and with the seaward remainder (respectively). Best-fit lines through the clustered values yield constant slopes in the landward part of the delta, and differ in the seaward part (see Table 7.1). These slopes can be interpreted as downstream HG exponents, whose variation across an arc with constant distance to the delta apex shows a transition from the landward to the seaward part of the delta. Negative values of β for the seaward part of the delta stem from the fact that at a given cross-section, channel area scales with the volume of water (the tidal prism) conveyed by the channel. The tidal prism invariably increases in the downstream direction. The trends in β values are the same for both parts of the delta: the absolute value of β is highest for P and lowest for Q_r.

With the best-fit relation between cross-section area and s/L, represented by the solid line in the bottom left panel of Fig. 7.4, characteristic relations can be calculated, which are shown as the continuous curved lines Fig. 7.9. The two linear functions approximate the characteristic relations, which supports the approach to establish these relations in Fig. 7.9. The characteristic relations show a good agreement with the cluster values in the landward part of the delta, whereas some divergence occurs in the seaward part associated with the variation among the distributaries. The results indicate that β in the downstream HG relation of cross-sectional area exhibits an abrupt change along the normalized along-channel distance. In the landward part $\beta \geq 1$ whereas in the seaward part $\beta < 1$. The shift in β coincides with the transition from river- to tide-dominated hydrodynamics. Table 7.1 shows the exponents for binned and un-binned data using $Q_r + P$ and $(\phi + 1)Q_r$ relations are very close to each other. The binning procedure was introduced only to improve the readability of the figures.

The results presented above can be partly understood from existing downstream HG studies in tidal channels. In a single tidal channel, the minimum shear stress τ_s needed to maintain a net zero gradient in the along-channel sediment transport results in downstream HG relations with values of β greater than unity in flood-dominated systems and smaller than unity in ebb-dominated systems (*Friedrichs*, 1995). The abrupt change in the downstream HG exponent may be partly related to an overall transition from flood to ebb dominance in the main distributaries of the Mahakam delta channel network. Towards the delta apex, the decrease in intertidal storage area and deepening of the channels become two competing factors, which may exert a variable influence on the ebb or flood dominance. In the seaward part of the delta, the absence of tidal flats in the numerical model, and the shallowing of the channels, explain flood dominance. However, rather than being driven purely by tides, the ebb/flood transition may
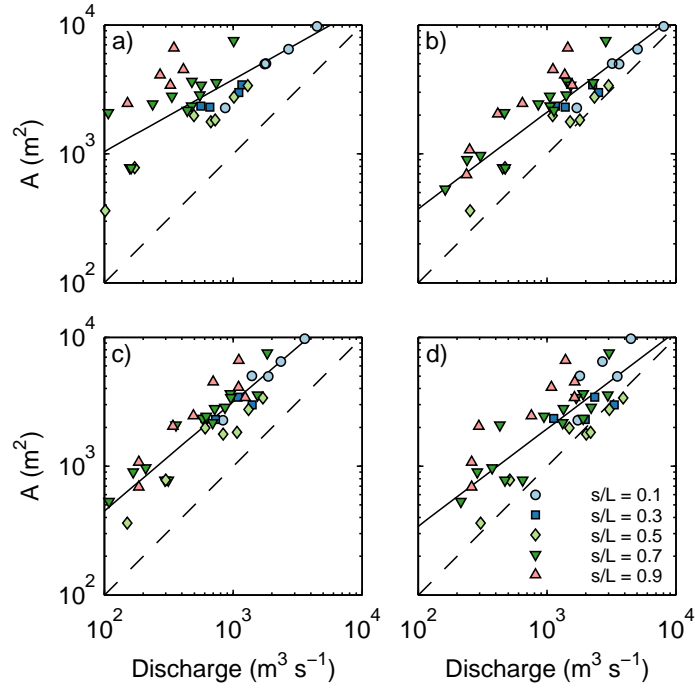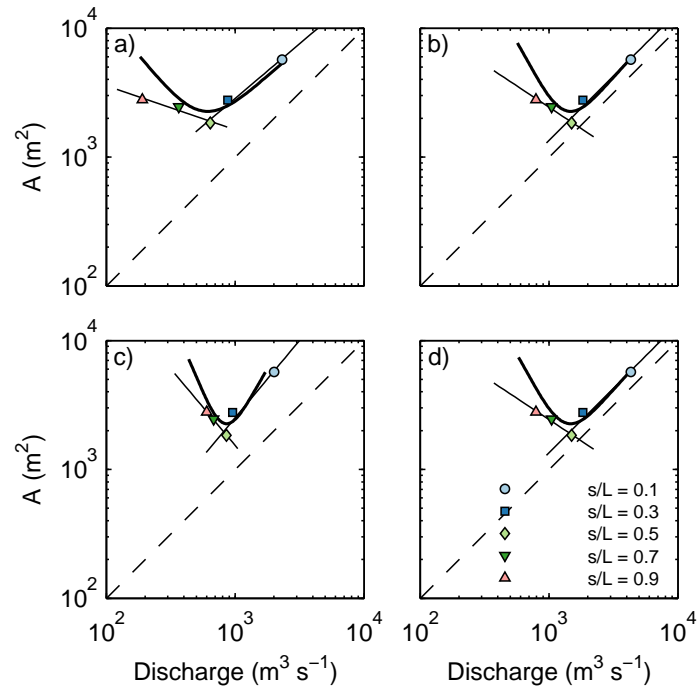
Figure 7.9: Downstream HG of cross-sectional area A and the discharge conveyed by the channel, using a) Q_r, b) $Q_r + P$, c) P and d) $(\phi + 1)Q_r$. Squares depict the cluster means for bins of s/L, as indicated. Solid lines represent the best-fit line through clustered data, in a sequence from the delta apex to the shore. The curve represented by the solid thick line that approximates the clustered data points portrays the relation between A and the discharge conveyed by the channel based on the results presented in Figs. 7.4 and 7.5. The dashed line indicates the line of equal values ($\beta = 1$).

likely be associated to the relative increase in the P/Q_r ratio. Since Q_r decreases seaward with each successive bifurcation, the occurrence of longer flood-flows relative to the tidally averaged discharge increases with bifurcation order. The negative values of the exponents can partly be related to the fact that P is not the tidal prism, but the maximum tidal discharge amplitude.

7.5   Tidal Impact on HG Relations

The downstream HG relations established in the previous sections may depend on the division of river discharge at bifurcations in the delta. The present section investigates the division of water discharge over bifurcates, aiming to isolate the tidal influence on the variation in β as much as feasible. A factor separation analysis (*Stein and Alpert*, 1993) was applied to the time-series of water discharge. Consequently, we ran the model with two sets of forcing conditions: 1) at the upstream boundary, bankfull river discharge is set to 2500 m^{3}s^{-1}, and at the marine boundary the water level is set to equilibrium (no tides); and 2) the model is forced with the same bankfull river discharge at the upstream boundary and with the tidal boundary conditions described in Section 7.2.2.

The division of river discharge at a bifurcation can be quantified as (*Buschman et al.*, 2010; *Sassi et al.*, 2011b):

$$\Psi = \frac{Q_1 - Q_2}{Q_1 + Q_2}. \tag{7.9}$$

For an equal discharge division, the discharge asymmetry index Ψ is zero; when discharge in the southern channel is larger, Ψ is positive up to a value of one when river discharge is carried completely by the southern channel, and vice-versa. We split the discharge asymmetry index in two components such that

$$\Psi = \Psi_{rt} - \Psi_r, \tag{7.10}$$

where Ψ_r denotes the asymmetry in the discharge division from simulations forced with river flow only and Ψ_{rt} denotes the asymmetry in the discharge division from simulations forced with river flow and tides.

The relative difference ratio Ψ/Ψ_r quantifies the tidal impact on river discharge division, as it increases with increasing contributions from tides and river-tide interaction. The tidal impact increases seaward (Figure 7.10), as Ψ/Ψ_r attains values of around -0.3. For $s/L < 0.5$, the tidal impact on river discharge division is low, as values of Ψ/Ψ_r remain below 0.1 in all distributaries. Because Ψ_{rt} is predominantly smaller than Ψ_r, Ψ/Ψ_r is typically negative, and we can conclude that the effect of tides is generally to counteract asymmetry in the division of river discharge at the bifurcations in the Mahakam delta.

Figure 7.11 shows spatial distributions of the quarterdiurnal (D_4), semidiurnal (D_2), diurnal (D_1) and fortnightly ($D_{1/14}$) contributions to surface level variation, averaged over the entire simulation period. In general, both D_4 and $D_{1/14}$ amplify towards the apex whereas D_2 damps out. Tidal damping of the main tidal species is generally attributed to frictional forces. Part of the semidiurnal tidal energy is transferred to the overtide and compound tide frequency bands, predominantly via non-linear interaction in the bottom friction term in the momentum balance.
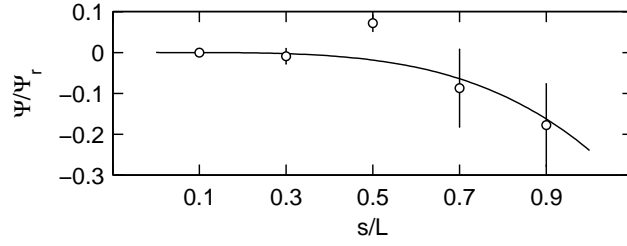
Figure 7.10: Relative difference of discharge asymmetry indexes (Ψ/Ψ_r) as a function of normalized along-channel distance s/L. Circles depict the cluster mean; the error bars denote one standard deviation.

Spatial variations in D_4 and $D_{1/14}$ resemble each other. In strongly convergent channels, the effects of convergence can surpass the effect of bottom friction, causing tidal amplification (*Lanzoni and Seminara*, 1998). D_2 depicts relatively large values in several tidal channels and in sections of distributaries which show to be strongly convergent. The diurnal species D_1 damp out in the southern branch, whereas it remains relatively constant in the northern branch. The outlets of the northern and southern branches show a different response to diurnal tidal forcing, which may be associated to D_1 variation along the coastline. North of the delta, the continental shelf adjacent to the delta is relatively narrow. Inside the delta, small length differences can be the cause of substantial differences in reflection of diurnal tidal energy. Discrepancies in tidal amplitudes (and phases) between channels may lead to a net flux that eventually steers more discharge to a one particular branch. Fig. 7.11 suggests that damping of the main tidal species mostly occurs in the radial direction, showing limited variability across channels along arcs with a constant distance to the delta apex. Only a few (mostly sinuous) channels depict large differences in amplitudes between bifurcating channels.

7.5.1 River-Tide Interaction

Figure 7.12 shows the mean water surface topography based on $\langle \eta \rangle$, where the brackets denote averaging over the entire simulation period (left panel), and the fortnightly contribution to water surface variation $D_{1/14}$ (right panel). The two panels show good resemblance. $D_{1/14}$ can be regarded as a surrogate for the strength of river-tide interaction (*Buschman et al.*, 2009). Since river-tide interactions not only generate $D_{1/14}$ but also result in a steady (non-periodic) rise in elevation (*Godin*, 1999; *Buschman et al.*, 2009), the resemblance in the spatial distributions of $\langle \eta \rangle$ and $D_{1/14}$ for a constant discharge suggests that river-tide interaction contributes substantially to the water surface topography. *Sassi et al.* (2011b) showed that for a seaward bifurcation in the Mahakam delta, the difference in rise of water surface elevation induced by river-tide interaction at a bifurcation led to a substantial reduction of the asymmetry in the division of river discharge, compared to the case without tides. Since the water surface topography $\langle \eta \rangle$ shows a clear relation to $D_{1/14}$, the present chapter generalizes this result, showing differential water level setup to be the dominant mechanism by which tides impact the division of river discharge at these bifurcations. This conclusion is supported by the fact that the ratio $D_{1/14}/\langle \eta \rangle$ (Fig. 7.12) depicts a very close relation to the ratio Ψ/Ψ_r (Fig. 7.10), when both are plotted as a function of normalized along-channel distance s/L.
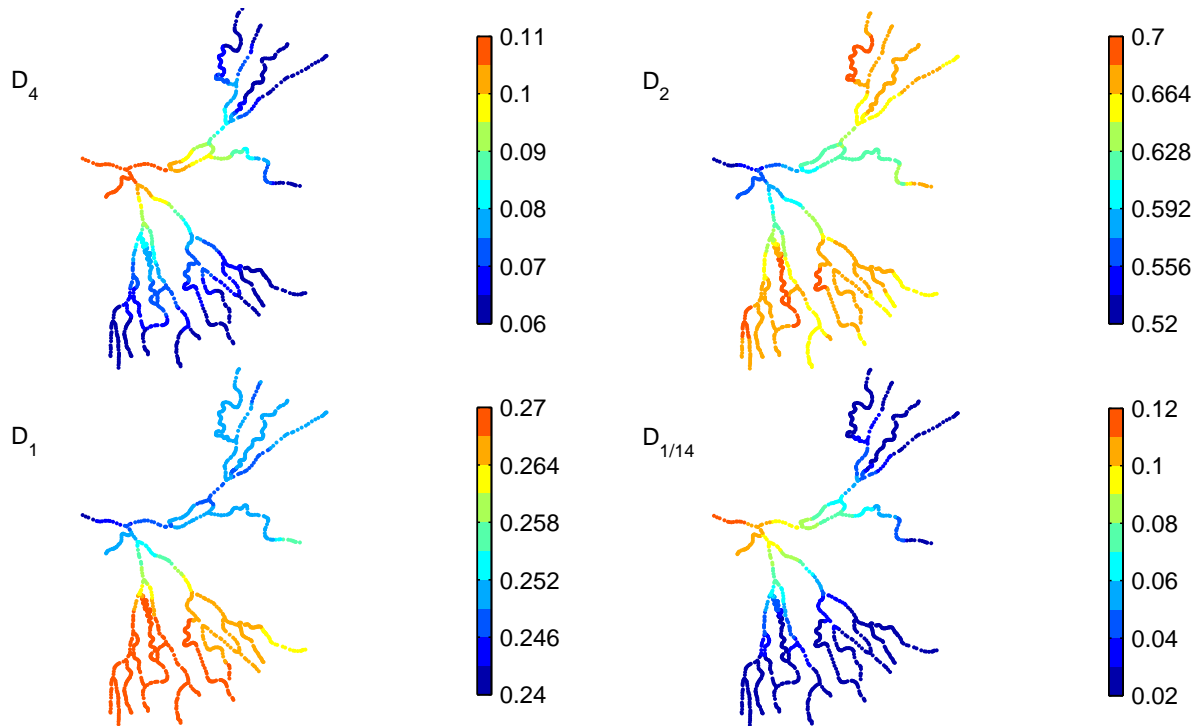
Figure 7.11: Spatial distribution of quarterdiurnal (D_4), semidiurnal (D_2), diurnal (D_1) and fortnightly ($D_{1/14}$) tidal contributions to water surface variation, in meters.
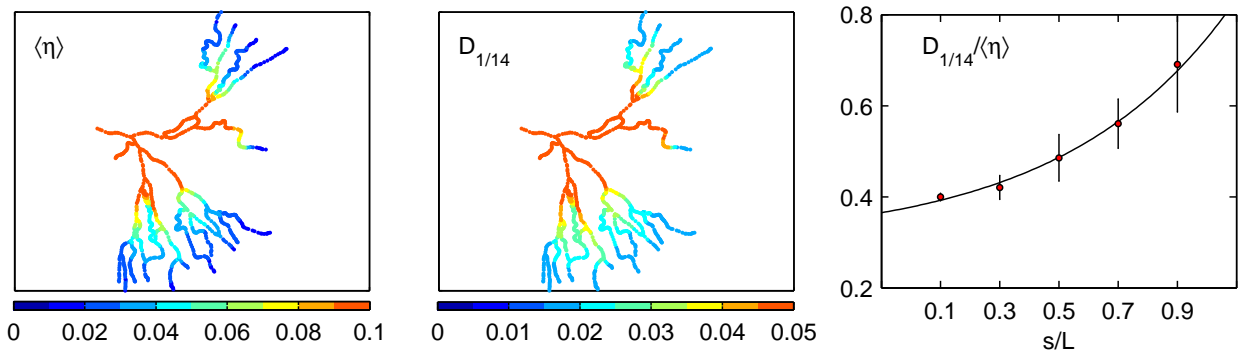
Figure 7.12: Spatial distribution of mean surface water level $\langle\eta\rangle$ and fortnightly tidal contribution to water surface variation $D_{1/14}$, in meters. In both panels the colorscale has been confined in order to better visualize variations towards the sea. Also shown the ratio of $D_{1/14}$ to $\langle\eta\rangle$ as a function of normalized along-channel distance s/L. Circles depict the cluster mean; the error bars denote one standard deviation.

156

Table 7.2: Summary of exponents in downstream HG of cross-sectional area A and flow velocity U. The exponents β and γ were obtained with the best-fit to clustered data and denoted with the subscript *land* and the subscript *sea*, for simulations forced with river flow $((\phi + 1)Q_r)$, and simulations forced with river discharge and tides $(Q_r + P)$. The variability is given by the standard error in the linear regression.

	$\beta_{land} \pm \delta\beta_{land}$		$\beta_{sea} \pm \delta\beta_{sea}$	
A	$(\phi + 1)Q_r$	$Q_r + P$	$(\phi + 1)Q_r$	$Q_r + P$
	1.1 ± 0.07	1.06 ± 0.17	-0.34 ± 0.09	-0.48 ± 0.12
	$\gamma_{land} \pm \delta\gamma_{land}$		$\gamma_{sea} \pm \delta\gamma_{sea}$	
U	$(\phi + 1)Q_r$	$Q_r + P$	$(\phi + 1)Q_r$	$Q_r + P$
	-0.03 ± 0.05	-0.03 ± 0.11	1.27 ± 0.09	1.05 ± 0.08

Figure 7.13 shows the downstream HG relations of the area A and the mean flow velocity U, for simulations forced with river flow (left panels) and simulations forced with river discharge and tides (right panels), using $(\phi+1)Q_r$ and Q_r+P, respectively, as a measure of the discharge conveyed by the channel. Note that for the simulations without tides, U is a mean flow velocity, whereas for simulations with tides, U represents a mean flow velocity plus the amplitude of the tidal species. The values of β and γ in the insets show the slopes of the best-fit line to values of A and U before binning, respectively. Since U is computed as the ratio between $(\phi + 1)Q_r$ (left panels) or $Q_r + P$ (right panels) and A, the sum of the exponents in the area (β) and flow velocity (γ) relations equals unity. Table 7.2 shows the estimates of the downstream HG exponents, separating the river-dominated part of the delta ($0 < s/L \leq 0.5$) from the remaining seaward part. Regarding the linear relations, the sums of the exponents obtained with A and U do not necessarily equal unity, because data has been clustered as a function of the normalized along-channel distance. When tides are included, variation of the exponents are more apparent in the seaward part of the delta than in the landward part. The inclusion of the tides leads to an increase in β_{sea} and to a decrease in γ_{sea}. The same occurs when the procedure is applied to the data before binning. In the landward part of the delta, tides have a limited influence on the exponents. This can be linked to the division of river discharge at the bifurcations, which experiences a significant tidal impact only in the seaward part of the delta beyond $s/L = 0.5$.

The effect of tides on the downstream HG relations of the Mahakam delta is, in general, to increase β and to decrease γ in the seaward part of the delta. For constant river discharge, cross-section areas are larger in the case of tides, due the steady water level setup induced by river-tide interaction. The surface slope steepens towards the sea (*Godin and Martinez*, 1994). In the landward part of the delta, the surface slope approaches asymptotically the surface slope of the river. Differential water level setup induced by river-tide interaction in the Mahakam generally acts to reduce the asymmetry in discharge division, distributing the flow more equally over the downstream branches. This reduces the subtidal peak flow velocities. By counteracting asymmetry in discharge division and reducing peak flow velocity, tides act to stabilize channel morphology.
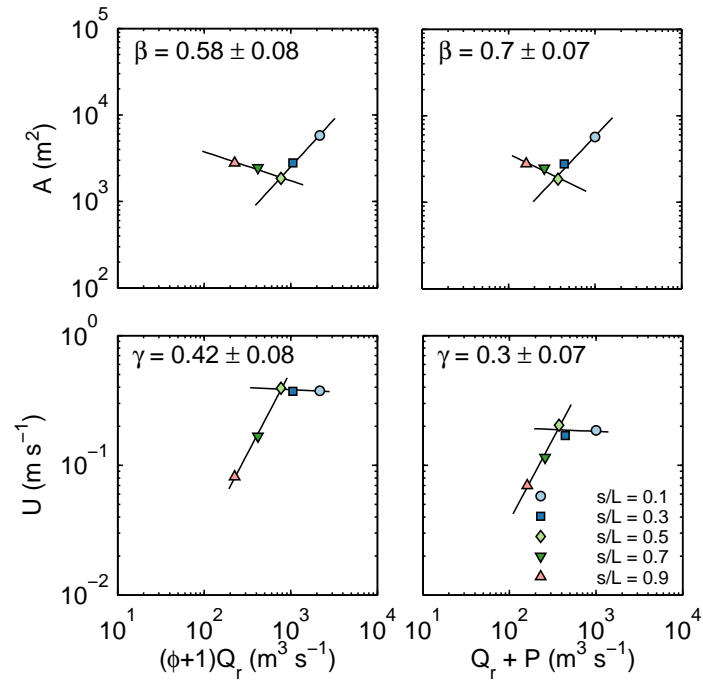
Figure 7.13: Downstream HG relation between cross-sectional area A (top panels) and mean flow velocity U (bottom panels) and the discharge conveyed by the channel, respectively, for simulations forced with river flow (left) and simulations forced with river discharge and tides (right). Squares depict the cluster means for bins of s/L, as indicated. Solid lines represent the best-fit to clustered data, grouped in a sequence from the delta apex to the shore. Exponents β and γ denote the slope of the best-fit line to the data before binning; the variability is given by the standard error in the linear regression.

7.6　Conclusions

A method to quantify the tidal signature on delta morphology has been developed, by applying the hydraulic geometry (HG) concept to a delta channel network. Downstream HG of distributaries in the Mahakam delta features distinct characteristics in two zones. From the delta apex to about half the radial distance to the sea, channel geometry scales similarly to alluvial channel geometries in river deltas, with cross-sectional area and width decreasing gradually in downstream direction, and depths fluctuating around a constant value. In the sea-connected remainder of the delta, distributaries resemble funnel-shaped estuaries, which become increasingly wide and shallow towards the channel mouths. The ratio of maximum tidal discharge, here quantified by the sum of the mean fortnightly, diurnal, semidiurnal and quarterdiurnal tidal discharge amplitudes, and bankfull river discharge scales with bifurcation order. Based on a simple theoretical analysis of HG equations and using a hydrodynamic model, we derive an equation that shows how tides modify downstream HG relations. By clustering selected cross-sections in bins of radial distance to the delta apex, a non-linear HG relation arises from regression analyses of the clustered data. The non-linear HG relation can be approximated by two asymptotic lines. The HG relations in the river-dominated part of the delta are robust because the line determined in a log-log plot of clustered values (Fig. 7.9) coincides with the analysis using the un-binned data (Fig. 7.4 and 7.5). In the tide-dominated part of the delta, the large variation in channel geometry between distributaries and the increased scatter found in cross-sections may mask the general trends. Recent studies on the physical mechanisms governing the division of discharge over downstream branches help to explain the HG complexity in the seaward portion of the delta. Nonlinear interaction of river discharge with the tidal motion creates a water level setup, which depends on channel geometry. The net effect of the tides in the Mahakam delta is to reduce the inequality in discharge division, especially at channel junctions near the sea. This effect, and the fact that part of river discharge is conveyed by tidal channels occasionally connected to the distributary network, exert a strong influence on the downstream HG of distributaries in mixed river-tide dominated deltas such as the Mahakam.

Chapter 8

Synthesis

The previous chapters 2 through 7 have contributed to progress in the fields of delta geomorphology, tidal hydrodynamics and river monitoring, and were each written with a disciplinary focus. In this section I aim to synthesize the main results and to place them into a wider perspective. I will do this by answering the research questions posed in the introduction, and by offering an outlook.

8.1 Answers to Research Questions

8.1.1 Tidal Rivers

Can tides modulate floods and low flows?

There are two ways in which tides can modulate river discharge in tidal rivers. In Chapter 3 it was shown that the mechanism of river-tide interaction creates oscillatory and steady gradients in subtidal water level that can induce modulation of the river flow. These gradients are balanced by subtidal friction; the sources of subtidal friction being river flow and river-tide interaction. For a constant river flow the oscillatory gradient is apparent and predictable, however, river flow can exhibit significant variation of an event-like character at temporal scales

ranging from hours to days (*Hidayat et al.*, 2011). Sudden variations in river flow may obscure the oscillatory flow component (see Fig. 3.7). The magnitude of the steady gradient was found to be strongly negatively correlated with river flow and remained one order of magnitude smaller than the contribution to subtidal friction due to river flow. Thus, it seems implausible that tides can modulate flood flows via the mechanism of river-tide interaction in the River Mahakam, although it is likely that they may have a significant impact on river flow during relatively low discharges. Since the relative magnitude of the contributions to subtidal friction depends on a non-linear fashion on river flow and tidal velocity amplitude, other river systems may radically differ from the present case study. Further understanding will be achieved by studying the behavior of subtidal friction as a function of river flow and tidal velocity amplitude in other tidal rivers, and by performing numerical simulations with idealized numerical models of river-tide interaction.

There is an unexplored way of flood modulation due to tides that may be particular to the River Mahakam. Although semidiurnal and diurnal tides bypass the lakes region (*Hidayat et al.*, 2011), most of the energy associated to the tides that enters the lakes is immediately damped by the lakes. On the contrary, fortnightly oscillations induced by river-tide interaction likely exert an influence on the surface level of the lakes (*Sassi et al.*, 2010). *Hidayat et al.* (2011) found that in the upstream regions of the River Mahakam, river discharge is characterized by variable backwater effects that excludes the option to predict river discharge using rating curves. Variable backwater effects, which can be linked to the presence of the lakes further downstream, may in part be associated with the fortnightly oscillations in subtidal water level induced by river-tide interaction. This periodicity is not observed in measured river discharge time-series upstream because variable backwater has a different dynamics than river-tide interaction. The dynamics of river-tide interaction is linked to the tidal amplitudes, which are controlled by the characteristic speed of propagation of the tidal wave. In this context, the fortnightly wave in the tidal river is a forced wave. The dynamics of the variable backwater, however, is linked to the storage of the lakes, which is very much related to the lakes geometry and connectivity to other basins. It is interesting to realize that any other form of storage such as the presence of floodplains or tributaries, may also induce variable backwater effects upstream when being forced by the fortnightly wave.

Which are the implications of river-tide interaction to sediment transport?

The most apparent implication of river-tide interaction to sediment transport probably relates to flow modulation. For a constant river discharge, subtidal variations in water discharge induced by river-tide interaction can be decomposed in three contributions (*LeBlond*, 1979): 1) the influence of the fortnightly surface elevation on the constant river flow, 2) the fortnightly modulation of the flow itself, and 3) the subtidal Stokes transport. In general, the effect of the fortnightly surface elevation is greater than the fortnightly modulation of the flow and the Stokes transport. Sediment transport is generally a non-linear function of flow speed that can be described by a power-law of exponent $b > 2$ (see Chapter 6). Thus, even small fluctuations in the flow around the constant mean value may have a significant influence on sediment transport. When considering the ubiquitous thresholds for sediment motion, the fortnightly modulation of the flow may assist in driving subtidal variations in sediment transport. In

tidal environments, unique depositional patterns originate from the different mixing conditions associated to the spring-neap cycle (*Jaeger and Nittrouer*, 1995). In tidal environments with significant fluvial influence, these patterns may be reinforced or weakened by the mechanism of river-tide interaction. Knowledge about the fortnightly modulation of sediment transport may help in explaining the characteristic depositional pattern that has been observed in cores taken in the Mahakam delta (*Storms et al.*, 2005).

8.1.2 Tidally-Influenced River Bifurcations

What is the effect of tides on water and sediment discharge division?

Intratidal variations in water and sediment discharge division have been observed at two bifurcations in the Mahakam delta (Chapter 4 and 6). Intratidal variations may or may not cancel out when averaging over several tidal cycles. However, the resulting division can be associated to the local geometry such as the bifurcation angle, the actual morphology such as the presence of bars – the bars were either fixed, migrating, alternating or in the middle of the channel –, and the hydraulic conditions. In Chapter 4 it was shown that subtidal variations in an index quantifying the asymmetry in water discharge division feature a covariation with subtidal water level. Since the division functions for sediment transport are similar to those for water discharge (Chapter 6), subtidal sediment discharge division is expected to feature a covariation with subtidal water level too. In the simulations, subtidal water level was mainly controlled by the fortnightly wave and the asymmetry in discharge division was explained by the imbalance between the Stokes and the return transports. When averaging over successive spring-neap cycles, fortnightly variations cancel out and the resulting effect of tides on discharge division depicts an increase with radial distance to the delta apex (Chapter 7). Several limitations in the hydrodynamical model hamper generalizing these results to sediment transport. For instance, the absence of inter-tidal flooding areas, such as the case in the Mahakam, affects the asymmetry of peak flows, which in turn impacts on differences in sediment transport between branches. Another site-specific aspect of the Mahakam case study is the limited intrusion of salinity. Stratification can potentially induce sediment retention at subtidal time scales, again leading to systematic differences between branches. In such a case, three-dimensional numerical models should be employed to resolve the vertical structure of the flow, and the associated sediment transport.

Which factors control sediment transport?

The preferred direction of sediment transport at a junction depends on regional, intratidal variations in tidal discharge and on local, complex non-linear interactions between the flow and the bathymetry. This effect may be unique of any branch. Yet another factor is that the phase of tidal constituents can be slightly different between branches and a periodic asymmetry in water and sediment discharge division may then be apparent. Unfortunately, 13-h period observations are too limited to distinguish between periodic and permanent asymmetries, which would require continuous monitoring stations (see Chapter 2) instead of surveys capturing a single tidal cycle. In Chapter 6 it was shown that even though the flow at the two bifurcations in the Mahakam delta is characterized by secondary circulation flow cells, sediment discharge

division is solely a function of the characteristics of the flow inherited upstream. If this is a general feature, sediment routing simulations in multi-channel networks (e.g. *Fassnacht*, 1997) remain sensitive to upstream conditions. Small errors in the division at the apex would accumulate further downstream, which calls for a multi-objective (both in time and particularly in space) calibration scheme. Remote sensing techniques (e.g. *Budhiman et al.*, 2012), with all the disadvantages they may have (*Bowers et al.*, 2009), may maximize the trade-off between spatial and temporal resolution and provide the basis for such calibration.

8.1.3 Delta Channel Networks

How is the topology of the Mahakam delta channel network related to the tides?

The topology of distributary channel networks arises as a result of two fundamental mechanisms, namely mouth-bar deposition and channel avulsion (*Jerolmack*, 2009). Mouth-bar distributary lengths scale with the width of the parent channel (*Edmonds and Slingerland*, 2007) whereas avulsive distributary lengths scale with the backwater length (*Jerolmack and Swenson*, 2007). In avulsive distributary channels, the upstream location of river avulsions is set by backwater hydrodynamics (*Lamb et al.*, 2012; *Chatanantavet et al.*, 2012) and the bifurcation stability critically depends on the backwater profiles of the bifurcating channels (*Edmonds*, 2012). Mouth-bar distributaries, in turn, exhibit a fractal structure due to the repeated mouth-bar deposition and bifurcation process (*Edmonds and Slingerland*, 2007). Their bifurcations are prevalently asymmetrical (*Edmonds and Slingerland*, 2008), whereas the network displays an increasing number and decreasing size of channels with distance from the delta apex (*Olariu and Bhattacharya*, 2006; *Edmonds and Slingerland*, 2007; *Jerolmack and Swenson*, 2007). *Jerolmack and Swenson* (2007) argued that in wave-dominated deltas, the diffusive effect of wave action on the coast inhibits mouth-bar bifurcation processes, virtually suppressing the fractal character of the network. In tidally-influenced deltas, a similar mechanism may take place, albeit acting differently. Numerical simulations performed by *Geleynse et al.* (2011) showed that elongated distributaries were formed by the tide-modulated river outflow. Channel elongation may inhibit the repeated process of mouth-bar deposition because the tide-modulated river flow creates a strong ebb-enhanced erosive jet that remobilizes incipient mouth-bars. Interestingly, the Mahakam delta channel network exhibits a mixed fractal/avulsive character that may be potentially linked to the mixed scaling behavior found in hydraulic geometry relations (Chapter 7). Thus, the degree of 'mixing' in network topology may be a direct consequence of tidal-influence.

Which are the implications of river-tide interaction to tidally-influenced river deltas?

It seems rather trivial that in order to quantify tidal-influence on river deltas in-depth knowledge about river-tide interaction is needed. In Chapter 7 it was shown that the variation of river discharge throughout the Mahakam channel network was governed by tides, leading to a clear behavior in the scaling of the network, which was captured by the variation in downstream hydraulic geometry exponents. The tidal impact on river discharge division was found to be driven by river-tide interaction, via the mechanism of differential water-level setup, and showed to be increasingly important towards the sea. These results are backed-up in Chapter 3: river-

tide interaction may be instrumental in driving discharge variations even at low flow rates, as may be the case in the terminal distributaries of the Mahakam delta (see Fig. 3.10). Results from the Mahakam delta show that the scaling behavior of the channel network is mixed and that a break in morphology and hydrodynamics exists at approximately halfway the radial distance from the delta apex to the sea. These results provide quantitative grounds to the, otherwise qualitative, scheme proposed by *Galloway* (1975). Generalizing the downstream hydraulic geometry approach to other deltas influenced by tides may help improving the latter classification scheme, which is heuristic in nature.

8.2 Outlook

8.2.1 Continuous Monitoring of Sediment Discharge

Capturing the widely-ranged spatial and temporal dynamics in sediment transport requires the use of surrogate techniques (*Gray and Gartner*, 2009). Initial efforts in monitoring suspended sediment discharge in fluvial environments showed that ADCPs are a valuable tool for detecting inhomogeneities in suspended sediment transport (*Reichel and Nachtnebel*, 1994). Water discharge can be continuously monitored with horizontally deployed acoustic Doppler current profilers (H-ADCPs); see Chapter 2. H-ADCPs may be used to continuously monitor suspended sediment discharge provided the H-ADCP backscatter signal is transformed to sediment concentration. It would be a sensible future step to explore the ability of H-ADCPs to continuously monitor sediment discharge using additional information from repeated surveys with a ship-mounted ADCP. The generic calibration procedure introduced in Chapter 5 can be used to translate H-ADCP backscatter profiles into horizontal profiles of mass concentration. Due to the long profiling range of the H-ADCP and the subtle changes in mass concentration typically found along a river cross-section, correcting the profiles for sound attenuation due to suspended sediments is utterly important. One approach to this problem is to obtain profiles of the sound attenuation per unit concentration along the H-ADCP profiles, by using ship-mounted ADCP data calibrated using the methodology developed in Chapter 5. The surveys employed to calibrate the discharge method can provide continuous transect data which yield estimates of mass concentration over time, covering nearly the entire cross-section of the river. Once the horizontal profiles of mass concentration are available, a second stage involves exploring the degree in which those H-ADCP estimates of mass concentration can be used to obtain time-series of the total suspended sediment discharge.

8.2.2 Implications for Delta Management

Tidally-influenced deltas such as the Mahakam are ubiquitous in coastal areas and are densely populated and key to national economies (*Goodbred and Saito*, 2012). Deltas in coastal areas around the world sink because of sediment retention upstream, accelerated subsidence due to exploitation of the delta's own sediments, and mean sea-level rise (*Syvitski et al.*, 2009). Human intervention on deltas around the world does not only affect land losses. For the sake of aquaculture and agriculture, deforestation of the delta plain increases the vulnerability of many deltas to coastal erosion (*Restrepo and Kettner*, 2012). As a result of land loss, intensive

dredging, or sand-mining of the delta channels, deltas experience increased tidal intrusion (*Zhang et al.*, 2010). Tidal intrusion has consequences for drinking-water supply and irrigation, but also drives morphological feedbacks in the delta channels that are often difficult to predict or quantify. In general, increased exploitation of natural resources such as sand, water, oil and gas, short-term climatic measures such as the construction of dikes and excessive river engineering of the delta channels can all disrupt the sedimentary balance that maintain river deltas stability. Predicting the response of deltas under the combination of natural and human activity is in an early stage because current modeling tools are too computationally demanding to play a central role in delta management and to provide answers to practitioners and decision-makers.

8.2.3 Hydraulic Geometry Applied to Deltas

This thesis has dealt with several aspects of tidal hydrodynamics and sediment transport in relation to scaling and stability of the Mahakam distributary channel network. The results presented in this thesis contribute in part to the process-based understanding of tidally-influenced deltas in general. Another valuable aspect of this thesis may be the applicability of hydraulic geometry relations and the use of continuous monitoring techniques in delta management practices. HG relations have proven to be of practical use for water management in channel networks (*Ghizzoni et al.*, 2006; *Mohamoud and Parmar*, 2006), for land use planning in wetland restoration projects (*Williams et al.*, 2002; *Hood*, 2002) and for habitat assessment in riverine and tidal networks (*Jowett*, 1998; *Hood*, 2007). In Chapter 7 it was shown downstream HG can be used to map tidal hydrodynamic processes onto a delta channel network, explicitly linking processes with form. Generalized HG relations could be used to interpret channel patterns and morphology in other deltas based on a limited number of input conditions such as tidal range, distance between the delta apex and the sea, and fluvial discharge. Locally, continuous monitoring of environmental flows in combination with downstream HG relations could become an attractive alternative to current modeling efforts, as a tool to explore delta response to external forcing.

Bibliography

Agrawal, Y., and H. Pottsmith (2000), Instruments for particle size and settling velocity observations in sediment transport, *Mar. Geol.*, *168*, 89–114.

Agrawal, Y., W. A., O. Mikkelsen, and H. Pottsmith (2008), Light scattering by random shaped particles and consequences on measuring suspended sediments by laser diffraction, *J. Geophys. Res.*, *113*, doi:10.1029/2007JC004403.

Allen, G. P., and J. L. C. Chambers (1998), *Sedimentation in the Modern and Miocene Mahakam delta*, Indonesian Petroleum Association, Jakarta, 236 pp.

Allen, G. P., D. Laurier, and J. Thouvenin (1977), Sediment distribution patterns in the modern Mahakam delta, in *Proceedings Indonesian Petroleum Association*, vol. 5, pp. 159–178.

Amos, C. L., M. Villatoro, R. Helsby, C. E. L. Thompson, L. Zaggia, G. Umgiesser, V. Venturini, D. Are, T. F. Sutherland, A. Mazzoldi, and F. Rizzetto (2010), The measurement of sand transport in two inlets of Venice lagoon, Italy, *Estuar. Coast. Shelf. Sci.*, *87*(2), 225–236.

Asselman, N. E. M. (2000), Fitting and interpretation of sediment rating curves, *J. Hydrol.*, *234*(3-4), 228–248.

Bagnold, R. A. (1966), An approach to the sediment transport problem from general physics, *U.S. Geol. Surv. Prof. Paper*, (1), 1–37.

Baker, E. T., and J. W. Lavelle (1984), Effect of particle size on the light attenuation coefficient of natural suspensions., *J. Geophys. Res.*, *89*(C5), 8197–8203.

Bartholoma, A., A. Kubicki, T. H. Badewien, and B. W. Flemming (2009), Suspended sediment transport in the German Wadden Sea-seasonal variations and extreme events, *Ocean Dynam.*, *59*(2), 213–225.

Berne, A., and R. Uijlenhoet (2007), Path-averaged rainfall estimation using microwave links: Uncertainty due to spatial rainfall variability, *Geophys. Res. Lett.*, *34*(L07403), doi: 10.1029/2007GL029409.

Bertoldi, W., and M. Tubino (2005), Bed and bank evolution of bifurcating channels, *Water Resour. Res.*, *41*.

Bertoldi, W., and M. Tubino (2007), River bifurcations: Experimental observations on equilibrium configurations, *Water Resour. Res.*, *43*(10), doi:10.1029/2007WR005907.

Biron, P. M., S. N. Lane, A. G. Roy, K. F. Bradbrook, and K. S. Richards (1998), Sensitivity of bed shear stress estimated from vertical velocity profiles: The problem of sampling resolution, *Earth Surf. Process. Landforms*, *23*(2), 133–139.

Blanckaert, K., and H. J. de Vriend (2010), Meander dynamics: A nonlinear model without curvature restrictions for flow in open-channel bends, *J. Geophys. Res.*, *115*(4), doi: 10.1029/2009JF001301.

Bolla-Pitaluga, M., R. Repetto, and M. Tubino (2003), Channel bifurcation in braided rivers: equilibrium configurations and stability, *Water Resour. Res.*, *39*, doi: 10.1029/2001WR001112.

Boss, E., W. Slade, and P. Hill (2009), Effect of particulate aggregation in aquatic environments on the beam attenuation and its utility as a proxy for particulate mass, *Opt. Express*, *17*(11), 9408–9420.

Bowers, D. G., K. M. Braithwaite, W. A. M. Nimmo-Smith, and G. W. Graham (2009), Light scattering by particles suspended in the sea: The role of particle size and density, *Cont. Shelf Res.*, *29*(14), 1748–1755.

Budhiman, S., M. Suhyb Salama, Z. Vekerdy, and W. Verhoef (2012), Deriving optical properties of Mahakam Delta coastal waters, Indonesia using in situ measurements and ocean color model inversion, *ISPRS J. Photogramm.*, *68*(1), 157–169.

Buijsman, M. C., and H. Ridderinkhof (2007), Water transport at subtidal frequencies in the Marsdiep inlet, *J. Sea Res.*, *58*(4), 255–268.

Bunt, J. A. C., P. Larcombe, and C. F. Jago (1999), Quantifying the response of optical backscatter devices and transmissometers to variations in suspended particulate matter, *Cont. Shelf Res.*, *19*(9), 1199–1220.

Burge, L. (2006), Patterns of channel bifurcation in gravel bed rivers, *Earth Surf. Process. Landforms*, *31*, 1211–1226.

Buschman, F. A., A. J. F. Hoitink, M. Van Der Vegt, and P. Hoekstra (2009), Subtidal water level variation controlled by river flow and tides, *Water Resour. Res.*, *45*(10), doi: 10.1029/2009WR008167.

Buschman, F. A., A. J. F. Hoitink, M. Van Der Vegt, and P. Hoekstra (2010), Subtidal flow division at a shallow tidal junction, *Water Resour. Res.*, *46*(12), doi:10.1029/2010WR009266.

Buschman, F. A., A. J. F. Hoitink, S. M. de Jong, P. Hoekstra, H. Hidayat, and M. G. Sassi (2012), Suspended sediment load in the tidal zone of an Indonesian river, *Hydrol. Earth Syst. Sci.*, *16*(11), 4191–4204, doi:10.5194/hess-16-4191-2012.

Camenen, B. (2007), Simple and general formula for the settling velocity of particles, *J. Hydraul. Eng.*, *133*(2), 229–233.

Cardoso, A. H., W. H. Graf, and G. Gust (1989), Uniform flow in a smooth open channel., *J. Hydraul. Eng.*, *27*(5), 603–616.

Cellino, M., and W. H. Graf (1999), Sediment-laden flow in open-channels under noncapacity and capacity conditions, *J. Hydraul. Eng.*, *125*(5), 455–462.

Chatanantavet, P., M. P. Lamb, and J. A. Nittrouer (2012), Backwater controls of avulsion location on deltas, *Geophys. Res. Lett.*, *39*(1).

Cheng, N. (1997), Simplified settling velocity formula for sediment particle, *J. Hydraul. Eng.*, *123*(2), 149–152.

Cheng, N., and L. H. C. Chua (2005), Comparisons of sidewall correction of bed shear stress in open-channel flows, *J. Hydraul. Eng.*, *131*(7), 605–609.

Cheng, R., C. Ling, J. Gartner, and P. Wang (1999), Estimates of bottom roughness length and bottom shear stress in South San Francisco Bay, California, *J. Geophys. Res.*, *104*, 7715–7728.

Cook, R. D., and S. Weisberg (1982), *Residuals and Influence in Regression*, Monographs on Statistics and Applied Probability, Chapman and Hall, NY, USA.

Crosato, A., and E. Mosselman (2009), Simple physics-based predictor for the number of river bars and the transition between meandering and braiding, *Water Resour. Res.*, *45*(3), doi: 10.1029/2008WR007242.

D'Alpaos, A., S. Lanzoni, M. Marani, and A. Rinaldo (2010), On the tidal prism-channel area relations, *J. Geophys. Res.*, *115*(1), doi:10.1029/2008JF001243.

Dargahi, B. (2004), Three-dimensional flow modelling and sediment transport in the river Klaralven, *Earth Surf. Process. Landforms*, *29*, 821–852.

Dargahi, B. (2008), Mitigation of sedimentation problems in the lower reach of the river Klaralven, *J. Hydraul. Res.*, *46(2)*, 224–236.

Davies, G., and C. D. Woodroffe (2010), Tidal estuary width convergence: Theory and form in north australian estuaries, *Earth Surf. Process. Landforms*, *35*(7), 737–749.

Davies-Colley, R. J., and D. G. Smith (2001), Turbidity, suspended sediment, and water clarity: A review, *J. Am. Water Resour. As.*, *37*(5), 1085–1101.

de Brye, B., A. de Brauwere, O. Gourgue, T. Kárná, J. Lambrechts, R. Comblen, and E. Deleersnijder (2010), A finite-element, multi-scale model of the Scheldt tributaries, river, estuary and ROFI, *Coast. Eng.*, *57*(9), 850–863.

de Brye, B., S. Schellen, M. Sassi, B. Vermeulen, T. Kárná, E. Deleersnijder, and T. Hoitink (2011), Preliminary results of a finite-element, multi-scale model of the Mahakam Delta (Indonesia), *Ocean Dynam.*, *61*(8), 1107–1120, doi:10.1007/s10236-011-0410-y.

Defendi, V., V. Kovačević, F. Arena, and L. Zaggia (2010), Estimating sediment transport from acoustic measurements in the Venice Lagoon inlets, *Cont. Shelf Res.*, *30*(8), 883–893.

Deines, K. (1999), Backscatter estimation using broadband Acoustic Doppler Current Profilers, in *Proceedings of the IEEE Sixth Working Conference on Current Measurement*, doi: 10.1109/CCM.1999.755249.

Deleersnijder, E., and P. F. J. Lermusiaux (2008), Multi-scale modeling: Nested-grid and unstructured-mesh approaches, *Ocean Dynam.*, *58*(5-6), 335–336.

Deleersnijder, E., V. Legat, and P. F. J. Lermusiaux (2010), Multi-scale modelling of coastal, shelf and global ocean dynamics, *Ocean Dynam.*, *60*, 1357–1359, doi:10.1007/s10236-010-0363-6.

Di Baldassarre, G., and A. Montanari (2009), Uncertainty in river discharge observations: A quantitative analysis, *Hydrol. Earth Syst. Sc.*, *13*(6), 913–921.

Dinehart, R. (2002), Bedform movement recorded by sequential single-beam surveys in tidal rivers, *J. Hydrol.*, *258*, 25–39.

Dinehart, R., and J. Burau (2005a), Averaged indicators of secondary flow in repeated acoustic Doppler current profiler crossings of bends, *Water Resour. Res.*, *41*, doi: 10.1029/2005WR004050.

Dinehart, R., and J. Burau (2005b), Repeated surveys by acoustic Doppler current profiler for flow sediment dynamics in a tidal river, *J. Hydrol.*, *314*, 1 – 21.

Dodov, B., and E. Foufoula-Georgiou (2004), Generalized hydraulic geometry: Insights based on fluvial instability analysis and a physical model, *Water Resour. Res.*, *40(6)*, doi: 10.1029/2004WR003,196.

Dottori, F., M. Martina, and E. Todini (2009), A dynamic rating curve approach to indirect discharge measurement, *Hydrol. Earth Syst. Sc.*, *13*(6), 847–863.

Downing, A., P. D. Thorne, and C. E. Vincent (1995), Backscattering from a suspension in the near field of a piston transducer, *J. Acoust. Soc. Am.*, *97*(3), 1614–1620.

Dronkers, J. J. (1964), *Tidal Computations in Rivers and Coastal Waters*, North-Holland, Amsterdam.

Droppo, I., and E. Ongley (1994), Flocculation of suspended sediment in rivers of southeastern Canada, *Water Res.*, *28*(8), 1799–1809.

Droppo, I. G., G. G. Leppard, D. T. Flannigan, and S. N. Liss (1997), The freshwater floc: A functional relationship of water and organic and inorganic floc constituents affecting suspended sediment properties, *Water, Air, Soil Pollut.*, *99*(1-4), 43–53.

Eaton, B. C., and M. Church (2007), Predicting downstream hydraulic geometry: A test of rational regime theory, *J. Geophys. Res.*, *112*(3), doi:10.1029/2006JF000734.

Edmonds, D., and R. Slingerland (2007), Mechanics of river mouth bar formation: Implications for the morphodynamics of delta distributary networks, *J. Geophys. Res.*, doi: 10.1029/2006JF000574.

Edmonds, D., R. Slingerland, J. Best, D. Parsons, and N. Smith (2010), Response of river-dominated delta channel networks to permanent changes in river discharge, *Geophys. Res. Lett.*, *37*(12), doi:10.1029/2010GL043269.

Edmonds, D. A. (2012), Stability of backwater-influenced river bifurcations: A study of the Mississippi-Atchafalaya system, *Geophys. Res. Lett.*, *39*(8).

Edmonds, D. A., and R. L. Slingerland (2008), Stability of delta distributary networks and their bifurcations, *Water Resour. Res.*, *44*(9), doi:10.1029/2008WR006992.

Edmonds, D. A., and R. L. Slingerland (2010), Significant effect of sediment cohesion on delta-morphology, *Nature Geosci.*, *3*(2), 105–109.

El-Jabi, N., G. Wakim, and S. Sarraf (1992), Stage-discharge relationship in tidal rivers, *J. Waterw. Port. C. Div.*, *118(2)*, 166–174.

Ericson, J. P., C. J. Vorosmarty, S. Lawrence Dingman, L. G. Ward, and M. Meybeck (2006), Effective sea-level rise and deltas: causes of change and human dimension implications, *Global Planet. Change*, *50*, 63–82.

Fagherazzi, S., and D. J. Furbish (2001), On the shape and widening of salt marsh creeks, *J. Geophys. Res.*, *106*(C1), 991–1003, doi:10.1029/1999JC000115.

Fagherazzi, S., E. J. Gabet, and D. J. Furbish (2004), The effect of bidirectional flow on tidal channel planforms, *Earth Surf. Process. Landforms*, *29*(3), 295–309.

Fassnacht, S. R. (1997), A multi-channel suspended sediment transport model for the Mackenzie Delta, Northwest Territories, *J. Hydrol.*, *197*, 128–145.

Federici, B., and C. Paola (2003), Dynamics of channel bifurcations in noncohesive sediments, *Water Resour. Res.*, *39*, doi:10.1029/2002WR001434.

Flinchem, E. P., and D. A. Jay (2000), An introduction to wavelet transform tidal analysis methods, *Estuar. Coast. Shelf. Sci.*, *51*(2), 177–200.

Friedrichs, C., and D. Aubrey (1988), Non-linear tidal distortion in shallow well-mixed estuaries: a synthesis, *Estuar. Coast. Shelf. Sci.*, *27*, 521–545.

Friedrichs, C. T. (1995), Stability shear stress and equilibrium cross-sectional geometry of sheltered tidal channels, *J. Coast. Res.*, *11*(4), 1062–1074.

Friedrichs, C. T., and D. G. Aubrey (1994), Tidal propagation in strongly convergent channels, *J. Geophys. Res.*, *99*(C2), 3321–3336.

Frings, R. M., and M. Kleinhans (2008), Complex variations in sediment transport at three large river bifurcations during discharge waves in the river Rhine, *Sedimentology*, doi: 10.1111/j.1365-3091.2007.00940.x.

Fugate, D. C., and C. T. Friedrichs (2002), Determining concentration and fall velocity of estuarine particle populations using ADV, OBS and LISST, *Cont. Shelf Res.*, *22*, 1867–1886.

Galappatti, G., and C. B. Vreugdenhil (1985), Depth-integrated model for suspended sediment transport., *J. Hydraul. Res.*, *23*(4), 359–377.

Gallo, M. N., and S. B. Vinzon (2005), Generation of overtides and compound tides in Amazon estuary, *Ocean Dynam.*, *55*(5-6), 441–448.

Galloway, W. E. (1975), *Deltas, Models for Exploration*, chap. Process framework for describing the morphologic and stratigraphic evolution of deltaic depositional systems, pp. 87–98.

Gartner, J. (2004), Estimating suspended solids concentrations from backscatter intensity measured by acoustic Doppler current profiler in San Francisco Bay, California, *Mar. Geol.*, *211*, 169 – 187.

Gartner, J., and K. Carder (1979), Method to determine specific gravity of suspended particles using an electronic particle counter, *J. Sediment. Petrol.*, *49*, 631–633.

Gartner, J., R. Cheng, P. Wang, and K. Richter (2001), Laboratory and field evaluations of the LISST-100 instrument for suspended particle size determinations, *Mar. Geol.*, *175*, 199–219.

Gastaldo, R. (1992), Sediment facies, depositional environments, and distribution of phytoclasts in the recent Mahakam river delta, Kalimantan, Indonesia, *Tech. rep.*, Society for sedimentary geology.

Geleynse, N., J. E. A. Storms, D. J. R. Walstra, H. R. A. Jagers, Z. B. Wang, and M. J. F. Stive (2011), Controls on river delta formation; insights from numerical modelling, *Earth Planet. Sc. Lett.*, *302*(1-2), 217–226.

Ghizzoni, T., M. Lomazzi, G. Roth, and R. Rudari (2006), Regional scale analysis of the altimetric stream network evolution, *Adv. Geosci.*, *7*, 79–83.

Godin, G. (1985), Modification of river tide by the discharge, *J. Waterw. Port. C. Div.*, *111(2)*, 257–274.

Godin, G. (1991a), Tidal hydraulics of Saint John river, *J. Waterw. Port. C. Div.*, *117(1)*, 19–28.

Godin, G. (1991b), Compact approximations to the bottom friction term, for the study of tides propagating in channels, *Cont. Shelf Res.*, *11(7)*, 579–589.

Godin, G. (1999), The propagation of tides up rivers with special considerations on the Upper Saint Lawrence River, *Estuar. Coast. Shelf. Sci.*, *48*, 307–324.

Godin, G., and A. Martinez (1994), Numerical experiments to investigate the effects of quadratic friction on the propagation of tides in a channel, *Cont. Shelf Res.*, *14(7)*, 723–748.

Gonzalez-Castro, J., and M. Muste (2007), Framework for estimating uncertainty of ADCP measurements from a moving boat by standardized uncertainty analysis, *J. Hydraul. Eng.*, *13(12)*, 1390–1410.

Goodbred, S., and Y. Saito (2012), *Principles of Tidal Sedimentology*, chap. Tide-dominated deltas, Springer.

Gostiaux, L., and H. van Haren (2010), Extracting meaningful information from uncalibrated backscattered echo intensity data, *J. Atmos. Oceanic Technol.*, *27*(5), 943–949.

Graf, W. H., and M. Cellino (2002), Suspension flows in open channels; experimental study, *J. Hydraul. Res.*, *40*(4), 435–448.

Gray, J. R., and J. W. Gartner (2009), Technological advances in suspended-sediment surrogate monitoring, *Water Resour. Res.*, *45*(W00D29), doi:10.1029/2008WR007063.

Green, M. O., and J. D. Boon III (1993), The measurement of constituent concentrations in nonhomogeneous sediment suspensions using optical backscatter sensors, *Mar. Geol.*, *110*(1-2), 73–81.

Grinsted, A., J. C. Moore, and S. Jevrejeva (2004), Application of the cross wavelet transform and wavelet coherence to geophysical times series, *Nonlinear Proc. Geoph.*, *11*(5-6), 561–566.

Groen, P. (1967), On the residual transport of suspended matter by an alternating tidal current, *Neth. J. Sea Res.*, *3*(4), 564–574.

Guo, J. (2002), Logarithmic matching and its applications in computational hydraulics and sediment transport, *J. Hydraul. Res.*, *40*(5), 555–565.

Ha, H. K., J. P. . Maa, K. Park, and Y. H. Kim (2011), Estimation of high-resolution sediment concentration profiles in bottom boundary layer using pulse-coherent acoustic Doppler current profilers, *Mar. Geol.*, *279*(1-4), 199–209.

Hardy, R. J., S. N. Lane, and D. Yu (2011), Flow structures at an idealized bifurcation: A numerical experiment, *Earth Surf. Process. Landforms*, *36*(15), 2083–2096.

Hidayat, H., B. Vermeulen, M. G. Sassi, P. J. J. F. Torfs, and A. J. F. Hoitink (2011), Discharge estimation in a backwater affected meandering river, *Hydrol. Earth Syst. Sc.*, *15*(2), 2717–2728, doi:10.5194/hess-15-2717-2011.

Hidayat, H., D. H. Hoekman, M. A. M. Vissers, and A. J. F. Hoitink (2012), Flood occurrence mapping of the middle Mahakam lowland area using satellite radar, *Hydrol. Earth Syst. Sc.*, *16*, 1805–1816, doi:1607-7938/hess/2012-16-1805.

Hill, A. E., and A. J. Souza (2006), Tidal dynamics in channels: 2. Complex channel networks, *J. Geophys. Res.*, *111*(11).

Hill, P. S., A. R. M. Nowell, and P. A. Jumars (1988), Flume evaluation of the relationship between suspended sediment concentration and excess boundary shear stress, *J. Geophys. Res.*, *93*(C10), 12,499–12,509, doi:10.1029/JC093iC10p12499.

Hill, P. S., J. P. Syvitski, E. A. Cowan, and R. D. Powell (1998), In situ observations of floc settling velocities in Glacier Bay, Alaska, *Mar. Geol.*, *145*(1-2), 85–94.

Hill, P. S., E. Boss, J. P. Newgard, B. A. Law, and T. G. Milligan (2011), Observations of the sensitivity of beam attenuation to particle size in a coastal bottom boundary layer, *J. Geophys. Res.*, *116*(C02023), doi:10.1029/2010JC006539.

Hoitink, A. J. F. (2004), Tidally-induced clouds of suspended sediment connected to shallow-water coral reefs, *Mar. Geol.*, *208*(1), 13–31.

Hoitink, A. J. F. (2008), Comment on "The origin of neap-spring tidal cycles" by Erik P. Kvale [Marine Geology 235 (2006) 5-18], *Mar. Geol.*, *248*(1-2), 122–125, doi: 10.1016/j.margeo.2007.04.001.

Hoitink, A. J. F., and P. Hoekstra (2005), Observations of suspended sediment from ADCP and OBS measurements in a mud-dominated environment, *Coast. Eng.*, *52*, 103 – 118.

Hoitink, A. J. F., P. Hoekstra, and D. S. Van Maren (2003), Flow asymmetry associated with astronomical tides: Implications for the residual transport of sediment, *J. Geophys. Res.*, *108*(10), 13–1, doi:10.1029/2002JC001539.

Hoitink, A. J. F., F. A. Buschman, and B. Vermeulen (2009), Continuous measurements of discharge from a Horizontal ADCP in a tidal river, *Water Resour. Res.*, *45*, W11406, doi: doi:10.1029/2009WR007791.

Holdaway, G. P., P. D. Thorne, D. Flatt, S. E. Jones, and D. Prandle (1999), Comparison between ADCP and transmissometer measurements of suspended sediment concentration, *Cont. Shelf Res.*, *19*(3), 421–441.

Hood, W. G. (2002), Landscape allometry: From tidal channel hydraulic geometry to benthic ecology, *Can. J. Fish. Aquat. Sci.*, *59*(8), 1418–1427.

Hood, W. G. (2007), Scaling tidal channel geometry with marsh island area: A tool for habitat restoration, linked to channel formation process, *Water Resour. Res.*, *43*(3).

Horrevoets, A. C., H. H. G. Savenije, J. N. Schuurman, and S. Graas (2004), The influence of river discharge on tidal damping in alluvial estuaries, *J. Hydrol.*, *294*, 213–228.

Hurther, D., P. D. Thorne, M. Bricault, U. Lemmin, and J. . Barnoud (2011), A multi-frequency Acoustic Concentration and Velocity Profiler (ACVP) for boundary layer measurements of fine-scale flow and sediment transport processes, *Coast. Eng.*, *58*(7), 594–605.

174

Immamoto, H., and T. Ishigaki (1988), Measurement of secondary flow in an open channel, in *Proc., 6th IAHR-APD Congress, Japan*, pp. 513–520.

Islam, G. T., M. Kabir, and A. Nishat (2006), Nodal point relation for the distribution of sediments at channel bifurcation, *J. Hydraul. Eng.*, *132:10*, 1105–1109.

Jaeger, J. M., and C. A. Nittrouer (1995), Tidal controls on the formation of fine-scale sedimentary strata near the Amazon river mouth, *Mar. Geol.*, *125*(3-4), 259–281.

Jay, D., and T. Kukulka (2003), Revising the paradigm of tidal analysis - the uses of non-stationary data, *Ocean Dynam.*, *53*, 110–125.

Jay, D. A. (1991), Green's law revisited: Tidal long-wave propagation in channels with strong topography, *J. Geophys. Res.*, *96*, 20.585–20.598, doi:10.1029/91JC01633.

Jay, D. A. (1997), Interaction of fluctuating river flow with a barotropic tide: A demonstration of wavelet tidal analysis methods, *J. Geophys. Res.*, *102*, 5705–5720, doi:10.1029/96JC00496.

Jay, D. A., and E. P. Flinchem (1999), A comparison of methods for analysis of tidal records containing multi-scale non-tidal background energy, *Cont. Shelf Res.*, *19*, 1695–1732.

Jerolmack, D., and J. Swenson (2007), Scaling relationships and evolution of distributary netwoks on wave-influenced deltas, *Geophys. Res. Lett.*, *34*.

Jerolmack, D. J. (2009), Conceptual framework for assessing the response of delta channel networks to holocene sea level rise, *Quaternary Sci. Rev.*, *28*(17-18), 1786–1800.

Johannesson, H., and G. Parker (1989), Velocity redistribution in meandering rivers, *J. Hydraul. Eng.*, *115*(8), 1019–1039.

Jowett, I. G. (1998), Hydraulic geometry of New Zealand rivers and its use as a preliminary method of habitat assessment, *River Res. Appl.*, *14*(5), 451–466.

Kawanisi, K., and S. Yokosi (1997), Characteristics of suspended sediment and turbulence in a tidal boundary layer, *Cont. Shelf Res.*, *17*(8), 859–875.

Kim, W., A. Dai, T. Muto, and G. Parker (2009), Delta progradation driven by an advancing sediment source: Coupled theory and experiment describing the evolution of elongated deltas, *Water Resour. Res.*, *45*(6), doi:10.1029/2008WR007382.

Kleinhans, M., H. Jagers, E. Mosselman, and C. Sloff (2008), Bifurcation dynamics and avulsion duration in meandering rivers by one-dimensional and three-dimensional models, *Water Resour. Res.*, *44*, doi:10.1029/2007WR005912.

Kolb, M. (1995), Experiences with vessel borne adcps in shallow waters, in *Proc. of the IEEE Fifth Working Conference on Current Measurements*, pp. 79–82, IEEE.

Kostaschuk, R., J. Best, P. Villard, J. Peakall, and M. Franklin (2005), Measuring flow velocity and sediment transport with an acoustic Doppler current profiler, *Geomorphology*, *68*, 25–37.

Kukulka, T., and D. Jay (2003a), Impacts of Columbia river discharge on salmonid habitat: 2. Changes in shallow-water habitat, *J. Geophys. Res.*, *108*, doi:10.1029/2003JC001829.

Kukulka, T., and D. Jay (2003b), Impacts of Columbia river discharge on salmonid habitat: 1. A nonstationary fluvial tide model, *J. Geophys. Res.*, *108*, doi:10.1029/2002JC001382.

Kvale, E. (2006), The origin of neap-spring tidal cycles, *Mar. Geol.*, *235*, 5–18.

Lamb, M. P., J. A. Nittrouer, D. Mohrig, and J. Shaw (2012), Backwater and river plume controls on scour upstream of river mouths: Implications for fluvio-deltaic morphodynamics, *J. Geophys. Res.*, *117*(1).

Lambert, B. (2003), Micropaleontological investigations in the Modern Mahakam Delta, East Kalimantan (Indonesia), *Carnets de Géologie / Notebooks on Geology*, *2*.

Lambrechts, J., R. Comblen, V. Legat, C. Geuzaine, and J. . Remacle (2008a), Multiscale mesh generation on the sphere, *Ocean Dynam.*, *58*(5-6), 461–473.

Lambrechts, J., E. Hanert, E. Deleersnijder, P. Bernard, V. Legat, J. Remacle, and E. Wolanski (2008b), A multiscale model of the hydrodynamics of the whole Great Barrier Reef, *Estuar. Coast. Shelf. Sci.*, *79*, 143–151.

Lane, S. N., and K. S. Richards (1998), High resolution, two-dimensional spatial modelling of flow processes in a multi-thread channel, *Hydrol. Process.*, *12*, 1279–1298.

Lanzoni, S., and G. Seminara (1998), On tide propagation in convergent estuaries, *J. Geophys. Res.*, *103*(C13), doi:10.1029/1998JC900015.

Lanzoni, S., and G. Seminara (2002), Long-term evolution and morphodynamic equilibrium of tidal channels, *J. Geophys. Res.*, *107*(1), doi:10.1029/2000JC000468.

Lavagnini, I., and F. Magno (2007), A statistical overview on univariate calibration, inverse regression, and detection limits: Application to gas chromatography/mass spectrometry technique, *Mass Spectrom. Rev.*, *26*(1), 1–18.

Le Coz, J., G. Pierrefeu, and A. Paquier (2008), Evaluation of river discharges monitored by a fixed side-looking doppler profiler, *Water Resour. Res.*, *44*, W00D09, doi: doi:10.1029/2008WR006967.

LeBlond, P. (1978), On tidal propagation in shallow rivers, *J. Geophys. Res.*, *83*, 4717–4721, doi:10.1029/JC083iC09p04717.

LeBlond, P. (1979), Forced fornightly tides in shallow rivers, *Atmosphere-Ocean*, *17(3)*, 253–264.

Lee, T. H., and D. M. Hanes (1995), Direct inversion method to measure the concentration profile of suspended particles using backscattered sound, *J. Geophys. Res.*, *100*(C2), 2649–2657.

Legleiter, C. J., and P. C. Kyriakidis (2007), Forward and inverse transformations between cartesian and channel fitted coordinate systems for meandering rivers, *Math. Geol.*, *38*, 927–958.

Leopold, L., and T. Maddock (1953), The hydraulic geometry of stream channels and some physiographic implications, *U.S. Geol. Surv. Prof. Paper*, *252*, 57.

Liu, W. ., W. . Chen, R. T. Cheng, M. . Hsu, and A. Y. Kuo (2007), Modeling the influence of river discharge on salt intrusion and residual circulation in Danshuei River estuary, Taiwan, *Cont. Shelf Res.*, *27*(7), 900–921.

Ludwig, K. A., and D. M. Hanes (1990), A laboratory evaluation of optical backscatterance suspended solids sensors exposed to sand-mud mixtures, *Mar. Geol.*, *94*(1-2), 173–179.

Lueck, R. G., and Y. Lu (1997), The logarithmic layer in a tidal channel, *Cont. Shelf Res.*, *17*(14), 1785 – 1801, doi:10.1016/S0278-4343(97)00049-6.

Lutz, G., D. Hubbell, and H. J. Stevens (1975), Discharge and flow distribution, Columbia River estuary, *Tech. rep.*, Geological Survey Professional Paper No. 433-P.

Marttila, H., H. Postila, and B. Kløve (2010), Calibration of turbidity meter and acoustic doppler velocimetry (Triton-ADV) for sediment types present in drained peatland headwaters: Focus on particulate organic peat, *River Res. Appl.*, *26*(8).

McMillan, H., J. Freer, F. Pappenberger, T. Krueger, and M. Clark (2010), Impacts of uncertain river flow data on rainfall-runoff model calibration and discharge predictions, *Hydrol. Process.*, *24*(10), 1270–1284.

Meade, R. H. (1996), *Sea-Level Rise and Coastal Subsidence: Causes, Consequences, and Strategies*, chap. River-sediment inputs to major deltas, pp. 63–85, Springer.

Medwin, H., and C. S. Clay (1998), *Fundamentals of Acoustical Oceanography*, 712 pp., Academic Press, San Diego, USA.

Mikkelsen, O., and M. Pejrup (2000), In situ particle size spectra and density of particle aggregates in a dredging plume, *Mar. Geol.*, *170*, 443–459.

Mikkelsen, O., and M. Pejrup (2001), The use of a LISST-100 laser particle sizer for in-situ estimates of floc size, density and settling velocity, *Geo-Mar. Lett.*, *20*, 187–195.

Milliman, J. D., K. L. Farnsworth, and C. S. Albertin (1999), Flux and fate of fluvial sediments leaving large islands in the East Indies, *J. Sea Res.*, *41*, 97–107.

Milliman, J. D., K. L. Farnsworth, P. D. Jones, K. H. Xu, and L. C. Smith (2008), Climatic and anthropogenic factors affecting river discharge to the global ocean, 1951-2000, *Global Planet. Change*, *62*, 187–194.

Miori, S., R. J. Hardy, and S. N. Lane (2012), Topographic forcing of flow partition and flow structures at river bifurcations, *Earth Surf. Process. Landforms*, *37*(6), 666–679.

Moate, B. D., and P. D. Thorne (2009), Measurements and inversion of acoustic scattering from suspensions having broad size distributions, *J. Acoust. Soc. Am.*, *126*(6), 2905–2917.

Mohamoud, Y. M., and R. S. Parmar (2006), Etimating streamflow and associated hydraulic geometry, the mid-atlantic region, usa, *J. Am. Water Resour. As.*, *42*(3), 755–768.

Moore, S. A., J. Le Coz, D. Hurther, and A. Paquier (2011), On the application of horizontal adcps to suspended sediment transport surveys in rivers, *Cont. Shelf Res.*, doi: 10.1016/j.csr.2011.10.013, article in Press.

Muste, M., K. Yu, I. Fujita, and R. Ettema (2005), Two-phase versus mixed-flow perspective on suspended sediment transport in turbulent channel flows, *Water Resour. Res.*, *41*(10), W10,402–1–W10,402–22.

Neukermans, G., H. Loisel, X. Mériaux, R. Astoreca, and D. McKee (2012), Title in situ variability of mass-specific beam attenuation and backscattering of marine particles with respect to particle size, density, and composition, *Limnol. Oceanogr.*, *57*, 124–144.

Nezu, I., and H. Nakagawa (1993), *Turbulence in open-channel flows*, Balkema, Rotterdam, The Netherlands.

Nezu, I., A. Tominaga, and H. Nakagawa (1993), Field mesurements of secondary currents in straight rivers, *J. Hydraul. Eng.*, *119*, 598–614.

Nielsen, P., and I. A. L. Teakle (2004), Turbulent diffusion of momentum and suspended particles: A finite-mixing-length theory, *Phy. Fluids*, *16*(7), 2342–2348.

Nihei, Y., and A. Kimizu (2008), A new monitoring system for river discharge with H-ADCP measurements and river-flow simulation, *Water Resour. Res.*, *44*, W00D20, doi: 10.1029/2008WR006970.

Nikora, V. I., and D. G. Goring (2002), Fluctuations of suspended sediment concentration and turbulent sediment fluxes in an open-channel flow, *J. Hydraul. Eng.*, *128*(2), 214–224.

Olariu, C., and J. P. Bhattacharya (2006), Terminal distributary channels and delta front architecture of river-dominated delta systems, *J. Sediment. Res.*, *76*(1-2), 212–233.

Orton, G. J., and H. G. Reading (1993), Variability of deltaic processes in terms of sediment supply, with particular emphasis on grain size, *Sedimentology*, *40*(3), 475–512.

Packard, G. C., and G. F. Birchard (2008), Traditional allometric analysis fails to provide a valid predictive model for mammalian metabolic rates, *J. Exp. Biol.*, *211*(22), 3581–3587.

Papanicolaou, A. N., M. Elhakeem, and R. Hilldale (2007), Secondary current effects on cohesive river bank erosion, *Water Resour. Res.*, *43*, W12418, doi:10.1029/2006WR005763.

Parker, G., and E. D. Andrews (1985), Sorting of bed load sediment by flow in meander bends., *Water Resour. Res.*, *21*, doi:10.1029/WR021i009p01361.

Parker, G., C. M. Toro-Escobar, M. Ramey, and S. Beck (2003), Effect of floodwater extraction on mountain stream morphology, *J. Hydraul. Eng.*, *129*(11), 885–895.

Parsons, D., J. Best, S. Lane, O. Orfeo, R. Hardy, and R. Kostaschuk (2007), Form roughness and the absence of secondary flow in a large confluence-diffluence, Rio Paraná, Argentina, *Earth Surf. Process. Landforms*, *32*, 155 – 162.

Pedocchi, F., and M. H. Garcia (2006), Noise-resolution trade-off in projection algorithms for laser diffraction particle sizing, *Appl. Opt.*, *45*(15), 3620–3628.

Petersen-Overleir, A. (2006), Modelling stage-discharge relationships affected by hysteresis using the Jones formula and nonlinear regression, *Hydrolog. Sci. J.*, *51*(3), 365–388.

Reichel, G., and H. P. Nachtnebel (1994), Suspended sediment monitoring in a fluvial environment: advantages and limitations applying an acoustic Doppler current profiler, *Water Res.*, *28(4)*, 751–761.

Rennie, C., and R. Millar (2004), Measurement of the spatial distribution of fluvial bedload transport velocity in both sand and gravel, *Earth Surf. Process. Landforms*, *29*, 1173–1193.

Rennie, C., and F. Rainville (2006), Case study of precision of GPS differential correction strategies: influence on aDcp velocity and discharge estimates, *J. Hydraul. Eng.*, *132(2)*, 225–234.

Rennie, C., R. Millar, and M. Church (2002), Measurement of bed load velocity using an Acoustic Doppler Current Profiler, *J. Hydraul. Eng.*, *128:5*, 473–483.

Restrepo, J. D., and A. Kettner (2012), Human induced discharge diversion in a tropical delta and its environmental implications: The Patía River, Colombia, *J. Hydrol.*, *424-425*, 124–142.

Richards, S. D., A. D. Heathershaw, and P. D. Thorne (1996), The effect of suspended particulate matter on sound attenuation in seawater, *J. Acoust. Soc. Am.*, *100*(3), 1447–1450.

Richardson, W., and C. Thorne (1998), Secondary currents around braid bar in Brahmaputra river, Bangladesh, *J. Hydraul. Eng.*, *124:3*, 325–328.

Richardson, W., and C. Thorne (2001), Multiple thread flow and channel bifurcation in a braided river: Brahmaputra-Jamuna River, Bangladesh, *Geomorphology*, *38*, 185–196.

Rinaldo, A., S. Fagherazzi, S. Lanzoni, M. Marani, and W. E. Dietrich (1999), Tidal networks 3. Landscape-forming discharges and studies in empirical geomorphic relationships, *Water Resour. Res.*, *35*(12), doi:10.1029/1999WR900238.

Rose, C. P., and P. D. Thorne (2001), Measurements of suspended sediment transport parameters in a tidal estuary, *Cont. Shelf Res.*, *21*(15), 1551–1575.

Sassi, M., S. Schellen, B. Vermeulen, Hidayat, E. Deleersnijder, and A. Hoitink (2010), Tidal impact on river discharge in the Mahakam River and Distributary Channels, East Kalimantan, Indonesia, in *Proceedings of the 15th Physics of Estuaries and Coastal Seas (PECS) conference, Colombo, Sri Lanka, 14–17 September 2010*.

Sassi, M., A. Hoitink, B. Vermeulen, and Hidayat (2011a), Discharge estimation from H-ADCP measurements in a tidal river subject to sidewall effects and a mobile bed, *Water Resour. Res.*, *47*(W06504), doi:10.1029/2010WR009972.

Sassi, M., A. Hoitink, B. de Brye, and E. Deleersnijder (2012a), Downstream hydraulic geometry of a tidally influenced river delta, *J. Geophys. Res.*, *117*(F04022), doi:10.1029/2012JF002448.

Sassi, M., A. Hoitink, and B. Vermeulen (2012b), Impact of sound attenuation by suspended sediment on ADCP backscatter calibrations, *Water Resour. Res.*, *48*(W09520), doi: 10.1029/2012WR012008.

Sassi, M. G., A. Hoitink, B. de Brye, B. Vermeulen, and E. Deleersnijder (2011b), Tidal impact on the division of river discharge over distributary channels in the Mahakam Delta, *Ocean Dynam.*, *61*, 2211–2228, doi:10.1007/s10236-011-0473-9.

Savenije, H. (2001), A simple analytical expression to describe tidal damping or amplification, *J. Hydrol.*, *243*, 205–215.

Savenije, H. H. G., and E. J. M. Veling (2005), Relation between tidal damping and wave celerity in estuaries, *J. Geophys. Res.*, *110*(4), 1–10, doi:10.1029/2004JC002278.

Shiono, K., and D. W. Knight (1991), Turbulent open-channel flows with variable depth across the channel, *J. Fluid Mech.*, *222*, 617–646.

Sime, L., R. Ferguson, and M. Church (2007), Estimating shear stress from moving boat acoustic Doppler velocity measurements in a large gravel bed river, *Water Resour. Res.*, *43*, W03418, doi:10.1029/2006WR005069.

Simpson, M. (2001), Discharge measurements using a broad-band acoustic doppler current profiler, *Tech. rep.*, United States Geological Survey.

Simpson, M., and R. Bland (2000), Methods for accurate estimation of net discharge in a tidal channel, *IEEE J. Ocean. Eng.*, *25(4)*, 437–445.

Singh, V. P., C. T. Yang, and Z. Q. Deng (2003), Downstream hydraulic geometry relations: 1. Theoretical development, *Water Resour. Res.*, *39*(12), SWC21–SWC215, doi: 10.1029/2003WR002484.

Slingerland, R., and N. D. Smith (1998), Necessary conditions for a meandering-river avulsion, *Geology*, *26*, 435–438.

Souza, A. J., L. G. Alvarez, and T. D. Dickey (2004), Tidally induced turbulence and suspended sediment, *Geophys. Res. Lett.*, *31*(20), L20,309 1–5.

Stein, U., and P. Alpert (1993), Factor separation in numerical simulations, *J. Atmos. Sci.*, *50*(4), 2107–2115.

Storms, J. E. A., R. M. Hoogendoorn, M. A. C. Dam, A. J. F. Hoitink, and S. B. Kroonenberg (2005), Late-Holocene evolution of the Mahakam delta, East Kalimantan, Indonesia, *Sedim. Geol.*, *180(3-4)*, 149–166.

Struiksma, N., K. W. Olesen, C. Flokstra, and H. J. de Vriend (1985), Bed deformation in curved alluvial channels., *J. Hydraul. Res.*, *23*(1), 57–79.

Sukhodolov, A., M. Thiele, and H. Bungartz (1998), Turbulence structure in a river reach with sand bed, *Water Resour. Res.*, *34*(5), 1317–1334.

Syvitski, J. P. (2008), Deltas at risk, *Sustain. Sci.*, *3*, 23–32.

Syvitski, J. P., and Y. Saito (2007), Morphodynamics of deltas under the influence of humans, *Global Planet. Change*, *57*, 261–282.

Syvitski, J. P., C. J. Vorosmarty, A. J. Kettner, and P. Green (2005a), Impact of humans on the flux of terrestrial sediment to the global coastal ocean, *Science*, *308*, 376–380.

Syvitski, J. P., A. J. Kettner, A. Correggiari, and B. W. Nelson (2005b), Distributary channels and their impact on sediment dispersal, *Mar. Geol.*, *222-223*, 75–94.

Syvitski, J. P. M., A. J. Kettner, I. Overeem, E. W. H. Hutton, M. T. Hannon, G. R. Brakenridge, J. Day, C. Vörösmarty, Y. Saito, L. Giosan, and R. J. Nicholls (2009), Sinking deltas due to human activities, *Nature Geosci.*, *2*(10), 681–686.

Talmon, A. M. (1992), Bed topography of river bends with suspended sediment transport, Ph.D. thesis, Communications on Hydraulic & Geotechnical Engineering - Delft University of Technology.

Tanabe, S., T. K. O. Ta, V. L. Nguyen, M. Tateishi, I. Kobayashi, and Y. Saito (2003), Delta evolution model inferred from the Holocene Mekong Delta, Southern Vietnam, in *Tropical Deltas of Southeast Asia: Sedimentology, Stratigraphy, and Petroleum Geology*, edited by F. H. Sidi, pp. 175–188, SEPM Special Publication.

Tanabe, S., Y. Saito, Q. Lan Vu, T. J. J. Hanebuth, Q. Lan Ngo, and A. Kitamura (2006), Holocene evolution of the Song Hong (Red River) delta system, northern Vietnam, *Sedim. Geol.*, *187*(1-2), 29–61.

Thomas, R. E., D. R. Parsons, S. D. Sandbach, G. M. Keevil, W. A. Marra, R. J. Hardy, J. L. Best, S. N. Lane, and J. A. Ross (2011), An experimental study of discharge partitioning and flow structure at symmetrical bifurcations, *Earth Surf. Process. Landforms*, *36*(15), 2069–2082.

Thorne, P. D., and D. M. Hanes (2002), A review of acoustic measurement of small-scale sediment processes, *Cont. Shelf Res.*, *22*, 603–632.

Thorne, P. D., and R. Meral (2008), Formulations for the scattering properties of suspended sandy sediments for use in the application of acoustics to sediment transport processes, *Cont. Shelf Res.*, *28*(2), 309–317.

Thorne, P. D., P. J. Hardcastle, and R. L. Soulsby (1993), Analysis of acoustic measurements of suspended sediments, *J. Geophys. Res.*, *98*(C1), 899–910.

Thorne, P. D., D. Hurther, and B. D. Moate (2011), Acoustic inversions for measuring boundary layer suspended sediment processes, *J. Acoust. Soc. Am.*, *130*(3), 1188–1200.

Tominaga, A., and I. Nezu (1991), Turbulent structure in compound open-channel flows, *J. Hydraul. Eng.*, *117*(1), 21–41.

Topping, D. J., S. A. Wright, T. S. Melis, and D. M. Rubin (2007), High resolution measurement of suspended-sediment concentrations and grain size in the Colorado River in Grand Canyon using a multi-frequency acoustic system, in *Proceedings of the 10th International Symposium on River Sedimentation*, vol. 3, World Assoc. for Sediment. and Erosion Res., Moscow, Russia.

Traykovski, P., R. Latter, and J. Irish (1999), A laboratory evaluation of the laser in situ scattering and transmissometery instrument using natural sediments, *Mar. Geol.*, *159*, 355–367.

Trump, C. L., and G. O. Marmorino (1997), Calibrating a gyrocompass using ADCP and DGPS data, *J. Atmos. Oceanic Technol.*, *14*, 211–213.

Uijlenhoet, R., and A. Berne (2008), Stochastic simulation experiment to assess radar rainfall retrieval uncertainties associated with attenuation and its correction, *Hydrol. Earth Syst. Sc.*, *12*(2), 587–601.

Urick, R. J. (1948), The absorption of sound in suspensions of irregular particles, *J. Acoust. Soc. Am.*, *20*(3), 283–289.

van Der Wegen, M., B. E. Jaffe, and J. A. Roelvink (2011), Process-based, morphodynamic hindcast of decadal deposition patterns in San Pablo Bay, California, 1856-1887, *J. Geophys. Res.*, *116*(2), doi:10.1029/2009JF001614.

van Rijn, L. C. (1984a), Sediment transport, part III: bed forms and alluvial roughness, *J. Hydraul. Eng.*, *110*, 1733–1754.

van Rijn, L. C. (1984b), Sediment transport, part II: suspended load transport, *J. Hydraul. Eng.*, *110*(11), 1613–1641.

van Rijn, L. C. (2007), Unified view of sediment transport by currents and waves. I: Initiation of motion, bed roughness, and bed-load transport, *J. Hydraul. Eng.*, *133*(6), 649–667.

Vanoni, V., and N. Brooks (1957), Laboratory studies of the roughness and suspended load of alluvial streams, *Tech. rep.*, Sediment. Lab., Calif. Inst. of Technol., Pasadena.

Vermeulen, B., A. J. F. Hoitink, and M. G. Sassi (2011), Coupled ADCPs can yield complete Reynolds stress tensor profiles in geophysical surface flows, *Geophys. Res. Lett.*, *38*(6), doi: 10.1029/2011GL046684.

Vincent, C. E. (2007), *Measuring suspended sand concentration using acoustic backscatter: A critical look at the errors and uncertainties, Geological Society Special Publication*, vol. 274, 7-15 pp., Geological Society Special Publication.

Wall, G. R., E. A. Nystrom, and S. Litten (2008), Suspended sediment transport in the freshwater reach of the Hudson river estuary in eastern New York, *Estuar. Coast.*, *31*, 542–553.

Wang, Z., R. Fokkink, M. de Vries, and A. Langerak (1995), Stability of river bifurcations in 1D morphodynamic models, *J. Hydraul. Res.*, *33*, 739 – 750.

Wang, Z. B. (1992), Theoretical analysis on depth-integrated modelling of suspended sediment transport, *J. Hydraul. Res.*, *30*(3), 403–421.

Wang, Z. B., and J. S. Ribberink (1986), Validity of a depth-integrated model for suspended sediment transport, *J. Hydraul. Res.*, *24*(1), 53–67.

Wang, Z. B., C. Jeuken, and H. J. de Vriend (1999), Tidal asymmetry and residual sediment transport in estuaries, *Tech. Rep. Z2749*, WL—Delft Hydraul., Delft, Netherlands.

Wargo, C. A., and R. Styles (2007), Along channel flow and sediment dynamics at North Inlet, South Carolina, *Estuar. Coast. Shelf. Sci.*, *71*, 669–682.

Warner, J. C., D. Schoellhamer, and G. Schladow (2003), Tidal truncation and barotropic convergence in a channel network tidally driven from opposing entrances, *Estuar. Coast. Shelf. Sci.*, *56*(3-4), 629–639.

Whitehouse, R. (1995), Observations of the boundary layer characteristics and the suspension of sand at a tidal site, *Cont. Shelf Res.*, *15*(13), 1549–1567.

Wilcock, P. R. (1996), Estimating local bed shear stress from velocity observations, *Water Resour. Res.*, *32*(11), 3361–3366, doi:10.1029/96WR02277.

Williams, P. B., M. K. Orr, and N. J. Garrity (2002), Hydraulic geometry: A geomorphic design tool for tidal marsh channel evolution in wetland restoration projects, *Restor. Ecol.*, *10*(3), 577–590.

Wolinsky, M. A., D. A. Edmonds, J. Martin, and C. Paola (2010), Delta allometry: Growth laws for river deltas, *Geophys. Res. Lett.*, *37*(21), doi:10.1029/2010GL044592.

Wren, D. G., B. D. Barkdoll, R. A. Kuhnle, and R. W. Derrow (2000), Field techniques for suspended-sediment measurement, *J. Hydraul. Eng.*, *126*(2), 97–104.

Wright, S., D. Topping, and C. Williams (2010), Discriminating silt-and-clay from suspended-sand in rivers using side-looking acoustic profilers, in *2nd Joint Federal Interagency Conference*, Las Vegas, USA.

Wu, H., J. Zhu, and B. Ho Choi (2010), Links between saltwater intrusion and subtidal circulation in the Changjiang Estuary: A model-guided study, *Cont. Shelf Res.*, *30*(17), 1891–1905.

Yang, S., J. Yu, and Y. Wang (2004a), Estimation of diffusion coefficients, lateral shear stress, and velocity in open channels with complex geometry, *Water Resour. Res.*, *40*, W05202, doi:10.1029/2003WR002818.

Yang, S.-Q. (2005), Interactions of boundary shear stress, secondary currents and velocity, *Fluid Dyn. Res.*, *36*, 121–136.

Yang, S.-Q., S.-K. Tan, and S.-Y. Lim (2004b), Velocity distribution and dip-phenomenon in smooth uniform open channel flows, *J. Hydraul. Eng.*, *130, 12*, 1179–1186.

Yen, B. (2002), Open channel flow resistance, *J. Hydraul. Eng.*, *128:1*, 20–39.

Young, R. A., J. T. Merrill, T. L. Clarke, and J. R. Proni (1982), Acoustic profiling of suspended sediments in the marine bottom boundary layer., *Geophys. Res. Lett.*, *9*(3), 175–178.

Zanichelli, G., E. Caroni, and V. Fiorotto (2004), River bifurcation analysis by physical and numerical modeling, *J. Hydraul. Eng.*, *130:3*, 237–242.

Zhang, W., X. Ruan, J. Zheng, Y. Zhu, and H. Wu (2010), Long-term change in tidal dynamics and its cause in the Pearl River Delta, China, *Geomorphology*, *120*(3-4), 209–223.

Zhou, J., H. H. Chang, and D. Stow (1993), A model for phase lag of secondary flow in river meanders, *J. Hydrol.*, *146*(C), 73–88.

Summary

The Mahakam delta in Indonesia constitutes a text book example of a mixed tide and fluvial dominated delta. Understanding the mechanisms that control the present water and sediment discharge dynamics in the delta is relevant in the contexts of geomorphology, ecology and engineering. In the Mahakam tidal river, the tide interacts with the river flow, modulating the flow and water level at specific frequencies, which in turn affects river discharge and sediment transport. Tidal and subtidal flow modulation along the river is critical to understand discharge regimes as well as sediment transport from sources to sinks. In the Mahakam delta channel network, bifurcations are responsible for the division of water and sediment discharge, contributing to the short-term sediment dispersal, and the middle- to long-term morphology of the delta. Flow and sediment division at tidally-influenced bifurcations depend on upstream as well as on downstream conditions. Thus, bifurcations create an internal feedback in the network that eventually exerts an impact on its evolution. Spatial and temporal aspects of delta evolution can be reflected in scaling relations. This thesis aims to understand tidal hydrodynamics and sediment transport in relation to scaling and stability of the Mahakam distributary network.

The method of approach relies on field-based observations and hydrodynamic modeling. A measuring network is set up along the lower 400 km of the river, for a period of about 18 months. It consists of several water level gauges, distributed along the river and in the delta. Two horizontally deployed acoustic Doppler current profilers (H-ADCPs) are installed near the delta apex and at an upstream location, respectively. Flow velocity, measured with the H-ADCP, is converted to river discharge using conventional shipborne ADCP discharge measurements and a new processing methodology. A depth-averaged, unstructured mesh, finite-element hydrodynamical model is used to simulate the hydrodynamics driven by river discharge and tides. Two-dimensional computational domains are defined to cover the delta, inland lakes and part of the coastal ocean, which are interconnected by a 1D domain representing the river, and several tributaries. Measured bathymetry is used in all domains except for the surrounding sea, where information from a global database is used. The model is forced with tides from a global ocean tidal model at open boundaries, located far away from the delta. At the upstream boundary, the model is forced with the measured discharge series. At the tributaries, discharge series are obtained from a rainfall-runoff model from the main subcatchment. The model is calibrated with water level time-series, measured at three locations in the delta, and flow measurements at the discharge station located near the river mouth, both spanning over the simulation period. A validation is performed by comparing model results with discharge division measurements at the two principal bifurcations in the delta.

Time-series of river discharge (Chapter 2) over one year and a half are decomposed in contributions from the tidal motion, from seasonal fluctuation in river discharge, and from a fortnightly contribution due to river-tide interaction. The fortnightly contribution features time-varying amplitudes, which depend mainly on the spring-neap cycle and on river discharge fluctuations. The mechanism of river-tide interaction is analyzed in detail (Chapter 3), based on observations of water levels along the river and flow velocities obtained at the discharge station. The results indicate that river-tide interaction can drive discharge variations in the tidal river, by imposing an oscillatory and a steady gradient in water level (backwater effect). Even for high river flow and low tidal velocity amplitude, river flow may enhance river-tide

interaction, since the latter varies in a non-linear fashion with the river flow. Due to the semi-deterministic nature of the system, a simple regression model using river flow and tidal velocity amplitude at the river mouth successfully predicts subtidal water levels at upstream locations.

The numerical model is employed to quantify the impact of tides on the division of river discharge over distributary channels (Chapter 4). Results indicate that tides alter the division ratio of river discharge by about 10% in most of the bifurcations, showing an increased tidal impact when moving seaward, where tides alter the division ratio of river discharge up to 30%. The largest tidal effect resulted from differences in mean water level rise induced by river-tide interaction between bifurcating branches, which was termed 'differential water level setup'. It is found that the effect of tides is to counteract the inequality in the division of river discharge that would occur in the case without tides.

To quantify suspended sediments in the Mahakam river and in the distributaries, acoustic backscatter profiles taken with a boat-mounted ADCP are converted to mass concentration of suspended matter. A new calibration strategy is developed (Chapter 5) that uses sets of two water samples, one collected near the ADCP transducer and one collected far away along the acoustic sound path. The proposed calibration approach significantly improves the range of application of ADCPs in field conditions. The generic calibration is applied to translate measurements obtained at the two principal bifurcations in the delta (Chapter 6). Transects are surveyed at bifurcating branches during semidiurnal tidal cycles at neap tide and at spring tide. Flow velocity and acoustical backscatter data are used to quantify suspended sediment discharge. Bed-load transport rates, based on shear velocity estimated from a fit to the measured velocity profiles, are found to be within 10% of the total sediment discharge. The division functions of water and sediment discharge are similar, whereas the division of bed-load is different. The flow in the bifurcating branches is characterized by counter-rotating, secondary-flow cells, which persist throughout the tidal cycle and inhibit the exchange of sediment that would occur when upstream of the bifurcation a single cell would span over the full channel width. Results indicate that the three-dimensional effect of suspended sediment transport at the bifurcations is rather limited, and that the sediment division mainly depends on the characteristics of the flow inherited from upstream.

The scaling behavior of the Mahakam delta channel network is finally investigated by casting downstream Hydraulic Geometry (HG) relations (Chapter 7). Based on a geomorphic analysis, it is shown that channel geometry of the fluvial distributary network scales with the bifurcation order until about halfway the radial distance from the delta apex to the sea, whereas in the remaining part of the delta the distributary channels resemble funnel shaped estuaries. The area of selected cross-sections in the delta features an unambiguous power law relation with total water discharge. Downstream HG exponents of the area show a transition from the landward part to the seaward part of the delta, revealing a clear break in both the morphology and in the hydrodynamic behavior. The variation of river discharge throughout the network, which is largely impacted by backwater effects induced by river-tide interaction, is captured in the variation of downstream HG exponents.

Results from this thesis are relevant for developing monitoring techniques in rivers and estuaries (Chapter 2 and 5), for selecting appropriate models of multi-channel networks (Chapter 4 and 6), and to better understand the evolution of river deltas under the influence of tides (Chapter 3, 4 and 7).

**Netherlands Research School for the
Socio-Economic and Natural Sciences of the Environment**

C E R T I F I C A T E

The Netherlands Research School for the
Socio-Economic and Natural Sciences of the Environment
(SENSE), declares that

Maximiliano Gabriel Sassi

born on 22 January 1978 in Telen, La Pampa, Argentina

has successfully fulfilled all requirements of the
Educational Programme of SENSE.

Wageningen, 11 February 2013

the Chairman of the SENSE board

the SENSE Director of Education

Prof. dr. Rik Leemans

Dr. Ad van Dommelen

The SENSE Research School declares that **Mr. Maximiliano Gabriel Sassi** has successfully fulfilled all requirements of the Educational PhD Programme of SENSE with a work load of 43 ECTS, including the following activities:

SENSE PhD Courses
o Environmental Research in Context
o Research Context Activity: Co-organizing Symposium on 'Role of laboratory experiments in water and sediment dynamics research', Wageningen, 11 February 2010

Other PhD Courses
o Complex flows, turbulence, morphodynamics and ecology in rivers
o PhD Scientific Writing
o Presentation Skills
o Techniques for Writing and Presenting Scientific Papers

Didactic Skills Training
o Supervision of two BSc theses

External training at a foreign research institute
o Setting up SLIM numerical model, UCL Louvain-La-Neuve, November 2012, Belgium

Oral Presentations
o *Tidal impact on river discharge in the Mahakam River and Distributary Channels, East Kalimantan, Indonesia.* Proceedings of the 15th Physics of Estuaries and Coastal Seas (PECS) conference, 14–17 September 2010, Colombo, Sri Lanka
o *Towards an extension of the hydraulic geometry concept to include tidally influenced delta channel networks.* River, Coastal and Estuarine Morphodynamics: RCEM2011, 5-7 September 2011, Beijing, China
o *Hydraulic Geometry of a tidally influenced delta channel network: the Mahakam Delta, East Kalimantan, Indonesia.* AGU Fall Meeting 2011, 1-5 December 2011, San Francisco, USA
o *Quantifying Suspended Sediment Discharge in the Mahakam River and Distributary Channels.* European Geosciences Union General Assembly 2011, 4-8 April 2011, Vienna, Austria
o *Discharge measurements using a horizontal acoustic Doppler current profiler.* Instituto Argentino de Oceanografia, 28-30 March 2011, Bahia Blanca, Argentina
o *Towards a continuous monitoring method of water and sediment discharge.* River Flow 2012, International Association Hydraulic Research, 5-7 September 2012, San Jose, Costa Rica

SENSE Coordinator PhD Education and Research

Mr. Johan Feenstra